OPTIMISATION AND TESTING OF LARGE CERAMIC-IMPREGNATED SOLID OXIDE FUEL CELLS (SOFCs)

Chengsheng Ni

A Thesis Submitted for the Degree of PhD
at the
University of St Andrews

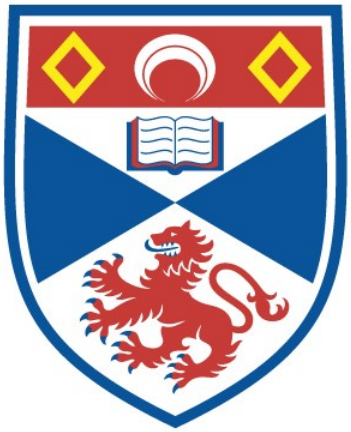

2014

Optimisation and Testing of Large Ceramic-Impregnated Solid Oxide Fuel Cells (SOFCs)

A thesis presented for the degree of PhD

by

Chengsheng NI

University of St Andrews

May 23th 2014

Supervisor: Prof. John T. S. Irvine

Acknowledgement

My years at St Andrews as PhD student have been priceless, fulfilling my greatest aspiration for professional and personal growth. I would like to thank those who have played important roles in the process to the completion of this thesis.

First, I would like to thank my supervisor, Prof. John Irvine, for his guidance, encouragement and trust, which are essential in accomplishing this work. It was a privilege to work with him. The guidance from Professor Ray Gorte and Professor John Vohs of UPenn is also appreciated. I also want to express my gratitude to the examiners of this thesis: Dr Richard Baker from university of St Andrews and Dr Alan Atkinson.from ICL.

Second, the group members in JTSI group also contribute a lot to my work. Without their help and advice, this work will carried out on a more zigzag trail. The help from research fellows Dr Mark Cassidy, Dr Maarten Verbraeken, Dr David Miller and Dr Cristian Savaniu is highly appreciated. I will also be grateful to the assistance from Thuy Muhl, Lanying Lu, and Akshaya Satapathy.

Third, I am also much obliged to the working of the technician team: Julie, Candy, Ross and Sylvia.

Finally, I especially thank my mom, dad, wife, brother and sister-in-law. Without the help of my hardworking parents, I would never have the opportunity to arrive at this stage of PhD study. The constant support from my wife, brother and sister-in-law always encourages me when I encounter setbacks.

Abstract

Solid oxide fuel cells (SOFCs) are the most efficient electrochemical devices to directly convert stored chemical energy to usable electrical energy. The infiltration of ceramic conductors and catalytic metals (e.g. Ni, Pt and Pd) into porous scaffolds that had been pre-sintered onto the electrolyte is regarded as an effective way of promoting the electrode performance via producing nano-scale particles by in-situ sintering at relatively low temperatures. Large-scale fuel cells (5 cm x 5 cm) are prepared with this method and tested to demonstrate its scalability so as to achieve industrial applications. Four configurations are examined in respect of variation in the thickness of cathode, anode and electrolyte to investigate their effect on the infiltration process and electrochemical losses. To further improve infiltration as a method of fabricating high-performance electrodes, much effort is also devoted to optimising and understanding the microstructure of pre-sintered scaffold and its effect on infiltration using image analysis and electrochemical impedance.

First, we have prepared the nano-structured electrodes on the 200-μm thick electrolyte-supported planar fuel cell with a 5 x 5 cm dimension. The 8YSZ scaffold is impregnated with $La_{0.8}Sr_{0.2}Cr_{0.5}Mn_{0.5}O_3$ (LSCM) for the anode and $La_{0.8}Sr_{0.2}FeO_3$ (LSF) for the cathode. The large planar cell achieved a maximum power density of 116 $mWcm^{-2}$ at 700 ^oC and 223 $mWcm^{-2}$ at 800 ^oC in humidified hydrogen. Moreover, with the addition of catalyst of 10 wt.% CeO_2 and 1 wt.% Pd, the cell performance reached 209 $mWcm^{-2}$ at 700 ^oC and 406 $mWcm^{-2}$ at 800 ^oC. Compared to the cell without catalysts, ceria and Pd are efficient in decreasing the electrochemical reaction resistance but making the diffusion resistance more obvious.

Second, supported thin electrolytes are prepared by scalable tape casting to reduce the ohmic losses as that in electrolyte-supported cell. The cell with thick LSF-infiltrated support is very efficient in decreasing the ohmic loss thanks to the high solubility of its nitrate precursors in water and fairly high electric conductivity, but the thick cathode causes higher diffusional losses, especially at 800 ^oC. Even though with thinner electrolyte, the ohmic loss from the cell with thick infiltrated anode is comparable to that of 200-μm electrolyte supported cell. The extra ohmic loss can be attributed to the compositional segregation of $La_{0.7}Sr_{0.3}VO_3$ (LSV) in the infiltration process in the anode, and lower loading, ca. 25 wt %. A trade-off between the

diffusional loss from the cathode and the extra ohmic loss from the thick anode can be achieved by sandwiching the electrolyte between electrodes with identical thickness. A flat large area cell prepared with this method can achieve a high performance of 300 mW cm^{-2} and 489 mW cm^{-2} at 700 ^{o}C and 800 ^{o}C, respectively, if Pd-ceria is added to the anode LSV as catalyst.

Third, image analyses and modelling are performed on the constrained sintering of porous thin film on a rigid substrate to study the evolution of pores at different stages. Result shows that both the anisotropy of the pore former/pores in the green body and transport of materials during the sintering process have effect on the orientation of the final microstructure. Specifically, the in-plane orientation of large-scale pores will be intensified during the constrained sintering process, while those small pores whose shape are subjected to materials transport during sintering tend to erect during the constrained sintering process at 1300 ^{o}C.

Fourth, image analyses and semi-quantification are used to predict the correlation between the microstructure and performance of the LSF-infiltrated electrode. Two types of YSZ powders, Unitec 1-μm powder with a broad particle-size distribution having two maxima at ~ 0.1 μm and 0.8 μm, and Unitec 2-μm powder with only one at ~1 μm are selected to fabricate the porous scaffold for infiltration. The porous structure using Unitec 2-μm powder shows finer YSZ grains and a higher boundary length than the 2-μm powder. Ac impedance on symmetrical cells was used to evaluate the performance of the electrode impregnated with 35-wt.% $La_{0.8}Sr_{0.2}FeO_3$. At 700 ^{o}C, the electrode from Unitec 2-μm powder shows a polarization resistance (R_p) of 0.21 Ω cm^2, and series resistance (R_s) of 8.5 Ω cm^2, lower than the electrode from Unitec 1-μm powder does. The quantitative study on image indicates that Unitec 2-μm powder is better in producing architecture of high porosity or long triple phase boundary (TPB), which is attributed as the reason for the higher performance of the LSF-impregnated electrode.

Finally, oxides of transition metals are doped into the YSZ-infiltrated LSF electrode and the impedances of symmetrical cells are tested to evaluate their effect on the ohmic and polarization resistance. Cobalt oxides are able to reduce the ohmic resistance and polarization resistance only when it is calcined at 700 ^{o}C, but nickel oxide can reduce both the ohmic and polarization resistance if it is well-mixed and fully reacted with the previously infiltrated LSF. Doping of manganese oxide into

LSF-YSZ electrode slightly changes the ohmic resistance but significantly increases the polarization resistance. Detailed analyses of the impact of infiltration process on the impedance data and oxygen reduction process are also presented.

Content

Chapter 1 Introduction

1.1 Background and basics of SOFC

1.1.1 Basic principles of fuel cells

Fuel cells are capable of converting chemical energy in fuels directly into electrical energy, so its energy efficiency is not limited by the Carnot cycle as in the conventional turbine power plant. The maximum efficiency of a thermal power plant is represented in Equation 1-1

$$\eta=\frac{W}{Q}=1-\frac{T_c}{T_h} \qquad 1\text{-}1$$

where W is the work done by the system (energy exiting the system as work),Q is the heat put into the system (heat energy entering the system), T_c is the absolute temperature of the cold reservoir, and T_h is the absolute temperature of the hot reservoir.

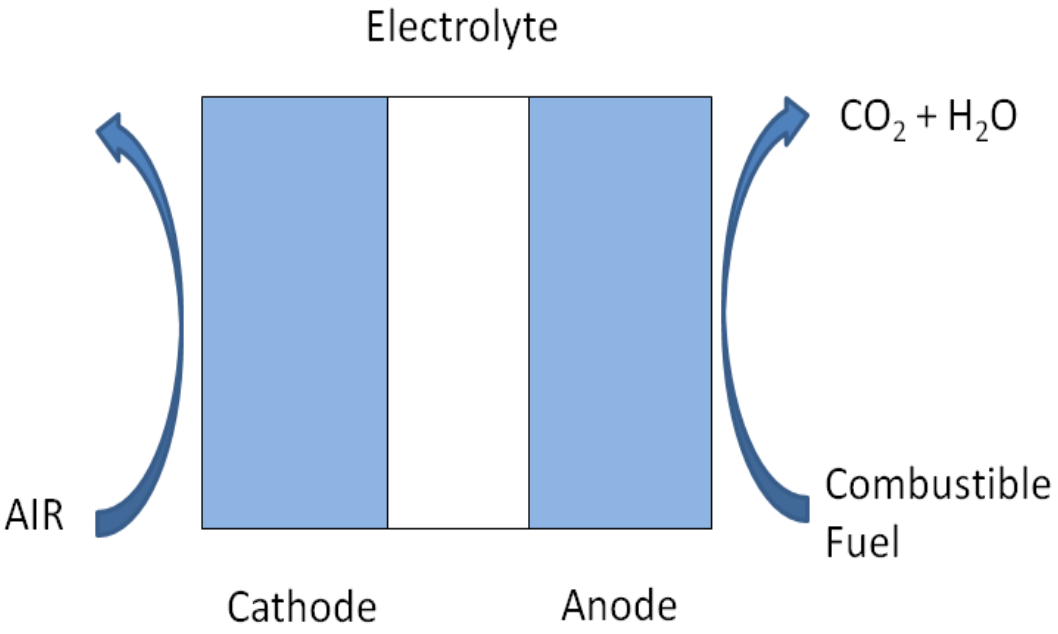

Figure 1 Schematic of the components of fuel cell: an electrolyte is sandwiched by an anode and a cathode.

A fuel cell, as shown in Figure 1, is generally composed of three core parts: an electrolyte, an anode (or fuel electrode) and a cathode (or air electrode). Five kinds of typical fuel cells are classified by the types of electrolytes: 1) polymer electrolyte fuel cell (PEFC), 2) alkaline fuel cell (AFC), 3) phosphoric acid fuel cell (PAFC), 4)

molten carbonate fuel cell (MCFC), and 5) solid oxide fuel cell (SOFC). Broadly, the electrolyte dictates the operating temperature of the fuel cell. For SOFC, the electrolyte is an ionic conductor while electronic insulator. While proton-conducting ceramics are known, the vast majority of work on SOFC has been performed with ceramics that are oxygen-anion conductors. Of the various electrolytes, yttria-stabilised zirconia (YSZ) is the state-of-the-art electrolyte for SOFC thanks to its stability in both oxidising and reducing atmosphere, good durability and relatively high ionic conductivity[1]. The anode contacts with the fuel on one side and electrolyte on the other. It is the place where fuel is oxidized, giving out electrons. On the contrary, the cathode serves to dissociate the oxygen molecules to form oxygen anions.

The electrochemical reactions on both sides of electrolyte involve the transit of ions or molecules in three phase boundaries (TPB). Taking the reactions on a cathode working with a YSZ electrolyte as an example, the oxygen molecules have to reach the surface of the cathode where they break up to form oxygen anions and give out electrons. The oxygen ion will transport through the electrolyte to the anode, while the electrons will pass through the cathode materials and go to current collector. On the anode side of a hydrogen-fuelled SOFC, water vapour will be produced from the combination of proton and the incoming oxygen anion from the electrolyte. To produce proton, the hydrogen molecules need to be dissociated on the anode materials.

A major advantage of SOFCs is that they are highly fuel flexible. Polymer membrane based fuel cells rely on the conduction of protons which requires that hydrocarbons must be reformed and purified to remove carbon monoxide prior to use as fuel. Because SOFCs are based on an O^{2-} conducting electrolyte, this allows the direct use of many higher hydrocarbons without a pre-reforming step.

1.1.2 SOFC thermodynamics

The maximum efficiency of an ideal fuel cell, η, is quoted as shown in Equation 1-2, ΔG^o being the Gibbs Energy and ΔH^o Enthalpy for the reaction of fuel with oxygen to produce water vapour and carbon dioxide, respectively. However, the energy losses in practice are significantly higher than the maximum efficiency because of the heat production and the enthalpy of water vaporisation if the fuel cell is operating higher than 100 ^oC.

$$\eta = \frac{\Delta G^{o}}{\Delta H^{o}} \qquad 1\text{-}2$$

Since the electrons produced at the anode are at a higher potential than those consumed at the cathode, they are therefore able to do work on an external circuit. The equilibrium voltage, *E*, of a fuel cell is determined through the Nernst equation as in

$$E_{nernst} = E^{o} + \frac{RT}{2F}\ln\left(\frac{P(O_{2\ cathode})^{1/2} P(H_{2\ anode})}{P(H_2O_{\ anode})}\right) \qquad 1\text{-}3$$

In this equation, E^{o} is the equilibrium potential for oxidation of H_2 at standard conditions (in Kelvin), which can be calculated by $\Delta G^{o}/2F$. F is Faraday's constant, R gas constant, and $P(O_{2\ cathode})$, $P(H_{2\ anode})$ and $P(H_2O_{\ anode})$ represents the partial pressure of cathodic oxygen, anodic hydrogen and water vapour, respectively.

For a fuel cell with hydrogen in the anode side, the open circuit voltage is very close to the Nernst equation predicted in Equation 1-3, However, when the fuel cell is under load, the potential is to be lower because of the irreversible process in the electrode and electrolyte. The loss from the electrolyte is easy to anticipate, mainly due to the joule heat from its ohmic resistance (R_{ohmic}), and can be calculated based on the resistivity and thickness of the electrolyte. The loss from the electrolyte can be minimised by using a thinner electrolyte.

The losses from the electrode contain two parts: ohomic losses and polarization losses. Generally, the ohmic losses for the electrodes are quite small since the electrode materials are typically made from materials with good electronic conductivity, like nickel in the anode and strontium doped $LaMnO_3$ for the cathode in a state-of-the-art SOFC. Mass transport of the gaseous reactants to the electrolyte interface and slow reaction kinetics for the electrode reactions (e.g. the transfer of electrons) can lead to potential drops, referred to as electrode overpotentials $\eta_{cathode}$ and η_{anode}. The voltage of the fuel cell under current density, *i*, is

$$E = E_{nernst} - i\,(R_{ohmic} + \eta_{cathode} + \eta_{anode}) \qquad 1\text{-}4$$

1.1.3 The three phase boundary (TPB)

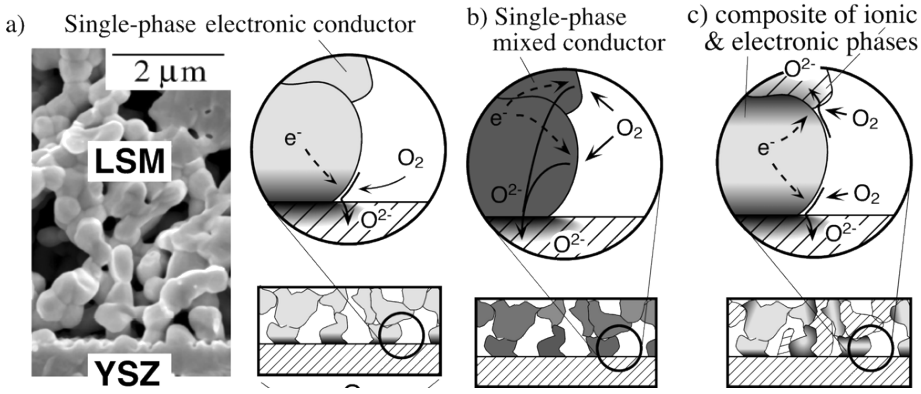

Figure 2 Common strategies for SOFC cathodes: (a) porous single-phase electronically conductive oxide such as (La,Sr)MnO_3 (LSM); (b) porous single-phase mixed conductor; (c) porous two-phase composite. Images are taken from reference 2.

The reactions take place in the vicinity of the three phase boundaries (TPB), which are the dots or lines of the conjunction of the gas, electrolyte and cathode materials[2]. Figure 2 illustrates the TPB in the cathode where oxygen, which wishes to be reduced to O^{2-}, diffuses into the open pores of the electrode and is reduced somewhere within this matrix. For a cathode with negligible ionic conductivity, e.g. LSM in Figure 2(a), reduction of oxygen is generally thought to be confined close to the electrode/electrolyte interface, where the gas has simultaneous access to both the electronically and ionically conductive phases. On the contrary, if the cathode is a mixed ionic and electronic conductor (MIEC), e.g. $La_{0.8}Sr_{0.2}FeO_3$ [3], the reaction sites can be extended to the surface of the MIEC, as shown in Figure 2(b). Another way of extending the reaction site for a purely electronically conductive material is to mix the ionic conductor with electronic conductor to make a composite electrode, as shown in Figure 2(c). The MIEC can also be used to produce such composite electrode. It is important to note that the connectivity of all three phases is essential in order for the reaction site to be effective. If any of the three phases are unable to reach a particular TPB site, the reaction will be unable to proceed at that site. It is a process of achieving balance among the volume and distribution of the three phases to optimise an electrode.

1.2 Materials for a fuel cell

1.2.1 Electrolyte

Various oxides, which conduct oxide ions (O^{2-}) or protons (H^{+}), have been found so far. To be a viable electrolyte for SOFC, it should show high ionic conductivity, low electronic conductivity, and chemically stability in both reducing and oxidizing environment. Of the available oxygen ion conducting materials, three main material systems for the electrolyte are partially cation-substituted ZrO_2, CeO_2 and $LaGaO_3$ and their conductivities are illustrated in Figure 3.

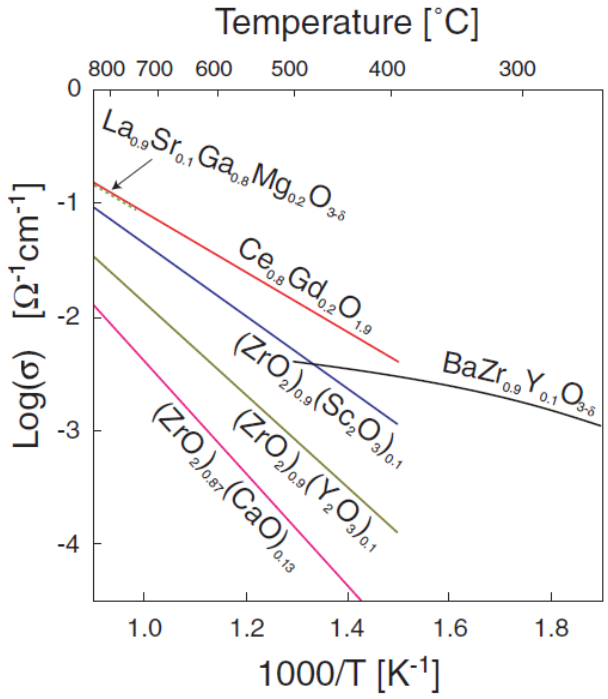

Figure 3 Conductivity of selected oxides. Doped ceria, zirconia, and lanthanum gallate are oxygen ion conductors, whereas doped barium zirconate is a proton conductor. Image is taken from reference 4.

Yttria-stabilised zirconia is highly stable over wide ranges of oxygen partial pressure and temperature, shows high ionic and low electronic conductivity, and has sufficient mechanical strength. Stabilized zirconia has been the major candidate for the electrolyte material ever since SOFC was proposed. Other oxide ion conductors, CeO_2 or $LaGaO_3$ based oxides, for example, have been considered as alternative electrolytes. Most SOFC stacks currently on the demonstration run utilize yttria-stabilized zirconia (YSZ) because of superior stability and reliability than other candidates.

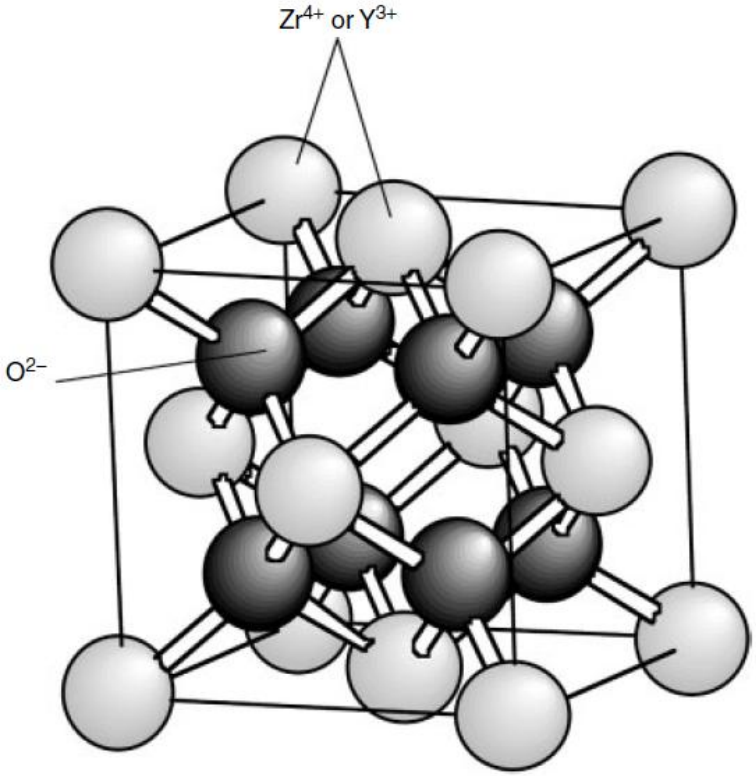

Figure 4 Crystal structure of yttria-stabilized zirconia.

Zirconia has a fluorite structure at high temperatures as illustrated in Figure 4, with eight-coordinate cations for A-site of Zr^{4+} and four-coordinate anions for B-site of O^{2-}. In the unit cell, the cations occupy the corner and face-center lattice sites, while oxygen atoms are located at eight tetrahedral sites. Zirconia is not a competitive electrolyte candidate due to low ion conductivity and low phase stability under operating conditions. Substituting Y^{3+} for Zr^{4+} on the A site increases not only ionic conductivity but also the stability of zirconia in oxidizing and reducing atmospheres. The ionic conductivity is increased by creating a large concentration of oxygen vacancies due to charge balance as shown in the following Kröger-Vink notation:

$$Y_2O_3 \xrightarrow{ZrO_2} 2Y_{Zr}' + 3O_o^{x} + V_o^{\bullet\bullet} \qquad 1\text{-}5$$

The number of oxygen ions is increased and subsequently increases oxygen ion conductivity. Oxygen ion conductivity varies as dopant concentration changes. It initially is increased and then decreased at higher dopant concentration due to defect ordering or electrostatic interaction. Usually, 8 mol% Y_2O_3 doped zirconia (8YSZ) is used as the practical SOFC. Operating temperature is attributed to ion conductivity of the YSZ as well, which follows an Arrhenius-type relationship. Oxygen partial

pressure does not have a strong effect on ion conductivity of YSZ due to small change in oxygen vacancy concentration at the practical partial oxygen pressure range (0.21 atm.- 10^{-25} atm).

Doped ceria is another fluorite well known for its ionic conductivity. The ionic conductivity of ceria is an order of magnitude higher than the conventional electrolyte YSZ (Figure 3), but CeO_2 has not been considered viable for fuel cell applications because of its high electronic conductivity, especially over 600 ^oC. Fortunately, the ionic transport number is higher than 0.9 at a temperature below 700 ^oC (and at an oxygen fugacity of 10^{-18}), a value that results in good fuel cell efficiency. The dopants in ceria show a significant effect on the conductivity. In particular, the conductivity increases and then decreases across the rare earth dopants series from Yb to La, peaking at Sm[5].

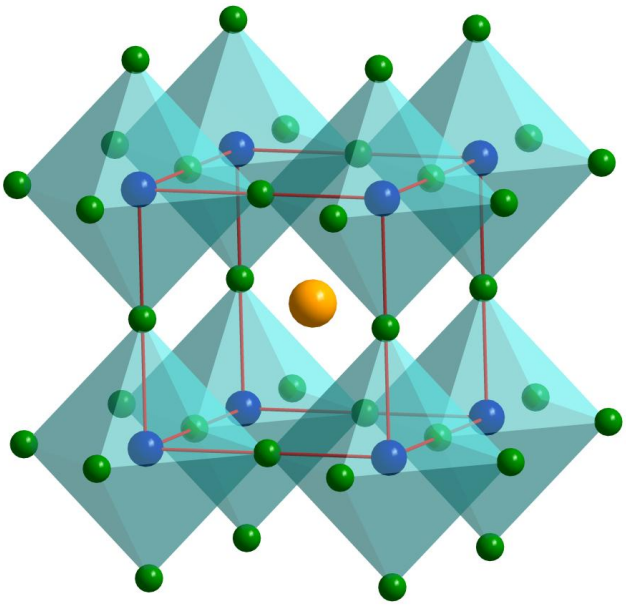

Figure 5 Perovskite lattice structure of a cubic structure. Yellow: A site atom; blue: B site atom; green: oxygen atom.

Strontium and magnesium co-doped $LaGaO_3$ (LSGM) is a perovskite showing high ionic conductivity (Figure 3) and the ionic transport number is close to one[6]. The perovskite oxides shows the general formula ABO_3 (A is a divalent or trivalent cation and B is a tetravalent or trivalent cation). The ideal perovskite structure is cubic, as shown in Figure 5. The easiest way to visualize the structure is in terms of the BO_6 octahedra which share corners infinitely in all 3 dimensions, making for a very nice

and symmetric structure. The A cations occupy every hole which is created by 8 BO_6 octahedra, giving the A cation a 12-fold oxygen coordination, and the B cation a 6-fold oxygen coordination. In the case of LSGM, the doping of divalent strontium on the A site and magnesium on the B site induces a large number of oxygen vacancies that facilitates significant bulk ionic oxygen transport.

1.2.2 Perovskite cathode materials

For fuel cell applications, the electrical conductivity of the oxides is often enhanced by substituting acceptor- or donor-type cations for either the A or B sites. The rare-earth perovskites, e.g. strontium doped $LaFeO_3$, $LaCoO_3$ or $LaMnO_3$, are commonly used as cathode materials for SOFC thanks to their ready availability and acceptable kinetic properties at high temperature.

LSM has been extensively used as cathode material in SOFC. Undoped $LaMnO_3$ is orthorhombic at room temperature, and shows an orthorhombic/rhombohedral transformation at about 600 ^oC because of the oxidation of Mn^{3+} to Mn^{4+} ions. LSM has a rhombohedral structure at room temperature, because doping divalent Sr on trivalent La site already causes the transition of Mn^{3+} to Mn^{4+} ions. $LaMnO_3$ might have oxygen excess, stoichiometry, or deficiency depending on the preparation conditions. At high temperatures, the oxygen stoichiometry of $LaMnO_3$ varies as a function of oxygen partial pressure and temperature. For example, at 1200 ^oC, the oxygen stoichiometry of $LaMnO_3$ ranges from 3.079 to 2.974 under oxygen partial pressure of 1 to $10^{-11.6}$ atm. For LSM, the level of oxygen excess decreases with increased dopant content. For SOFC applications, significant change in oxygen stoichiometry of $LaMnO_3$ should be avoided to minimize undesired dimensional changes. In addition to oxygen stoichiometry, $LaMnO_3$ can also show La deficiency or excess. $LaMnO_3$ with La excess may contain La_2O_3 second phase, but $LaMnO_3$ can have up to 10 % La deficiency without any second phase formation.

$LaMnO_3$ has intrinsic p-type conductivity due to the formation of cation vacancies. The material has an electrical conductivity of 10^{-4} S cm^{-1} at room temperature and about 0.1 S cm^{-1} at 700 ^oC. LSM is the most widely used SOFC cathode because of its relatively high conductivity and matched CTE with other cell components. The electrical conductivity of LSM takes place via the small polaron conduction mechanism. The electrical conductivities of doped and undoped $LaMnO_3$ show little dependence on oxygen partial pressure in the range of high oxygen activity.

Composites of LSM-YSZ are the standard materials for the cathode of SOFC. Strontium doped $LaMnO_3$ shows high electronic conductivity (greater than 200 S cm^{-1} at 800 ^oC) under typical cathode conditions but has negligible ionic conductivity. LSM will not react with YSZ until the firing temperature is above 1250 ^oC and is stable under the operating condition of SOFC.

LSC or $LaCoO_3$ possesses both high oxygen ionic conductivity and sufficienct p-type electronic conductivity at elevated temperature. This makes $LaCoO_3$ a mixed ionic/electronic conductor (MIEC). Compared with YSZ+LSM composite cathode, MIEC cathode materials extend electrochemical active sites from one-dimensional TPB to two dimensional surfaces as shown previously. Similar to $LaMnO_3$, the conductivity of $LaCoO_3$ can be improved by doping Sr on the La site. LSC exhibits even higher electronic conductivity than LSM under the same condition. Although more attractive in conductivity, $LaCoO_3$ shows significant disadvantages on YSZ electrolyte compared with $LaMnO_3$, including the CTE mismatch and chemical reaction with the YSZ electrolyte. LSC is more noted as cathode materials for ceria- or lanthanum gallate based electrolyte due to its extraordinary catalytic activity at intermediate temperatures. Even so, the CTE mismatch between LSC ($16\text{-}22\times10^{-6}$ K^{-1}) and the potential electrolytes is still a problem.

Sr-doped $LaFeO_3$ (LSF) cathode offers the best compromise between performance and stability for electrode. The electronic conductivity of LSF is lower than that of LSM but still higher than 50 S cm^{-1} under normal SOFC operating conditions. LSF may not be suitable for the conduction layer of the electrode but its conductivity would appear to be sufficiently high for use in the functional layer of SOFC cathodes. The lack of electronic conductivity should be more than compensated by the high ionic conductivity of LSF, reported to be 5×10^{-3} S cm^{-1} at 800 ^oC at atmospheric pressures for $La_{0.8}Sr_{0.2}FeO_3$. Even higher ionic conductivities are possible with increased Sr doping. These values are an order of magnitude lower than that of YSZ but many orders of magnitude higher than that of LSM. LSF does not seem to react with YSZ at a temperature lower than 1200 ^oC, so it can be used with YSZ to form a composite electrode as a stable cathode for SOFC. In this work LSF is used as the material for infiltration of porous YSZ to produce a high-performance cathode.

1.2.3 Ni(O)-YSZ cermet for SOFC anode

Nickel is used extensively in SOFC because of its wide availability and good catalytic effect on the oxidation of hydrogen in the anode environment. In order to maintain porous structure and longer TPB length, YSZ is incorporated into nickel as support. YSZ serves to inhibit the coarsening process of YSZ and adjust the coefficient of thermal expansion (CTE) of the support to match that of YSZ electrolyte.

A variety of methods are used to make the Ni(O)-YSZ cermet anode, including screen printing, tape casting, chemical vapour deposition, et al.. In most cases, the SOFC anode is first made with NiO and YSZ. The NiO is then reduced in situ to nickel metal when exposed to the fuel in the fuel cell. The reduction of nickel oxide produces some porosity, because of the weight loss and density increase in the process of NiO/Ni conversion. The thus produced porosity is depending on the volume percent of NiO in the composite, and pore former is used to produce higher porosity if needed.

The main concerns with the stability of the nickel/YSZ anode relate to the electrode dimensional change in reduction-oxidaton (redox) cycle and the sintering of nickel particles in long-term operation at elevated temperatures. The dimensional change of the Ni electrode causes the gas leaking problem because of the cracking of electrolyte. One practical problem in Ni(O)-YSZ cermet is that if the YSZ net work is not able to provide a support to the electrode, the dimension of the electrode is going to change with time.

1.3 Direct oxidation of hydrocarbon

For the fuel cell using hydrocarbon as fuel, the reaction on the anode side can be represented as Equation 1-6， if alkane is taken as the example.

$$C_nH_{2n+2} + (3n+1)O^{2-} \rightarrow nCO_2 + (n+1)H_2O + (6n+2)\,e^- \qquad 1\text{-}6$$

The relationship between the partial pressure and equilibrium cell potential is the following

$$E_{nernst} = E^\circ + \frac{RT}{(6n+2)F} \ln \frac{P(O_{2\ cathode})^{(3n+1)/2} P(C_nH_{2n+2\ anode})}{P(H_2O_{\ anode})^{n+1}\, P(CO_{2\ anode})^{n}} \qquad 1\text{-}7$$

The standard potentials for oxidation, E^o, are similar for methane (1.05 V at 700 ^oC) and for H_2 (1.01 V at 700 ^oC). For the calculation, the alkane is assumed to be oxidized to produce water and carbon dioxide without any other intermediate products.

A primary issue in the operation of any fuel using hydrocarbon fuels, whether or not steam is present with the hydrocarbon fuel, is the requirement that the fuel cell not be fouled by deposition of carbon-containing residues. At the high operating temperatures of an SOFC, hydrocarbons can react on the surface of the anode, on the interconnect plates, and on the tubing leading into the anode. Hydrocarbons can also react in the gas phase via free-radical cracking and polymerization, forming tars that can then deposit on the anode surface. Because of this issue, it is common to map the region of stability for hydrocarbon fuels based on thermodynamic calculations of the carbon stability. However, these stability maps must be viewed with great caution since kinetics, not thermodynamics, are primarily responsible for stability. For example, thermodynamic calculations imply that one could steam reform n-octane over a traditional Ni catalyst using a H_2O:C ratio of two so long as the temperature is above 473 K. However, attempts to perform steam reforming using a H_2O:C ratio of 2 on Ni catalysts will result in catastrophic formation of carbon for hydrocarbons other than methane. Furthermore, the choice of catalytic materials used for steam reforming strongly affects the parameter space over which materials are stable, showing that one must look more carefully at the mechanism that is responsible for carbon formation in a given system. Finally, the chemical nature of the carbonaceous deposits differs with the catalysts present in the systems.

The formation of carbon over Ni, Fe, and Co has been extensively studied, both for catalytic applications and for “dusting” or “drying corrosion”, the problem of pitting when steels are exposed to hydrocarbons at high temperatures. Recently, the properties of Ni for forming carbon have even been proposed for use in manufacture of carbon nanofibers[7]. The mechanism on each of these metals, involves deposition of a carbon source onto the metal surface, dissolution of the carbon into the bulk of metal, and finally precipitation of carbon as a fibre at some surface of the metal particle. It is important to recognize that with this mechanism the nickel is physically “lifted” from its initial surface and is not merely covered by carbon[8]. The mechanism also explains why it is necessary to use very high H_2O:C ratio for steam reforming of hydrocarbons lager than methane on nickel catalysts. Filament formation on Ni occurs when carbon deposition onto the Ni surface occurs more rapidly than carbon removal by steam, even if thermodynamic calculations show that carbon will not be stable in equilibrium.

Two basic strategies can be used to directly convert hydrocarbons to electrical energy in an SOFC. The first one is to operate the fuel cell with high concentration of steam or at high temperature regime that inhibits the formation of carbon on the surface of Ni-YSZ cermet anode[9]. Alternatively, the anode that does not catalyze the formation of carbon can be used for an SOFC system[10].

1.4 Alternative anode for carbonaceous fuel

1.4.1 Cu-based anode

Copper is chosen to be the alternative anode because of its poor catalysis in the deposition of carbon and high electronic conductivity. Copper overtakes gold (another metal inactive in catalyzing carbon deposition) because of its relatively lower cost. The problems of Cu as a wide-spread anode are associated with the low melting point of CuO_x, which causes a problem in the process with YSZ as cermet, and the growth of particle sizes under fuel environment. The infiltration of precursors for Cu into the pre-formed YSZ porous structure that is supporting a thin electrolyte is the beginning of infiltration as a method to prepare alternative electrode for SOFC[11]. The recent work reported by Tucker and et. al. shows that the sintering of Cu-YSZ cermet under a reducing atmosphere at a temperature above the melting point of metallic Cu produces good a Cu network[12]. The growth of Cu particles would damage the interconnection between the particles that decreases the electronic conductivity[13]. The addition of oxidation catalyst is also necessary for the enhancement of the performance of the Cu-based electrode.

1.4.2 Ceramic anode

Limitations of cermet anodes for direct hydrocarbon utilization led to the exploration of oxide anode materials, which is effective in decreasing the deposition of carbon. To be a good ceramic anode, it should satisfy the following criteria[14];

1) Good electronic conductivity (preferably > 100 S cm-1) at anode operating potentials (0.7-0.9 V);

2) Predominant anion lattice disorder to enhance oxygen diffusion coefficients;

3) Good oxygen surface exchange kinetics;

4) Fabrication of porous adherent films with minimal processing problems;

5) Compatibility with solid electrolyte.

There are several types of ceramic anodes in terms of crystal structure including fluorites, rutiles, pyrochlores and perovskites[15]. Unfortunately, there are few oxides fulfilling all the criteria, but the exploration in this area leads to the discovery of ceramic materials satisfying some of them. For example, ceria shows fairly high ionic conductivity in fuel environment and decent catalysis to the oxidation of hydrogen, but the electronic conductivity if fairly low (<0.02 S cm^{-1} at 700 ^{o}C). On the contrary, lanthanum doped strontium titanate (an n-type conductor) shows high conductivity in reducing atmosphere (>10 S cm^{-1}) at 800 ^{o}C, but its catalysis towards the oxidation of hydrogen is poor. $La_{0.75}Sr_{0.25}Cr_{0.5}Mn_{0.5}O_3$ (LSCM) is a p-type perovskite that is stable and fairly conductive in fuel atmosphere (1.5 S cm^{-1} at P_{O2} = 10^{-21} atm at 900 ^{o}C[16]) and shows good catalysis and stability in CH_4 as a fuel.

Composite anodes of the ceramic with ionic conductor or catalysts are generally used in real practice for high performance electrode. This leads to processing issues at the ceramic anode with the electrolyte materials and the mixing materials, such as thermal expansion coefficient (TEC) match, chemical compatibility during high temperature sintering and physical robustness in the redox environment.

1.5 Infiltration as a method to fabricate composite electrode

The conventional approach for fabricating composite electrodes involves sintering the mixture of YSZ and electrochemically active materials, such as YSZ-LSM (Sr-doped $LaMnO_3$) for cathode and YSZ-Ni for anode, at elevated temperature to ensure the connectivity of YSZ. The choice of the sintering temperature should be above the minimum sintering temperature of YSZ, above 1000 ^{o}C, but below the maximum temperature at which the solid-state reaction between YSZ and the active materials happens. This will constrain the choice of electrode materials. For example, Sr-doped $LaCoO_3$ (LSCo) is so good a mixed electronic and ionic conductor (MEIC) that it gives a better cathode performance than LSM and LSF (Sr-doped $LaFeO_3$) do, but it is not widely used because it reacts rapidly with YSZ at temperature of 1000^{o}C. However, the fabrication of composite electrodes by infiltrating the electron conductive materials into the well-sintered porous scaffold and sintering again at relatively low temperature is able to solve this problem and brings about some accompanying advantages.

First, because of the addition of the conductive phase to the pores of the existing scaffold, the composites prepared by infiltration are not random. In this case, a high

conductivity with volume fractions lower than 30% can be achieved, resulting in the percolation for random composites, thereby leading to greater possibility to optimize the microstructure of the electrode[17]. Because of the existence of the non-random structure, the coefficient of thermal expansion (CTE) of the electrode is compatible to that of the YSZ component, rather than the weighted average of the two phases. As a result, the choice of electrochemically active materials is not limited by the close CTE match. Second, the low sintering temperature decreases the grain growth of the active materials and thus is beneficial to produce long TPB. Finally, the sequential adding of active materials or catalyst to the porous structure makes the effect of each component clearer to be singled out. In addition, the layered structure can also decrease the solid-state reaction of the separated layers with a layer in between.

1.6 Structure of a fuel cell

A typical SOFC is composed of three parts as described previously: anode, cathode and electrolyte. Any one of these three parts can be used as the support for the fuel cell. For the SOFC operating at high temperature, a thick YSZ electrolyte can be chosen to provide support for the thin anode and cathode since the conductivity of the electrolyte at high temperature (above 800 ^{o}C) is high enough to provide low ohmic resistance. Over the past decade, considerable progress has been achieved in bringing the temperature down to an intermediate temperature (IT) range of 650 to 800 ^{o}C so that metallic interconnects could be used to reduce cost[18]. The thickness of the electrolyte needs to be reduced to decrease the ohmic loss by employing cathode- or anode-supported thin electrolyte. The support needs to be strong but porous enough to allow the fast transport of reactant and product (water vapour, carbon dioxide, etc.) between the gas phase and electrode/electrolyte interface.

1.7 Objective of this work

Since the impregnation of active materials has the aforementioned advantages, it would be quite promising if it can be used in a real fuel cell stack. Tests on button cells are extensively reported, but the scale-up of the fuel cell fabrication using impregnation has not been proven.

Electrolyte-supported fuel cells are fabricated by screen printing a porous YSZ scaffold plus impregnation. In order to achieve an optimized microstructure of the porous structure, tests with button cells were done to assess the microstructure

evolution during sintering process and the selection of raw materials for better infiltrated electrodes. Image analyses and modeling were also performed to quantify the porous structure.

Tape casting of supported thin electrolytes on porous structures is also carried out in an attempt to enhance the performance of the large scale fuel cell. The techniques of making flat porous structures are also developed for a simpler process and higher overall performance.

Chapter 2 General experimental techniques

2. 1 Ceramic processing techniques

2.1.1 Screen printing

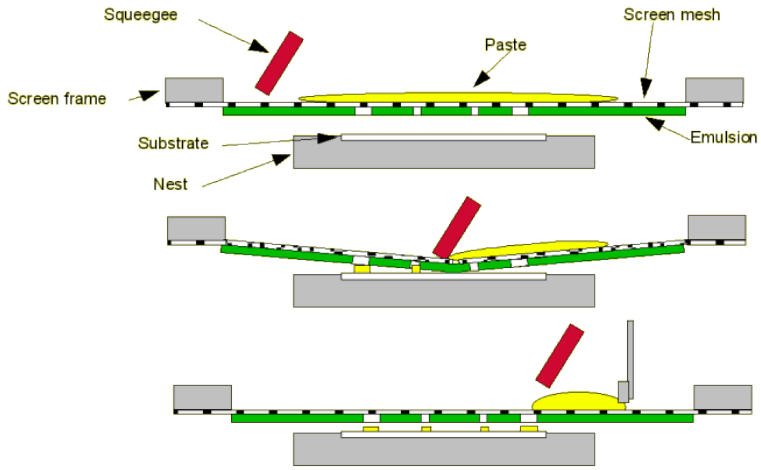

Figure 6 Basics of screen printing process. Image is taken from reference 19.

Screen printing uses a quantity of ink or other viscous compound and deposits it in a film of controlled pattern and thickness. In the case of screen printing this entails squeezing ink through a gauze or mesh onto a surface beneath. Screen printing can produce thin films in an efficient and reproducible manner, so it can be used to produce thin electrode of SOFC. Figure 6 illustrates the working process of a screen printing machine. The screen is placed over and just above the article to be printed so that it is accurately aligned to deposit the printing layer in the desired position. The gap between the substrate and screen is called printing gap (about 1-2 mm). The mesh of the screen is brought into line contact in a short time with the article by the squeegee as it is moved across the screen. Ink is pushed into the open area forming the pattern and the surplus is removed by the edge of the squeegee. The mesh should peel away from the surface immediately behind the squeegee, leaving all the ink that was through the mesh deposited on the printing surface. The screen printing process was performed using a computer-controlled machine (248 Dek Printing Machines (Shenzhen) Co. LTD. China).

2.1.2 Tape casting

Tape casting has matured into a full-blown manufacturing technique for the formation of thin, essentially two-dimensional sheets of just about any material that can be

produced as a powder. It allows production of a wide variety of controlled morphologies, from highly porous to fully dense microstructures, such as electrodes and electrolytes. Green layers can be easily superimposed if one wants to co-sinter the multilayer in a one-step operation[20].

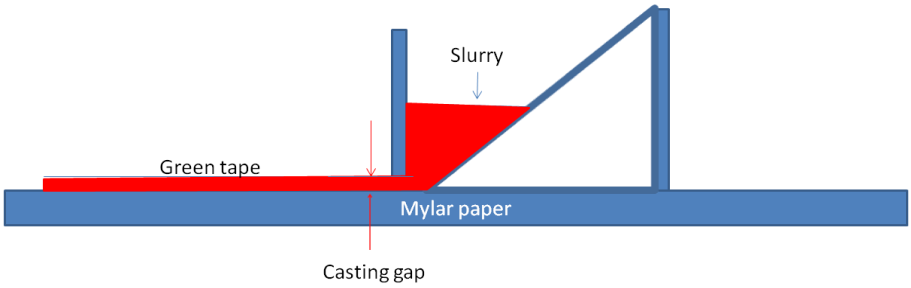

Figure 7 Schematic of a laboratory tape-casting setup

Organic additives are added to the powder to form the slurry. The slurry is then mixed and ground mostly by ball-milling to ensure homogenization and destruction of agglomerates. The slurry will be cast on a Mylar^{TM} paper to produce the green tape after the evaporation of solvent. The casting process is illustrated in Figure 7. The different layers with solvent can then be cast on top of the others via dedicated technical systems, which is called co-casting. The organics including solvent, binder and plasticisers are used in this study to make a flexible green tape after the evaporation of the solvent. To fabricate a scaffold with graded porosity, two different ceramic contents are used to co-cast on top of the green tape of electrolyte, step by step.

2.2 Electrochemical characterisation

2.2.1 Current-voltage performance measurement (IV)

The performance of the fuel cell is measured by IV curves and calculation of power generation. An external circuit was connected to the electrical lead wires from the cell. When no current is drawn from the cell, the potential that can be read by connecting a voltmeter between the anode and cathode is the open circuit voltage (OCV). The OCV usually is lower than the theoretical potential provided by the Nernst equation due to the crossover of gas or the slow reaction process that impedes the equilibrium of oxygen partial pressure. When a current is drawn from the cell, the potential is reduced due to the irreversibilities occurring in the cell. For each point of the IV curve, the product of the voltage by the current density will be the power density. The IV

curves are plotted as a function of the current density (A cm^{-2}), meaning that the current is divided by the cell active area.

2.2.2 Electrochemical spectroscopy (EIS)

There are different kinetic processes involved in SOFC electrochemical reactions. EIS is a powerful technique that can provide information for separating these different processes. Essentially, this technique imposes a sinusoidal current perturbation, $I(\omega t)$, onto the working SOFC while monitoring the frequency-dependent, sinusoidal output.

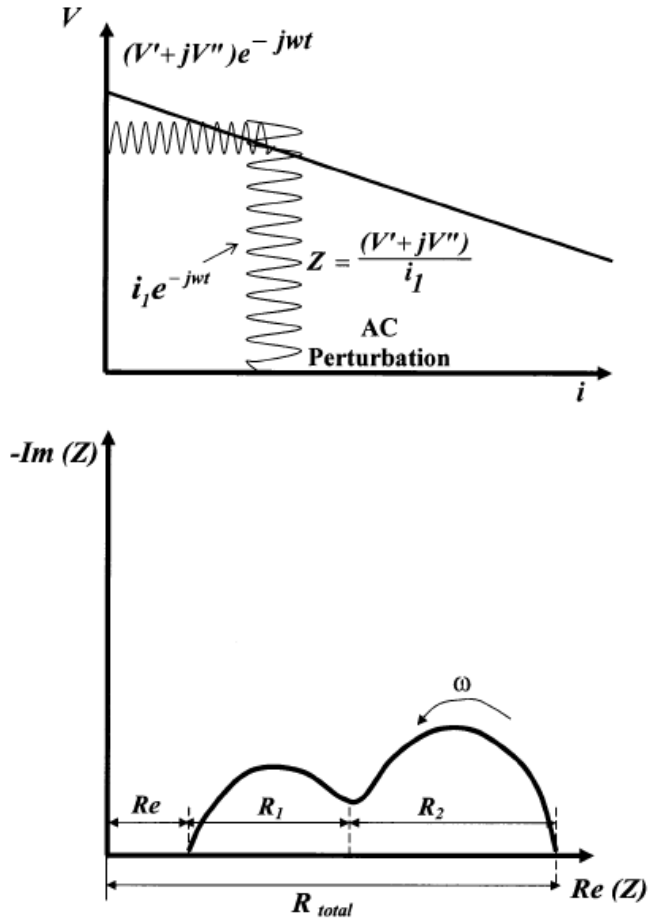

Figure 8 Schematic of EIS principle (top) and typical Nyquist plot (bottom)

For time independent processes, such as one observes with simple resistors, ratio of potential and current is a constant and the phase of the perturbation and the output are the same. But processes involving chemical reactions, gas-phase diffusion, and charge diffusion are time-dependent and exhibit a phase-shifted output. By varying the frequency of the current perturbation, ω, the frequency-dependent impedance can be measured and presented as a Nyquist diagram. The principle and typical Nyquist plot are shown in Figure 8.

Ideally, impedance spectraon a Nyquist plot consist of semi-circles and arcs or straight lines. The first real axis intercept at high frequency corresponds to the cell ohmic resistance, which primarily comes from the fuel cell electrolyte. However, for the fuel cell with thick electrode and ceramic anode, a large ohmic resistance from the electrode is also possible. The intercept at the very low frequency corresponds to the total resistance. Between these two intercepts are fuel-cell losses coming from the electrodes. The characteristic frequency, identified from the peak point within each arc, provides kinetic information.

The ac impedance measurement was carried out on a Solartron 1260 frequency response analyzer (FRA) by applying a sine signal of 10 mV in the range from 10 kHz to 0.04 Hz. In each frequency decade, more than five points were retrieved to give discernible arcs.

2.2.3 Testing workstation

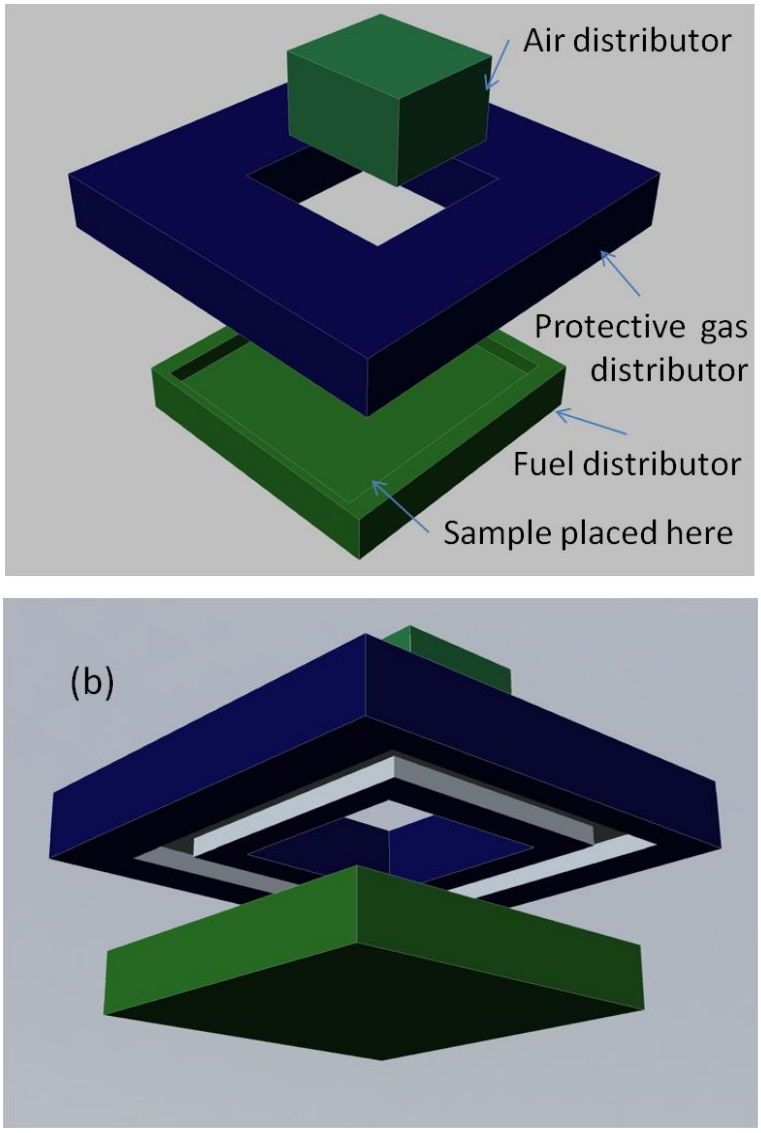

Figure 9 Schematics of the ECN jig. (a) shows the assembly of the ceramic components for holding the fuel cells; (b) is the bottom view to show the channels of the protective gas distributor. The current collectors on the fuel and air distributor are not shown.

Figure 9 shows the schematics of the ECN testing workstation whose core components are made of alumina ceramics except the Pt current collector on the air distributor or the nickel mesh on the fuel distributor. These three parts will be assembled to provide sealing and current collection for the testing. The protective gas distributor contains a channel on the marginal area of the cathode side as demonstrated in Figure 9(b). The fuel is introduced into the anode from the bottom

while the oxidant from the top. The gas from the cathode and anode side will mix in the end on the way to leave the reaction chamber along with protective nitrogen gas.

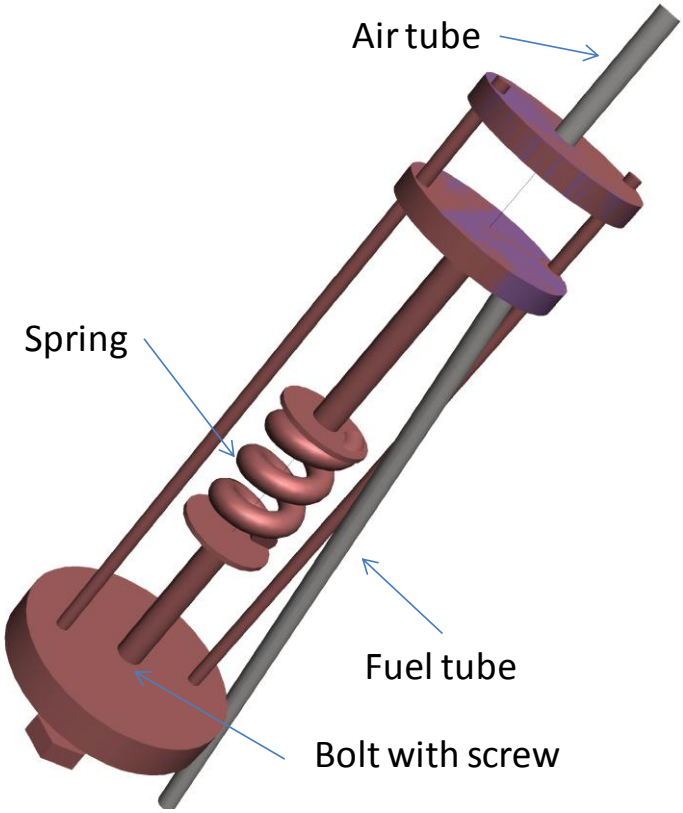

Figure 10 Schematics of the Versa jig. The current collector is silver wool placed on both sides of the fuel cell.

The Versa jig (Figure 10) is made of nickel based superalloy and is much safer to be used for the testing with methane. A porous alumina paper (Zircar Ceramics, Inc.) is used to prevent the short-circuiting of the anode and cathode and also to provide the cushion for a possible uneven fuel cell. Silver paste on the fuel cell is used for the current collection and better contact can be provided by twisting the bolt to apply force on the spring. Because the force controls the microstructure of the soft alumina paper on the anode side, the diffusion of gas may be blocked by too much pressure on the fuel cell.

2.3 Materials characterisation

2.3.1 X-Ray diffraction (XRD)

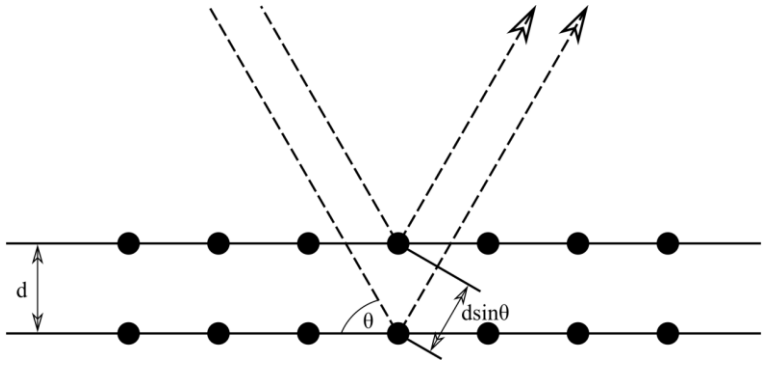

Figure 11 The Bragg equation derived by treating layers of atoms as reflecting planes: X-rays interfere constructively when the additional path length $2d\sin\theta$ is equal to the wavelength λ.

Diffraction is the interference between waves that occurs as a result of an object in their path. Diffraction of X-rays that have a wavelength in the range of 0.01 to 10 nanometers can be used to detect the repeated arrangement of atoms in a crystal. If we think of two adjacent parallel planes in a crystal is separated by a distance d (Figure 11) then the incidental angle of the X-ray at which constructive interference between waves of wavelength λ is given by the Bragg equation:

$$2d\sin\theta = \lambda \qquad 2\text{-}1$$

The intensity of the diffraction depends on the details of the crystal structure and the identity of the atoms. How well an atom scatters X-ray is related to how many electrons it possesses and its location in the unit cell. Thus measurement of diffraction angles and intensities allow us to work backwards to structure information.

In this study, XRD is used to identify the phases produced in the solid state reaction or impregnation. The reflective XRD pattern was recorded on a PANalytical X-ray diffractometer with a Cu K_α radiation (λ = 1.5418 Å), employing a scan rate of 1.5 °min $^{-1}$ in the 2θ range of 10 °to 100 °.

2.3.2 Scanning electron microscope (SEM)

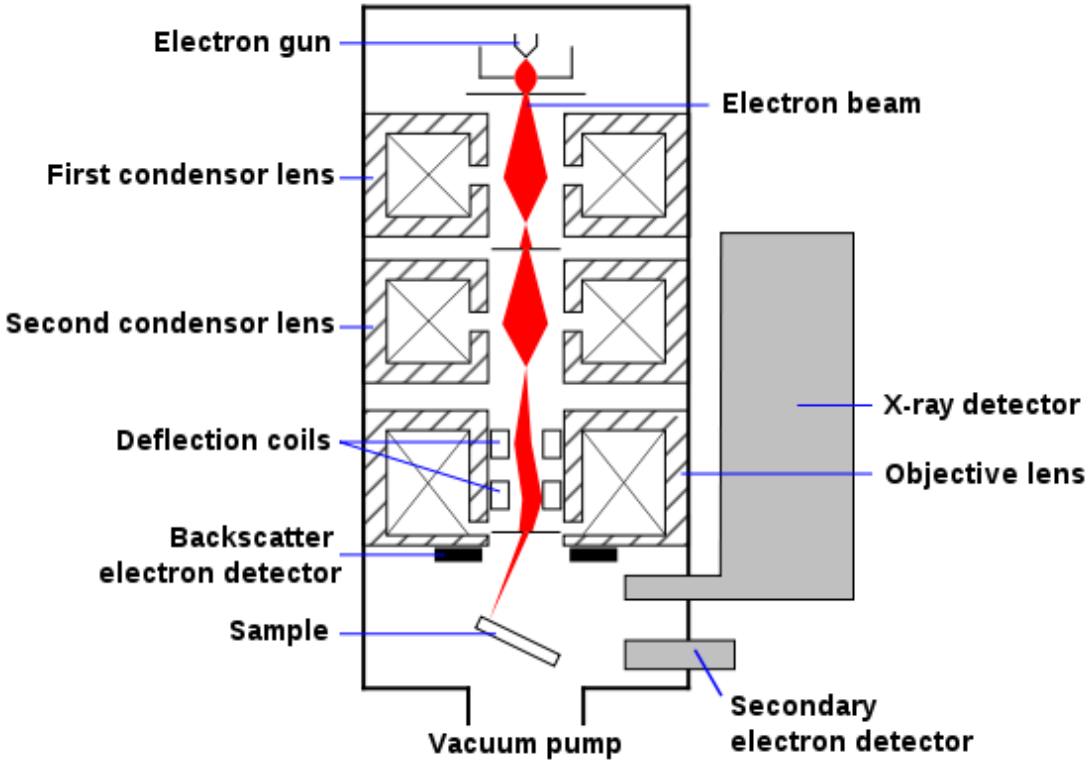

Figure 12 Schematic of an SEM.

In an SEM, an electron beam is emitted from an electron gun fitted with a cathode. The electron beam, which can have an energy ranging from 0.2 keV to 40 keV, is focused by one or two condenser lenses to a spot about 0.4 nm to 5 nm in diameter as shown in Figure 12. The beam passes through pairs of scanning coils in the electron column, typically in the final lens, which deflect the beam in the x and y axes so that it scans in a raster fashion over a rectangular area of the sample surface. Other than the standard tungsten filament, electron emitters include lanthanum hexaboride (LaB_6) cathodes can be used if the vacuum system is upgraded. The field emission gun (FEG) can produce high primary electron brightness and small spot size even at low accelerating potentials in the range of 0.3- 4 kV.

When the primary electron beam interacts with the sample, the electrons lose energy by repeated random scattering and absorption within the interaction volume (0.1- 5 μm into the sample) that depends on the electron's landing energy, the atomic number of the specimen and the specimen's density. The energy exchange between the electron beam and the sample produces the reflection of high-energy electrons by elastic scattering, emission of secondary electrons by inelastic scattering and the

emission of electromagnetic radiation. All these emissions and the beam current absorbed by the specimen can be detected in respective detectors to create images. The emissions from the atoms at the top surface can be detected to give an image of the surface and is called Secondary Electron Imaging (SEI). On the other hand the re-emerged beam, which is sensitive to the mass of the atoms that scatter the incident beam, can be used to create an image (called Back-Scattered Imaging, BSE) that is efficient in distinguishing heavy atoms. Each pixel of computer video memory is synchronized with the position of the beam on the specimen in the microscope, and the resulting image is therefore a distribution map of the intensity of the signal being emitted from the scanned area of the specimen.

The microstructure and composition of the electrodes is inspected by SEM on a JEOL 6700F FEG-SEM with an Energy-dispersive X-ray spectroscopy (EDS). Some of the samples were mounted in an epoxy, and then cut, polished for back-scattering electron imaging.

2.3.3 Focused ion beam (FIB)

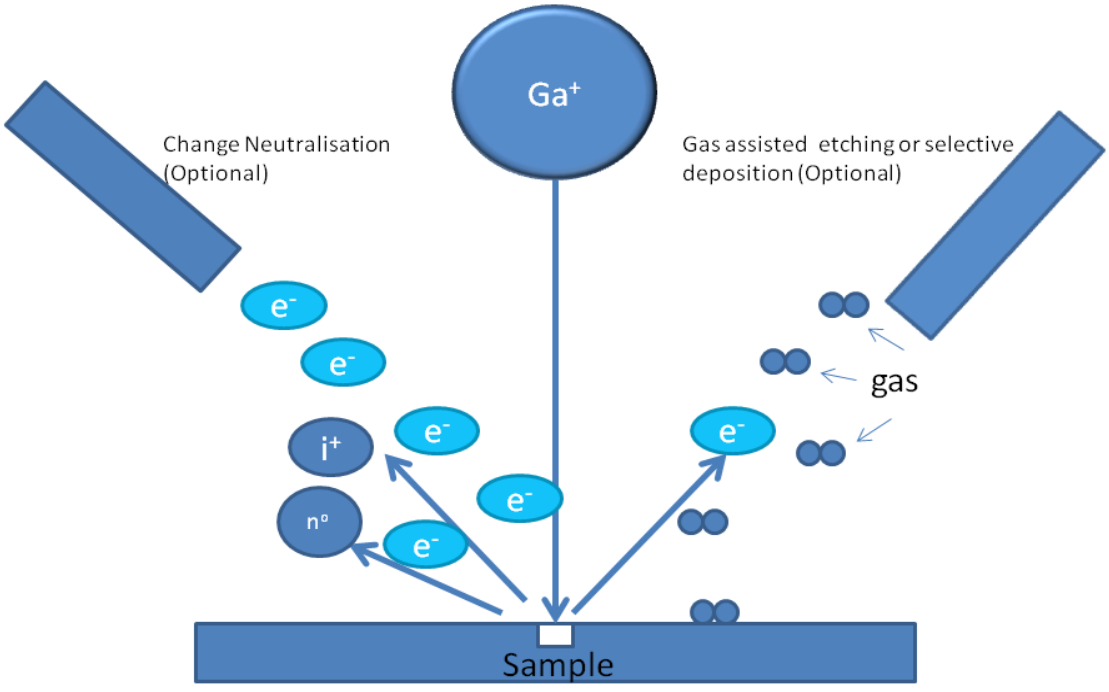

Figure 13 Principle of FIB

Focused ion beam (FIB), is a technique used particularly in the semiconductor industry, materials science and increasingly in the biological field for site-specific analysis, deposition, and ablation of materials. An FIB setup is a scientific instrument

that is similar to a scanning electron microscope (SEM), except that an ion beam rather than an electron beam is used as the incidental beam. In most commercially available systems, Ga ions are used thanks to its low melting point (30 ^{o}C), low vapor pressure (1 Pa at 1310 K) and narrow energy distribution (concentration ratio of Ga^{2+}/G^{+} is about 10^{-4} at 10 μm). The gallium (Ga^{+}) primary ion beam hits the sample surface and sputters a small amount of material, which leaves the surface as either secondary ions (i^{+} or i^{-}) or neutral atoms (n^{0}), as is shown in Figure 13. The primary beam also produces secondary electrons (e^{-}). As the primary beam rasters on the sample surface, the signal from the sputtered ions or secondary electrons is collected to form an image.

Since very little material is sputtered at low primary beam currents, the modern FIB systems can easily achieve 5 nm imaging resolution (imaging resolution with Ga ions is limited to ~5 nm by sputtering and detector efficiency). At higher primary currents, a large quantity of material can be removed by sputtering, allowing precision milling of the sample down to a sub micrometre scale. In this work, FIB is used to mill the sample and then SEM is used to observe the morphology of the sample.

2.3.4 Particle size analysis (PSA) by laser

Laser diffraction is the most widely used technique for particle size analysis. In laser diffraction particle size analysis, a representative cloud or ‘ensemble’ of particles passes through a broadened beam of laser light that scatters the incident light onto a Fourier lens. This lens focuses the scattered light onto a detector array and, using an inversion algorithm, a particle size distribution is inferred from the collected diffracted light data. Sizing particles using this technique depends upon accurate, reproducible, high resolution light scatter measurements to ensure full characterisation of the sample. The particle size analysis (PSA) of the two 8-YSZ powders is performed on a Mastersizer 2000 particle size analyzer (Malvern Instruments LTD)

2.3.5 Dilatometery

A dilatometer is a scientific instrument that measures volume changes caused by a physical or chemical process. To determine the thermal expansion and density change of the material, the pellet of samples is analyzed with a high-temperature dilatometer (Netzsch, DIL 402C) in a flowing air atmosphere. The measurement is conducted from room temperature to 1350 ^{o}C.

2.3.6 Thermogravimetric analysis (TGA)

TGA is a type of testing performed on samples that determines changes in weight in relation to a temperature program in a controlled atmosphere. TGA is commonly employed in research to determine characteristics of materials such as polymers, to determine degradation temperatures, absorbed moisture content of materials, the level of inorganic and organic components in materials, and solvent residues. The TGA in this work is carried out on a Netzsch TG 209.

Chapter 3 A large area electrolyte-supported SOFC prepared by ionic infiltration

3.1 Introduction

The conventional SOFC uses 8 mol % ytrria-stabilized zirconia (8YSZ) as electrolyte, Ni(O)-YSZ cermet as anode and LSM-8YSZ composite as cathode. Heat treatment at a temperature above 1100 ^{o}C is preferred to obtain a well-sintered electrolyte. However, the high sintering temperature may preclude the utilization of some alternative conductors other than Ni(O) or LSM by causing a solid-state reaction with 8YSZ to form the insulating phases[21] and/or the undesired growth of grain size of the active materials[22]. Therefore, an alternative method for fabrication is performed by impregnating the liquid precursors into the porous 8YSZ scaffold and then sintering at low-temperature to form the oxide phase [23 , 24 , 25 , 26]. Studies have shown that $La_{0.8}Sr_{0.2}FeO_3$ (LSF) from the impregnation of nitrate solution forms particles of less than 100 nm diameters when sintered at 850 ^{o}C, while forms a dense layer on 8YSZ at 1100 ^{o}C [27,28,29]. Since the electrochemical reactions of the electrodes involve ions, electrons and gas molecules in three distinct phases, the polarization loss from electrode reaction may be minimized by carefully optimizing the triple-phase boundary (TPB)[30]. The nano-particle-sized electrode is critical to high-performance SOFC operating in the intermediate temperature range between 500 and 800 ^{o}C[2,31]. Moreover, the impregnation of the functional materials into the well-sintered and stablised 8YSZ porous scaffold on the dense 8YSZ electrolyte will also resolve the mismatch in CTE values between the electrolyte and the functional materials due to this non-random structure[17,32]. In addition, the percolation limit of the conductive materials will be lower than 30 vol.% in conventional electrode since they sit on the surface of the 8YSZ grains[17]. For a system where more than one material is added to the porous scaffold, the contribution of an individual material can easily be examined by investigating the effect on the performance and characteristic of the cell by the sequential addition of the material [32]. For instance, the addition of a catalyst (e.g. Pd, Ni and Fe) has been reported to decrease significantly the polarization loss of $La_{0.8}Sr_{0.2}Cr_{0.5}Mn_{0.5}O_3$ (LSCM) –8YSZ electrode without changing the ohmic loss[33].

The development of impregnation as a method to fabricate high-performance electrode has been demonstrated by testing on the small-scaled button cells, but it is

important to scale-up the impregnation process for the industrial feasibility. Even though the impregnation of LSCF into the porous 8YSZ as cathode has been tested on a large anode Ni(O)-8YSZ-supported fuel cell (81 cm^2) [34], the high sintering temperature of the NiO-8YSZ support prevents the use of ceramic anode due to the potential solid state reaction.

In this study, an electrolyte-supported fuel cell is prepared by impregnating on both the anode and cathode sides, and the achieved performances of these cells are compared to the reported results on the button cells with similar electrodes. In addition, this study also investigates the performance of the large fuel cells with respect to diffusion polarization at different fuel flow rates of humidified H_2 or oxygen partial pressures of oxidant.

3.2 Experimental

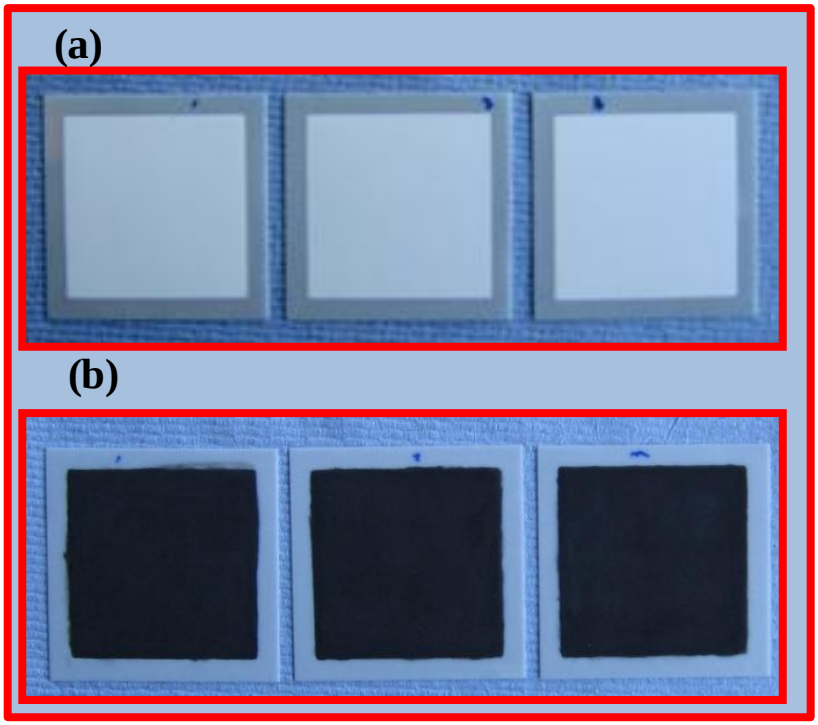

Figure 14 Images of the fuel cells before (a) and after (b) the impregnation of LSCM. The dimensions of the electrolyte and electrode are 50 x 50 x 0.2 mm and 40 x 40 x 0.04 mm, respectively.

Dense 8YSZ electrolytes in the dimension of 50 x 50 x 0.2 mm were purchased from Kerafol Keramische Folien GmbH. Four layers of ink containing 8YSZ (UCM Advanced Ceramics GmbH, Laufenburg, Germany) and pore forming agent (PFA)

(graphite and glassy carbon) were screen-printed onto both sides of the electrolyte to produce a 40 x 40 mm active area and then sintered at 1300 ^{o}C for 3 hours to form the porous scaffolds for impregnation, as shown in Figure 14(a). The porosity of scaffold is determined to be ~ 62 vol. %. In order to determine the porosity, the weight of the porous structure was calculated by deducting the weight of dense pellet from the total weight of the sample and then the volume of porous structure, V_p, is determined using the density of YSZ, 6.0 g cm^{-3}. De-ionized water is impregnated into the porous structure to occupy the open pores and the volume of water, V_w, is calculated using the density of 1 g cm^{-3}. The open porosity, Π, is calculated with the formula

$$\Pi = V_w/(V_w+V_p) \qquad 3\text{-}1$$

$La(NO_3)_3$•$6H_2O$ (Aldrich Chemistry, 99.99%), $Sr(NO_3)_2$•$9H_2O$ (Aldrich, 99 + %), $Cr(NO_3)_3$•$9H_2O$ (Sigma Aldrich, 99 %), $Mn(NO_3)_2$•xH_2O (Alfa Aesar, 99.98 %, x is assumed to be 6) and citric acid (Fisher Scientific, 99.5%, one mole per mole cations) were used to prepare the 1 M (total concentration of metallic ions) aqueous solution for $La_{0.8}Sr_{0.2}Cr_{0.5}Mn_{0.5}O_3$. The promising ceramic anode, $La_{0.8}Sr_{0.2}Cr_{0.5}Mn_{0.5}O_3$, was chosen because it has successfully demonstrated excellent redox stability under both cathode and anode condition[35]. The solution was impregnated into the porous structure then heated up to 450 ^{o}C to decompose the nitrate. About 20 impregnation cycles were repeated to reach a desired loading of 45 wt.% LSCM and then sintered at 1200 ^{o}C for 4 h to form the pure oxide phase, as demonstrated in reference 33. The perovskite material for the cathode, $La_{0.8}Sr_{0.2}FeO_3$, was impregnated using also 1 M (total concentration of metallic ions) solution from $La(NO_3)_2$•$6H_2O$ (Aldrich Chemistry, 99.99%), $Sr(NO_3)_2$(Aldrich, 99 + %), $Fe(NO_3)_3$•$9H_2O$ (Fisher Scientific, Analytical agent grade) and citric acid. Multiple cycles were infiltrated into the cathode to obtain a final LSF loading of 35 wt. %. Finally, it was fired at 850 ^{o}C for 4 h to form the pure oxide phase. XRD was used to verify the phases of the perovskite materials. For the fuel cell impregnated with 10 wt.% CeO_2 and 1 wt.% Pd, the nitrate solution was used sequentially to infiltrate into the LSCM-8YSZ anode and then heat treated at 500 ^{o}C to completely decompose the nitrate. Pt paste (Gwent, C2000904P3) was painted on the whole surface of both electrodes and then sintered at 850 ^{o}C for 30 min.

The fuel cell was loaded into the ECN jig and heated up to the testing temperature at a rate of 1 ^{o}C ml min^{-1}. A protective 250 ml min^{-1} N_2 flowed on the cathode side around

the active area to provide sealing and to prevent any leaking H_2 from the anode to mix with any outflow oxygen from the cathode. Pt meshes of size 3.5 x 3.5 cm were used as current collector. On one side of the Pt meshes, a thick Pt wire was used to conduct the current while a thin one to measure the voltage. The pure H_2 was saturated with 4.2 vol. % of H_2O by following the fuel through a 30 ^oC humidifier before entering the anode chamber. In order to investigate the effect of the fuel flow rate on the performance of the cell, tests were carried out at different flow rate between 100 ml min^{-1} and 500 ml min^{-1} on the anode side while keeping a constant 500 ml min^{-1} flow of air on the cathode side. For the impedance spectroscopy, a sine ac perturbation of 10 mV was applied to the cell at the frequency ranging from 10^4 to 0.05 Hz using a Solartron 1260 frequency response analyser (FRA). The IV curve was retrieved by a Kikusui Electronic Load and the area of Pt mesh was used to calculate the current density. The microstructure of the electrodes was observed using the JEOL 6700F scanning electron microscope (SEM). Some of the samples were mounted in the epoxy and then cut, polished for back-scattering electron imaging.

3.3 Results and discussion

3.3.1 Overview of the arrangement of electrolyte supported fuel cell

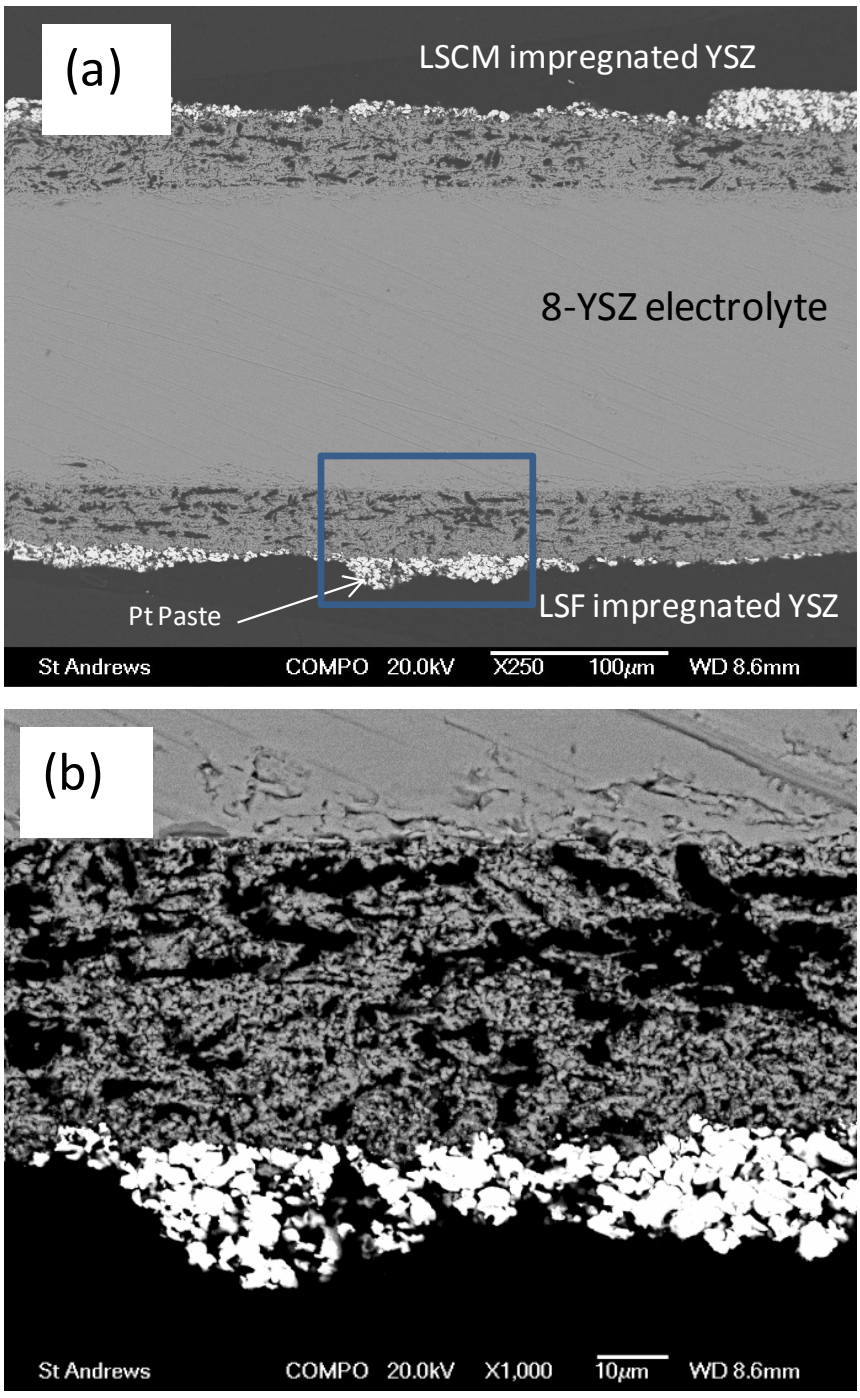

Figure 15 Back-scattering-electron (BSE) images of the 200-μm 8YSZ electrolyte-supported fuel cell impregnated with LSCM and LSF. (a) is the general view and (b) the enlarged area of the rectangle in (a).

Screen-printing is a scalable and effective method in producing thin films on rigid substrates. It can be used as an industrial process for the mass production of the scaffold. The back-scattering electron image of the cross-section of LSF- and LSCM-impregnated porous electrodes is shown in Figure 15. The image shows a dense electrolyte with a thickness of 200-μm. The 40-μm thick porous scaffold support has particles less than 10 μm that form interconnected large pores as well as small ones. The porous electrode after the impregnation of perovskites still maintains good adhesion with the electrolyte as shown in Figure 15(b). The porous Pt paste on the surface is less than 20 μm (shown in Figure 15) to assist the current collection, while allowing the transport of gas. The catalytic effect of Pt on the electrode may be a concern, but this Pt paste has been specially designed purely for current collection and no catalytic activity has been reported[36].

3.3.2 Effect of ceria-Pd catalyst and flow rate on the performance

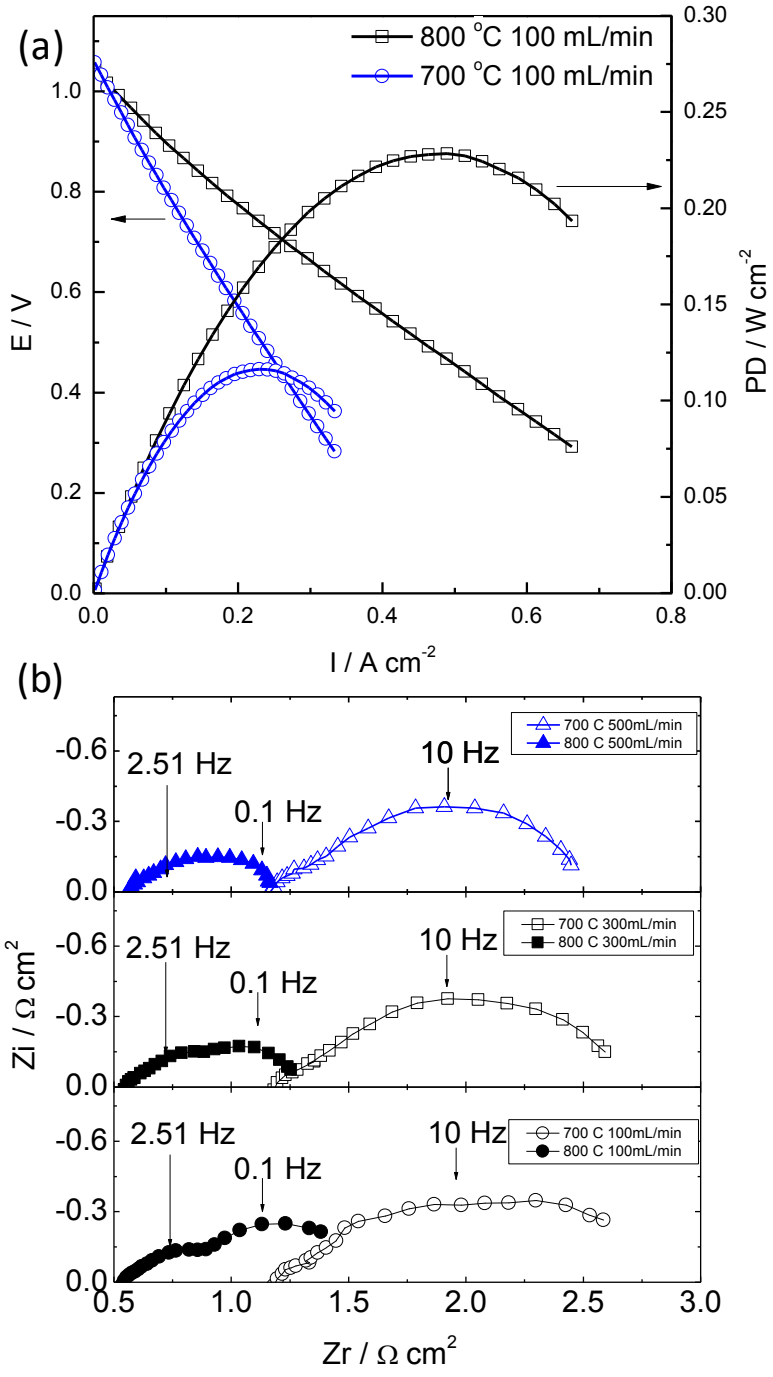

Figure 16 (a) Performance curves for the cell at different temperatures when the LSCM anode is operated under 100 ml min^{-1} wet (4.3 % H_2O) H_2; (b) electrochemical impedance spectra of the cell at different fuel flow rates and temperatures.

Performance of the cell infiltrated with 35 wt. % LSF and 45 wt. % LSCM was observed. As shown in Figure 16, the cell obtained a high OCV value of 1.06 V at

700 ^{o}C, which is close to the theoretical Nernst value, 1.08 V, considering that the wet H_2 contains 4.3 vol. % H_2O. With the H_2 flow rate of 100 ml min^{-1}, the cell achieves a maximum power density of 116 mW cm^{-2} at 700 ^{o}C and 223 mW cm^{-2} at 800 ^{o}C. Although not shown in the IV plot, the electrical energy produced by the cell was not affected by the fuel flow rate. However, the increasing flow rate enhances the electrochemical performance of the cell as shown in Figure 16 (b). The low-frequency region of the arc at both 700 ^{o}C and 800 ^{o}C decreases in size as the flow rate of H_2 increases from 100 ml min^{-1} to 500 ml min^{-1}, while the high-frequency region of the arc remains unchanged. Since the concentration polarization is strongly affected by the hydrogen concentration at the reaction site, the flow rate could affect the water concentration in the anode side by changing the oxygen leakage in this semi-sealing system. At 700 ^{o}C, the cell has an ohmic resistance, Rs, of 1.16 Ω cm^2, which is close to the calculated value, 1.05 Ω cm^2, for a 200-μm thick electrolyte. The slight discrepancy can be explained by the interfacial resistance or the ohmic resistance of the ceramic electrode [33,37,38]. At 700 ^{o}C, the cell has a polarization resistance, Rp, of 1.6 Ωcm^2 and decreases to 1.3 Ωcm^2 as the flow rate increases. Though the active area of the cell in this study is about 45 times larger than of the button cell, the obtained Rp value is almost half of the previously reported value, 2.4 Ω cm^2, of a button cell with also LSF and LSCM impregnated into the scaffold for the cathode and anode respectively [32].

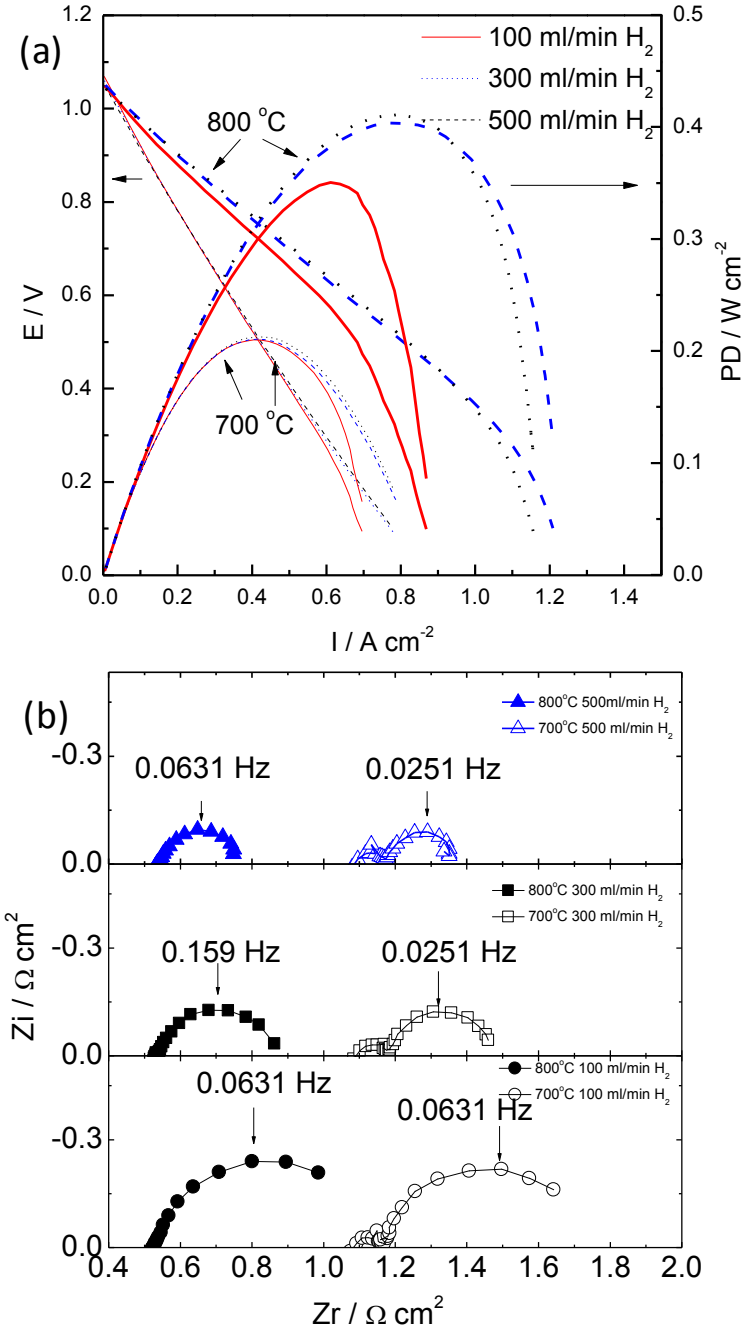

Figure 17 (a) Performance curves and (b) impedance spectra of the fuel cell with LSCM and ceria + Pd as catalyst at different temperatures under different flow rates of wet (4.3 % H_2O) H_2 while keeping the flow rate of air constant at 500 ml min^{-1}.

Although LSCM-8YSZ composite electrode shows poor electrochemical activity toward the oxidation of H_2, enhancement in the cell performance has been reported on a button cell when ceria and Pd were impregnated as catalysts[39]. The feasibility of

impregnating catalyst on a large-area fuel cell is observed using the SEM. The IV curves and the corresponding impedance spectra of the tested cell with an anode having 45 wt.% LSCM, 10 wt.% CeO_2 and 1 wt.% Pd are shown in Figure 17. At 700 ^oC in H_2 containing 4.3 vol. % H_2O, the cell achieved a maximum power density of 209 mW cm^{-2} as shown in Figure 17(a). There is little change in the performance of the cell as the flow rate increases from 100 ml min^{-1} to 500 ml min^{-1}. However, the mass transport appears to limit the performance in the high current density region when the flow rate is at 100 ml min^{-1}. Interestingly, as the flow rate increases from 100 ml min^{-1} to 500 ml min^{-1}, the Rp improves from 0.56 Ω cm^2 to 0.27 Ω cm^2 at 700 ^oC. At 800 ^oC with the fuel flow rate of 500 ml min^{-1}, the maximum power density of the cell reaches 406 mW cm^{-2}, which is about 4.97 W each cell. The cell performance at the flow rate of 500 ml min^{-1} is much better than of the one with a flow rate of 100 ml min^{-1}. Impedance spectra of the cell at different flow rates at 700 ^oC in humidified H_2 show two distinct arcs that joined at the frequency of 15.84 Hz. The Rs of the cell with catalysts, 1.08 Ωcm^2, is similar to the one without, 1.16 Ωcm^2, because the impregnation of 10 wt. % ceria + 1 wt. % Pd does not contribute to the electronic resistance of the electrode [40]. The size of the arcs in the low frequency region decreases as the flow rate increases. However, the high frequency remains unchanged. At 800 ^oC, the high frequency and the low frequency of the impedance spectra is incorporated into one arc. Moreover, the characteristic of the impedance spectra at different flow rates is very similar to the low-frequency region of the impedance spectra at 700 ^oC. The diameter of the low-frequency arcs at 700 ^oC at different flow rates is smaller than the respective diameter at 800 ^oC, indicating that the reaction at 800 ^oC may be more dependent on the mass transport[41].

3.3.3 Air vs. oxygen as the oxidant on the cathode

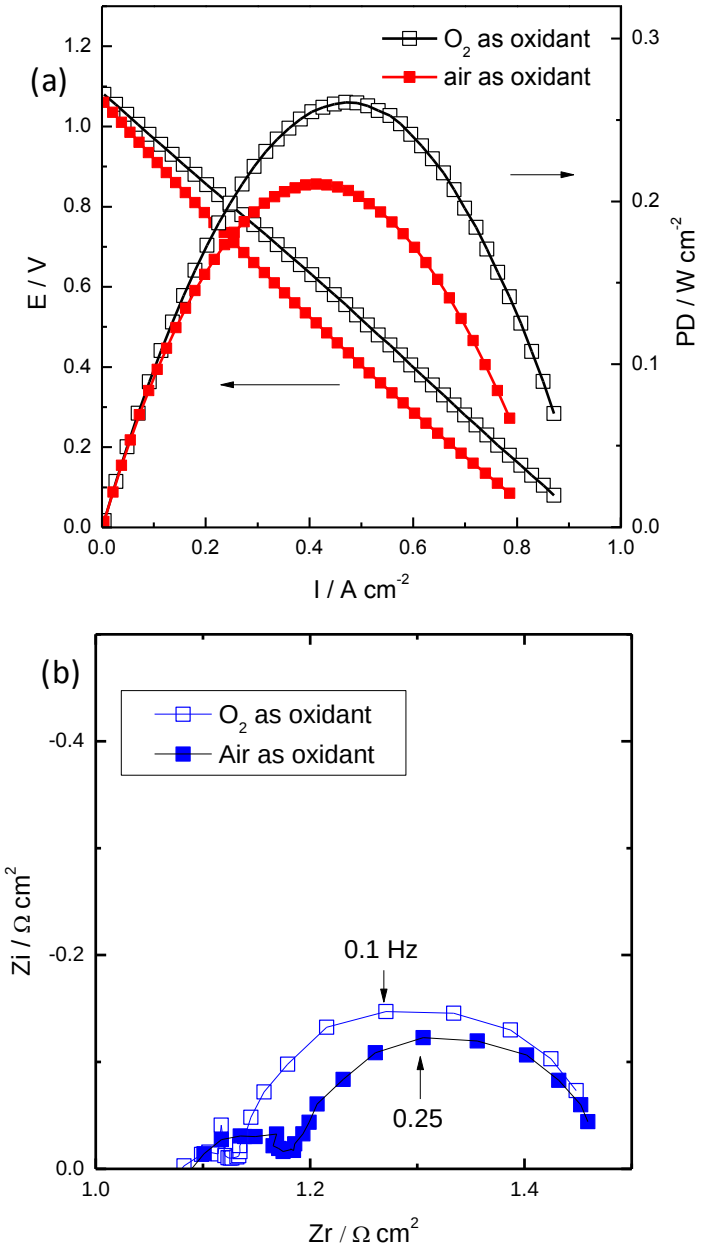

Figure 18 (a) IV curves and (b) impedance spectra of the cell operating at 700 °C under pure oxygen or air as oxidant at 500 ml min^{-1} and humidified H_2 as fuel at 300 ml min^{-1}.

In order to investigate the cathodic contribution to the polarization resistance, pure oxygen flow was used as the oxidant. As shown in Figure 18(a), the IV curve for the cell operating under air or pure oxygen at 700 °C indicates that the cell has an area specific resistance (ASR) of 1.29 Ω cm^2 or 1.19 Ω cm^2, respectively. The impedance

spectra in Figure 18(b) indicate that the ASRs in both conditions are quite similar to each other. However, the size of the first arc decreases when pure O_2 was used as the oxidant. This implies that the high-frequency region of the arc is related to the cathodic process[42].

3.3.4 Microstructure of the impregnated electrode before and after testing

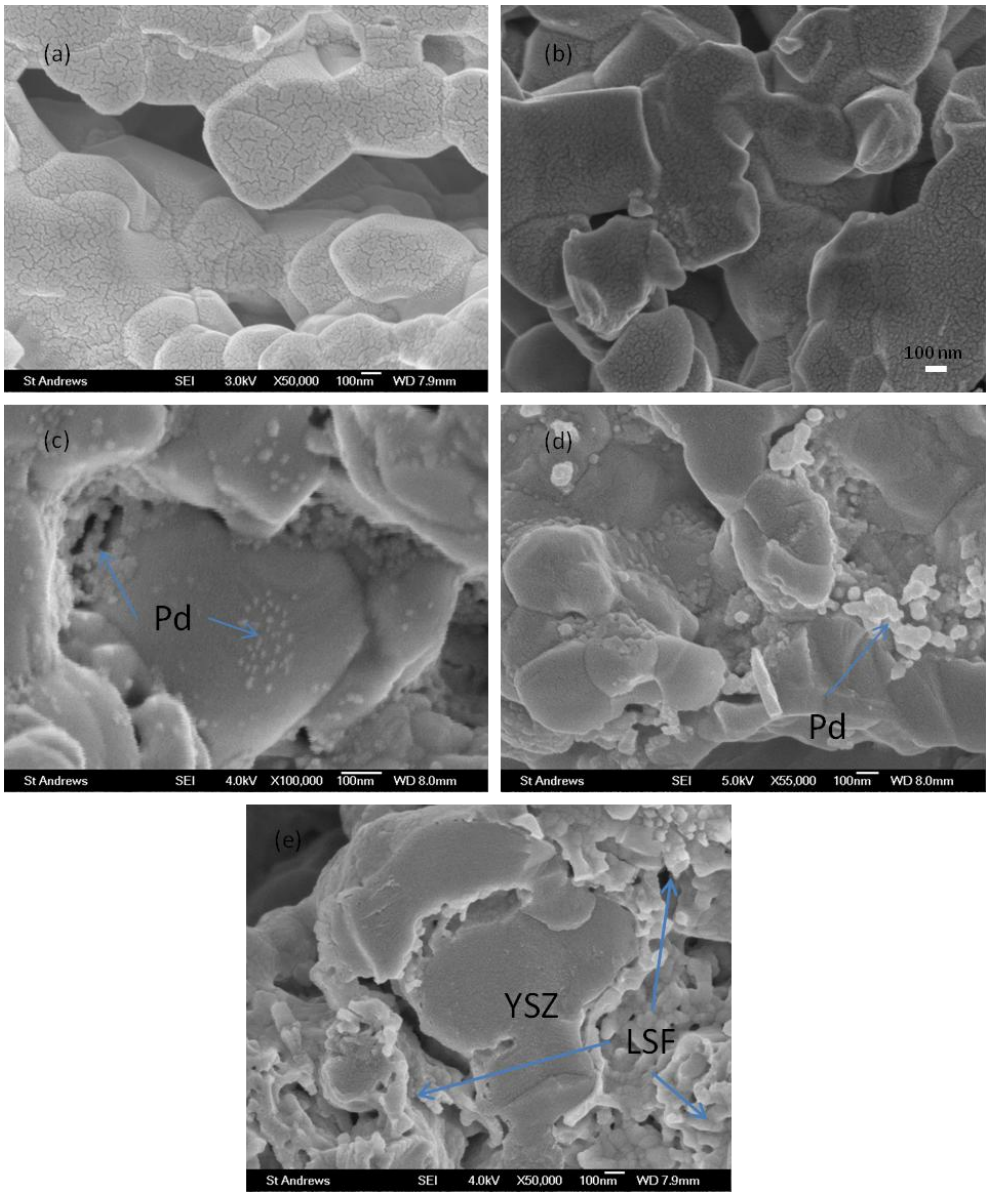

Figure 19 SEM images of the LSCM -8YSZ anodes before (a) and after (b) testing; SEM images of the Pd nano-particles in the anode containing 45 wt.% LSCM +10 wt. % ceria before (c) and after (d) testing; (e) SEM image of LSF/YSZ electrode.

The impregnation of these cells requires the solution to spread over a larger surface area than that of a button cell, therefore it is crucial to examine the homogeneity of

the distribution of the solution. Figure 19 shows the captured images of the microstructure of the impregnated anode before and after testing. Figure 19(a) and (d) show that the impregnated electrodes form a uniform layer of very fine and well dispersed nano-sized LSCM or LSF particles on the porous 8YSZ scaffold, which has been previously reported on button cells[27,39]. After a reduction in humidified hydrogen at 800 ^{o}C, LSCM transforms into a layer of finer and smaller nano-sized particles around 10 nm. Figure 19(a) and (c) demonstrate that the Pd particles of about 10 nm in size reside on the uniform surface of the ceria coating rather than directly on the LSCM layer in order to retard the sintering of Pd in hydrogen[43]. After testing at 800 ^{o}C in humidified hydrogen, the Pd particles aggregate from around 10 nm to 100 nm. These fractured cross-section images confirm that the impregnation of a large area is as successful as the ones on the button cell because the nitrate solution is able to spread over the entire surface of the substrate thanks to the capillary force.

3.4 Conclusion

A solid oxide fuel cell of 16 cm^{2} was successfully fabricated using an alternative method, the impregnation of a nitrate solution into the 8YSZ scaffold for both cathode and anode. At 800 ^{o}C, the large planar cell achieved a maximum power density of 223 mW cm^{-2} in humidified hydrogen. However, the power density of a single cell reaches 406 mW cm^{-2} when ceria and Pd are added as catalysts. The increase in fuel flow rate enhances the performance of the cell.

Chapter 4 Sintering and controlling of the shape of the scaffold

To manufacture a large fuel cell by impregnation, the fabrication of a flat and mechanically strong skeleton is the first step. In the last chapter, the fuel cell was produced by screen printing on a dense substrate which determines the macroscopic shape and mechanic strength of the skeleton. The forthcoming three chapters will focus on supported fuel cells whose skeletons will be prepared from green tape by tape casting, so it is necessary to sketch the fabrication and sintering of the scaffold.

4.1 Tape casting for green body of the scaffold

The slurry formulation is a crucial step for tape-casting, as it is also important for further processes for extra layers such as screen-printing, spin or dip-coating. Roughly, a good slurry is the one in which the ceramic grains are sterically interacting so that the particles are the farthest away from each other, that no agglomerates are formed, that the effect of gravity is negligible, hence no sedimentation occurs, and so that the viscosity is low enough to allow for an easy casting, and high enough for the green tape to have a sufficient creep resistance to maintain its geometry. Because the scaffold contains a dense electrolyte on a porous support, fugitive pore-forming agent (PFA) is used to take the position in the green tape for the porous layers.

In this study, co-casting is used because it can produce a membrane assembly with good adhesion. Two co-cast layers with different pore-forming agent (PFA) contents on a green tape for dense electrolyte are used to produce a graded porosity for the electrode. The characteristics of green layers are in turn completely determined by the slurry composition and powder morphology, the way the layers are superimposed and bonded, and how the multilayer is being dried prior to sintering. Tape calendaring could be one option by roll-milling tapes for the electrolyte and porous support to form a single membrane assembly. However, the adhesion between the dry tapes after lamination is likely to introduce bubbles because of the air caught in between the two layers in large area lamination. Moreover, the adhesion energy between the two laminated layers might not be higher than that generated from the difference of shrinkage kinetics that induces the delamination between layers. It is important to note that a good final bonding between two layers requires that at least one layer is wet (e.g. screen printing, dip coating, spin coating) and this can be achieved by co-casting the green tapes on another dried tape.

Table 1 Recipies for the slurry of dense and porous YSZ scaffold

	Electrolyte	**Co-cast layer-1**	**Co-cast layer-2**
	g	g	g
YSZ	20.00	20.00	15.08
graphite	0.00	12.32	13.20
Solvent	15.00	23.00	23.00
Polyethylene glycol (PEG)	1.69	2.43	2.43
Di-n-butyl phthalate (DBP)	1.43	2.19	2.19
Butvar	2.24	3.36	3.36
[a]: 33 wt.% ethanol in Methyl Ethyl Ketone (MEK)			

A green tape for dense electrolyte was made by casting the slurry containing YSZ powder (DKKK, 8-YSZ, Japan), solvent and organics. Two slurries (co-cast layer-1 and co-cast layer-2) for YSZ plus varied amounts of graphite as PFA were cast sequentially on the top of green tape of YSZ with 1-h drying after each casting. The ingredients for the slurry of green tapes are shown in Table 1. The green tape was cut and sintered in a programmed furnace up to 1400 ^{o}C for 5 hours.

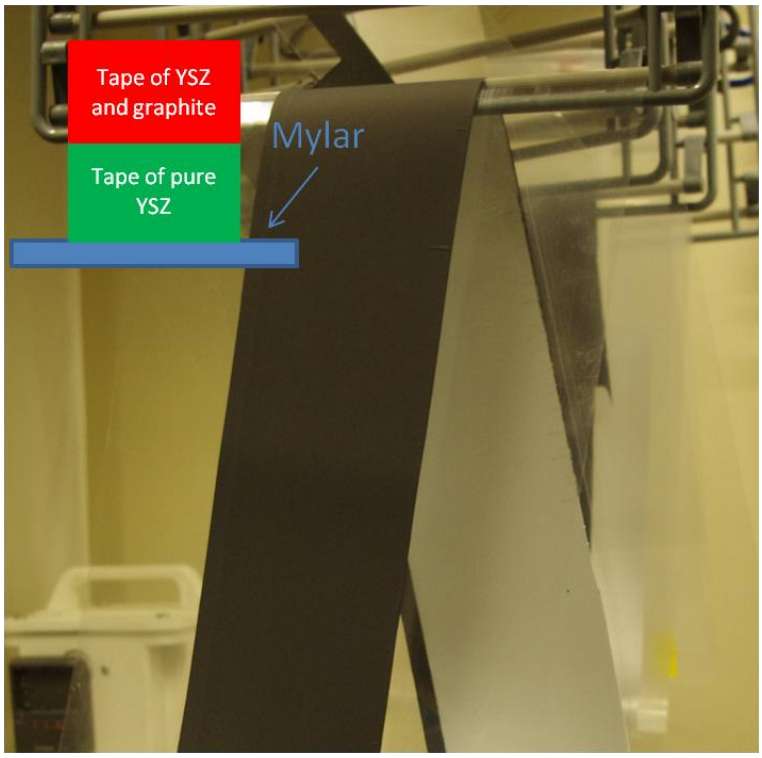

Figure 20 Image of a co-cast tape made by casting the slurry of YSZ and graphite (black) onto a green tape of pure YSZ (white); the insert shows a schematic of the arrangement of cocasting.

Figure 20 shows a final tape by casting the slurry containing YSZ and graphite onto a green tape containing pure YSZ. The good bonding from the co-casting can be ascribed to the partial dissolution of the dried YSZ green tape in the solvent of the slurry for porous YSZ. However, the dynamic dissolution process if poorly controlled could damage the integrity of the electrolyte. The extent of dissolution is determined by the amount of the solvent in the co-cast layer and the casting gap. In extreme cases, the slurry of the porous YSZ can penetrate through the green tape of electrolyte if the casting gap of the co-cast layer with PFA is larger than certain value as demonstrated in Figure 21(a), where black dots are visible, in contrast to the clean surface of smaller casting gap.

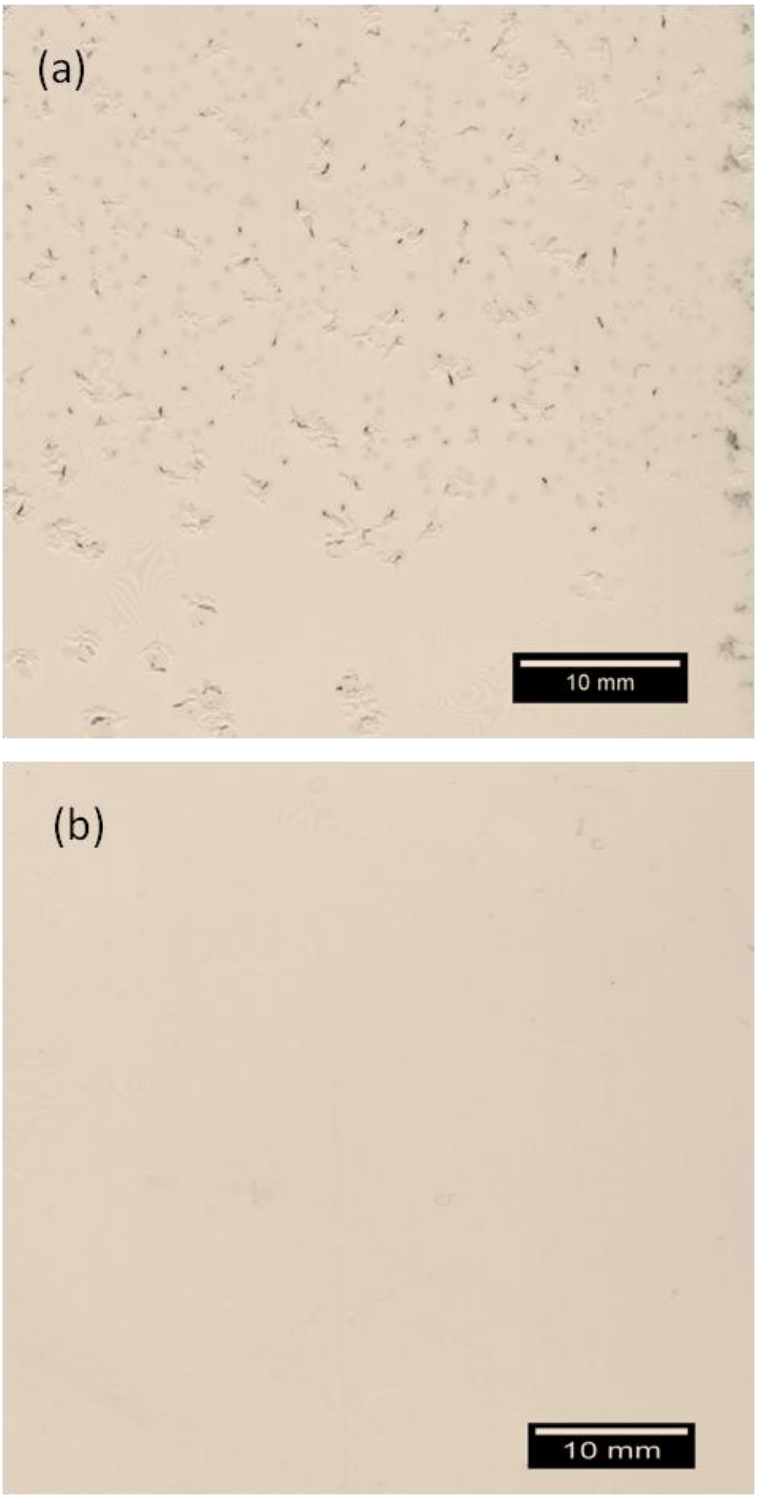

Figure 21 Images of the green tapes of pure YSZ under a co-cast layer of slurry with a casting gap of 1.47 mm (a) and 0.38 mm (b): the black spots in (a) are from the slurry for porous YSZ. The casting gap of the tape for the electrolyte is 0.25 mm.

4.2 Sintering of the green tapes

4.2.1 Determining the sintering program

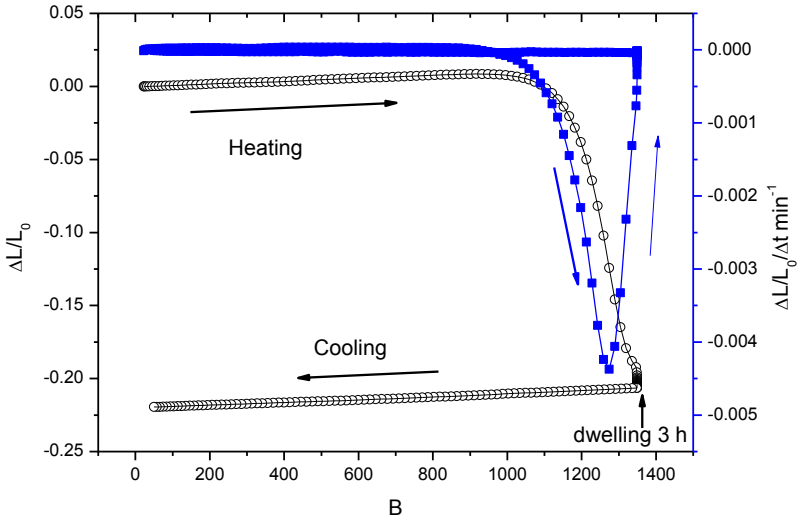

Figure 22 Shrinkage curves for YSZ; shrinkage ($\Delta L/L_0$) is represented with circle and; shrinkage rate ($\Delta L/L_0/t$) with square.

Deformation during sintering is composed of four terms: elastic deformation, thermal deformation, visco-plastic deformation and shrinkage due to the densification. The last one is by far the largest contribution to the overall deformation; its driving force is the reduction of surface energy and curvatures, hence the disappearance of the porosity. The shrinkage rate of the YSZ powder starts at 1000 ^{o}C and reaches the peak rate at 1270 ^{o}C as shown in the dilatometry graph (Figure 22). The sintering temperature is usually chosen to correspond to the temperature where the sintering rate reaches the maximum[44], i.e. 1270 ^{o}C for YSZ. In this study, in order to accommodate the mechanical strength requirement of the scaffold, a sintering temperature of 1400 ^{o}C is used to sinter the ceramic at final step, but the sample dwells at 1250 ^{o}C for 3 hours in case of too high a shrinkage rate.

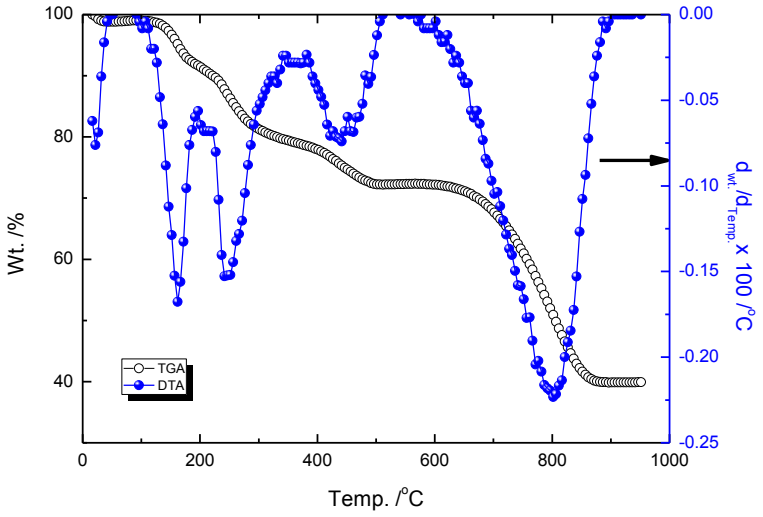

Figure 23 TGA of the green tape containing YSZ and graphite. The sample (about 3 mg) was measured at a ramp rate of 3 ^{o}C min^{-1} in air.

The role of heating ramps and plateaus at the onset of the sintering has more to do respectively with the plastic deformation of the green layers, due to a differential behaviour with temperature, and with the complete combustion of the organic slurry compounds. It is highly important that the combustion occurs gently and completely at the lowest possible temperature so that the evacuation of gas is rendered easily via the widely open porosity that the combustion has just created. Any increase of gas pressure inside the layers is obviously highly detrimental for the sample integrity (deformation, stresses, cracking…). The length of all the plateau is determined by thermal analysis so that the corresponding organic compounds can totally disappear. The TGA curve of the green tape for porous YSZ (Figure 23) indicates that YSZ consists only of 42 wt.% of the total weight, in agreement with the recipe of co-casting layer. The green tape (about 3 mg) were put in a small alumina crucible and measured with a thermogravimetric analyser with a ramp rate of 3 ^{o}C min^{-1}. The derivative curve of the TGA shows five peaks, the one at the 800 ^{o}C can be attributed to the combustion of graphite because the organics generally burn off below 700 ^{o}C. In order to avoid defects from the deformation of the green tapes, a ramp rate of 1.0 ^{o}C min^{-1} up to 750 ^{o}C and then a dwelling of 3 hours for the slow combustion of graphite was applied. Then the temperature rises to 1250 ^{o}C at 3 ^{o}C min^{-1} and then dwells for 3 hours to avoid too high shrinkage rate. The temperature rises again to 1400 ^{o}C (3 ^{o}C min^{-1}) and is held for five hours to produce a fully dense electrolyte. In

the cooling process, the furnace cools down to room temperature at 3.5 ^{o}C min^{-1}. The program is shown in Figure 24. In the sintering of laminated green tapes of YSZ and NiO-YSZ, the low ramp rate is crucial to the integrity and warping of final ceramic[45] by decreasing the difference in shrinking rate, whereas for the sintering of ceramic from the same batch of YSZ, the difference in shrinkage rate is less a concern. The high ramp rate after the burning off of pore former is effective in decreasing the processing time and avoiding the possible surface diffusion that might retard the densification process.

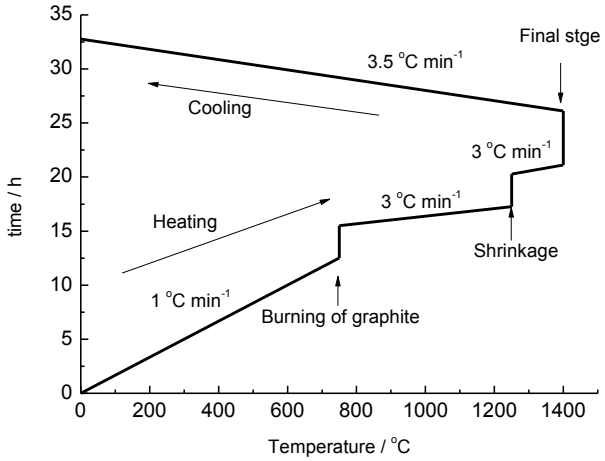

Figure 24 Temperature programming for the sintering of green tapes.

4.2.2 Firing setter arrangement

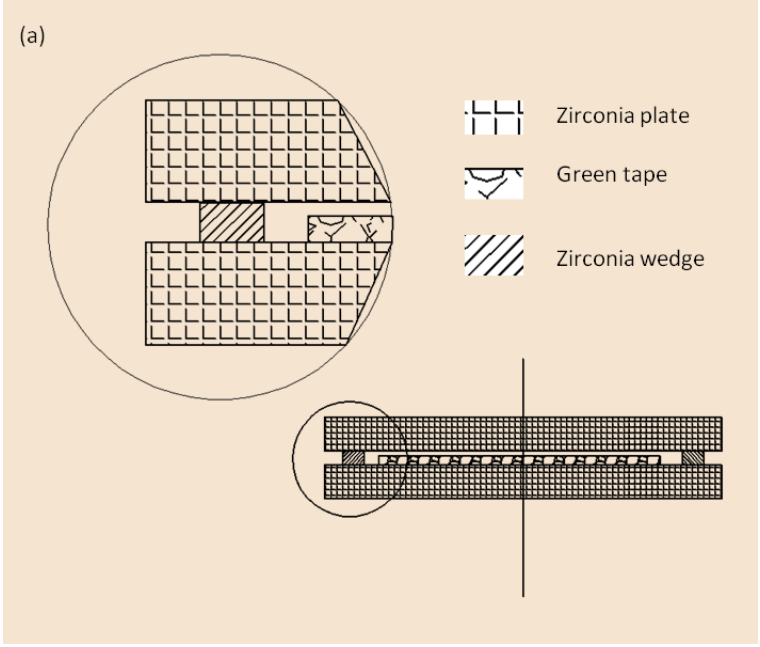

Figure 25 (a) Scheme of the sintering set-up; (b) a stacking system in practice.

The defect, such as pinholes or cracks, of the scaffold is either from the flaw of the green tape or the sintering process as mentioned in the last section[46]. For example, a pinhole in the electrolyte would enlarge in the sintering process and the friction between the firing setter and the ceramic would undermine the integrity of the final product. Moreover, the bending of the scaffold can be a result of the warping of the green tape or the mismatch of shrinkage rate of the different layers. It may even be

effective to put a light weight on top of the samples to maintain its flatness. But the weight is very difficult to control: it should not be too heavy to affect the porosity of the ceramic or the shrinkage since a highly porous ceramic is mechanically weak before the final stage of sintering, nor too light to be effective in controlling the shape. In this work the size of the green tape is in the range of 7.0 cm to 8.5 cm in length, and the final ceramic is 5.1 cm to 6 cm. The farthest distance that a YSZ powder might move is on the corner, 1.68 cm; the addition of weight on the green tape is very likely to interfere with this process and, in the end, the quality of the scaffold. As a result, a set-up shown in Figure 25 (a), a wedge of similar thickness to the green tapes is used to support the cover plate which controls the shape of the green tapes while not affecting the sintering process. In practice, the cover plate is positioned about 100-μm higher than the top surface of green tapes. Furthermore, the cover plate is also possible to distribute the uneven radiation from the element of the furnace that causes temperature gradient. At the end of the sintering process, the thickness of final scaffold is about 25 % less than the green tape, adding to the gap between the cover plate and the top of the ceramic. This implies that warping is still possible and proportional to the thickness of the green tape even if the top surface of the green tape is tuned perfectly to be just in touch with the cover plate. As shown in Figure 25(b), this set-up is easy to stack up and the wedges prevent the crush on the green tape.

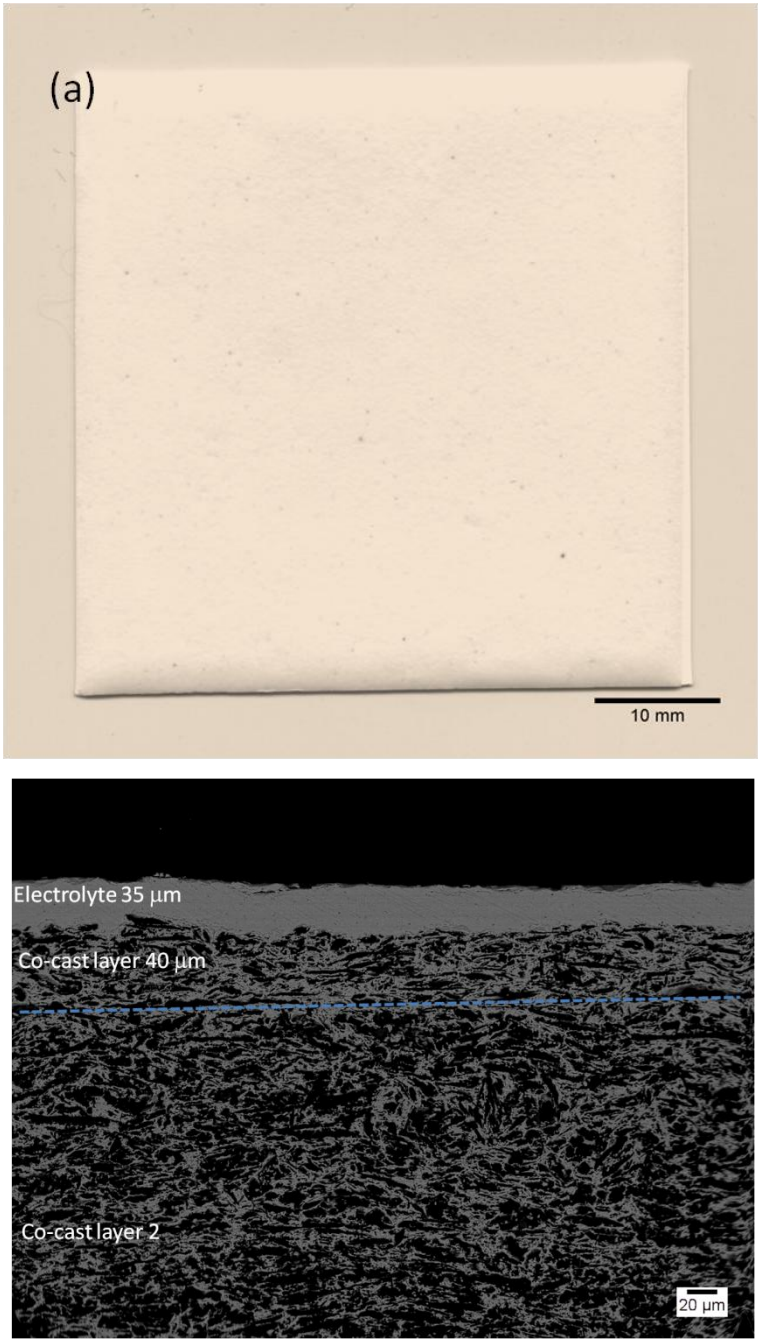

Figure 26 Image (a) and microstructure (b) of the sintered scaffold from the co-cast green tapes. Image (a) shows the electrolyte side of the scaffold.

The image of the sintered scaffold from a co-cast green tape is shown in Figure 26 (a), indicating that the scaffold is fairly flat and the warping is confined to the edges. The microstructure (Figure 26(b)) indicates that a dense electrolyte adheres well to the porous support. A rugged interface between the electrolyte and co-cast layer-1 also refers to the dissolution process that takes place in the co-casting process. The co-cast layer-1 shows a lower porosity than co-cast layer-2 thanks to the lower percentage of

graphite in the slurry. This gradient design can be advantageous in three aspects in comparison with the uniformly distributed porous structure: (1) the thin layer of YSZ plus graphite close to the electrolyte works as an barrier layer to avoid the dissolution of the green tape for electrolyte; (2) it provides more pores for the support where the liquid for infiltration and fuel/oxidant for reaction pass through; and (3) the low porosity in the vicinity of electrolyte is effective in decreasing the possibility of pores in the electrolyte.

4.3 Conclusion

In conclusion, the recipes of the green tapes, and programme of firing process with specially designed setters are introduced and discussed in this chapter and a flat scaffold with a fully dense electrolyte on a support of gradient porosity has been fabricated for the latter use. In the later chapters, the scaffold based on the green tapes will be infiltrated and tested as a fuel cell.

Chapter 5 A large area SOFC with thick cathode

5.1 Introduction

A cathode supported planar cell is well known to have inferior performance to the anode-supported counterpart with nickel cermet as anode in terms of ohmic resistance and polarization resistance[47]. However, when oxide is used to replace the nickel as anode materials to avoid the deposition of carbonaceous materials, the conductivity of perovskites for cathode (e.g. 80 S cm^{-1} at 700 ^{o}C for LSF in air) is advantageous: a majority of oxide anode materials show lower electronic conductivity in fuel environment than perovskite materials in cathode environment. Even though titanate and vanadate are reported to show high conductivity[26], [48] their precursors (e.g. Dihydroxy-bisammonium, lactate titanium (IV), 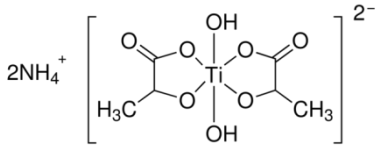 for Ti and ammonium metavanadate, NH_4VO_3) show low solubility in water, which requires increased repetitions to reach the desired loading to be conductive. $SrMoO_3$ shows a high conductivity, but it needs a reduction at 800 ^{o}C and shows a 40% volume change in the reduction process[49]. The doping of iron into the molybdate can reduce the reduction temperature and the volume change in reduction process, but the chemical compatibility with YSZ is a concern[50].

A thin anode and electrolyte on a thick cathode is effective in reducing the ohmic resistance loss [51] where the relatively low-conductivity materials are used for electrolyte and anode. Ceria shows a total electric conductivity in the same order of magnitude to YSZ at 700 ^{o}C[13,52] in reducing atmosphere and can be used in the functional layer of a solid oxide fuel cell[40]. The high solubility of cerium nitrate also makes the infiltration process more convenient. In this study, a large-scale (5 cm by 5 cm) fuel cell with thick cathode but thin anode is prepared by infiltrating the cathode part with LSF precursors and the anode part with ceria nitrate. The fuel cell is tested both in hydrogen and methane to demonstrate the scalability of infiltration as a method to produce fuel cells.

5.2 Experimental

5.2.1 Fabrication of large-area scaffold for impregnation

A green tape for dense electrolyte was made by casting the slurry containing YSZ powder (DKKK, 8-YSZ, Japan), solvent and organics. Two slurries (co-cast layer-1 and co-cast layer-2) for YSZ plus varied amount of graphite as pore-forming agent (PFA) were cast sequentially on the top of green tape of YSZ with intermediate of 1h for drying. The ingredients for the slurry of green tapes are shown in Table 1 (also in Table 2). The green tape was cut and sintered in a programmed furnace up to 1400 ^{o}C for 5 hours. On top of the electrolyte, a layer of ink containing YSZ and PFA (shown in Table 2) was printed, fabricated and sintered at 1300 ^{o}C for 4 hours to produce scaffold for the anode.

Table 2 A summarized ingredients of the slurry and inks used for making the scaffold.

	Electrolyte	Co-cast layer-1	Co-cast layer-2	Ink
Unit	g	g	g	g
YSZ	20.00	20.00	15.08	10.00
graphite	0.00	12.32	13.20	2.40
glassy carbon	-	-	-	0.60
Solvent[a]	15.00	23.00	23.00	-
Polyethylene glycol (PEG)	1.69	2.43	2.43	-
Di-n-butyl phthalate (DBP)	1.43	2.19	2.19	-
Polyvinyl butyral (PVB)	2.24	3.36	3.36	
Vehicle[b]				6.00

[a]:33 wt.% ethanol in Methyl Ethyl Ketone (MEK)

[b]:5 wt.% PVB dissolved in terpineol

5.2.2 Infiltration and testing under hydrogen or methane as fuel

$La_{0.8}Sr_{0.2}FeO_3$ was impregnated into the thick support under vacuum using 1 M (total concentration of metallic ions) solution from $La(NO_3)_3$•$6H_2O$ (Aldrich Chemistry, 99.99%), $Sr(NO_3)_2$ (Aldrich, 99 + %), $Fe(NO_3)_3$•$9H_2O$ (Fisher Scientific, Analytical agent grade) and citric acid. After each impregnation, the scaffold was fired at 700 ^{o}C for 0.5 h with a ramp rate of 2 ^{o}C/min. A thick cathode containing 35 wt.% LSF was

prepared with multiple impregnations and a final 4-hour firing at 850 ^{o}C. Saturated cerium nitrate solution was impregnated into the printed layer and fired at 450 ^{o}C until the remnant ceria consists of 45 wt % for the electrode. The catalyst 1-wt.% Pd is infiltrated into the anode after the impregnation of ceria. Pt paste (Gwent, C2000904P3) was applied on both sides of the electrode and then the whole cell was fired at 850 ^{o}C for 30 min to densify the Pt paste. For the sample tested on the Versa jig, silver paste is applied on both sides and dried in an oven at 80 ^{o}C for 2 hours.

5.3 Result and discussion

5.3.1 Structure of the scaffold

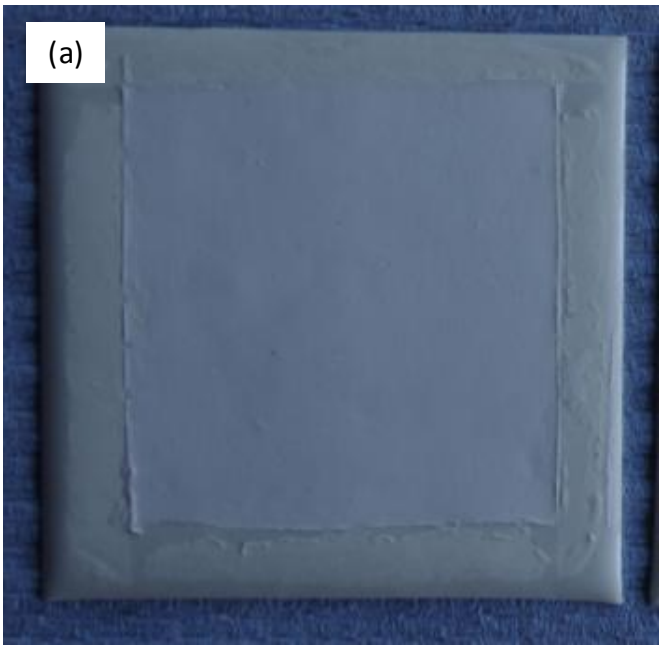

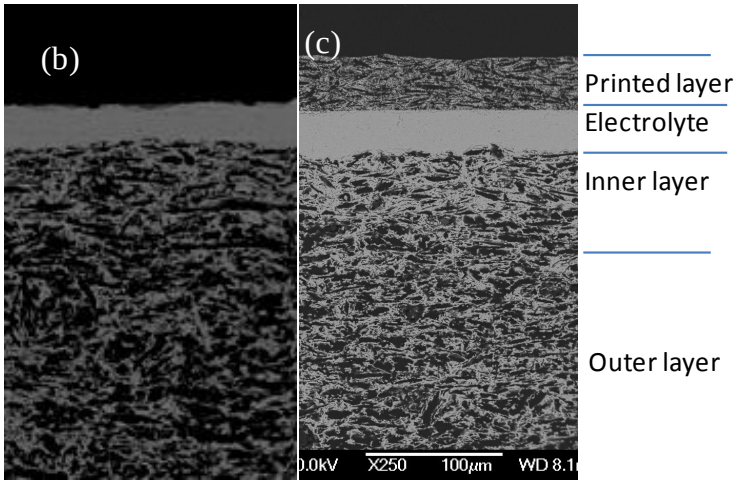

Figure 27 Image of the 5 cm x 5 cm scaffold for impregnation via the two-step process; SEM of the scaffold showing stepped gradient porous support with a dense electrolyte without (b) and with (c) the porous electrode.

The scalable methods, tape and screen-printing, are used to fabricate a 5 cm by 5 cm scaffold (Figure 27(a)) for the subsequent impregnation. The casting gap and amount of graphite in the green tapes were adjusted to produce the scaffold whose cross-section is shown in Figure 27(b). The 30-µm inner layer in contact with dense electrolyte is of 52 % porosity. The thick outer layer (67 % porosity) is fabricated for

the mechanical strength without blocking the transport of gas. After the application of ink and densification at 1300 ^{o}C, the 40-μm porous structure for the anode is shown in Figure 27(c). After the impregnation, the overview of the cross section is shown in Figure 28, indicating a thick support of 350 μm with lower porosity compared to the scaffold before impregnation. A magnified image (Figure 28(b)) showing the interface of the cathode/electrolyte/anode implies a good adherence between the three components.

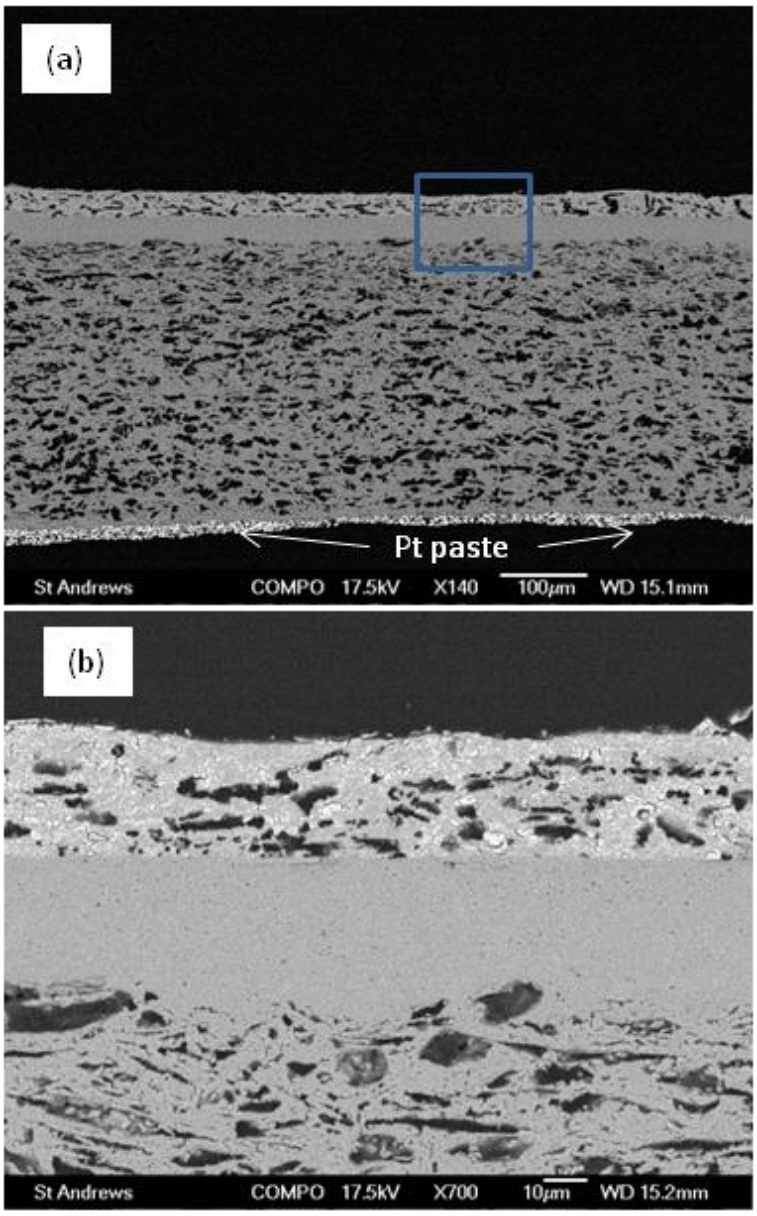

Figure 28 (a) SEM of fuel cell after impregnation of LSF in the thick support and ceria. (b) is the enlarged view of the rectangle in (a)

5.3.2 Microstructure after testing

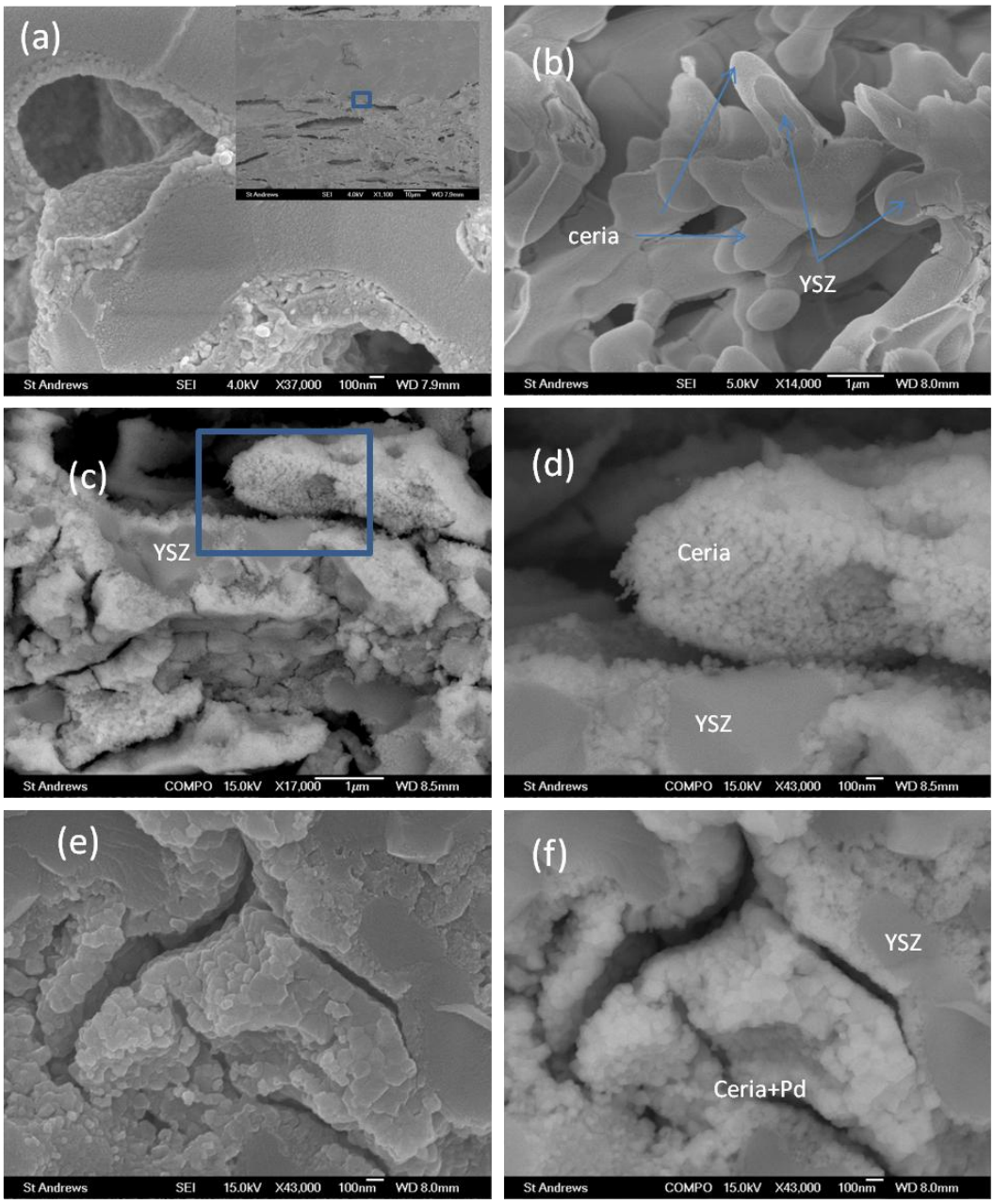

Figure 29 SEM image of of (a) LSF/YSZ electrode and (b) ceria coating on YSZ before testing. (c) and (d) are BSE images of ceria/YSZ electrode after the testing at 800 ^{o}C for 1 hour at different magnifications. (e) and (f) show the SEI and BSE images of the Ceria+Pd/YSZ electrode, respectively. The rectangle in the insert of (a) shows the zone of the image and (d) is located by the rectangle in (c).

A high-magnification fractured surface image (Figure 29(a)) at the interface of cathode/electrolyte shows that the precursor solution for perovskite reaches the interface and produces nano-sized LSF particles. The ceria forms a dense coating on

the surface of YSZ as shown in Figure 29 (b). The particle size of ceria after the testing is less than 20 nm after the testing at 800 ^{o}C as indicated in Figure 29 (c,d). The ceria nano-particles show agglomerates and cracks in between, but they adhere to the YSZ scaffold very well. After aging at 800 ^{o}C for 50 hours (Figure 29(e,f)), the diameter of the ceria + Pd grains is about 100 nm and denser than the ceria/YSZ electrode because of the longer annealing time and incorporation of metallic Pd. A comparison of the secondary-electron image (e) and back-scattering electron image (f) indicates that the Pd particles and ceria are very difficult to distinguish from each other. The crack on the ceria coating after testing maybe originate from the chemical expansion[53] caused by the Ce^{3+}/Ce^{4+} shifting under the H_2O/H_2 atmosphere. Moreover, the current passing through the electrode will alter the ratio of Ce^{4+}/Ce^{3+} shift in the vicinity of reaction sites as observed by Zhang and et. al.[54,55] with in-situ X-ray photoelectron spectroscopy (XPS). The cracks can be contributed to the increase of ohmic resistance in a ceria impregnated anode after high temperature annealing[1]. The severe agglomeration may decrease the triple phase boundary where the reduction of oxygen happens, but the recent study shows that the oxidation reaction can also proceed on the surface of ceria which is a mixed ionic and electronic conducting material[56].

5.3.3 Performance of the fuel cell under hydrogen as fuel

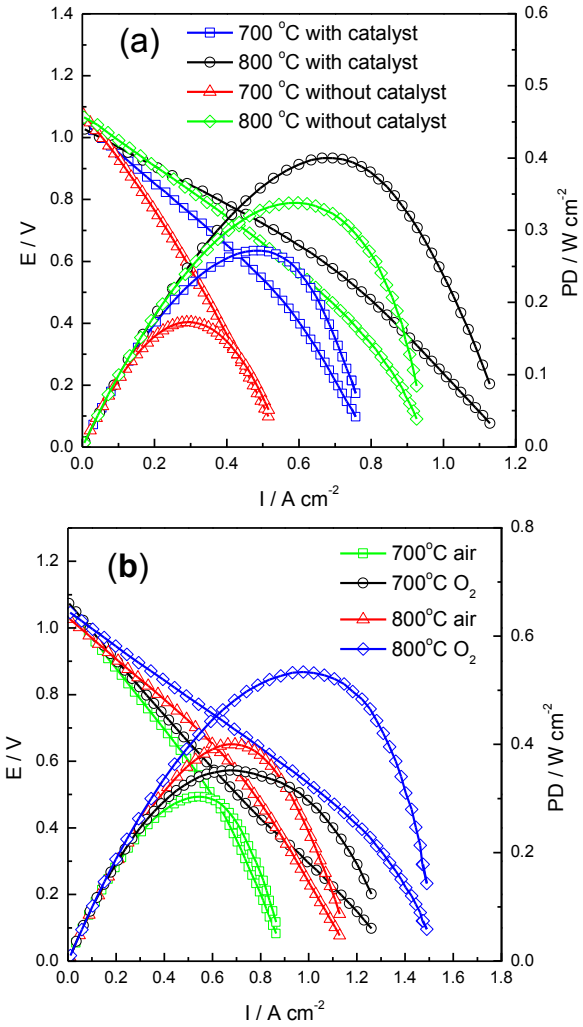

Figure 30 (a) The performance for the fuel cell with and without catalyst if air is used as oxidant; (b) the performance of the cell with catalyst operating if air or pure oxygen is used as oxidant. The flow rate of wet H_2 is 250 ml min^{-1}; the flow rates of oxygen and air are 500 ml min^{-1} and 2500 ml min^{-1}, respectively.

The IV curve of the cell with and without catalyst is shown in Figure 30(a). The cell without Pd on the anode shows a peak power density of 175 mW cm^{-2} and 336 mW cm^{-2} at 700 °C and 800 °C, respectively. With the impregnation of Pd, the maximum power density at 700 °C increased by 60 % to 270 mW cm^{-2}, while the one at 800 °C increased by 20 %. The curvature in IV curves at 800 °C may imply a diffusion-controlled process at the high-current region. The change of oxidant from air to oxygen increases the performance of fuel cell at both 700 °C and 800 °C, but

more obvious at 800 °C. In the case of oxygen as oxidant, the IV curve at 700 °C becomes straight and the diffusion limiting current increases significantly, showing the mass transport in the cathode side limits the performance of the fuel cell.

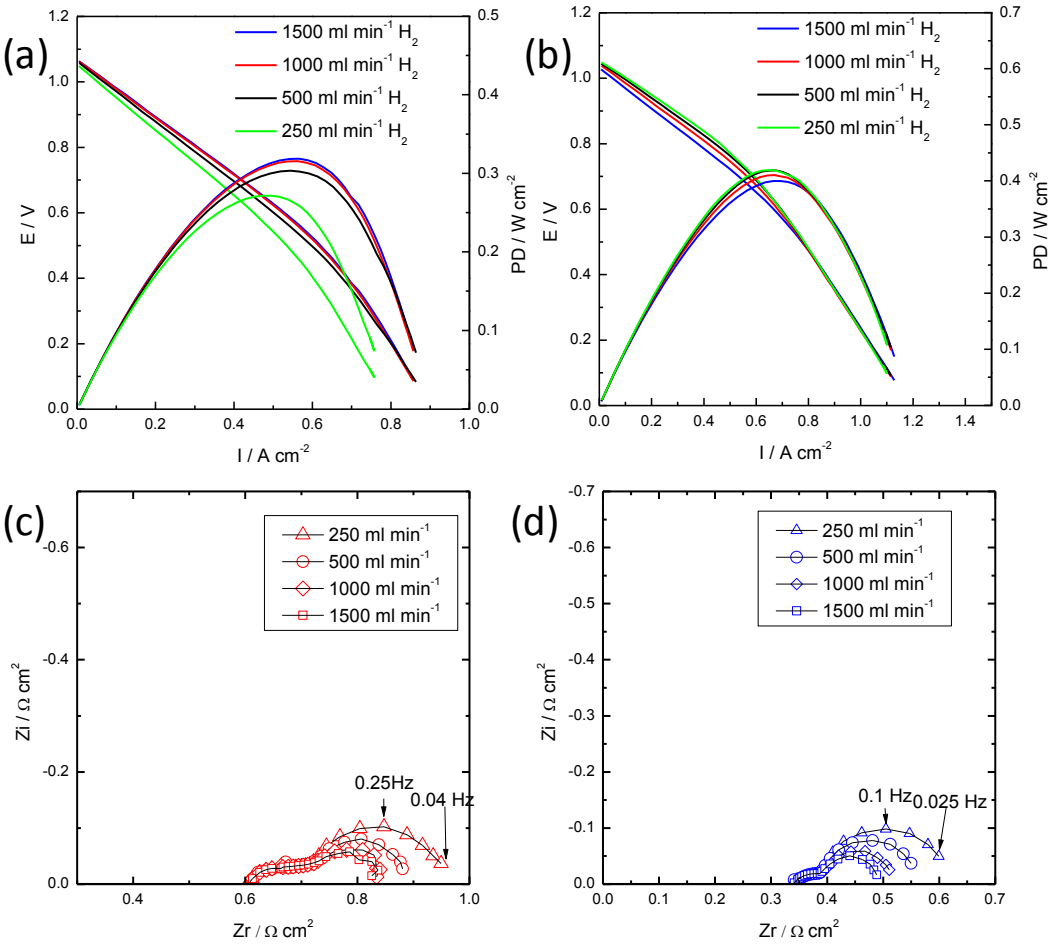

Figure 31 (a) and (b) The performance for the fuel cell with Pd as catalyst under different fuel flow rate at 700 °C and 800 °C, respectively; (c) and (d) Nyquist plots for the fuel cell under different flow rates of fuel at 700 °C and 800 °C, respectively. The flow rate of air as oxidant is 2500 ml min^{-1}.

Figure 31 shows the impact of flow rates on the performance of the cell with Pd as catalyst on the anode side. The change of flow rates does not alter the IV curve at 800 °C except for the OCV thanks to the balance of gas flow in the sealing area. The IV curves concur at the high current region, indicating that the change of OCV also does not have any effect on the performance of the fuel cell if the diffusion at the cathode is limiting the performance. Since the change of flow has no effect on the IV

curve at high current region, indicating the diffusion limiting comes from the cathode part. The IV curves at 700 ^{o}C do not change with flow rate except for the one with a flow rate of 250 ml min^{-1}. On the contrary, the change of flow rates exerts obvious impact on the low-frequency arc in the impedance at OCV, as shown in the Nyquist plots in Figure 31 (c) and (d). The discrepancy of the impedance and IV curve in predicting the performance of fuel cell lies in the irreversibility of system when a current is applied through the fuel cell. The arcs at low frequency (characteristic frequency of 0.25 and 0.1 Hz at 700 and 800 ^{o}C) are affected by the flow rate, while those at higher frequency are not. This could indicate that the arc at low frequency is associated (perhaps not entirely) with the diffusion process at anode.

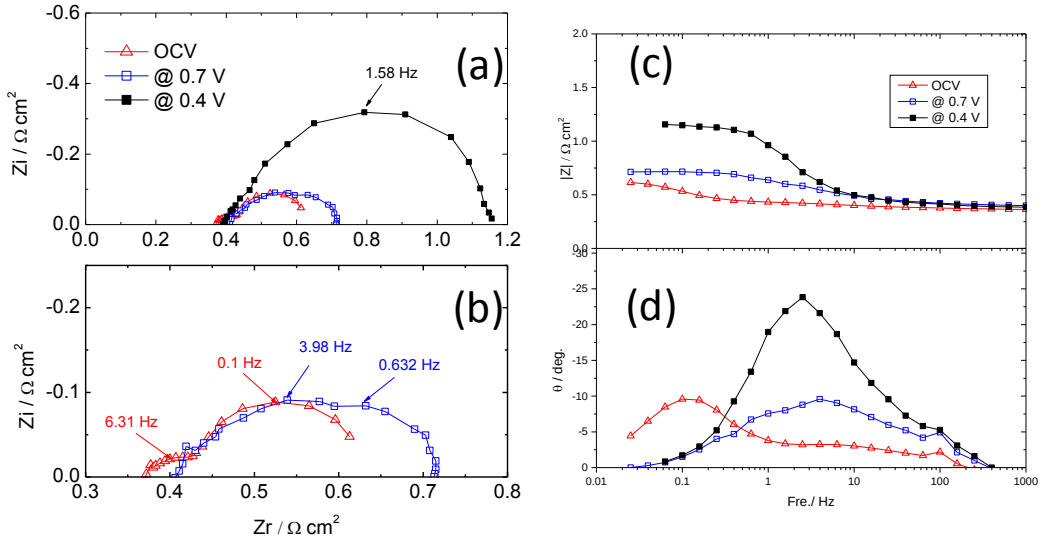

Figure 32 Nyquist and Bode plots for the fuel cell with catalyst under bias at 800 ^{o}C. (b) is the zoom-in to highlight the plot at OCV and 0.4V in (a). (c) and (d) are the plots of |Z| and phase angle vs. frequency. The flow rates of humidified H_2 as fuel and air as oxidant are 500 ml min^{-1} and 2500 ml min^{-1} respectively.

The superimposed Nyquist plots of the fuel cell at 0.4 V, 0.7 V and OCV are shown in Figure 32. At 0.7 V, the R_s estimated from the intersection of the Nyquist plot and real axis increases by 0.04 Ω cm^{-2}, compared to the one at OCV. In order to exclude temperature variation because of the Joule heat from the current passing through the fuel cell as a possible reason for the change of R_s, repeated test cycles at OCV and 0.7 V are used to verify the significance of this effect. The good reproducibility of impedance spectroscopy indicates the Joule heat is not a significant factor in

controlling the impedance. The increase of R_s at 0.7 V could be thus explained by the change of conductivity from either cathode or anode due to the change of oxygen partial pressure. Ceria is an n-type oxide whose electric conductivity decreases with oxygen partial pressure, while LSF is p-type. Under bias, the production of water vapour in the anode decreases the conductivity of ceria due to the increase of oxygen partial pressure in the area close to ceria[52,40], while the transport of oxygen from cathode decreases the oxygen partial pressure in cathode near the cathode/electrolyte interface[57,58] , a possible reason for the reduction of conductivity of LSF.

The application of current has a significant effect on the polarization resistance. Since the arc at 0.1 Hz can be attributed to the diffusion resistance on the anode side according to the impedance measurement under different flow rates, the application of current does not increase the diameter of the arc at this frequency, as shown the Bode plots in Figure 32(c). In contrast, the Bode plots indicate a clear increase of the phase angle and moduli for the arc with a characteristic frequency around 10 Hz. At 0.4 V, the large arc has a characteristic frequency of 1.58 Hz and a diameter as twice as that at OCV, indicating diffusion process of the cathode side dominates the electrochemical process in correspondence with the analysis of IV curve at different flow rates.

5.3.4 Stability test at 800 °C

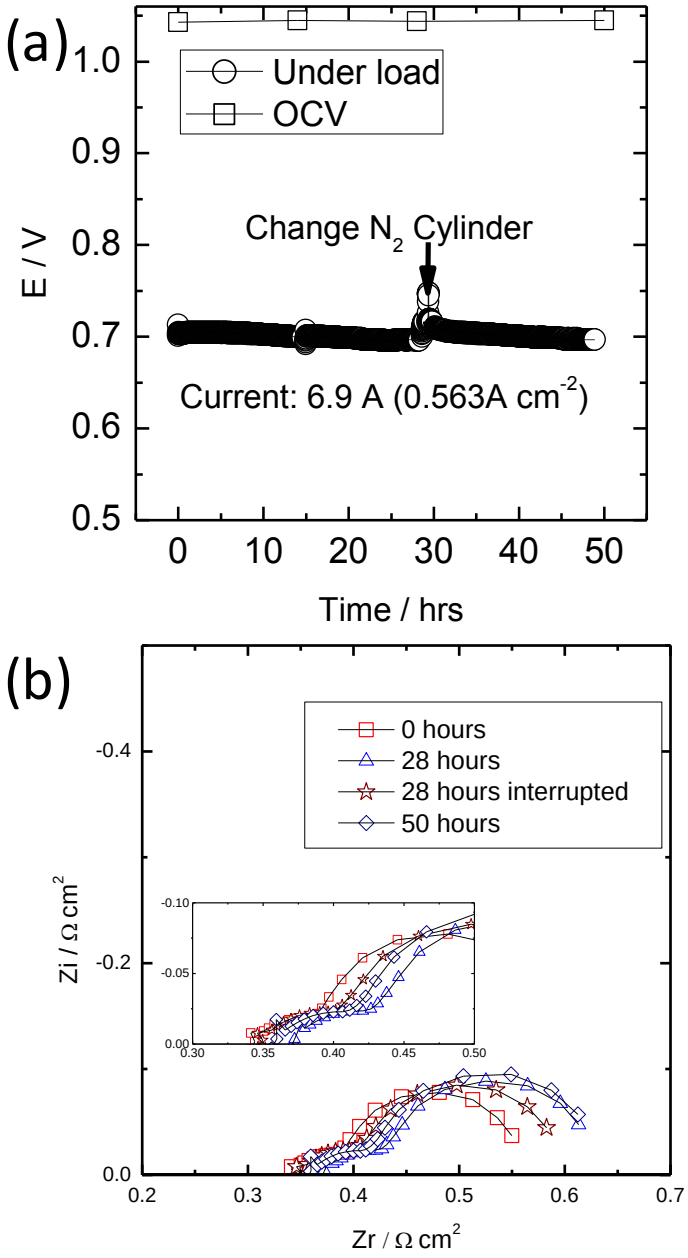

Figure 33 Stability test (a) and Nyquist plots (b) for the fuel cell with catalyst under different flow rate of fuel at 800 °C, respectively; the flow rates of air as oxidant are 500 ml min^{-1} and 2500 ml min^{-1}. The gases are switched off during the interruption owing to change of N_2 cylinder at 28 h.

A current of 6.9 A (0.563 A cm^{-2}) is applied on the cell to keep it at around 0.7 V, simulating the industrial typical application condition for around 50 hours. The

degradation of voltage is within 1% in the whole testing duration. The output of the fuel cell is approximately 5 W and the fluctuation of voltage and intermittent OCV is recorded in Figure 33(a). The OCV stabilizes at 1.05 V through the whole testing process, meaning the degradation is not likely to be induced by the cross-over of gases. In the first 28 hours the voltage decreases slightly but constantly and the impedance in this stage (Figure 33(b)) shows increase in R_s and R_p. However, the interruption of experiment at 28 hours decreases the R_s while the R_p does not change, and the fluctuation of temperature can be an explanation in this short period. However, the degradation resumed after the interruption. In order to figure out if this degradation is caused totally by the possible fluctuation of temperature in the slow thermal flow balance, the values of R_s and R_p through the stability test is tabulated in Table 3. The value of R_s/R_p decreases from 2.14 to 1.62 from 700 ^oC to 800 ^oC, but in the dwelling process, this value still decreases with time, in a direction of rising temperature. On the contrary, the increase of R_s along the ageing process indicates a decrease in temperature. Therefore, the imbalance of thermal flow or temperature change cannot explain solely the degradation. This paradox can be explained by the change of microstructure of the cathode that can simultaneously increase the R_p value and R_s value. At 800 ^oC, the increase of R_p is foreseeable thanks to the growth of nanoparticles[27,59] , especially the metallic catalyst in the anode[43].

Table 3 R_s and R_p, ASR and R_s/R_p at different times of the stability test

Time (h)	R_s (Ω cm^2)	R_p(Ω cm^2)	ASR(Ω cm^2)	R_s/R_p
0	0.34	0.21	0.55	1.62
14	0.36	0.23	0.59	1.56
28	0.37	0.24	0.61	1.54
28 after interrupt.	0.35	0.23	0.58	1.52
50	0.36	0.25	0.61	1.44
0[a]	**0.60[a]**	**0.28[a]**	**0.88[a]**	**2.14[a]**

[a]: data for the same fuel cell at 700 ^oC

5.3.5 Testing under methane as fuel with Versa jig

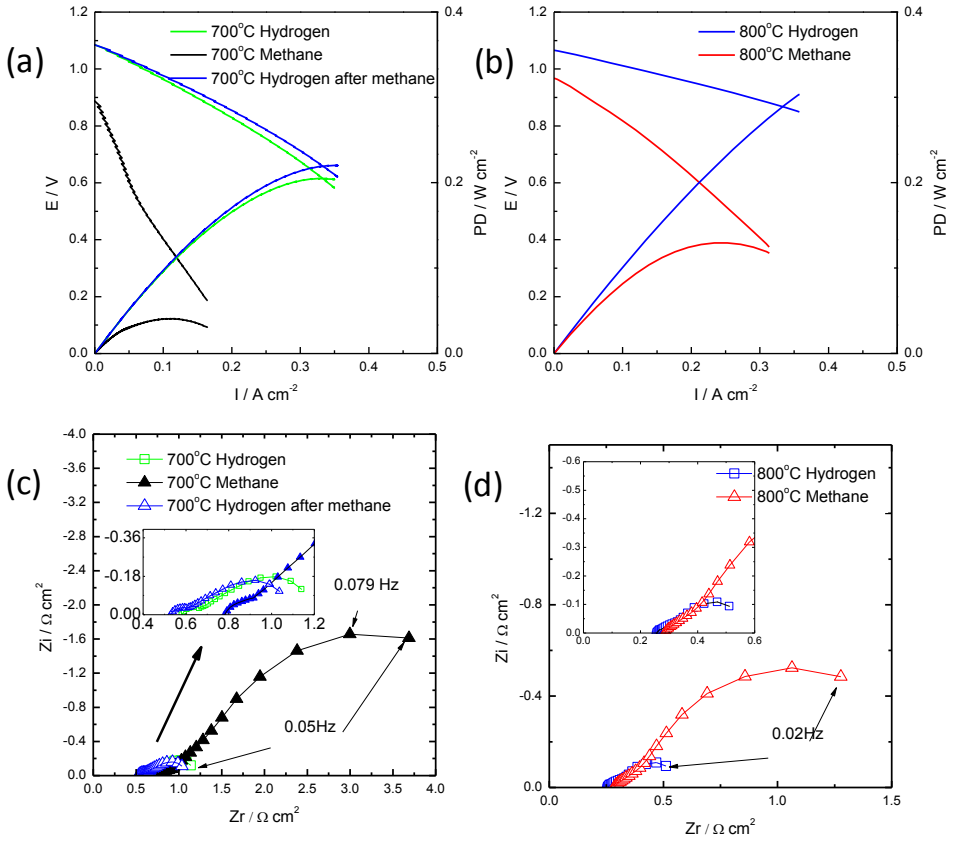

Figure 34 (a) and (b) show the IV curve at 700 °C and 800 °C under hydrogen and methane gas as fuel. (c) and (d) show the corresponding Nyquist plots of impedance measurement. The flow rates of air and wet hydrogen are 250 ml min^{-1} and 180 ml min^{-1}, respectively. The methane is 100 ml min^{-1}.

The fuel cell with thick cathode is also tested with methane as fuel in the Versa jig. At 700 °C, the IV and impedance is shown in Figure 34(a) and (c). If hydrogen is firstly used as fuel at 700 °C, the OCV is 1.09V and the ASR from impedance is ca. 1.2 Ω cm^2.The slope of IV curve shows an ASR of 1.32 Ω cm^2, comparable to the ASR value, 1.70 Ω cm^2, calculated from IV curve in the same voltage range (Figure 30(a)) from a cell tested with ECN jig. The application of methane causes the drop of OCV to 0.87 V at 700 °C and increase of R_s and R_p, as indicated in the impedance plots. The cracking of methane can be catalysed on the stainless tubing or steel plates (nickel based alloys)[60], which possibly increases the content of hydrogen and the OCV. The OCV of 0.87 V at 700 °C is comparable to the reported result from button cell testing, about 0.8 V[40], indicating that the catalytic effect is insignificant in our

case. The maximum output power density at 700 is 40 mW cm^{-2}. At 800 ^{o}C, the OCV increases to 0.97V and the power density peaks at 131 mW cm^{-2}.

5.4 Conclusion

A fuel cell with thick cathode support has been fabricated by infiltrating both sides of a tri-layer scaffold prepared by tape casting and screen printing. The infiltration of LSF into the 350-μm support and ceria into the screen-printed layer effectively decreases the ohmic resistance of the fuel cell, but the oxygen diffusion can be a limiting factor for the fuel cell under high current region. A power of 5 W was continuously drawn out from the cell at 800 ^{o}C during the initial 50 hours. The slight degradation of the performance is attributed to the degradation of electrode by analysing the ratio between R_s/R_p along with time. A lower OCV and higher polarization resistance were obtained when the fuel is changed from hydrogen to methane due to the lacking of catalytic effect of ceria on oxidizing hydrogen.

Chapter 6 A large-area SOFC with thick anode

6.1 Introduction

An SOFC with thin supported electrolyte is one method that can decrease the ohmic resistance arising from the electrolyte. A fuel cell with thick cathode differs from the one with a thin cathode in terms of the concentration polarisation that is associated with the resistance for transport reactant species to and product species from the reaction sites[61]. Excessive mass transfer resistance originated from the blocking effect of the thick porous electrode may cause a current limitation if the reactant concentration at the reaction site becomes small. For example, in an anode supported cell with thickness of the anode, la, significantly larger than that of the cathode, lc, the limiting current density, i_{as}, when the interfacial concentration of H_2 near the electrolyte, $p_{H2}^{(a)} \approx 0$, is given by

$$i_{as}=\frac{2Fp_{H2}^{o}D_{a(eff)}}{RTl_a} \qquad 6\text{-}1$$

while for a cathode supported fuel cell with air as oxidant, the O_2 limiting current density, i_{cs}, can be derived under the similar assumption:

$$i_{cs}=\frac{4Fp_{O2}^{o}D_{c(eff)}}{RTl_c\frac{P-p_{O2}^{o}}{P}} \qquad 6\text{-}2$$

where F is Faraday constant, P_{H2}^{o} and P_{O2}^{o} is the respective partial pressure of hydrogen and oxygen, P is the pressure of air, $D_{a(eff)}$ and $D_{c(eff)}$ is the effective binary diffusion coefficient given in terms of binary diffusion coefficient ($D_{H2\text{-}H2O}$, $D_{O2\text{-}N2}$), porosity ($V_{a/c}$) and tortuosity (τ_a or for anode and cathode τ_c): $D_{a(eff)}=\frac{V_aD_{H2\text{-}H2O}}{\tau_a}$

$D_{c(eff)}=\frac{V_cD_{O2\text{-}N2}}{\tau_c}$ Because the anode binary diffusion coefficient, $D_{H2\text{-}H2O}$, is about four times that of the cathode counterpart, $D_{O2\text{-}N2}$, the cathode would have a much larger concentration polarisation than that of the anode for similar thickness, porosity and tortuosity. A fairly thick anode may be viable without incurring excessive loss. Therefore, the performance of an anode-supported cell is superior to that of an electrolyte-supported cell or a cathode-supported cell for the same materials used, same electrode kinetics and same operational constraints[62]. When it comes to impregnation as the method to fabricate a fuel cell with ceramic electrode, the

diffusion polarisation can also be the determining loss of the fuel cell, the selection of a particular cell component as the support/substrate of the fuel cell can also be the determining factor to develop a high-performance SOFC. In this chapter, we devote to demonstrate a fuel cell with a thick anode as support and a thin cathode.

6.2 Experimental

The same scaffold for the fuel cell with thick cathode in Chapter 5 was used in this study. The precursors for $La_{0.7}Sr_{0.3}VO_{4-\delta}$ (LSV_{ox}) as anode and LSF as cathode were impregnated to the thick support and thin porous layer on both sides of the electrolyte. In each pre-calcination process, the scaffold and the contents are heated up to 700 ^{o}C with a ramp rate less than 2 ^{o}C to avoid the violent combustion of organics that would damage the scaffold. After 0.5-hour dwelling, the impregnated structure is cooled to 100 ^{o}C or below. Ten impregnations are used to achieve the desired content, 25 wt% LSV_{ox} and 35 wt.% LSF for anode and cathode, respectively. Ceria nitrate is infiltrated into the anode and calcined at 500 ^{o}C, followed by infiltration of nickel nitrate with calcinations at 700 ^{o}C again. The final loading of ceria and nickel are 5 wt.% and 2 wt.%, respectively. After the impregnations, the residue of the oxides from the precursor on the surface of the anode is scrubbed off with sandpaper to avoid unwanted vanadates. For the fuel cell test with ECN jig, the sample is calcined at 900 ^{o}C for 30 minutes after the application of Pt paste for densification and forming of desired phases. On the other hand, the sample for Versa jig is calcined at 900 ^{o}C for 30 minutes before the application of silver paste. The diffraction data were refined by the Rietveld method, using the program General Structure Analysis System (GSAS). The EDX data for the La, Sr, and V are corrected with phase pure $La_{0.7}Sr_{0.3}VO_{4-\delta}$.

6.3 Result

6.3.1 Compositional segregation of infiltration and phase analysis

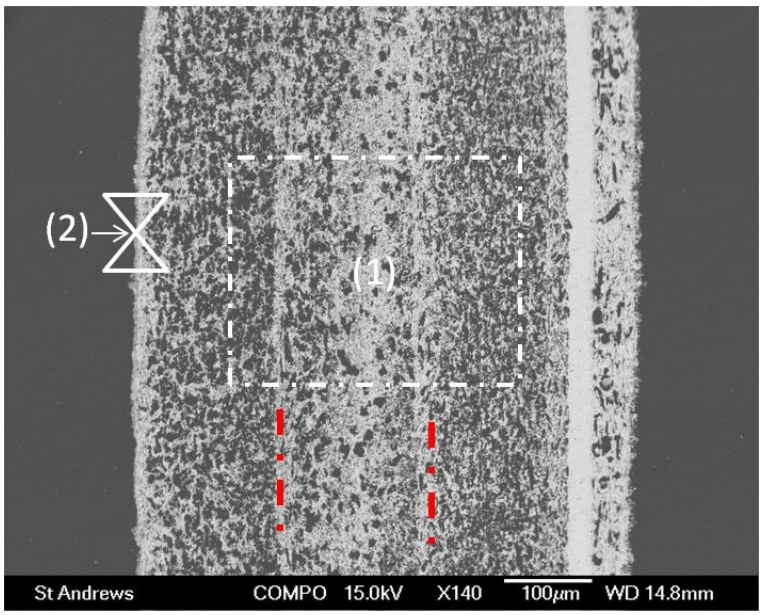

Figure 35 Back-scattering image of the cross-section of the anode supported fuel cell with impregnation on both sides. Sites (1) and (2) indicate the position for EDX.

The cross section of the impregnated fuel cell is shown in Figure 35(a), where the thin electrolyte (30 μm) is sandwiched between a thick (486 μm) anode impregnated with LSV and a thin (40 μm) cathode impregnated with LSF. In the anode side, there is a thin layer on the surface across site (2), which is a result of the excessive precursor solution on the surface. Two layers of porous support in addition to the co-cast layer can be easily identified in the image as indicated in the red dashed lines. The bright area is a result of higher porosity on the interface that will absorb more precursors for vanadates in the infiltration process.

The EDX data (Table 4) for site (1) demonstrates that the overall stoichiometry of $La_{0.7}Sr_{0.3}V_{1-y}O_{4-\delta}$ was B-site deficient (y=0.23), which possibly lowers the conductivity of the electrode, while decreasing the possibility of poisoning from the diffusion of vanadium. The deviation of this value from the stoichiometry of the solution can be a result of precipitation of vanadate from the cooling solution on the surface of the porous scaffold. On the surface of the impregnated anode (as at site *2*), there is a vanadium rich layer that proves the exsolution process, as indicated in the

EDX shown in Table 4. The stoichiometry of the vanadate can be represented as $La_{0.7}Sr_{0.3}V_{1+y}O_{4-\delta}$ (y=0.31).

Table 4 EDX data for the site (1) and (2).

Element	Weight%	Atomic%	Weight%	Atomic%
	Site (1)		Site *2*	
O K	24.38	64.76	24.45	64.62
V K	5.5	4.59	1.61	1.34
Sr L	3.65	1.77	0.61	0.30
Y L	7.71	3.69	11.5	5.47
Zr L	45.09	21.01	59.44	27.55
La L	13.67	4.18	2.39	0.73

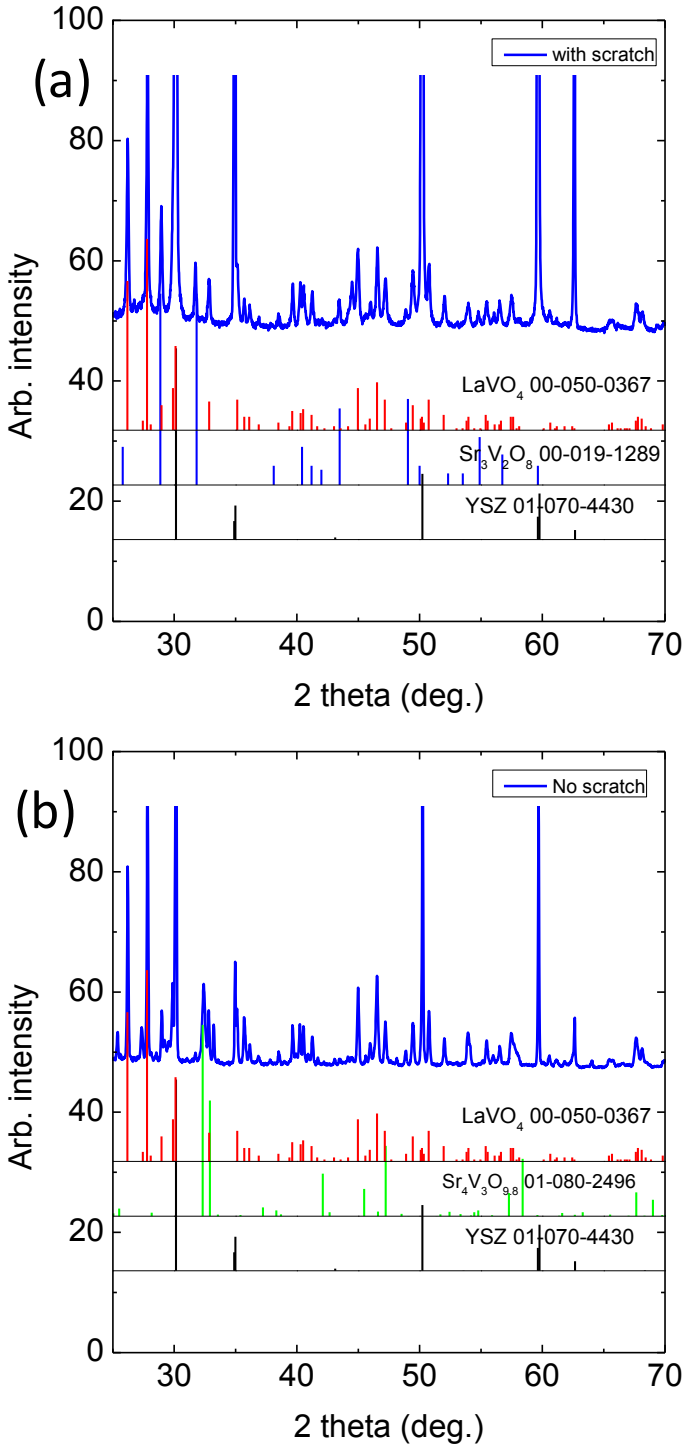

Figure 36 XRD patterns for the vanadate –YSZ composite electrode at site (1) and (2) in Figure 35 are presented in (a) and (b), respectively.

Figure 36 shows the XRD patterns for the oxides sintered at 900 ^{o}C at sites (1) and *(2)*. The XRD at site (1) is obtained by scratching the surface with a sandpaper to remove the materials in region (2). After the high temperature firing at 900 ^{o}C for 30 min, the

XRD pattern for site (1) is retrieved by scratching off the surface layer, as shown in Figure 36(a). $Sr_3V_2O_8$ and $LaVO_4$ are identified as the phases in the B-site deficient LSV. The A-site deficient vanadate at site (2) contains $Sr_4V_3O_{10-\delta}$ as the impurities as shown in the XRD pattern in Figure 36(b). Because the low melting point of the V_2O_5, the firing at 900 ^oC could cause the loss of vanadium on the surface of the electrode. This vanadium rich layer will be sanded away to avoid the possible side-effect on the performance of fuel cells.

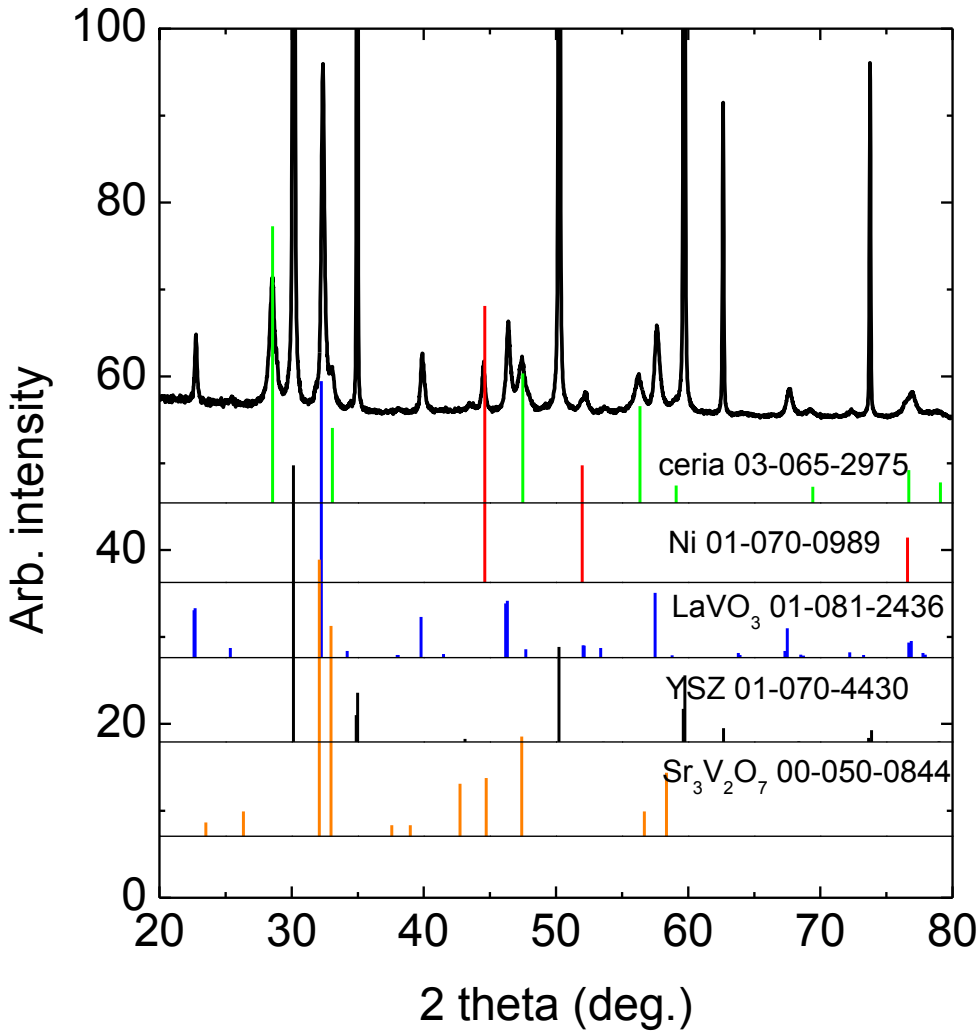

Figure 37 XRD of the post-test sample with Ni ceria as catalyst: the sample is reduced in humidified hydrogen at 800 ^oC.

After the test at 800 ^oC with hydrogen as fuel, the XRD of the anode is shown in Figure 37. The vanadates are fully reduced to perovskite and metallic nickel is detected after the testing. The $Sr_3V_2O_8$ that persists at 700 ^oC [63] in humidified

hydrogen can be reduced at 800 °C to form the layered perovskite $Sr_3V_2O_7$. The impregnated nickel precursor is fully reduced to metallic state. The cell parameters of the LSV in YSZ porous structure are calculated by refining the intensive XRD data of LSV/YSZ (Figure 38) to avoid the peaks of ceria and nickel. The structure of infiltrated LSV is refined as orthorhombic with a=5.5326(4) Å, b=7.8237(5) Å, c=5.5499(2) Å and *V*= 240.23 Å. The volume of the unit cell of $La_{0.7}Sr_{0.3}VO_{3-\delta}$ is slightly larger than that of $La_{0.9}Sr_{0.1}VO_{3-\delta}$ [64], 240.16 Å^3. The incorporation of a Sr^{2+} at the position of La^{3+} should expand the unit cell due to the larger ion radius of Sr^{2+}. Even though pure $La_{0.7}Sr_{0.3}VO_3$ crystals are observed with calcination at 2000 °C under Ar/H_2 gas [65], the annealing of $La_{0.7}Sr_{0.3}VO_{4-\delta}$ will eventually lead to the segregation appearance of $SrVO_3$ apart from the orthorhombic $LaVO_3$ phase in the temperature range of 800-1100 °C[64,66] in reduction with H_2. The refinement in this study is not able to eliminate the existence of cubic $Sr_{1-x}La_xVO_3$ (x<0.5) or tetragonal $Sr_3V_2O_7$ phase.

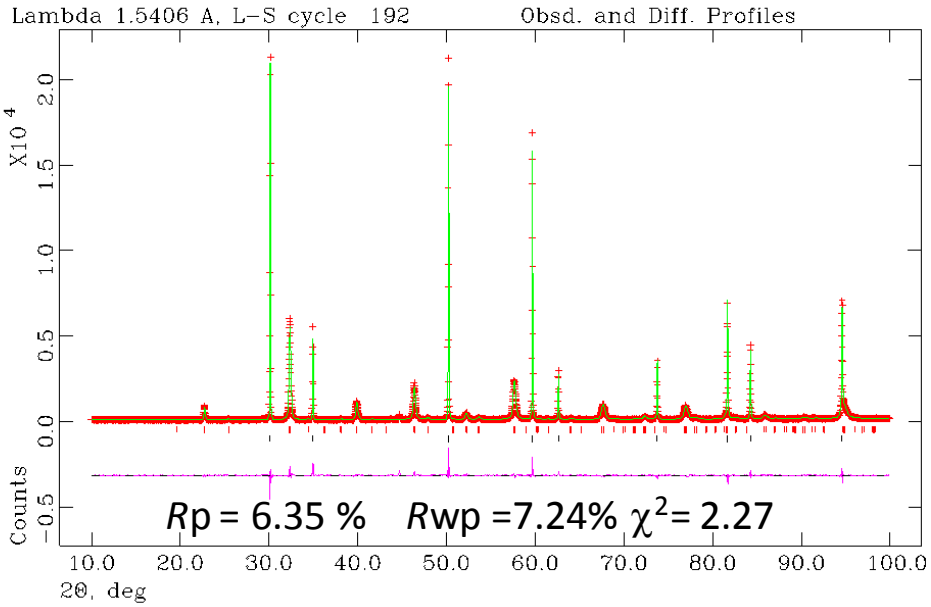

Figure 38 XRD pattern of LSV/YSZ composite electrode after reduction at 800 °C 4.2% steam containing H_2. The dots are observed data and the line is calculated data. The vertical bars are calculated reflections for phases. Upper red represents LSV orthorhombic with symmetry Pbma and bottom black belongs to YSZ cubic with symmetry Fm-3m.

6.3.2 SEM image of LSV-Ni electrode

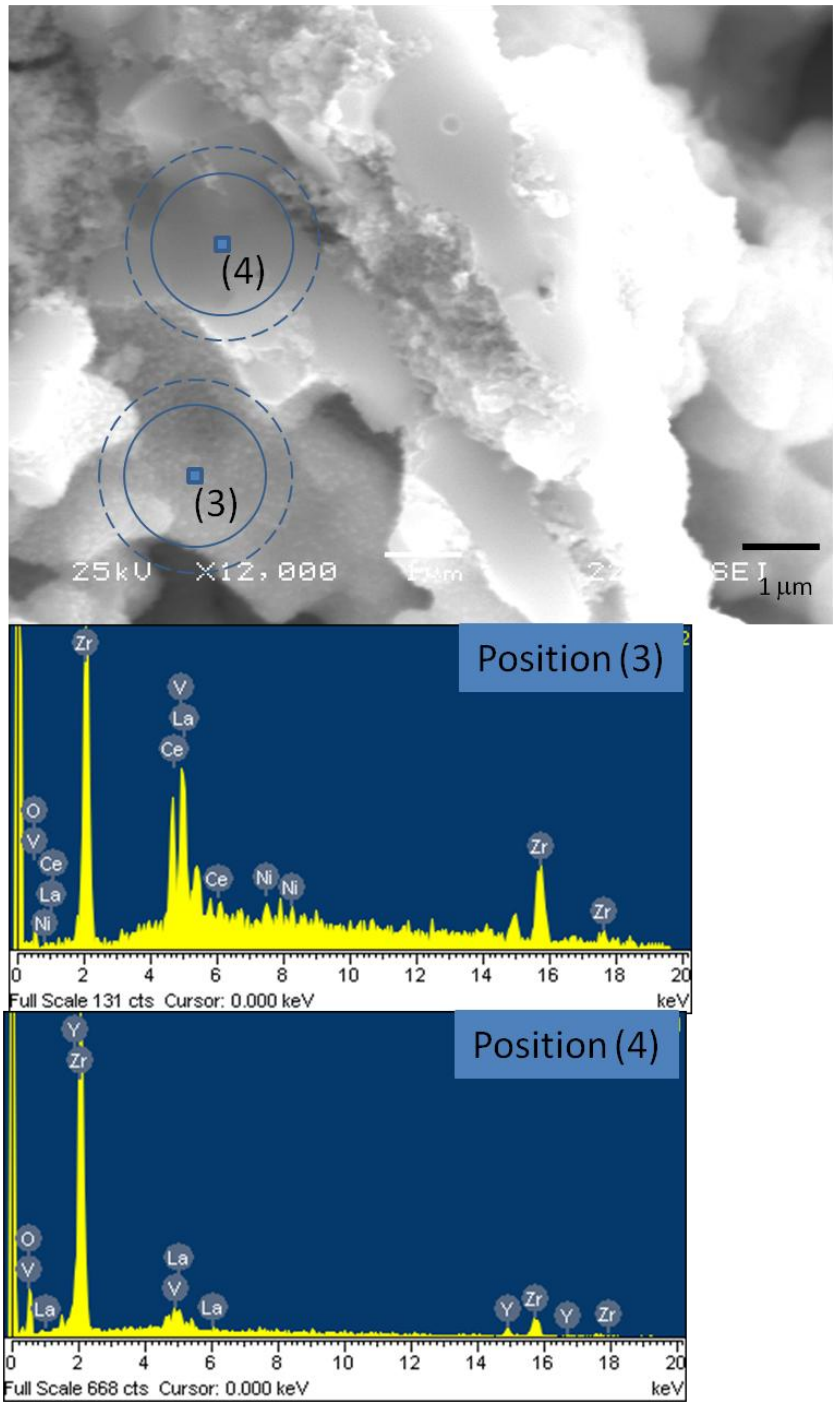

Figure 39 SEM of post-test sample with Ni and ceria as catalyst and the EDX profile at sites (3) and (4). The circles in the image indicate the interaction area of the beam with materials.

The SEM of the reduced sample is shown in Figure 39, where the impregnated LSV, ceria and nickel forms porous coating composed of nano-sized particles and adheres well to the porous backbone. The EDX at position (3) indicates that the composition

at the coating includes YSZ, vanadate, ceria and nickel, in agreement with the infiltration process, in contrast with that of YSZ at position (4), which shows very small amount of vanadate. A high-magnification image (Figure 30) shows that the particles of the infiltrated content are varied from place to place, but in the range of 20 nm to 200 nm.

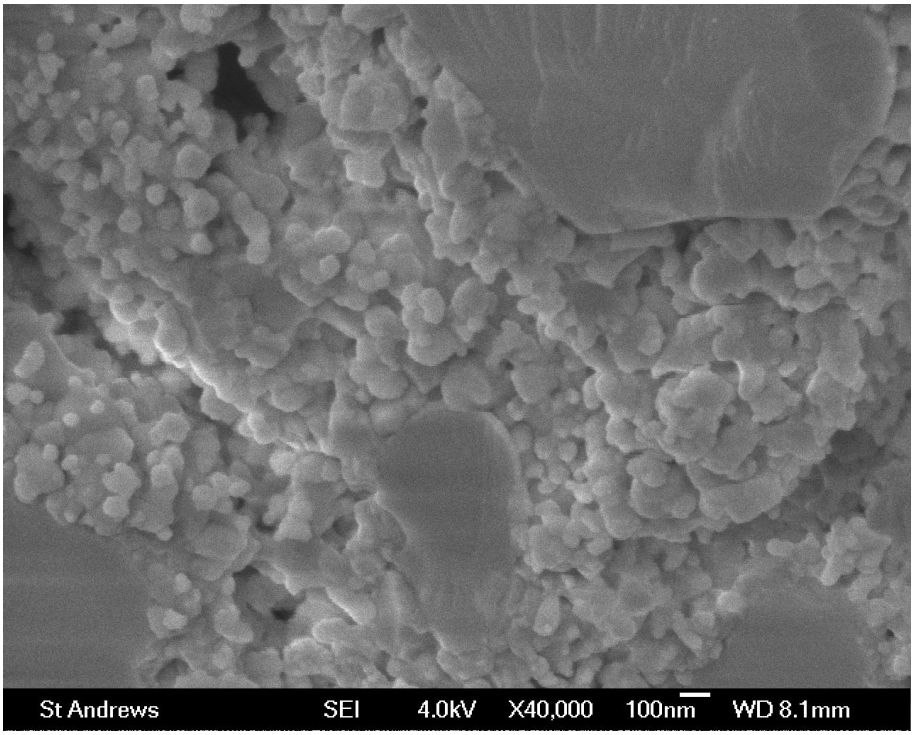

Figure 40 High-magnification image of the LSV/YSZ electrode iwth ceria and nickel as catalyst after testing in humidified hydrogen at 800 ^{o}C

6.3.3 Electrochemical performance under hydrogen and methane as fuel

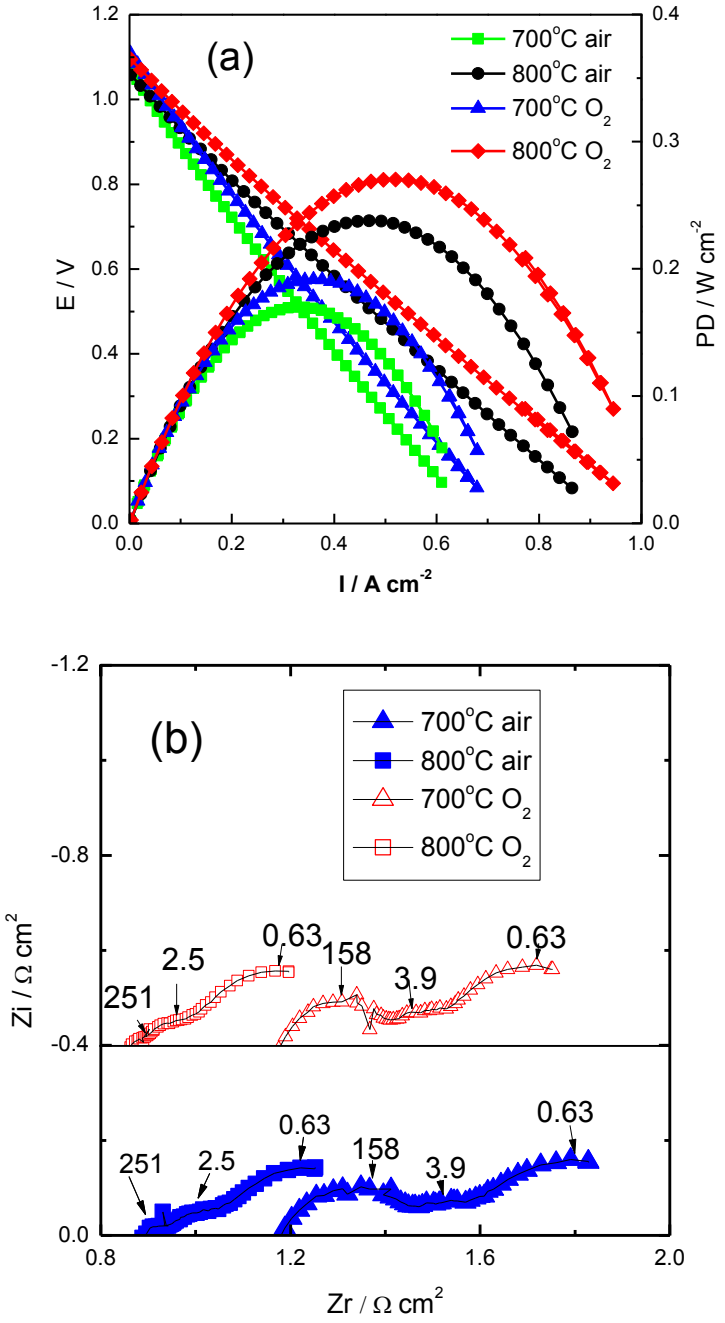

Figure 41 IV curve (a) and impedance spectra (b) for the fuel cell with thick anode support and thin cathode. The result is retrieved with ECN jig. The flow rate of wet H_2 is 500 ml min^{-1}; the flow rates of oxygen and air are 500 ml min^{-1} and 2500 ml min^{-1}, respectively

The performance and impedance of the cell with ceria+ Ni as catalyst on the anode side is shown in Figure 41. At 700 °C, the OCV is higher than 1.08 V if air is used as

oxidant, indicating a dense electrolyte and the peak output of the cell is 170 mW cm^{-2}. The ASR calculated by fitting the IV curves (Figure 41 (a)) in the 0.1 V range of OCV gives a value of 1.84 Ω cm^2 and 1.76 Ω cm^2 for the test under air and oxygen respectively. The small difference (< 5%) of the two values suggests that the cathode may contribute a small proportion to the total resistance. Except in the region near OCV, the IV curves for the cell tested under air or oxygen mirror each other even at high current density region, indicating diffusion resistance on the cathode is not the limiting factor in this current range. At 800 ^oC, the maximum power density is 240 mW cm^{-2} if the cathode is exposed to air and the cathode is not the rate limiting factor following the same analysis as that at 700 ^oC.

The impedance data (Figure 41 (b)) give ASR values of 1.83 Ω cm^2 and 1.75 Ω cm^2 for the cell with air or oxygen as oxidant at 700 ^oC, very close to those of IV curve. In particular, the R_s, ca. 1.2 Ω cm^2, comprises two thirds of the ASR and is much higher than the theoretical resistance from the 30-μm electrolyte, ca. 0.15 Ω cm^2 at 700 ^oC. Because the ohmic resistance of the 40-μm cathode is negligible, the anode contributes 1.05 Ω cm^2 to the series resistance. Three arcs can be easily identified in the Nyquist plots at 700 ^oC and 800 ^oC. The arc at high frequency decreases dramatically as the temperature increases, where as those at middle and low frequency shows slight change with temperature. The characteristic frequency of the high frequency arc, 158 Hz, is the same as the symmetrical testing of the cathode in Chapter 3, suggesting the contribution of cathode to this arc.

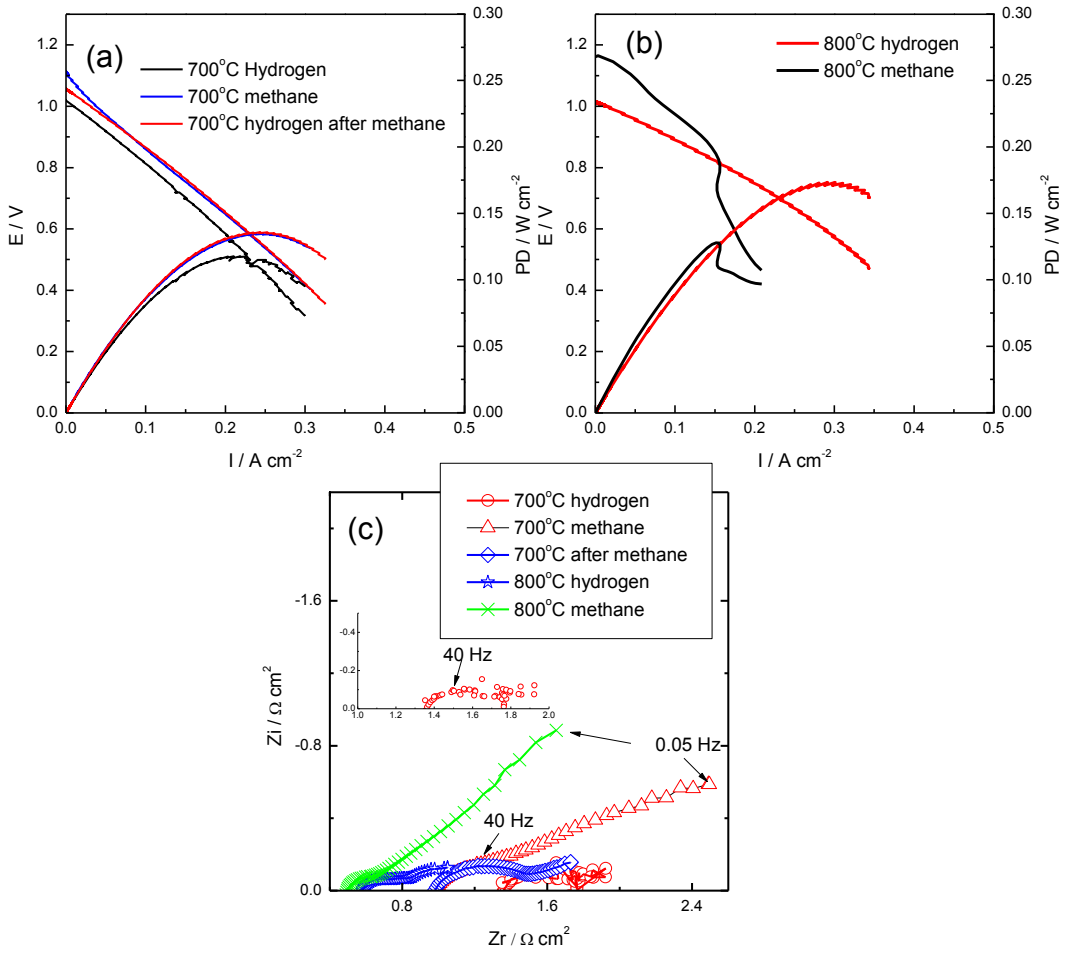

Figure 42 IV curves (a and b) and impedance (c) for the fuel cell with thick anode tested on Versa jig with hydrogen and methane as fuel: ceria and nickel is impregnated sequentially into the anode as catalyst. The flow rates of wet H_2 and methane are 150 and 50 ml min^{-1}; the flow rate of air 140 ml min^{-1}, respectively

Figure 42 shows the performance of the cells with thick anode obtained with the Versa jig. At 700 °C, the peak power density, 117 mW cm^{-2} under hydrogen as fuel, is lower than the one obtained with ECN jig, 170 mW cm^{-2}, which resulted from the lower OCV and curvature in IV curve at high current density. If the fuel is changed to methane, a high OCV of 1.11 V is achieved and the power density increases to 135 mW cm^{-2}. After working under methane for 2 hours, the fuel cell still works if the fuel is changed back to hydrogen. The IV curves before and after methane as fuel are in good alignment with each other, suggesting a similar ASR in the two cases.

At 800 ^{o}C, the OCV decreases to 1.0 V and the power density is 170 mW cm^{-2}. Under methane as fuel, the OCV jumps to 1.18 V, but the abrupt decrease of voltage at 0.15 A cm^{-2} and afterwards means that the power density peaked at 0.82 V.

The ASR value from the impedance at 700 ^{o}C for the testing with H_2 is about 1.9 Ω cm^2, slightly higher than the measurement performed on ECN jig. The difference can be accounted for with the higher Rs measured with Versa jig. After the application of methane on the anode side, the R_s value decreases by 0.3 Ω cm^2 because of the deposition of graphite in the case of nickel as catalyst[67]. The polarization resistance for hydrogen is increased by 0.2 Ω cm^2 after the intermediate testing with methane, as a result of the deposition of graphite that might change the microstructure of the anode.

6.4 Conclusion

A fuel cell with thick LSV as anode is prepared by infiltration and tested in both hydrogen and methane as fuel. The ohmic resistance of the thick anode contributes to a large portion of the ASR of the fuel cell, while the thin cathode is effective in facilitating the transport of oxygen to the cathode/electrolyte interface. The deposition of graphite in the thick anode if methane is used as fuel decreases the ohmic resistance but increases the polarization resistance.

Chapter 7 A large area SOFC with thin electrolyte on bi-layer support

7.1 Introduction

Compared to proton membrane exchange fuel cells (PEMFCs) that require pure hydrogen as fuel, solid oxide fuel cells (SOFCs), utilizing an oxygen ion conducting electrolyte, can oxidize either hydrogen or hydrocarbon fuels. In the last decade, much effort has been devoted to developing conductive oxide-based anodes (e.g. (La, Sr) TiO_3 [68,69], (La, Sr) (Cr, Mn) $O_{3-\delta}$[35,70] and $Sr_2Mg_{1-x}Mn_xMoO_{6-\delta}$ (x=0-1) [71]) to enhance the fuel flexibility of SOFCs because they are more stable against carbon-formation in hydrocarbon-based fuels and less sensitive to oxidation and reduction (redox) cycles than the state-of-the-art Ni (O) cermet does. However, two major problems are associated with the ceramic anode. First, compared with Ni (O) cermet, the electrode-performance characteristics of most of these materials are poor at intermediate temperatures (600-800 ^oC) because many of these oxides are not good catalysts for the oxidation of the fuel [72]. The introduction of reducible transition metals into the functional layer is one approach that can be used to enhance the catalytic activity[33]. The infiltration of ceramic conductors and catalytic metals (e.g. Ni, Pt and Pd) into porous scaffolds that had been pre-sintered onto the electrolyte is regarded as an effective method of promoting the electrode performance via producing nano-scale particles by in-situ sintering at relatively low temperatures [24,25,73,74]. The nano-scale particles are able to increase the length of triple phase boundaries (TPBs) that provide the reaction sites for the fuel oxidation[51]. Second, the low conductivity of most ceramics in a fuel environment prohibits a configuration with a thick anode because of the large ohmic losses it might cause[51]. In this study, we decided to use $L_{0.7}Sr_{0.3}VO_{3-\delta}$ (LSV_{red}) as the anode material as it has recently been shown to provide decent electronic conductivity [75,76,77]. For example, the electronic conductivity of 30 wt. % LSV_{red} impregnated into an YSZ scaffold was reported to be higher than 1 S cm^{-1} at 700 ^oC [76].

Although lots of effort has been devoted to developing infiltration as an effective way of fabricating high-performance electrodes and avoiding the undesired solid-state reaction between the perovskite and YSZ as in conventional sintering process of composite electrodes[23], there are some concerns that it might not be easily scaled up

for mass production of commercial devices. First, the infiltration process usually requires multiple infiltrations and pre-sintering steps[59] to deposit enough oxides to form a conductive layer of interconnected particles, and it is unknown that if the infiltration on a large-scale cell is possible or as effective as on button cells. Second, the transport of solution in several hundred micrometers of pore structure to the electrode/electrolyte interface is another concern in the mass production of large-scale anode- or cathode-supported SOFCs[78]. Finally, the fabrication of a thin gastight electrolyte of large area on a highly porous substrate, in fact, is a primary challenge in the co-sintering of powders as the cost-effective method[79].

In this study, the scalable and cost-effective tape casting is used to prepare the large-area dense electrolyte on porous scaffold and then concentrated aqueous solutions of precursors are used to impregnate the cathode and anode before each pre-sintering to obtain a loading of 25 wt. % $L_{0.7}Sr_{0.3}VO_{4-\delta}$ (LSV_{ox}) for anode and 35 wt.% $La_{0.8}Sr_{0.2}FeO_3$ (LSF) for cathode in ten impregnations. In order to avoid infiltrating one very thick support, we choose to impregnate two identical YSZ scaffolds for cathode and anode.

7.2 Experimental

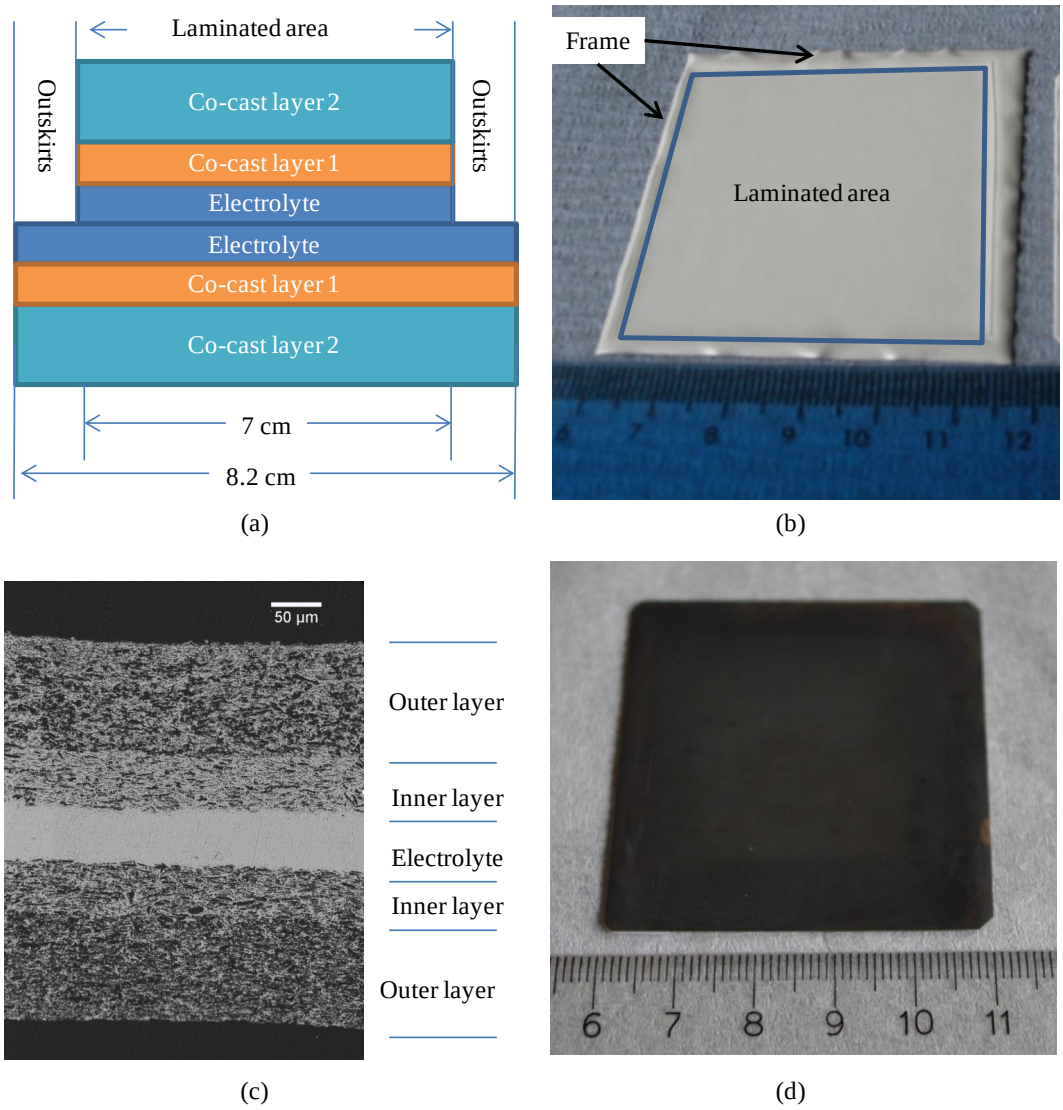

Figure 43 (a) Schematic illustration of the lamination of the YSZ green tapes with two co-cast layers containing YSZ and varied amount of graphite; (b) the scaffold sintered at 1400 °C having a flat laminated area and a warping frame from the outskirts of green tapes; (c) SEM cross-section of the scaffold with a dense electrolyte and two identical gradient porous structure for the electrodes; (d) image of the fuel cell (cathode side) after impregnation and scraping off the frame.

Slurry for the green tapes of electrolyte was prepared by milling the YSZ (HSY-8, DKKK, Japan) with binder (Polyvinyl butyral) and plasticizers (Polyethylene glycol and Di-n-butyl phthalate) in ethanol – Methyl Ethyl Ketone solvent and then cast on

to a Mylar paper. Two layers of green tape containing YSZ and 65 wt % and 85 wt. % graphite (compared to the weight of YSZ) were cast sequentially on the top of the ysz green tape with 1-hour interval for drying[80]. Two co-cast green tapes were laminated together (Figure 43(a)) to produce a tri-layer green tape for YSZ wafer. The green tapes were fired at 1400 ^{o}C for 5 hours on a zirconia plate to prepare the scaffold for impregnation (Figure 43(b)).

Stoichiometric amounts of $La(NO_3)_3.6H_2O$, $Sr(NO_3)_2$, NH_4VO_3 and $Fe(NO_3)_3.9H_2O$ were dissolved in de-ionized water together with citric acid (1:1 mole to metallic ion) for the impregnation of $La_{0.8}Sr_{0.2}FeO_3$ (LSF) and $La_{0.7}Sr_{0.3}VO_{4-\delta}$ (LSV_{ox}). Considering the low solubility of metavanadate in water at room temperature, the solution for LSV_{ox} was heated up to 60 ^{o}C on a hot plate and then impregnated into one side of the porous scaffold, followed by the impregnation of LSF on the other side of the scaffold. The scaffold with the content is pre-sintered hereafter at 700 ^{o}C for 30 minutes after each impregnation. Ten impregnations had been performed to get the loading of LSF and LSV_{ox} reaching 35 wt. % and 25 wt. %, respectively. For the cell with catalyst, solution of Ce nitrate and Pd nitrate were impregnated into the anode after the final 700 ^{o}C firing, followed by a firing at 500 ^{o}C. Pt paste ((Gwent, C2000904P3)) was applied on both sides of the electrode and then the whole cell was fired at 900 ^{o}C for 30 min to densify the Pt paste and produce the correct phase of the perovskite.

A single cell was tested on a non-sealing device that uses N_2 around the edges of cathode side of the cell as a separating gas[81]. A weight of 4 kg was put onto the cell to improve contact after the installation. The sample was heated up to 700 ^{o}C at a ramp rate of 1 ^{o}C min^{-1}, and then wet hydrogen (4.3 % H_2O) was applied to replace the initial nitrogen flow on the anode to allow a 2-hour reduction. The flow rate of air was 2500 ml min^{-1} and those of pure oxygen and hydrogen were 500 ml min^{-1}. For the thermal and redox cycle, the tested fuel cell was taken out of the testing device, fired at 900 ^{o}C for 30 min and tested again. Electrochemical characterization was performed under ambient pressure. The measurement of porosity was carried out on the back-scattering images with the software ImageJ (National Institute of Health, Bethesda, MD).

7.3 Result and discussion

7.3.1 Images and structure of bi-electrode supported fuel cell

The scheme (Figure 43(a)) illustrates the lamination of the co-cast green tapes for co-sintering. Since YSZ powder from the same batch is the only ceramic involved in the sintering process at elevated temperature, the mismatch in the rate of shrinkage is less a concern than that in the co-sintering of different materials. The outer edge of the sintered scaffold (Figure 43 (b)) contains a stretching frame from the outskirt of the larger green tape that enables the large central flat laminated area, with only the outer edge being constrained during sintering. In the case of YSZ supported on titanate, a second firing of the warping ceramic under load is used to flatten it [82]. The microstructure (Figure 43(c)) of the scaffold contains a 55-μm electrolyte sandwiched between two identical YSZ layers of gradient porosity; the porous inner layer in contact with electrolyte is 52 % porous (48-μm thick) measured by image analysis and the outer layer is 67 % porous (112-μm thick). This gradient design is beneficial for producing a dense electrolyte on the porous structure while providing enough porosity for mass transport [78,83]. The inner layer with finer pores can also increase the surface area for the LSV or LSF particles to sit on and decrease the pore size for smaller interface resistance. After impregnation, the frame is rubbed off to produce a 5 cm by 5 cm fuel cell (Figure 43(d)).

7.3.2 Electrochemical characterization

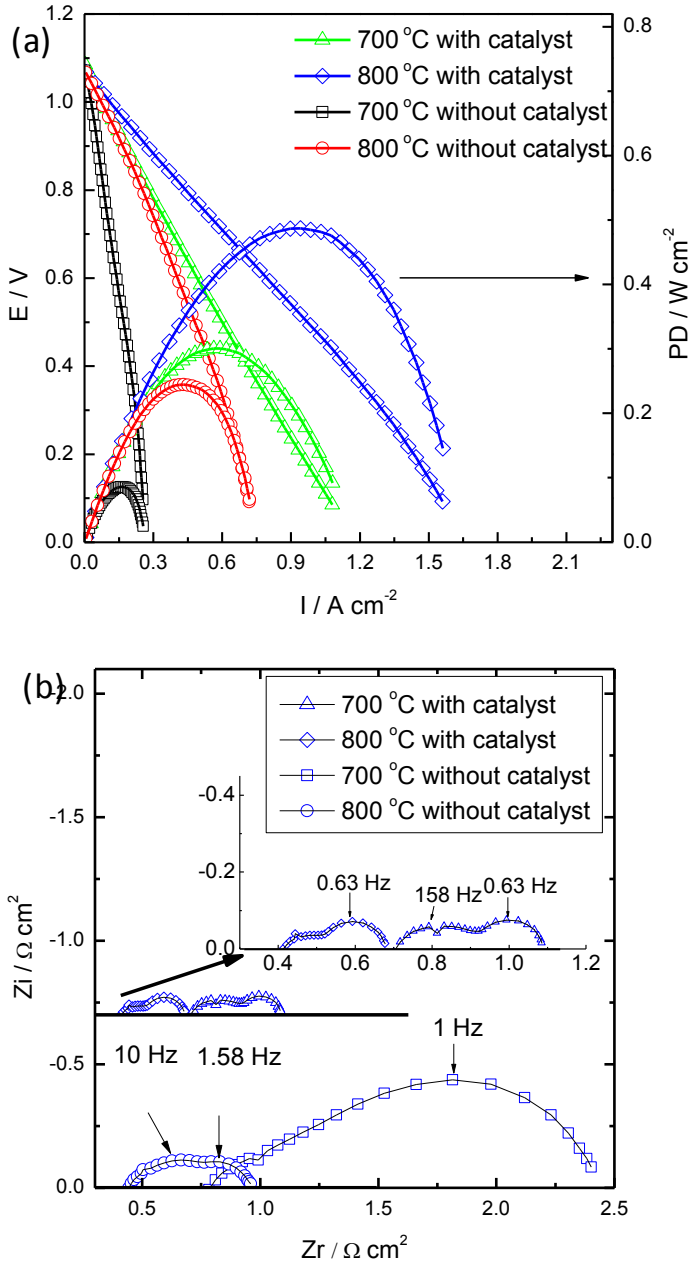

Figure 44 Performance of an LSV/LSF- impregnated large fuel cell with and without ceria + Pd as catalyst under wet (4.2 vol. % H_2O) H_2 fuel. (a) I – V and I – P curves; (b) Nyquist plots of impedance spectra. The gas flow rates are 2.5 L min^{-1} air and 500 ml min^{-1} wet H_2. The insert in (b) is the magnified plot for the cell with ceria + Pd as catalyst.

LSV/LSF- impregnated cells with a current-collected area of 3.5 cm x 3.5 cm were electrochemically characterized at 700-800 ^{o}C using humidified H_2 (4.2 vol. % H_2O)

as fuel and air as oxidant. In Figure 44(a), the open circuit voltages (OCVs) are above 1.07 V at both temperatures for all cells with or without impregnation of 10 wt.% ceria + 1 wt.% Pd as catalyst. Considering the non-sealing property of the testing station, this OCV is high enough to imply a dense electrolyte. The maximum power densities (Figure 44(a)) for the cell without catalysts on the anode side are 84 mW cm^{-2} and 245 mW cm^{-2} at 700 ^{o}C and 800 ^{o}C, respectively. The addition of 10 wt.% ceria + 1 wt.% Pd enhances the performance significantly: highest power densities of 300 mW cm^{-2} and 489 mW cm^{-2} are achieved at 700 ^{o}C and 800 ^{o}C, respectively. The maximum power is 6 W for a single cell at 800 ^{o}C. Compared with the cell without catalyst, the dramatic decrease of the electrode polarization resistance, R_p, which is represented by the distance between the high and low frequency intercepts of the curve with the real impedance axis (Figure 44(b)), confirms that the high electrode losses come from the anode of the cell without catalyst, similar to the ceramic anode of LSCM[84]. In order to study the contribution of the cathode losses, pure oxygen is used as the oxidant for the cell with 10 wt.% ceria + 1 wt.% Pd in the anode. The slope of the IV curve (Figure 45(a)) and the R_p estimated from impedance plot (Figure 45(c)) change slightly with the increase of the partial pressure of oxygen, indicating that 160-μm cathode contributes only an insignificant part to the R_p in the region above 0.7 V.

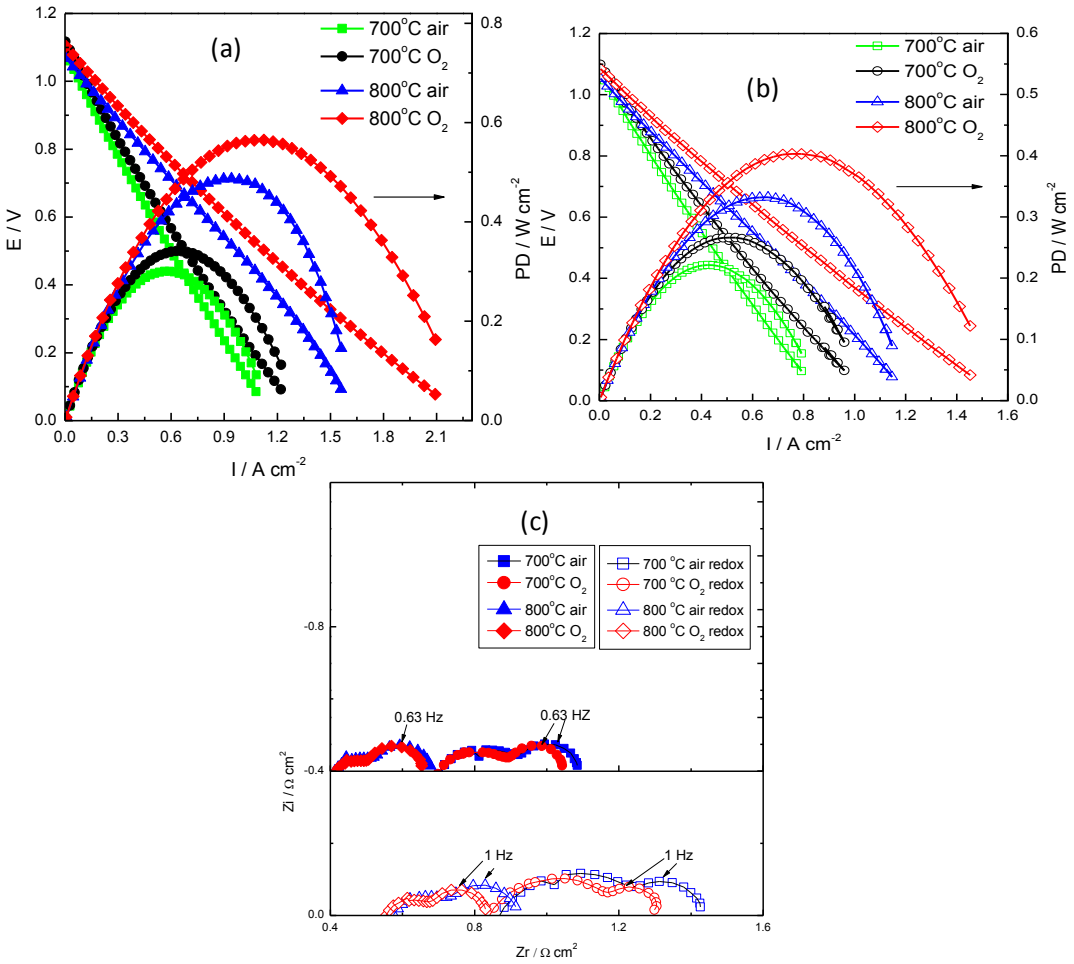

Figure 45 Performance of fuel cells with ceria + Pd as catalyst under air or oxygen as oxidant before (a) and after (b) redox cycle at 900 °C. (c) Nyquist plots of impedance spectra at OCV under air or oxygen as oxidant.

The performance of the fuel cell after thermal and redox cycle at 900 °C is shown in Figure 45(b). The maximum power density at 700 °C decreases to 220 mW cm^{-2}, but the OCV does not change, meaning the conversion between LSV_{red} and LSV_{ox} does not exert any damage to the integrity of the electrolyte, in contrast to the electrolyte on the nickel cermet-supported fuel cell[85]. The sintering of nano-particles, especially metallic Pd, might be a concern at a redox temperature as high as 900 °C[86], but this fuel cell can still be used at intermediate temperatures. The redox cycle is supposed to change the microstructure of the anode, including LSV_{red}, ceria and Pd[63], but the sintering of LSF on the cathode side can also contribute to the increase of impedance

because the difference of the partial pressure of oxygen exerts greater influence on the R_p value [87], as shown in Figure 45(c).

7.3.3 SEM images of the nano-structured electrodes

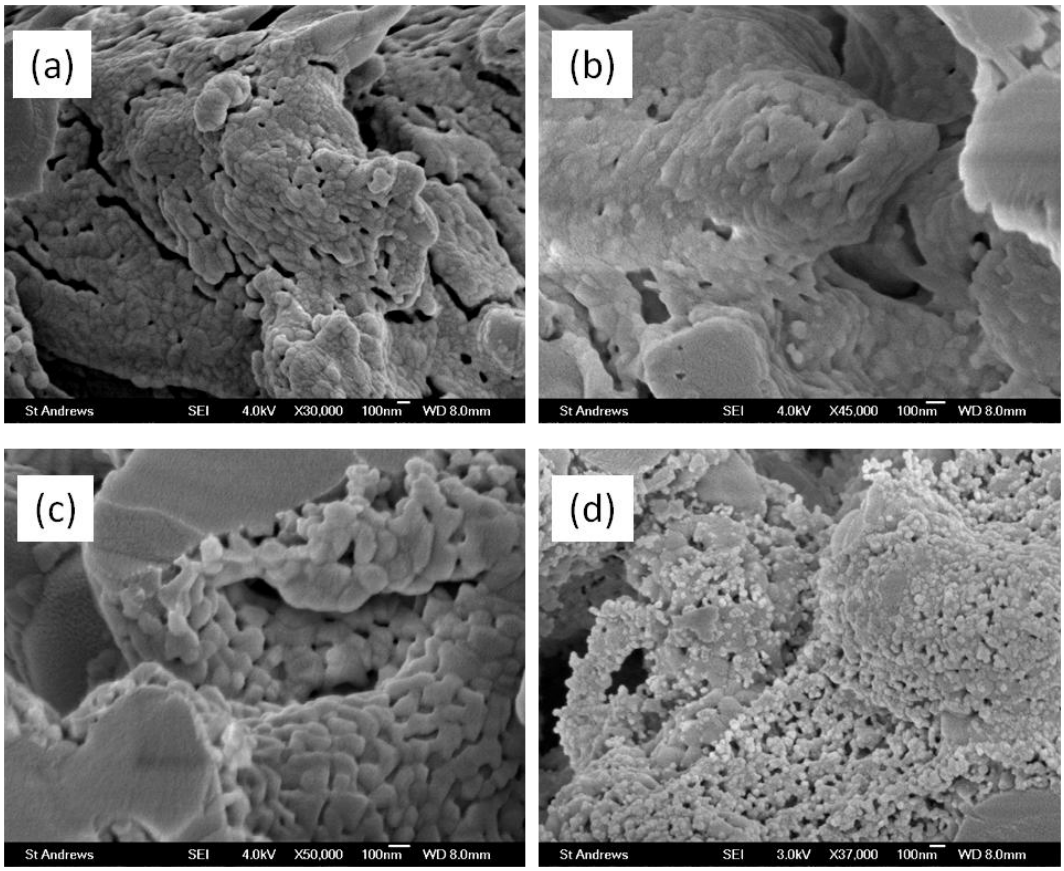

Figure 46 SEM images of LSF/ YSZ (a), LSV_{ox}/YSZ (b) and post-test LSV_{red}/YSZ (c) electrode; (d) is that of LSV_{ox} / YSZ with ceria and Pd after a calcination at 900 ^oC for 30 min. The white particles in (d) are Pd nano particles

Figure 46 shows the SEM images of the electrodes. After the calcination at 900 ^oC in air, both the LSV_{ox} and LSF form a coating of 100 nm particles on the surface of YSZ, similar to the observation of LSCM on YSZ after firing in air[31], LSV_{red} particles contracted in humidified H_2 at 800 ^oC, exposing the underneath YSZ scaffold partially to the fuel. This morphology can decrease the electronic conductivity of the LSV_{red} structure but provide more TPBs for electrochemical reaction. The ceria particles supporting the Pd particles of approximately 20 nm form a porous network on the surface of LSV_{ox} after calcinations at 900 ^oC, which is thought to inhibit the poisoning of metal catalyst caused by direct contact with vanadium and slow down the growth of Pd nanoparticles [75,86].

7.4 Conclusion

In conclusion, a 5 cm by 5cm flat tri-layer scaffold of YSZ has been prepared for the first time using the inexpensive and scalable tape casting method and impregnated with perovskites for cathode and anode. The configuration of gradient porosity and identical scaffold for cathode and anode simplifies the sintering process and the impregnation process. Furthermore, the fuel cell shows excellent performance thanks to the nano-sized perovskite formed at intermediate temperatures and the 160-μm cathode does provide sufficient mass transport of oxygen and does not limit the performance of the cell.

Chapter 8 Image analysis and modelling of the orientation of pores in constrained sintering process: a balance of scales and stages

8.1 Introduction

Porous ceramics are of significant interest in many fields due to their wide range of applications in energy-conversion and piezoelectric materials, biomaterials, catalyst supports and infiltration membranes[88]. Among the methods used to prepare porous ceramics, screen printing is a low-cost method that is scalable and well-suited for the fabrication of very thin film (10 - 50 μm) on rigid substrate. For example, the pre-sintered porous YSZ scaffold via screen printing can be infiltrated with conductive perovskite to prepare highly active electrode for solid oxide fuel cell[34,89]. The addition of pyrolyzable pore former is simpler but more effective in producing a porous ceramic sintered at high sintering temperature for better connectivity and/or bridging between the components, compared to the alternative partial-sintering method. Graphite is a popular choice as PFA because of the vast availability and compatibility with the organic solvent, but its two-dimensional shape causes the anisotropy of the ceramics.

The preferred orientation (or texturing) is of great interest because it is common in ceramics and has an influence on physical properties such as strength[90], mass transport[91,92], electrical conductivity[93], and optical property[94,95]. To be specific, the shape and array of pores in the electrode of a solid oxide fuel cell dictates the tortuosity of the gas permeation[96] and the distribution of the infiltrated phases[97,98]. The non-uniform packing density of green body prepared by tape casting and the anisotropy from the particle forms are thought to be some of the reasons for the orientation in the final sintered ceramic[99,100,101,102,103]. For the green body fabricated using screen printing or tape casting, the particle rearrangement by capillary forces takes place when the solvent evaporates and the surface of slurry retracts to the substrate. This arrangement is able to change the orientated pores to a direction closer to the in-plane direction. On the other hand, in the case of a screen printed film where no in-plane shrinkage is allowed in a continuum system, the orientation can also arise from the constrained sintering process of a screen-printed layer for dense ceramic; the pores align along the thickness direction that is normal to the substrate[104,105] owing to

the uneven materials transport between the in-plane and thickness direction. The anisotropy from the two sources is perpendicular to each other. As a result, a balance of the two reasons for anisotropy should be balanced in the screen printed porous ceramic on a rigid substrate.

In this work, image analysis and a modelling based on continuum assumption of the green body or ceramic film is used to study the microstructure orientations at different stages starting from the application of inks to the final sintered ceramic. Inks with graphite (plate-like in shape) or glassy carbon (spherical in shape) are used to direct the orientation evolution of different stages of sintering. Moreover, the images with two-dimensional anisotropic pores from varied particle size distribution are generated to demonstrate the pores of two-scale from small interstitial of ceramic to large pore former.

8.2 Experimental

8.2.1 Materials

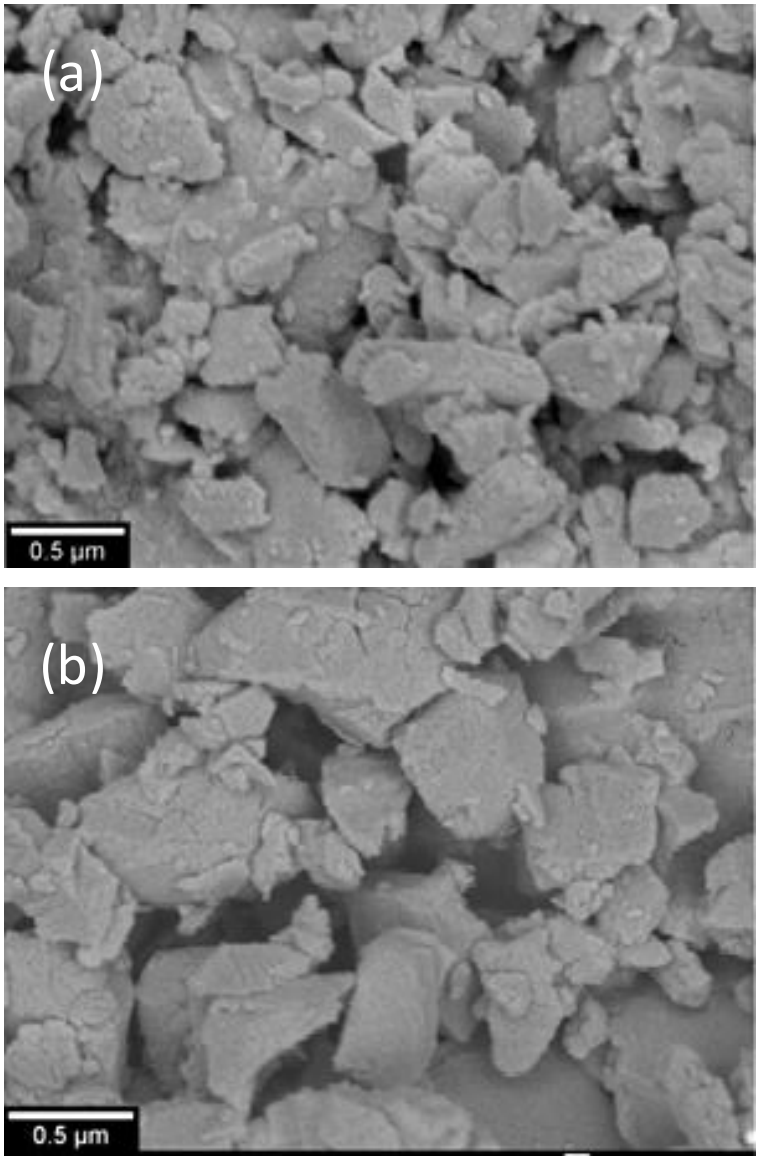

Figure 47 SEM images of the as-received YSZ powders: (a) Unitec 1-um powder and (b) Unitec 2- µm.

Two types of 8 mol.% Y_2O_3-stabilised ZrO_2 (8-YSZ) were used in the ink making process, Unitec 13 wt.%- (8 mol.%) YSZ 1-µm and 2- µm powder (denoted as Unitec 1- µm and 2- µm powder) both from UCM Advanced Ceramics GmbH, Laufenburg, Germany. Images of the as-received powders are shown in Figure 47, where, Figure 47(a) shows the image of Unitec 1- µm powder and Figure 47(b), the Unitec 2- µm powder. The particle size analysis (PSA) of the two 8-YSZ powders was performed

on a Mastersizer 2000 particle size analyzer (Malvern Instruments LTD) after ball milling in an isopropanol solution containing 2 wt.% triton for 24 h to simulate the ink-making de-agglomeration process. The size distributions are shown in Figure 48(a), and are consistent with the SEM images, showing that the Unitec 1- μm powder contains finer particles. The PSA data of 2- μm powder show only one peak at ~1 μm, while those of 1- μm powder exhibit two peaks at 0.1 μm and 0.8 μm.

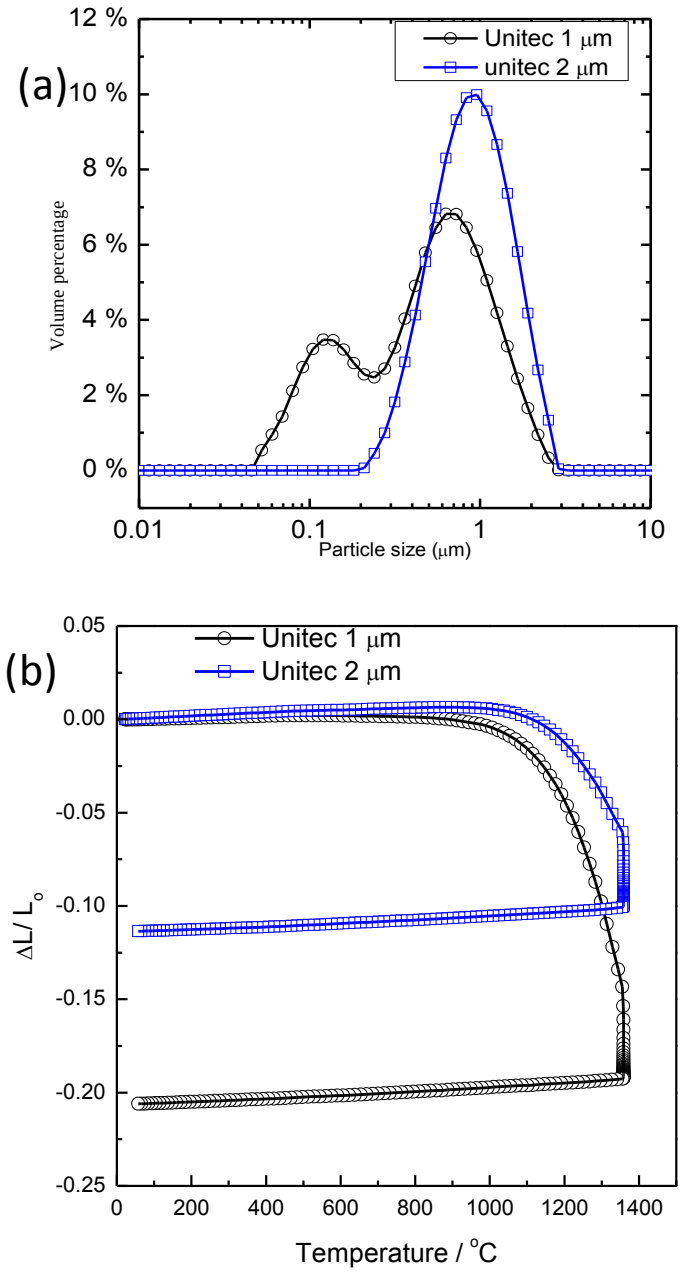

Figure 48 (a) Particle size analysis of the Unitec 1- μm and 2- μm powder after ball milling for 24 h in isopropanol containing 2 wt.% triton. (b) Dilatometry of the pellets from two powders pressed under 149 MP.

A pellet of 13 mm in diameter and 1 mm in thickness was obtained by pressing the powder under a uniaxial pressure of 149 MP and then its sinterability was measured via a dilatometer (Netzsch, DIL 402C) with a heating rate of 3 ^{o}C/min up to 1350 ^{o}C, as shown in Figure 48(b). After the sintering at 1350 ^{o}C, the density of the pellet from Unitec 1-mm powder is 5.72 g cm^{-3} (94% relative density), in contrast to 5.26 g cm^{-3} (86% relative density) from Unitec 2-μm powder. Results show that the Unitec 1- μm

powder started to sinter at 1000 ^{o}C and the other would not sinter until the temperature reaches 1100 ^{o}C. The shrinkage of the pellets from Unitec 1- μm powder is twice that from Unitec 2- μm powder after dwelling for 3 h.

8.2.2 Sample preparation and image analysis

Table 5 Recipes of the inks with and without pore forming agent (PFA)

No.	ceramic	PFA	viechle	KD-1	vol.% of ceramic[a]/ V_c	vol.% of PFA[b]/ V_p
1	Unitec 1 μm 20.0 g	-	7.80 mL	0.40 g	30.0%	-
2	Unitec 2 μm 20.0 g	-	7.80 mL	0.40 g	30.0%	-
3	Unitec 1 μm 5.0 g	graphite 1.0 g	4.18 mL	0.12 g	15.0%	9.0%
4	Unitec 1 μm 5.0 g	glassy carbon 1.0 g	4.18 mL	0.12 g	14.6%	11.7%

[a]: density of YSZ 6.0 g/cm^3

[b]: gaphite 2.0 g/cm^3 and glassy carbon 1.5g/cm^3

In the ink-making process, Hypermer KD-1 (Croda Inc. UK) was used as dispersant, and terpineol containing 5 wt. % PVB as a vehicle. The pore former is graphite (325 mesh, Alfa Aesar) or glassy carbon (Alfa Aesar). The graphite is composed of aggregated plates with varied dimensions while the glassy-carbon particles are 10-20 μm spheres. A mixed powder containing the YSZ powder, PFA (if any), and pore former was put into a plastic bottle containing 36 1-cm diameter zirconia balls, and then acetone was added to cover the surface of zirconia balls and powders. The bottle was sealed and put on a roller at 160 rpm for 24 h. When the milling time was complete, the contents, except zirconia balls, were transferred to a beaker, which contained vehicle. The acetone was allowed to evaporate while stirring on a magnetic plate, resulting in a well-dispersed viscous ink. The recipes of the inks with or without PFAs are shown in Table 5. The amount of PFAs is controlled to be small in order to avoid their possible interaction.

3.7 g 8 -YSZ (HSY-8, DKKK, Japan) powder was uniaxially pressed at a static pressure and sintered at 1500 ^{o}C for 10 h to result in a dense pellet of 2-mm thickness and 2 cm in diameter. The screen-printed pellets with ink 1, 2 and 4 were then sintered at 1300 ^{o}C for three hours using a heating ramp of 1 ^{o}C/min before 1000 ^{o}C and 3 ^{o}C/min afterwards with a cooling ramp of 3 ^{o}C/min. The pellet with ink 3 was sintered at 1100 ^{o}C for 3 hours with a heating ramp of 1 ^{o}C/min and cooling rate of 1 ^{o}C/min. The sintered samples were vacuum mounted in an epoxy, cut with a diamond saw and polished to 1- μm using diamond polishing paste. The backscattered electron images were taken on a JOEL 6700F to give highly contrasting images which were binarized and analyzed with ImageJ software (National Institute of Health, Bethesda, MD). The evaluation of particle orientation was accomplished by circumscribing a best-fit ellipse to every single particle, as demonstrated in reference 99. The angles of the particles are converted into the range 0-π/2. The particles with an area less than 0.01 μm^2 or 0.2 μm^2 for the image of ink without PFA or with PFA were respectively excluded due to the difference in magnification of the images.

8.3 Modelling of the rearrangement of PFA/pore

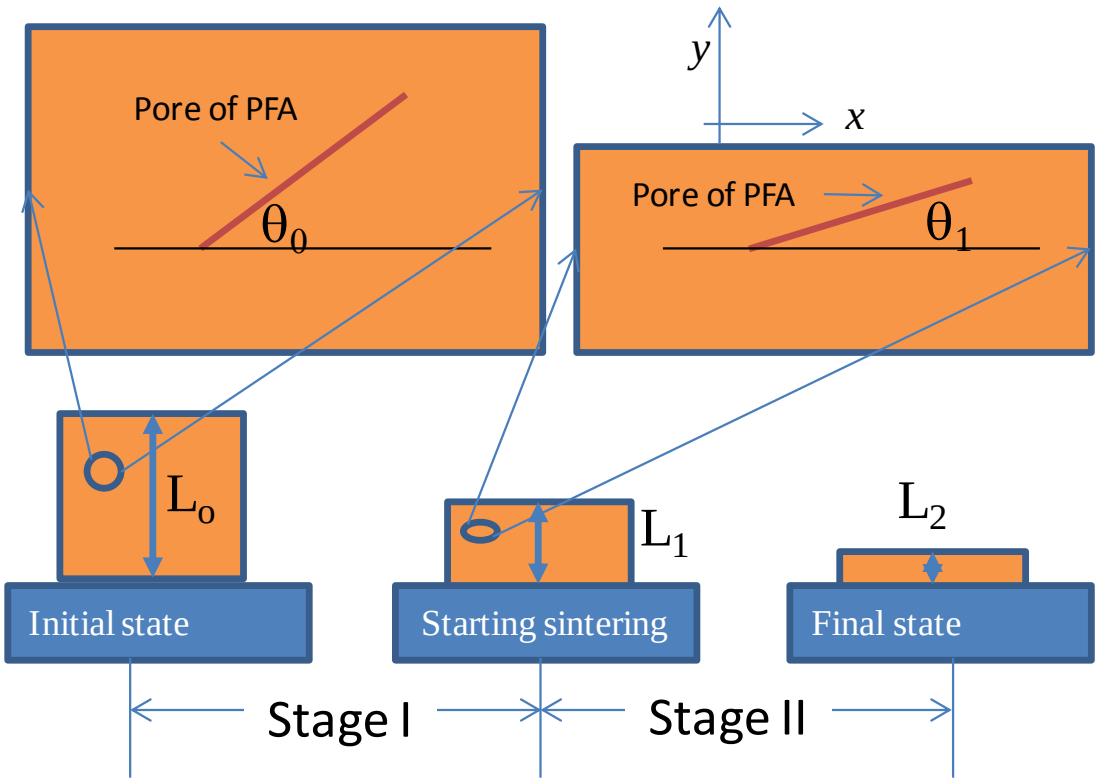

Figure 49 Schematics of the thickness of the deposited film and the orientation of the pore/PFA at different stages.

The sintering properties of ceramic are, to some extent, dependent on the local interaction between the particles and macroscopic properties[106]. The use of continuum mechanics, which has been successfully applied to the analysis of compaction of porous bodies, is extended to the whole process starting from the spot when the slurry is deposited on the rigid substrate, as demonstrated in Figure 49. L_0 is the thickness of the inks on the surface of the substrate and L_1 is the thickness when the sintering is about to start after the drying process and burning off the organics and pore former. After the sintering at the final temperature, the thickness of the film becomes L_2. In the whole process, a plate-like graphite/attendant pore is going to rotate and move toward the surface of the substrate as shown in the magnified area in Figure 49, where a continuum of the system is assumed. The plate-like graphite burns off at a temperature below 800 ^{o}C to produce pores of the same shape, so the plate-like pore former is assumed to be interchangeable with the pores in the modelling process. The interaction among pore formers is also neglected since the amount of PFA is small.

Because of the rigid substrate, the reaction or shrinkage in the in-plane direction is negligible and the relation between θ_0 and θ_1 can be represented in the equation:

$\theta_1 = atan(L_f/L_0 * tan(\theta_0))$ 8-1

where L_f is the thickness of the film in the range of [L_0, L_1]; θ_0 and θ_1 represents the angle of the graphite and pore in relation with the x axis. The shrinkage of film, δ, is determined by equation:

$\delta = 1 - L_f/L_0$ 8-2

Specifically, the shrinkage in stage I, τ, and the shrinkage in stage II, κ, defined as

$\tau = 1 - L_1/L_0$ 8-3

$\kappa = 1 - L_2/L_1$ 8-4

It should be noted that before the removal of graphite, the length of graphite as pore former in the modeling varies with the rotation process, but this is more applicable to the situation of pores after the burning of PFA.

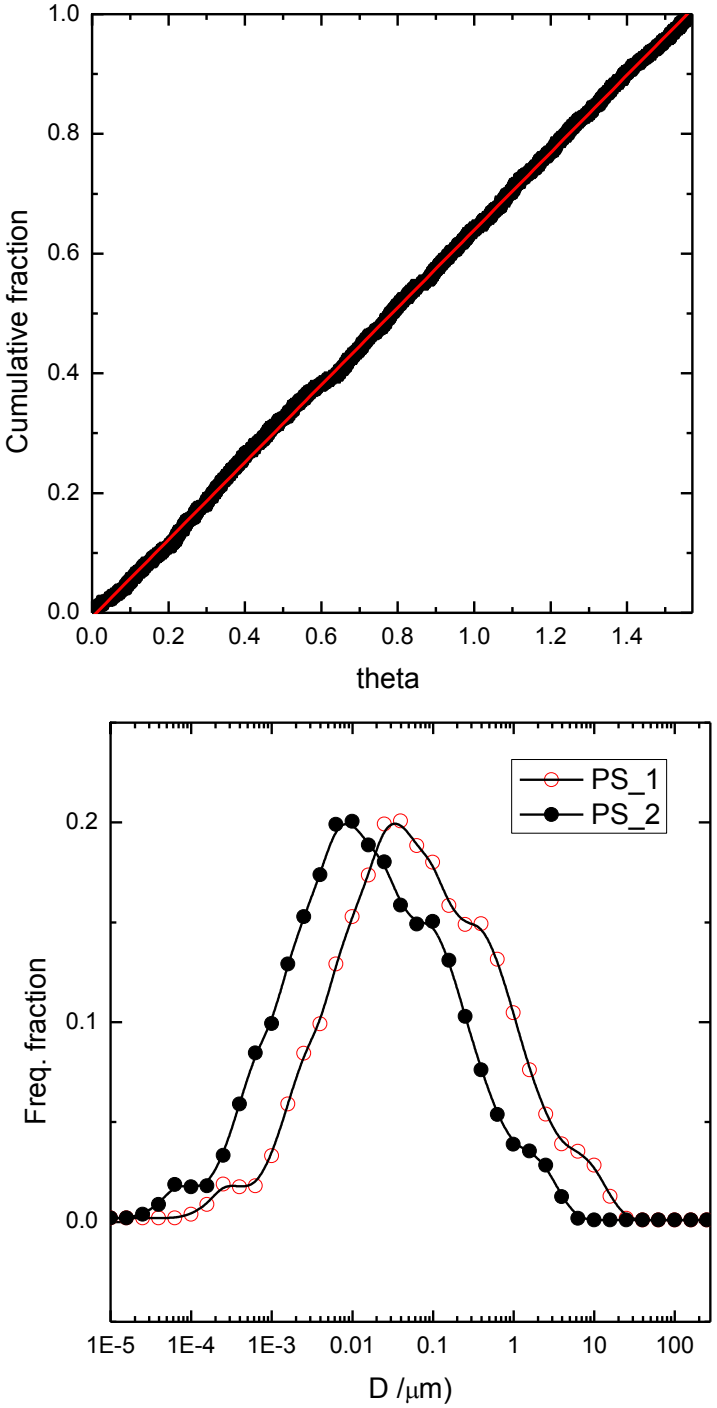

Figure 50 (a) Cumulative angle distribution of the particles in the simulation work; (b) discrete particle size fraction of the 2D pores/PFAs used in the modelling, PS_1 is 4 times larger than PS_2.

One thousand graphite particles of normalized length distribution were randomly generated on a 50 μm by 50 μm area. The linear angle distribution, Figure 50(a), indicates a random distribution of the pore former in the initial stage, suggesting that 1000 pore formers/pores are sufficient to represent a random system. The particle size

distribution of the pore formers / pores is indicated in Figure 50(b), represented as PS_1 and PS_2. The particle sizes cover about 5 decades. The anisotropic image is intensified as δ increase from 0 to 0.9 in slurry based system. Patwardhan[107] studied the anisotropy of tape-cast ceramic in y direction, and found out that low-solid-loading slurry produces more intense anisotropy, and this could be understood by a smaller δ value for a film with less solvent. Actually, this model also indicates that a looser-packing system is more prone to produce anisotropy given the same final density, similar to the study of Zainuddin[108].

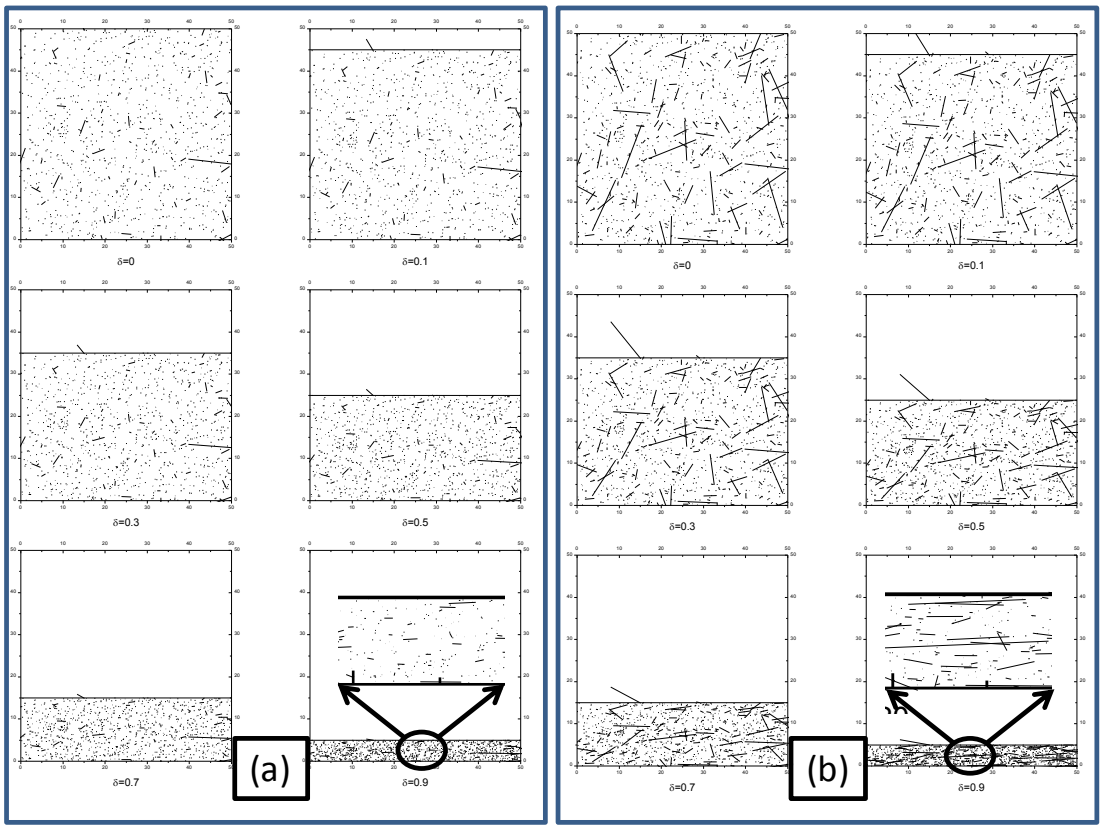

Figure 51 Image evolution with pores/PFAs of random angle distribution at different shrinkage values. The length of the pore/PFAs in figure (a) and (b) is PS_1 and PS_2, respectively.

The image of the film at different shrinkages, δ, is shown in Figure 51, where the length of each particle in (a) is elongated by a factor of 5, as shown in (b). The image was then compressed to simulate the drying process and constrained sintering in the y-axis without considering the variation of pores by transport process. A tape-cast film with coarser powders is found to be more orientated than that with finer powders of similar geometry[110]. The image simulation indicates that only the large pores are

obvious in the image. The comparison of these two images also suggests that image analysis at an inappropriate magnification is misleading sometimes because of the capacity of the information in the images.

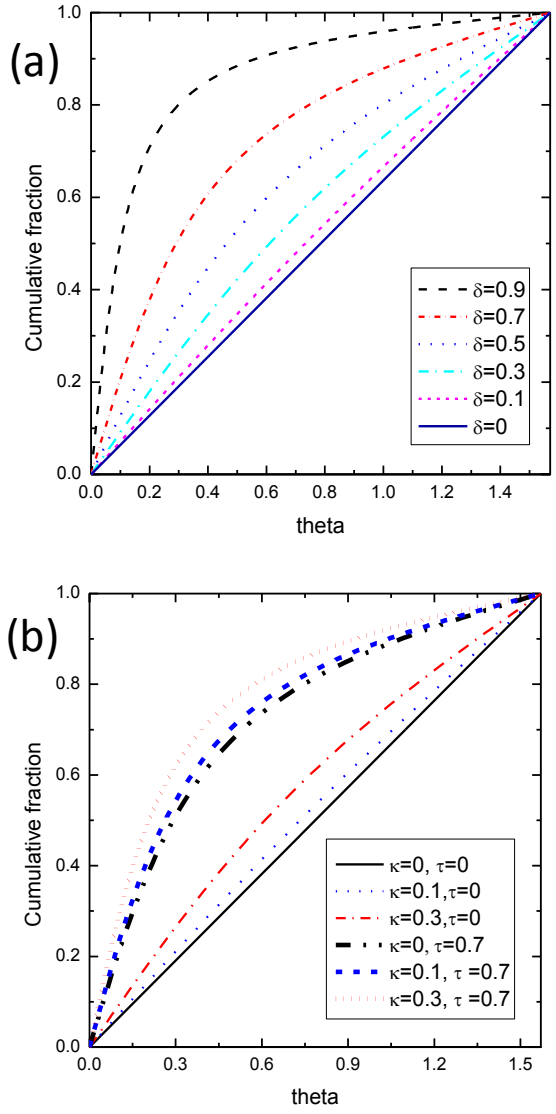

Figure 52 (a) statistics of the angle of the particles at different shrinkage in terms of δ value (a) and different τ , κ (b).

The cumulative percentage of orientation profile at different stage of sintering is showing in Figure 52(a) if equation 8-1 is used to predict the angle change from a randomly distributed system. The cumulative probability equation is

$$\Gamma=(2/\pi)atan((1-\delta)^{-1}tan(\theta)) \qquad 8\text{-}5$$

where Γ is the cumulative probability of the particles with an angle less than θ.

The percentage of the particles within $\pi/4$ is used to index the anisotropy of the film[109,110], even though Guillon et al. [104,111] and Mucke [112] et al proposed different parameters to indicate the pore orientation. For instance, when δ is 0.9, 90 % of the particles have an angle less than $\pi/4$. In order to single out the anisotropy induced during the sintering process, the shrinkage of the stage II, κ, coupled with the shrinkage in stage *I*, τ, is used to predict the orientation, and the result is shown in Figure 52(b), and can be represented in formula:

$$\Gamma=(2/\pi)atan((1-\kappa)^{-1}(1-\tau)^{-1}tan(\theta)) \qquad 8\text{-}6$$

When τ equals zero, the orientation of particles is governed totally by the sintering process. The one dimensional shrinkage value κ is different from the parameter measured from the dilatometery data because the constrained densification is greatly retarded compared to the free sintering[113,114]. However, if there is a massive transport of materials between the ceramic particles, the orientation profile will deviate completely from the prediction above as analyzed below.

8.4 Results and discussion

8.4.1 Image analysis of the anisotropy of the film without PFA

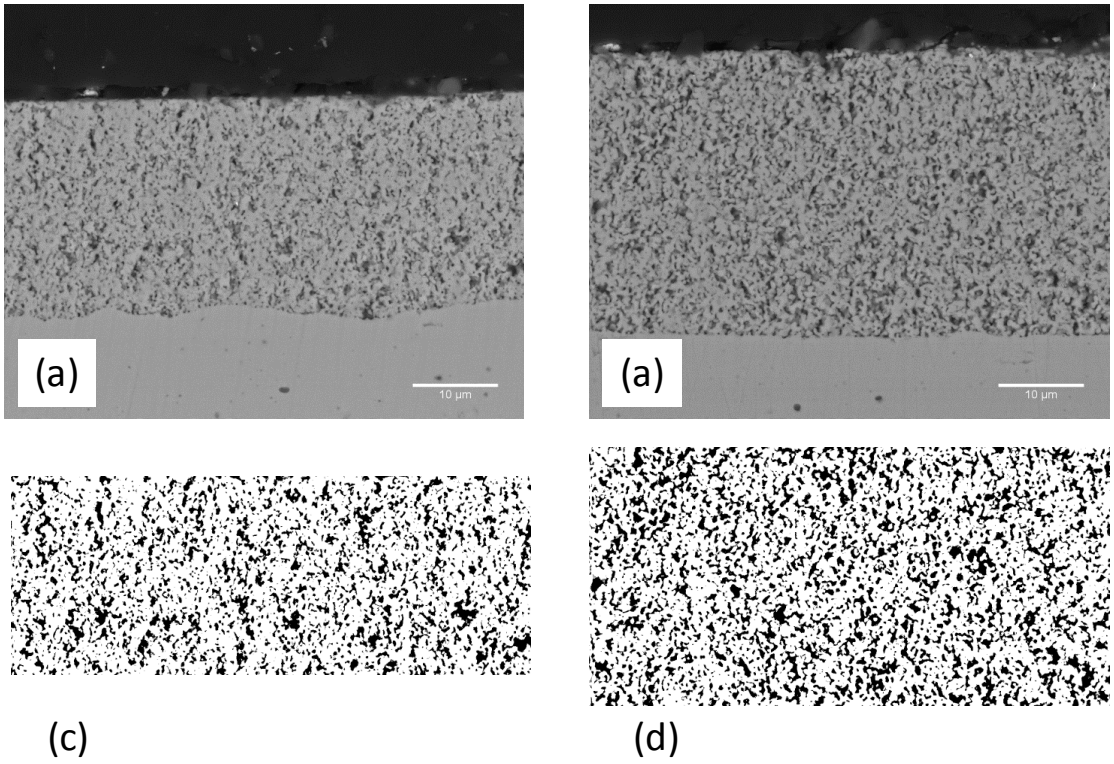

Figure 53 Back-scattered images of the film sintered at 1300 °C with ink containing Unitec 1- µm (a) and 2- µm (b) YSZ powder: (c) and (d) is the respective binarized image for calculation of porosity, pore orientation and pore size.

The cross-sectional image of the two films from Unitec 1-µm and 2- µm powder are shown in Figure 53(a) and (b) and the corresponding binary images of the film are shown accordingly in (c) and (d). The porosity of the two films is 25.1% (25 µm thick) and 31.6% (33 µm thick) respectively. Based on the conservation of the mass of the ceramic in the porous structure and ink, the thickness of ink L_0 can be calculated:

$$L_0=L_f(1-\phi)/V_c \qquad 8\text{-}7$$

ϕ is the porosity of the film and V_c is the volume fraction of the ceramic in the ink.

In combination with equation 8-2 and 8-7 gives

$$\delta= 1- V_c/(1-\phi) \qquad 8\text{-}8$$

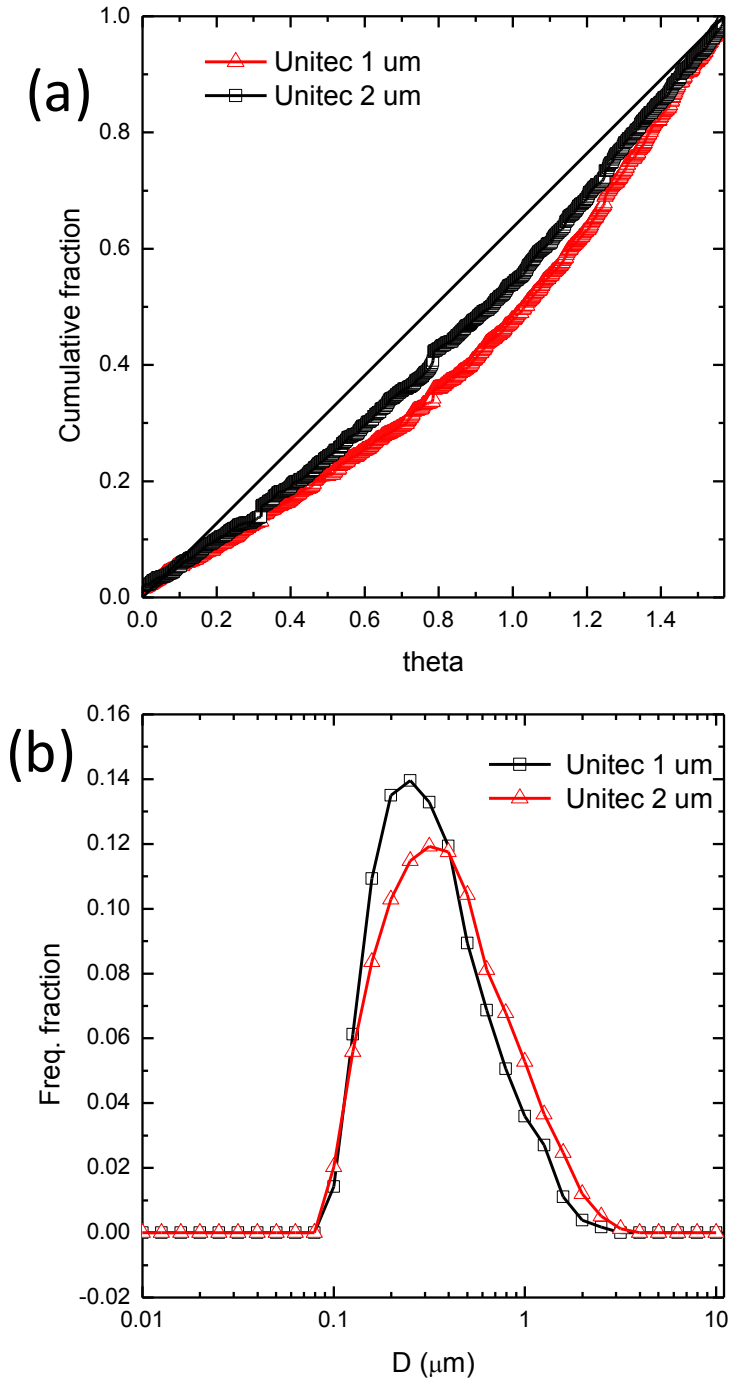

Figure 54 Pore size distribution (a) and cumulative fraction (b) of the constrained film from Unitec 1- μm and 2- μm YSZ powder.

The cumulative percentage of the diameter and angle of the pores are presented in Figure 54(a) and (b). The particle size covers less than two decades, peaking at 0.25 μm and 0.32 μm for the ink with Unitec 1- μm and 2- μm powder, respectively, in the same order of the grain size measured by PSA, though the 2-D image analysis cannot

represent the 3-D pore size very precisely. The asymmetry of particle size distribution and the narrow range comparing to the simulation can be explained by the cut-off length of particles for counting or the sintering process that causes the disappearance of finer pores[105]. If the V_c value for the ink in Table 5 is used, the shrinkage of ink, δ, with Unitec 1- μm and 2-μm powder should be 0.60 and 0.53, respectively. The percentage of the particles with $\pi/4$ is less than 50%, meaning the particles tend to be perpendicular to the substrate, in contrast to the prediction in Figure 54, considering the δ value. Unitec 1-μm powder tends to produce a more orientated microstructure with lower porosity, indicating anisotropy is intensified by the degree of sintering. This trend coincides with the experimental result of Guillon et al.[104] but contradicts that of Wang et al.[105]. According to the simulation of Wang et al.[105] and Cannon[115,116], the anisotropy caused by the faster in-plane grain diffusion with respect to grain boundary that causes the spheroidization of the pores; anisotropy was found to increase then decrease along with the densification process[115]. The ultra-fine powder in the bi-model Unitec 1- μm powder is beneficial in promoting the grain boundary diffusion in the sintering process, which explains the higher degree of anisotropy of the film from Unitec 1- μm powder at this stage of sintering. The diffusion of the materials through the grain boundary in the densification process has significant influence on the pore shape in the attendant pores, but the possible initial in-plane anisotropy cannot be excluded.

8.4.2 Image analysis of the constrained film with plate-like pore former

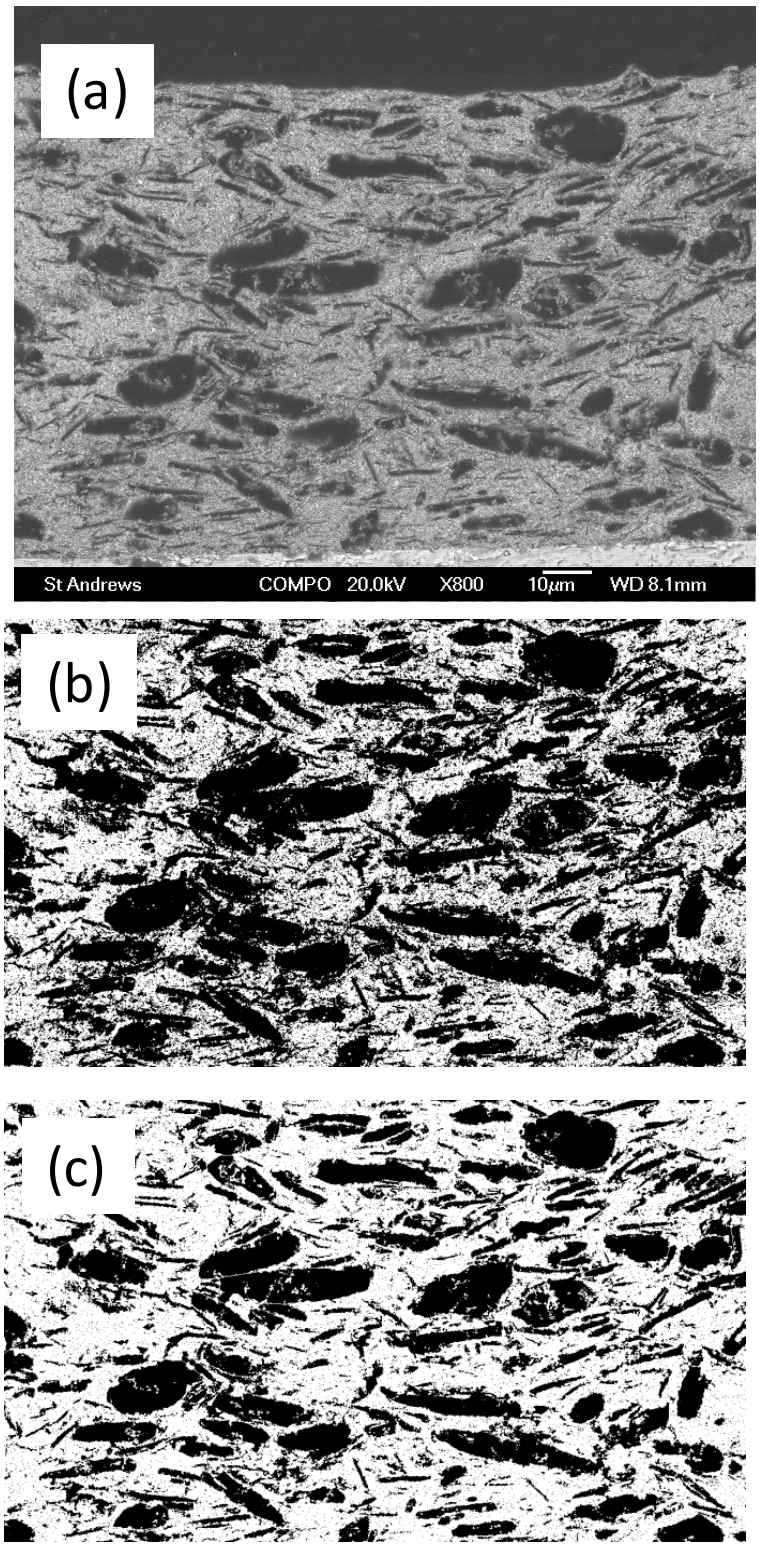

Figure 55 (a) back-scattered image of the film sintered at 1100 °C with the ink containing YSZ and graphite; (b) binarized image for measurement of porosity and (c) despeckled image for measurement of pore size and orientation.

To study the anisotropy in stage I where the densification process has not even started, the ink with pore former (ink 3) is fired at 1100 ^{o}C, and the cross-sectional image is shown in Figure 55(a). The microstructure could be considered as the starting-sintering stage, given the dilatometery data provided in Figure 48(b). This image is dominated by long pores aligning along the x-axis, similar to the image in Figure 51, but more information about the pore size and orientation profile can be obtained with image analysis. Although the anisotropy is affected by the substrate and densification process, in-plane anisotropy of the elongated $BaLa_4Ti_4O_{15}$ without PFA at the initial stage of sintering is also reported, and no proper explanation is proposed[117]. The binarized image is shown in Figure 55(b), a porosity of 56.4%. The despeckling is used to delete the very fine pores and a white line to separate some of the overlapping large pores manually for better analysis (Figure 55 (c))[110].

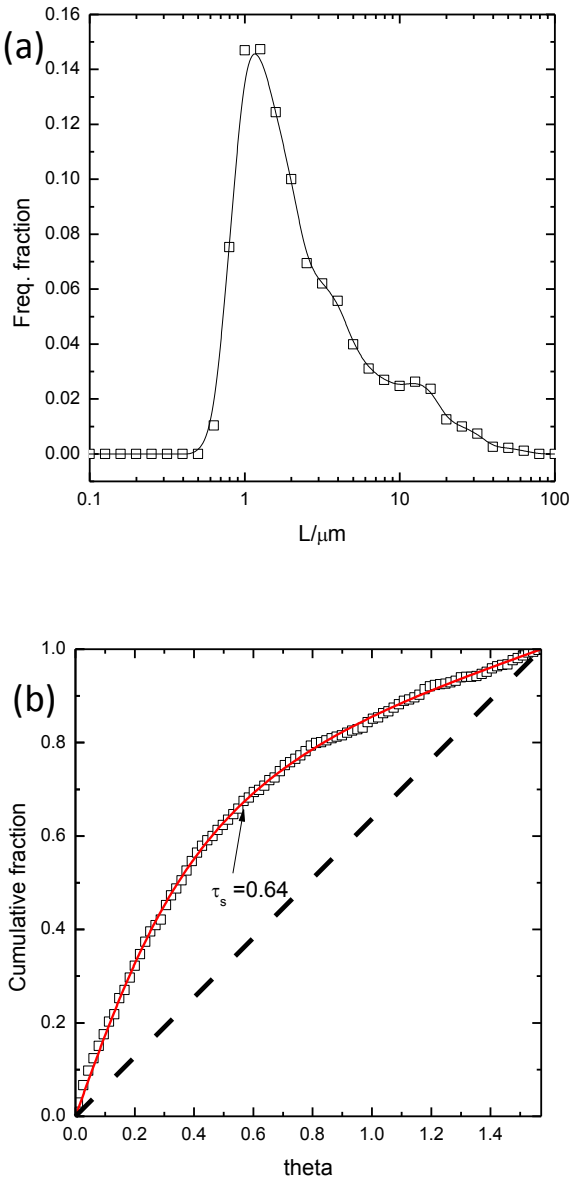

Figure 56 (a) Pore size distribution and (b) cumulative fraction of the pores at different angle. The line in (b) shows the simulated fraction with τ_s=0.64.

The Feret diameter was employed to evaluate the length of these extremely elongated pores and the discrete frequency profile is plotted in Figure 56(a). The pore size is peaking at 1.18 μm, and contains a significant fraction of pores around 10 μm. Even though the cut-off diameter of the pore size in the image analysis process is different, the attendant pores cannot be rule out because the comparison of the distributions in Figure 54(a) and Figure 56(a) shows an overlapping in the range of 0.5-2 μm. The profile of the distribution and the best-fitting curve with a parameter τ_s=0.64 is shown in Figure 56(b). The τ value is calculated to be τ_c=0.66 in equation 8-8 using the

measured porosity and V_c in Table 5, which indicates that the model is correct in predicting the orientation of pores. The good match between τ_s and the calculated τ_c indicates the orientation profile is generally independent of the particle size distribution. The direct observation of the attendant pores at 1100 ^oC may be one way to detect the anisotropy at stage I, but the poor mechanical property and small size of the pores makes the result unreliable and difficult to analyze.

8.4.3 Image analysis of the constrained film with spherical pore former

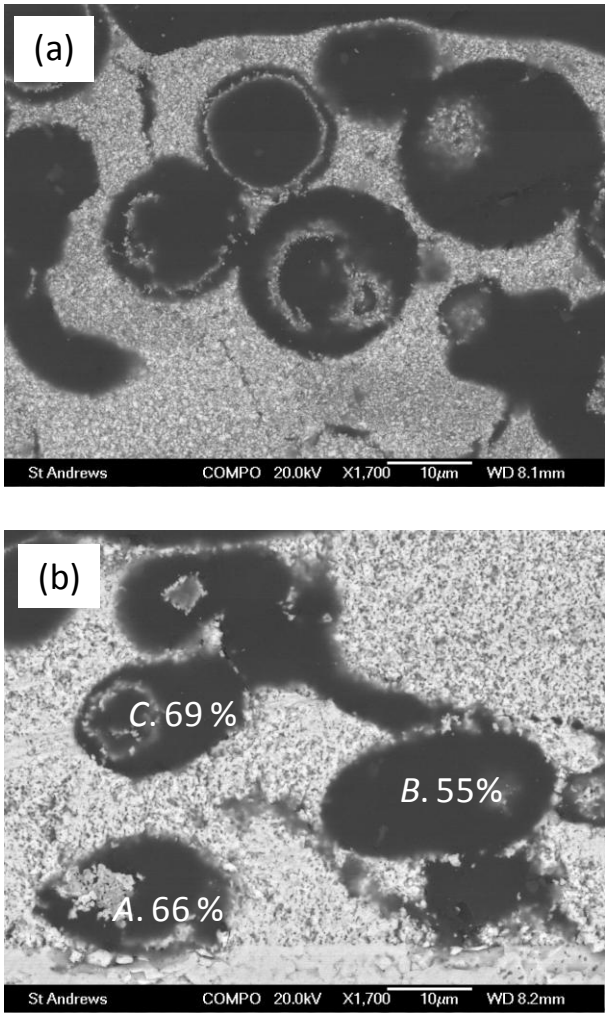

Figure 57 Back-scattered images of the film sintered at 1100 ^oC (a) and 1300 ^oC (b) from the ink containing YSZ and glassy carbon. The percentage in the image shows the percentage of the Feret length in y axis out of that in x axis.

Figure 57(a) shows the image from the ink with glassy carbon (ink 4) fired at 1100 ^oC for 3 hours, showing round pores resulted from the vestige of glassy carbon. Each pore contains an inner shell separated from the porous YSZ matrix and this could be

explained by the contraction of the glassy carbon coated with YSZ powder in the heating process[118]. However, after sintered at 1300 ^{o}C, the pores from glassy carbon is compressed in y-axis direction to form ellipses as shown in Figure 57(b), in contrast to spherical particles in a free sintering system where no anisotropy was observed[119,120]. Albano et al.[118] found good match between the shape of pore former in the green tape of tape casting and pores formed after being freely sintered. Because glassy carbon particles are spherical, the rotation in stage I does not exert any orientation in the green body of the film in stage I at the length scale of glassy carbon, ie, the anisotropy is attributed totally to the constrained sintering process. Due to the large length scale of pores from glassy carbon, the anisotropy from the diffusion is negligible in comparison with the dimension of glassy carbon. The numbers in each pore in Figure 57 indicate the percentage of the Feret length of the pores in y axis direction in comparison to the Feret length in x axis. For the pore *A* in image (b), the Feret length in y direction is only 66 % of that in x direction, indicating the sintering from 1100 ^{o}C to 1300 ^{o}C causes a shrinkage of 0.34 in y direction, i.e, $\kappa=0.34$. Most of the pores can be chosen to indicate the shrinkage because a continuous film of certain thickness is uniformly stressed except for those on the edge of the film where the pores show better densification[121]. However, for pore B, the film starts to fall apart and the Feret length is stretched longer than the one in continuum state, so the shrinkage calculated from these two pores is not accurate. The unbalanced force caused by the tilting of pore C, makes the calculation unrepresentative. If the same density is conserved, this linear κ value of 34 % corresponds to a shrinkage value of 12.9 % in a 3-D shrinkage, which is slightly lower than the shrinkage measured from dilatometry at 1300 ^{o}C, ca. 15 %. For a system containing plate-like pores sintered at elevated temperature to the final state, the κ and τ should contribute together to enhance the anisotropy as calculated in Figure 52(b). But the real situation is more complex because the difference in coordination number may result in a change in the morphology of the pores[122], transport that causes the disappearance or growth of pores[105] and the defect evolution in the constrained film[123].

8.5 Conclusion

Two stages of orientation process are identified in this work without considering the transport of materials: the in-plane alignment caused by the confinement of the film in

the forming of green body and the constrained sintering process. If the pores are in the scale of particles, the uneven material transport will alter the shape of the pores to a direction normal to the substrate. The image simulation offers more information that could be neglected in the real image analysis process, and a comparison of these parameters suggests that the anisotropy in the porous ceramic just before sintering is independent of particle size.

Chapter 9 Image analysis of the porous yttria-stabilized zirconia (YSZ) structure for the impregnated electrode of SOFC

9.1 Introduction

For an SOFC utilizing a YSZ electrolyte, La-based perovskites are widely used cathode materials, and with strontium-doped $LaMnO_3$ (LSM) being the most common, for the sake of being stable in the standard SOFC preparation processes involving the sintering of mixed powders to form composite electrode structures (such as those containing LSM and YSZ)[1]. These high sintering temperatures (above 1300 ^oC to get a proper sintering of YSZ) preclude the use of many potential La-based perovskites because of the reaction with YSZ forming insulating $La_2Zr_2O_7$, or the lack of chemical/physical stability at the process temperatures. To avoid exposure of these more reactive materials to the high-temperature sintering process, impregnation of perovskites materials into a porous well-sintered structure of YSZ scaffold was used to fabricate the composite electrode[23,25,59]. For example, strontium-doped $LaFeO_3$ (LSF) or (La, Sr)(Co,Fe)O_3 (LSCF) can be used to make a high-performance cathode at intermediate temperatures between 600 ^oC to 800 ^oC with the mixed ionic and electronic conductivity (MIEC) in this material leading to high electrochemical performance[3,27,34,57,, 124 , 125]. Compared with the conventional mixed-powder method, the structure of separately formed YSZ can be engineered into specific microstructures that will allow the percolation of subsequently infiltrated perovskite materials at very low content, much lower than that of ~ 30 vol.% in mixed powders[17] Moreover, the low forming and sintering temperature of the perovskite materials can produce nano-particles, increasing the length of triple phase boundary (TPB) of electrolyte, electro-catalyst and gas phase, where charge-transfer reactions take place[2]. LSF fired at 850 ^oC will form particles smaller than 100 nm on the surface of YSZ, producing longer TPB sites for the adsorption and reduction of oxygen than the one forming a dense film on the surface of YSZ at a sintering temperature of 1100 ^oC [27,29].

The YSZ scaffold dictates the distribution of the solution and the resulting perovskite particles. Previous work shows a porous YSZ scaffold formed using finer pore former has small pores, larger surface area and thus lower polarization resistance strontium-doped $LaFeO_3$ or $LaCoO_3$ was impregnated into it as cathode material[28,126].In addition, the network

of YSZ also controls the transport of oxygen ions from the electrolyte and oxygen molecules in the porous electrode. When a nano-fiber YSZ powder was used to prepare the scaffold for an LSM-impregnated cathode, the fast ionic transport in the fiber was thought to be the reason for a high performance exhibited at intermediate temperatures[97]. Further materials in addition to the perovskites phase can also be added into the overall structure during the impregnation and can alter the morphology of the perovskites by altering the location where they sit on the skeletal support. Various materials were added into the LSF-impregnated YSZ electrodes to enhance the electrochemical performance of the electrode, and it was found that the microstructral change of the electrode seems to be overruling the catalytic / ionic conducting effect of the additions[127]. The dual impregnation of SDC particles and LSM into YSZ scaffold decreased the R_p resistance of the electrode, and the change of microstructure was thought to be one of the factors inducing the enhancement of electrode performance[128].

As can be seen, optimization of the microstructure of the YSZ scaffold will enhance the performance of the infiltrated electrode, and the optimization of microstructure, at large, is particularly useful in promoting and understanding the performance of electrodes [22,31,89,129,130]. Through the quantification of images of composite electrodes it is also possible to determine their properties in terms of particle/pore size distribution, grain size, constituent shape factors, TPB, and descriptive functions [91,22, 131 , 132 , 133]. After quantifying a scanning electron microscopy (SEM) image of a Ni-YSZ electrode, Lee [131] determined the anisotropic packing and connectivity of conducting and pore phases, and found that anisotropy of the YSZ net work lowered the conductivity of the electrode. Duong [133] studied the correlation between the microstructure of LSM-YSZ composite cathode and performance by a 3D modeling, and concluded that lower TPB and surface area due to the use of coarser powders of LSM/YSZ caused a lower performance of the electrode. However, the sintering of the YSZ network in the porous structure for impregnation differs from that in composite electrode because of the addition of a fugitive pore former, such as graphite or glassy carbon, without any persistent material, such as LSM or NiO as in the conventional mixed-powder processing. Image analysis is also used in characterizing highly porous scaffold materials [134,135] and thus can easily be used in quantifying the scaffold optimization since only one phase is involved and the nano-particles are thought to be sitting on the surface of the scaffold.

In this study, high-resolution SEM images are analyzed and quantified to understand the effect of particle size of YSZ on the microstructure of the porous scaffold, and, in the end, the

electrochemical performance of the impregnated LSF-YSZ composite electrode was evaluated by ac impedance. The SEM image quantification is found to be consistent with the sintering behavior of the YSZ powder as was the performance of the impregnated electrode.

9.2 Experimental

9.2.1 Materials and ink making

The two batches of zirconia powder, herein named Unitec 1-μm and 2-μm, are the same as those in the last chapter. In the ink-making process, Hypermer KD-1 (Croda Inc. UK) was used as dispersant, and terpineol containing 5 wt. % PVB (butvar) as a vehicle. The pore formers are graphite (325 mesh, Alfa Aesar) or glassy carbon (Alfa Aesar). The graphite is composed of aggregated plates with varied dimensions while the glassy-carbon particles are 10-20 μm spheres. A mixed powder containing 10.0 g YSZ, 2.4 g graphite, 0.6 g glassy carbon and 0.26 g KD-1 was put into a plastic bottle containing 36 1-cm diameter zirconia balls, and then acetone was added to cover the surface of zirconia balls and powders. The bottle was sealed and put on a roller at 160 rpm for 24 h. When the milling time was complete, the contents, except zirconia balls, were transferred to a beaker, into which contained 7.8 ml vehicle. The acetone was allowed to evaporate while stirring on a magnetic plate, resulting in a well-dispersed viscous ink.

9.2.2 Image Processing and analysis

The backscattered electron images were taken on a Joel 6700F to give a highly contrasting image of the polised samples as described in last chapter. The high-magnification images of the focused-ion-beam (FIB) etched sample and fractured sample are used to observe the impregnated LSF on the scaffold.

The software ImageJ (National Institute of Health, Bethesda, MD) was used to process and analyse the images. The porous layer was cropped from the whole image and the SEM image was converted into a binary image by adjusting the threshold intensity. Because a large quantity of YSZ grains is in contact owing to the sintering process, watershed segmentation is used to separate them [136]. The size distribution of grain size is measured using the watershed segmentation image. Five images for each sample are analysed to get a better statistic validity.

9.2.3 Impregnation and electrochemical tests

Circular symmetrical cells with a round area of 1.13 cm^2 on each side of the dense YSZ pellet (diameter 2 cm and thickness 2 mm) were fabricated by impregnating the porous structure with the aqueous solution using $La(NO_3)_3 \cdot 6H_2O$ (Aldrich Chemistry, 99.99%), $Sr(NO_3)_2$ (Aldrich, 99 + %), $Fe(NO_3)_3 \cdot 9H_2O$ (Fisher Scientific, Analytical agent grade) and citric acid (Fisher Sientific, 1:1 mole ratio to the metallic ions). The stoichiometry of the resultant LSF is $La_{0.8}Sr_{0.2}FeO_3$ after the firing at 850 ^oC to form the perovskite phase. The loading of LSF was controlled at 35 wt. % on both sides. To facilitate current collection samples were coated with gold paste plus firing at 800 ^oC for 1 h, impedance from symmetrical cells were measured in static air over a temperature range of 550 ^oC to 700 ^oC using a Solartron 1260 frequency response analyser (FRA) generating a sine wave ac signal with a magnitude of 5 mV in the range of 10000 Hz to 0.05 Hz. Results were analysed using Scribner Associates Z-plot. The resistance of the lead wires is deducted from the series resistance.

9.3 Results and discussion

9.3.1 Image analysis of the microstructure of the porous zirconia

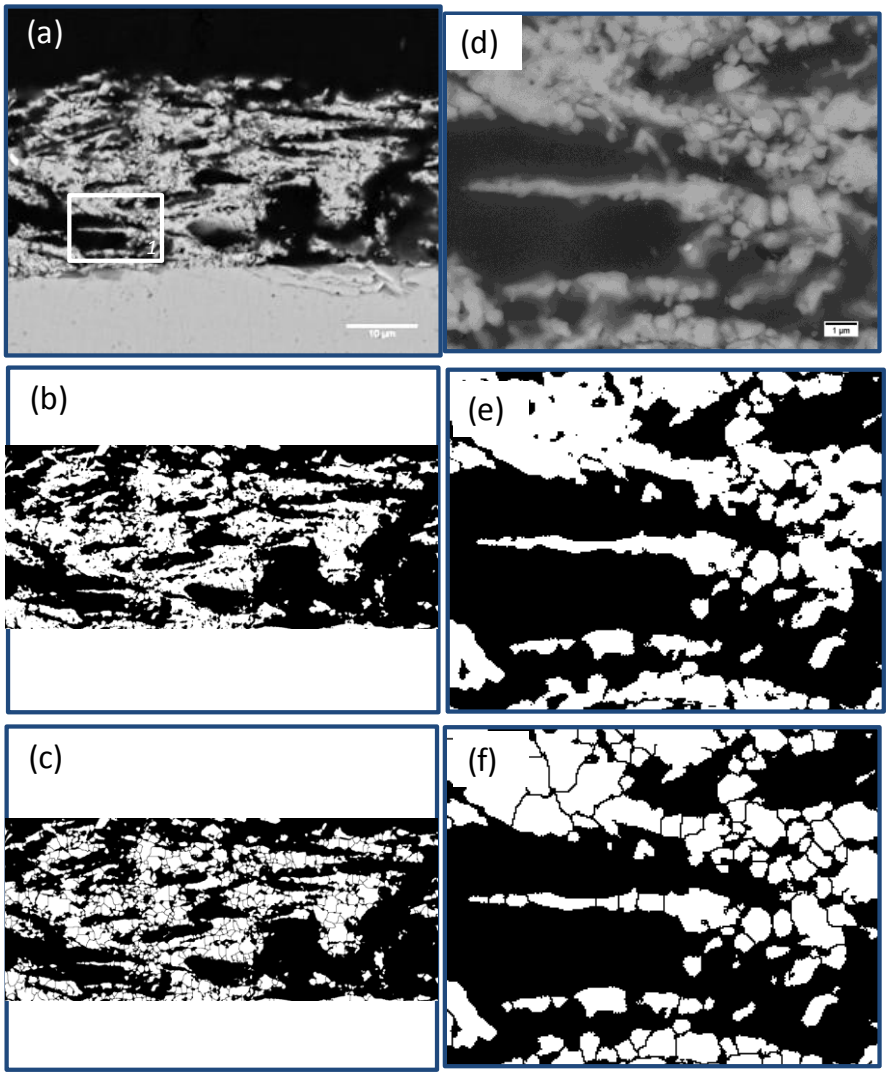

Figure 58 (a) is the backscattered image for porous film from Unitec 1-μm powder; (b) is the binary image separating YSZ and resin and used to calculate the boundary of YSZ particles and porosity; (c) is the image using watershed segmentation to separate the YSZ grain in order for the grain distribution. (d) is the high magnification image for the region 1 in (a). (e) and (f) are the zoom-in images corresponding to the region 1 in (b) and (c) respectively.

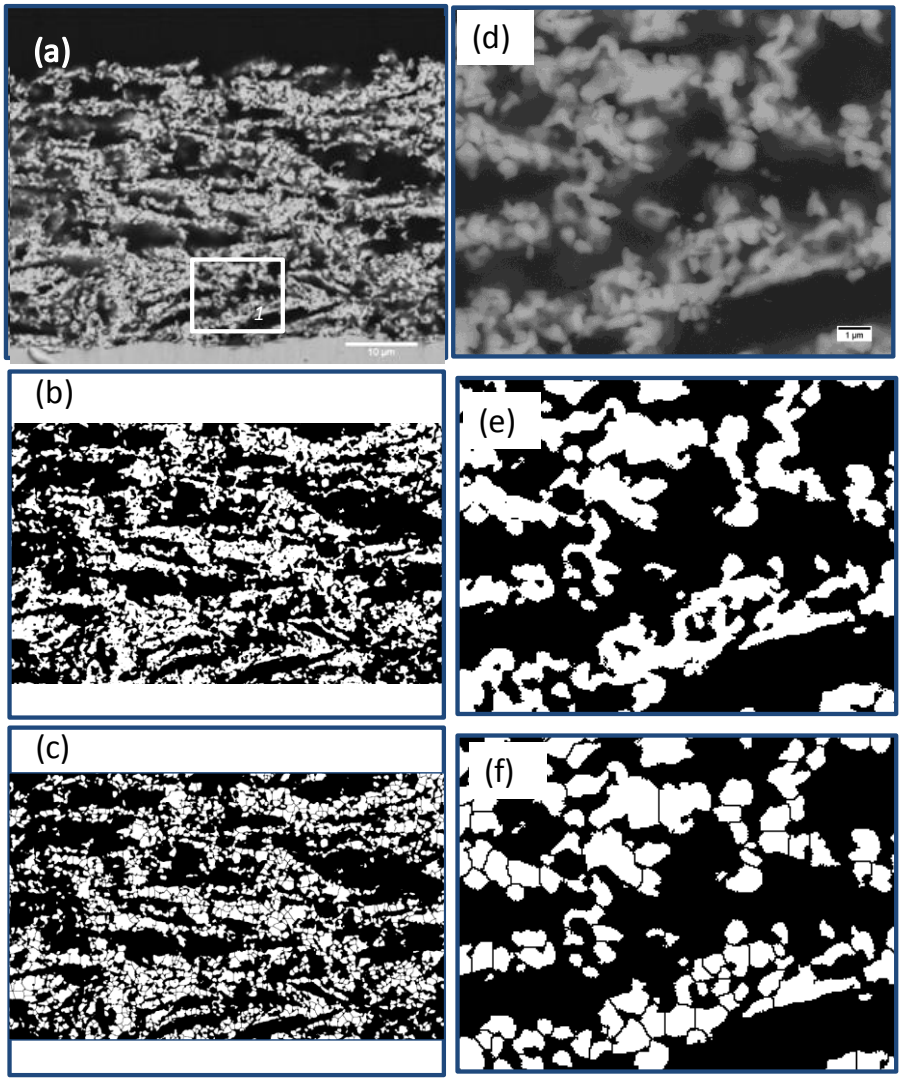

Figure 59 (a) is the backscattered image for porous film from Unitec 2-μm powder; (b) is the binary image separating YSZ and resin and used to calculate the boundary of YSZ particles and porosity; (c) is the image using watershed segmentation to separate the YSZ grain in order for the grain distribution. (d) is the high magnification image for the region 1 in (a). (e) and (f) are the zoom-in images corresponding to the region 1 in (b) and (c) respectively.

The typical microstructures of porous scaffolds for the 1-μm and 2-μm powders are shown in Figure 58 and Figure 59, respectively. The thickness is 27 μm for the 1-μm powder and 40 μm for the 2-μm powder. In both figures, (a), (b) and (c) show the low magnification backscattered electron image (a) of the porous skeleton from Unitec 1-μm or 2-μm powder, and the corresponding binary image without (b) and with (c) watershed segmentation. (d) is

the high-magnification image for the region *1* in (a). (e) and (f) are the zoomed-in image of (b) and (c) in the corresponding region *1* respectively without new processing of image (d). The porosities and the area specific perimeters of the particles in Figure 58(b) and Figure 59(b) are listed in Table 6. For comparison, the porosities of the samples were also measured using Archimedean method. It is evident that the film from Unitec 2-μm is more porous than the one from 1-μm powder; the result of image analysis is consistent with the porosity measurement of Archimedean method. The perimeters of the particles are the boundary of YSZ scaffold and resin, indicating longer YSZ /air boundaries.

Table 6 Parameters of the image analysis for the porous structures from Unitec 1-and 2-μm powder. The numbers in the parentheses indicate the error window by analysing five images.

	Porosity measured with Archimedean method	Porosity measured with imageJ	Area-specific boundary length /μm^{-1}	Estimated LSF diameter /nm	TPB length μm^{-2}
1-μm powder	54 (3)%	57 (2) %	0.97(9)	0.055	35(3.3)
2-μm powder	62(4)%	62(2)%	1.41(6)	0.055	51(2.2)

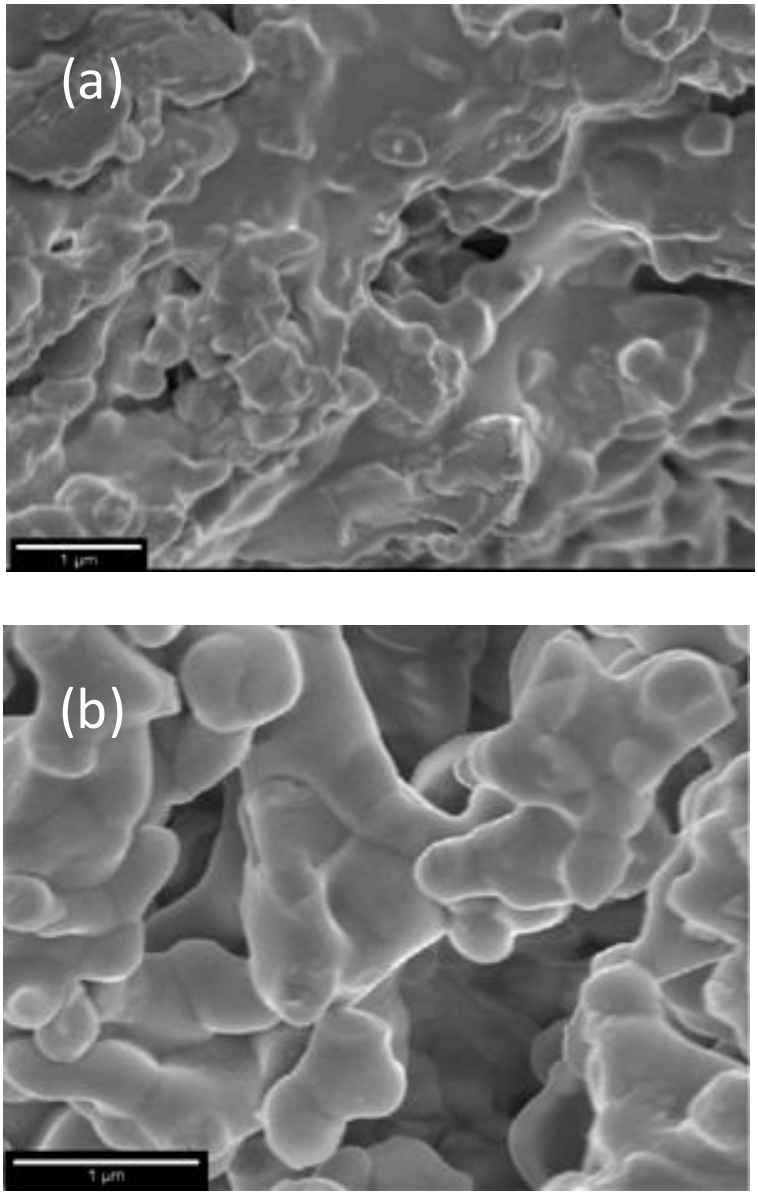

Figure 60 Fractured surface images of the porous structure after firing at 1300 °C for three hours from the two types of powders: (a) Unitec 1-µm powder and (b) Unitec 2-µm powder.

After the comparison between (d) and (f) in both figures (Figure 58 and Figure 59), it can be easily seen, that the watershed segmentation created an image similar to higher magnification image and separated the YSZ grains for quantification, compensating the drawback of the low magnification image, whose resolution is not high enough to separate the grain boundary. Figure 60 reveals the fracture surfaces for the porous structures from the two inks. In Figure 60(a), the fractured surface of film from 1-µm powder, small round nodules are attached to

large dense large particles and only some of them are discernible. On the other hand, the spherical grains of Unitec 2-μm powder are attached to each other but they can be easily distinguished. It is well known that the edge of YSZ particles will blunt during a high temperature sintering process, and can also be seen from the microscopy comparison between Figure 47 and Figure 60. The consistency between the high-magnification image of area *1* in Figure 58(a) and Figure 59(a) and the enlarged images of the corresponding area in Figure 58(c) and Figure 59(c) is due to the fact that spherical objects in contact can be separated by the watershed segmentation very precisely [136].

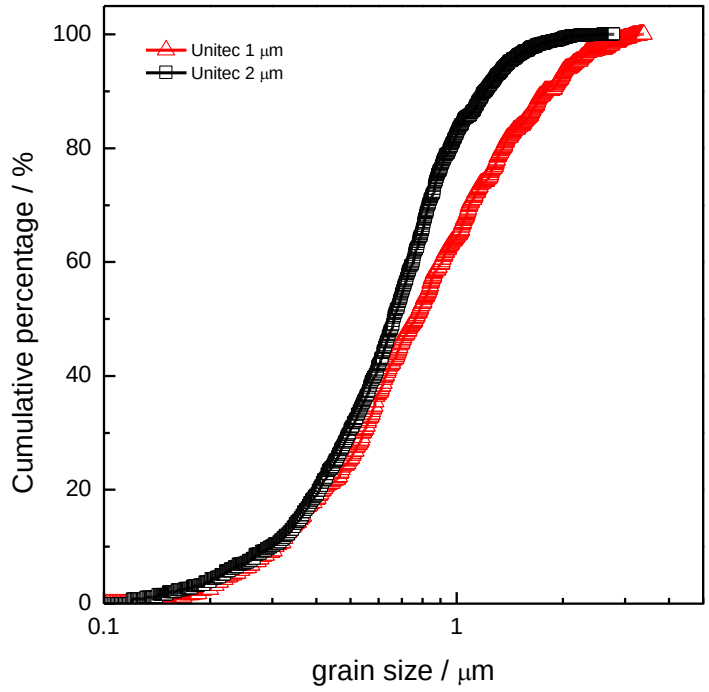

Figure 61 The YSZ grain distribution obtained through separating the particles by watershed segmentation. The corresponding images are Figure 58(c) and Figure 59(c).

The cumulative percentage of the area of grains in Figure 61 indicates that 80 % the YSZ grains from the 2-μm powder are smaller than 1 μm, but about only 50 % of the grains from 1-μm powder are smaller than 1 μm. This trend is in contrast to the PSA data, where Unitec 1 μm powder contains finer powder. The possible explanation to the larger grain growth is that the wide particle size distribution of the Unitec 1-μm powder increases the area of contact, leading to an enhanced particle rearrangement [137]. In addition, the fine particles around the peak ~0.1 μm in PSA can easily lose their shapes by incorporating with other particles at

1300 ^{o}C via a coarsening mechanism. The presence of these fine particles initiates a sintering at 1000 ^{o}C as shown in the dilatometry results. It has also been shown that a YSZ powder with a particle size of 0.2 μm will be 99.5 % dense at a sintering temperature of 1100 ^{o}C if no pore former is added[138]. On the other hand, the particles of Unitec 2-μm powder with a narrow particles size distribution band around 1 μm are well dispersed, giving porous scaffold with a comparable grain size distribution to the PSA of as-received powder as they sinter at a slower but more consistent rate.

9.3.2 SEM of the infiltrated electrode

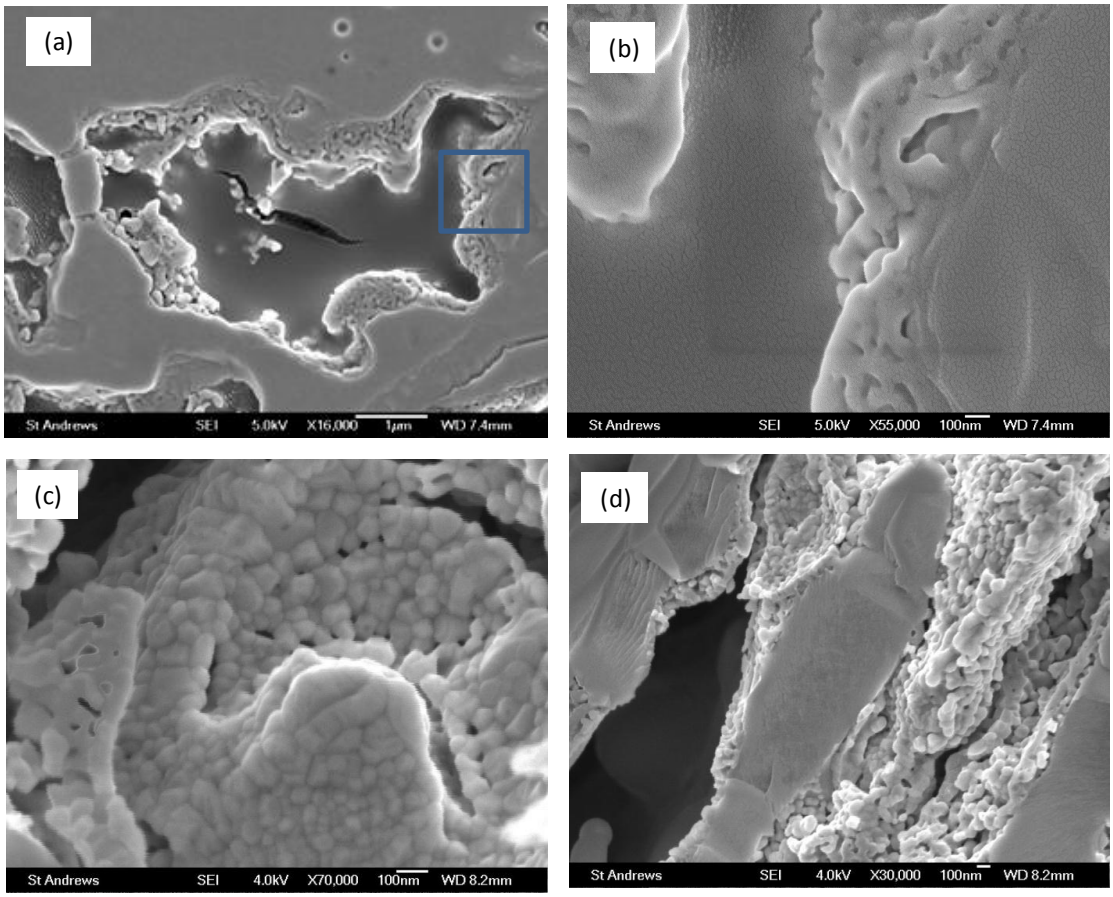

Figure 62 Morphology of nano-particles of LSF on YSZ: (a) and (b) are focused ion beam etched sample; (c,d) fractured surface indicating the particle size of LSF is about 30 nm to 80 nm. (b) is the enlargement of the rectangular in (a)

Since the quantification has been done on the scaffold, the TPB density is easy to calculate because the nano-particles will sit on the scaffold, as shown in the FIB etched sample (Figure 62(a,b)). The fractured micrographs, Figure 62(c,d), indicates that the particle size of LSF is

in the range between 30 nm and 80 nm, which is much smaller than the grain size of the skeleton. If the median particle size of LSF, 55 nm is used, the number of particles on area-specific boundary will be 17.64 μm^{-2} and, 25.56 μm^{-2} and the TPB density will be 35.28 μm^{-2} and 51.16 μm^{-2} , Table 6, for the scaffolds from the Unitec 1-μm and 2-μm powder, respectively, since each LSF particle will produce 2 TPBs. These values are very similar to the reported result of Zhan [139] for Ni-impregnated strontium- and magnesium-doped lanthanum gallate (LSGM) scaffold at a Ni loading of 2.51 vol. %. For the conventional LSM-YSZ composite electrode, the highest value would be 20.68 μm^{-2}, depending on the particle size of the starting powders[133].

9.3.3 Impedance measurement

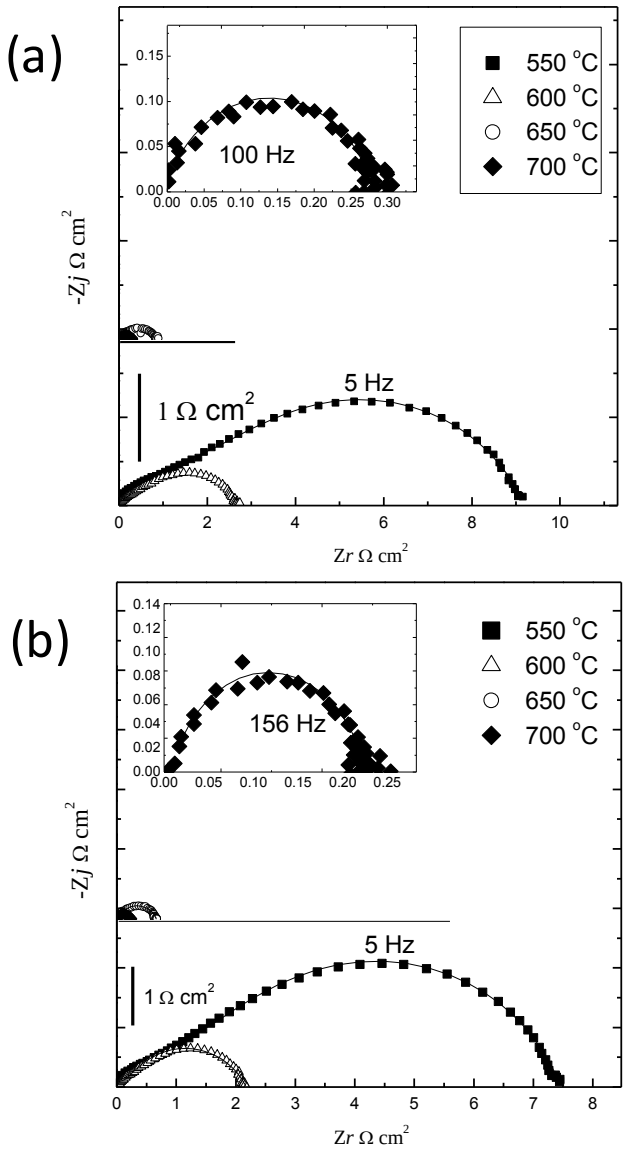

Figure 63 Nyquist plots of the impedance measurement on symmetrical LSF-YSZ electrodes using scaffold from (a) Unitec 1-μm and (b) 2-μm powder, respectively. The electrolyte resistance is subtracted to make the high frequency point of Z_r at 0. Inserts are the enlarged impedance plots at 700 °C.

Figure 63 shows the impedance data of the impregnated scaffolds at different temperatures. The series resistance has been subtracted from each spectrum to allow for comparison of the arcs. The impedance data for scaffolds from 1-μm powder and 2-μm powder are composed of two arcs at 550 °C and 600 °C, but at 700 °C, the arc at the high-frequency part is

indistinguishable. The R_p values were obtained by subtracting the series resistance (high-frequency intercept) from the *Z*r value at the low-frequency intercept. The R_s and R_p values are plotted vs. 1000/T as shown in Figure 64(a) and (b) respectively. The R_s value for a 2-mm YSZ pellet is different if different YSZ powder were used to fabricate the scaffold. At 700 ^oC the R_s values for 2-μm and 1-μm powder are 8.5 Ω cm^2 and 10.0 Ω cm^2 respectively. The R_s is in a reasonable range for pressed pellet sintered at 1500 ^oC having an ionic conductivity of ~0.0205 S cm^{-1} at 700 ^oC [140]. The activation energies, E_a, of the R_s values are very close to each other and slightly lower than that of pure 8YSZ, 1.0 eV, implying the existence of the lateral resistance from the electrode. The resistance measurement of electrolyte resistance associated with cathode can be attributed to the resistance on the interface of cathode/electrolyte resistance and electrolyte materials because the resistance of cathode materials is negligible[38]. The coarse grain size of the scaffold from Unite 1-μm powder maybe diminishes the contact area between LSF and YSZ, causing ineffective current collection area.

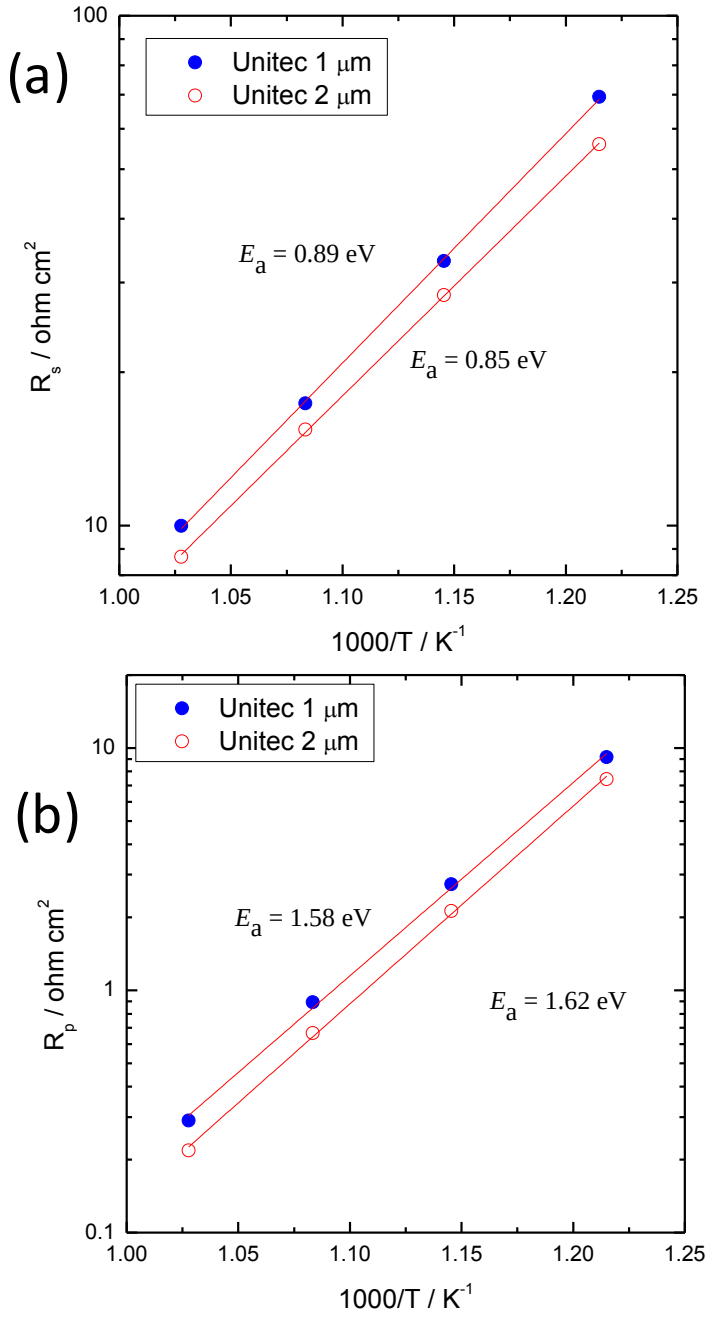

Figure 64 (a) The electrolyte resistance R_s and (b) the polarization resistance R_p as a function of the temperature measured on symmetrical cells with LSF-YSZ electrodes.

The electrode using Unitec 2-μm powder shows lower R_p than the one using Unitec 1-μm powder, but the E_a is slightly higher. At 700 ^oC, the R_p value of Unitec 2-μm based scaffold is 0.21 Ω cm^2, higher than the reported value of LSF-impregnated YSZ[27], 0.13 Ω cm^2, but this

difference can be explained by the ionic conductivity of scaffold materials because of the difference in sintering temperature of the scaffold, thermal history of the sample or the difference in current collection paste. Nonetheless, this value is lower than the reported R_p for LSM-impregnated cathode at 700 ^oC, above 0.25 Ω cm^2[2,141]. In a modeling study on the length of TPB produced by impregnation[142], the smaller particle size of the scaffold and/or impregnated materials promotes longer TPB, so it is reasonable to conclude that the smaller grain size can increase the site of reaction of O_2. This can be inferred from the lower R_p value of the electrode using Unitec 2-μm powder. Actually, the long area-specific boundary of the YSZ phase of the scaffold from Unitec 2-μm powder also corroborates the assumption of longer TPB by providing a large area for LSF particles to sit on, since the impregnation is the same.

9.4 Conclusion

In this work, two types of powders showing different sintering behaviors are utilized to prepare porous YSZ scaffolds for impregnation. The powder with fine particle volume fraction and bimodal distribution in the powder induces the faster YSZ grain growth and decrease in surface area when compared to powders with narrower size distribution and larger size. These results were confirmed using image analysis, and the further quantification estimated the TPB length, which is higher than for the electrodes from conventional mixed powder processing owing to the nano-scale particles of the impregnated materials. The electrode using scaffolds made from the YSZ powders with narrow particle size distribution shows better performance with decreasing the polarization resistance and contact resistance, i.e., in agreement with the prediction of the image analysis.

Chapter 10 Study of the oxides of transitional metal as dopants for the strontium-doped $LaFeO_3$

10.1 Introduction

The state-of-the-art cathode for a fuel cell with yttria-stabilised zirconia (YSZ) as electrolyte is strontium doped $LaMnO_3$ (LSM) because of its chemical compatibility with YSZ and structural stability at high temperature for extended operating times. The choice of high operating temperature (above 800 ^oC) results in high costs and demanding materials requirements. In order to get a better performance at intermediate temperatures (600-800 ^oC), those mixed-ionic-and-electronic-conducting (MIEC) materials tending to react with YSZ at high-temperature sintering can be synthesised in-situ by infiltrating their precursors into a pre-formed porous YSZ structure and fired at a relatively low temperature[23,143]. Nonetheless, the highly ionic-conducting strontium-doped $LaCoO_3$ (LSC) reacts with the YSZ scaffold even at a testing temperature as low as 700 ^oC[126]. $La_{0.8}Sr_{0.2}FeO_3$ (LSF) is a viable cathode material to be used at intermediate temperatures due to the lower probability of reacting with YSZ scaffold and decent performance over 2500 hours has been demonstrated by Wang et al.[27]. At 700 ^oC, the electrode loss of the composite electrode from infiltration of LSF calcined at 850 ^oC is about 0.1-0.2 Ω cm^2 and can be further improved by tailoring the microstructure[28,98] or ionic conductivity of the scaffolds[29]. However, the microstructure or ionic conductivity of the scaffold is pre-determined during the initial processing, so it would be more desirable to change the reduction kinetics of oxygen on the surface of electrode to make further improvement. The reduction of oxygen includes the adsorption and disassociation of the oxygen molecule, and the diffusion of oxygen species on the surface or through the bulk of perovskite to the triple phase boundary (TPB) where the charge transfer process takes place[2,144,145]. Accordingly, three ways can be used to enhance the electrochemical reaction: (1) optimisation of the microstructure of the perovskite to enhance the TPBs, (2) dopants that catalyze surface reaction between the electrode materials and oxygen molecules and (3) addition of oxides of fast oxygen conductor.

In an electrode made from infiltration, the decrease of the grain size of the perovskite is one method to create more TPB. Unfortunately, because a minimum temperature is required to fabricate the pure perovskite, there is little room to decrease the

calcination temperature. Moreover, the operating temperature also requires relatively high calcination temperature to ensure long-term stability; e.g. the LSF-YSZ electrode prepared by infiltration is usually fired at 850 ^{o}C to gain pure phase and ensure a stable performance at 700 ^{o}C. Alternatively, the addition of oxide that stabilizes the surface property of the perovskite[146] can enhance the surface diffusion and also the electrochemical performance of the electrode[145].

The addition of CoO_x to LSM has been reported to enhance the oxygen exchange between the gas phase and the perovskite surface[147], and an obvious improvement in electrochemical performance induced by the infiltration of cobalt nitrate is identified for the LSM-YSZ composite electrode calcined at 1150 ^{o}C [148,149,150]. However, the addition of cobalt oxide into a LSM-YSZ electrode prepared by infiltration plus calcination at 850 ^{o}C does not have any effect on the polarisation resistance or the series resistance[151]. Therefore, the microstructure of the electrode before the addition of the catalyst could play an important role in the rate-determining step in the reduction of oxygen[127].

The ionic conducting oxides, such as $Sm_{0.6}Sr_{0.4}CoO_{3-\delta}$(SSC)[152], LSF[152], $Ce_{0.8}Sm_{0.2}O_2$ (SDC)[128] and $La_{0.8}Sr_{0.2}CoO_3$(LSC82)[151], can be infiltrated into LSM-YSZ electrode to improve the polarisation resistance, but the long-term stability could still be a problem for the cobalt-containing perovskite[151]. In the case of LSF-YSZ electrode, the influence of SDC is unknown because of the higher ionic conductivity of LSF (8.3 x 10^{-4} S cm^{-1}) than that of LSM (<10^{-10} S cm^{-1})[23,3].

In this study, precursors for Co, Ni and Mn, other than their (La, Sr)-containing perovskites, are infiltrated into the LSF-YSZ electrode for the first time to avoid possible formation of insulating phases and modify the performance of the electrode. The pre-calcination of LSF is used to control the particle size and phase purity of the porous structure in which the forthcoming nitrate precursor for MO_x (M=Mn, Co or Ni) dopants will be impregnated. Electrochemical impedance spectroscopy (EIS) based on symmetrical cells was used to study the effect of the pre-calcination of LSF and the final calcination on the series and polarization resistance. The electrochemical performance is correlated to the phase analysis with X-ray diffraction and the final morphology of the electrodes observed with scanning electron microscope (SEM).

10.2 Experimental

The symmetrical electrochemical cells used in this study were similar to those for the bi-electrode supported fuel cell. The diameter of the porous structure on the symmetrical cell is about 9.5 mm. The aqueous solution for LSF is prepared by dissolving the stoichimetric nitrates of lanthanum, strontium and iron. Citrate acid is added to the solution to make a 1:1 molarity to LSF. The resultant solution is dripped on the surface of the porous structure. The infiltration is performed on both sides before calcinations at 700 ^{o}C for 30 min. The infiltration process is repeated until the weight loading of LSF reaches 35 wt.%. The thus impregnated cells will be fired at different temperatures for testing or will be doped with oxides of nickel, iron or cobalt by further impregnating the nitrate solution of these metals.

Table 7 Cacination schemes for the sample without or with Co, Ni and Mn as dopant.

Name	Calcination before dopant	Calcinations after dopant
LSF_700_only	700 ^{o}C 30 min	-
LSF_850	850 ^{o}C 4 hours	-
Dopant [a]_700_only	700 ^{o}C 30 min	700 ^{o}C 1 hour
Dopant [a]_700	850 ^{o}C 4 hours	700 ^{o}C 30 min
Dopant [a]_850	700 ^{o}C 30 mins	850 ^{o}C 4 hours
Dopant [a]_850 _8hrs	850 ^{o}C 4 hours	850 ^{o}C 4 hours

[a:] Dopant represents Ni, Fe or Mn: e.g. Co_700_only represents the sample calcined at 700 **^{o}C** before and after Co doping.

The difference of the infiltrated LSF varies in both morphology and phase purity when the calcinations temperature increase from 700 ^{o}C to 850 ^{o}C, which will affect the secondary infiltration process of Co, Ni or Mn nitrate. Therefore, the infiltration and calcination scheme for the addition of dopant by infiltration is listed in Table 7. The weight of CoOx, NiO and MnO_2 is controlled to be about 3 wt.% through the tuning of molar concentration of the corresponding nitrates.

Silver wires (diameter 0.25 mm) will be attached on to both sides of the symmetrical cell using silver paste. Four probes (two on either side) are used in the electrochemical impedance tests on a Solartron 1260 frequency response analyser

(FRA) generating a sine wave AC signal with a magnitude of 10 mV in the range of 100 kHz to 0.05 Hz. The sample is heated up in a tube furnace under static air to 700 ^{o}C and then cools down to the desired measurement temperatures at a rate of 3 ^{o}C min^{-2} and held for 30 minutes before each measurement. XRD measurements were carried out on a Panalytical diffractometer with a Cu target. The fractured surface was examined with a Jeol 6700 scanning electron microscope.

10.3 Results

10.3.1 XRD analysis

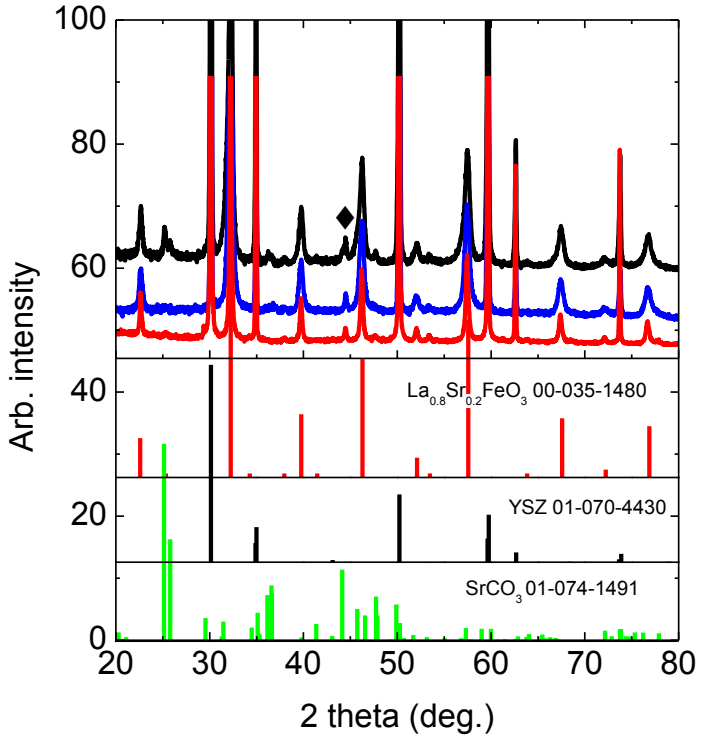

Figure 65 XRD patterns for LSF-YSZ electrode calcined at only 700 ^{o}C with (blue line) and without (black line) Co doping; the red line represents the LSF-YSZ electrode calcined at 850 ^{o}C. The standard diffraction patterns are provided for comparison. The ♦ indicates the peak of stainless steel sample holder.

The XRD patterns for the composite electrode calcined only at 700 ^{o}C with and without Co doping is shown in Figure 65, where a set of peaks for $SrCO_3$ is visible after the doping of cobalt oxide. The residual $SrCO_3$ is the product of the reaction between the carbon dioxide in air and the strontium species. Even though no peaks for

cobalt oxide or the resultant product is visible in the XRD pattern, the cobalt oxide can be inferred to react with the impregnated content for LSF.

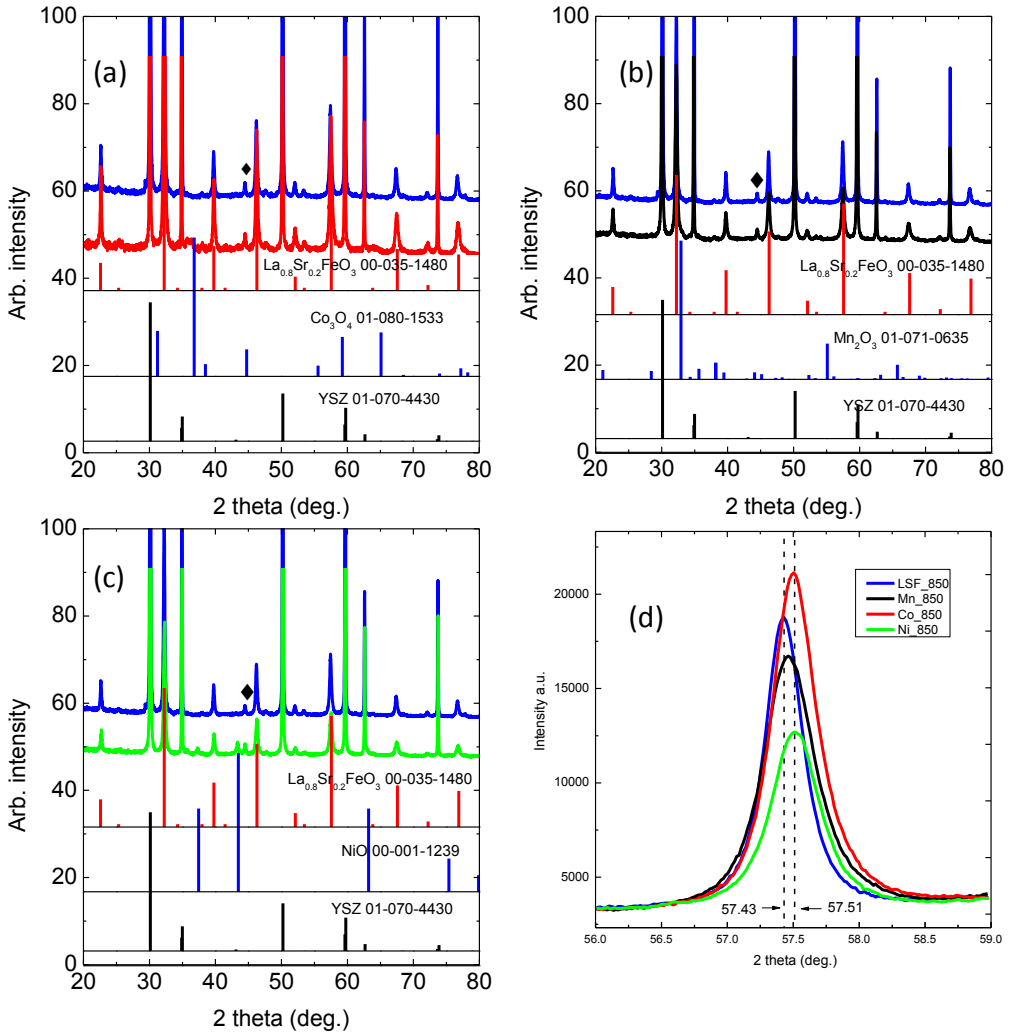

Figure 66 XRD pattern for Co_850 (a), Ni_850 (b), Mn_850 (c) and the superimposed image in the range of 56-59° The XRD pattern of LSF_850 (blue lines) is provided for comparison. The selected PDF files for the transition metal oxide are proved for comparison. The ♦ mark indicates the minor peak from the stainless steel sample holders.

The XRD patterns for the LSF-YSZ electrode with Co-, Ni- or Mn-dopant after the calcination scheme of Dopant_850 are shown in Figure 66. After the calcinations at 850 °C for 4 hours, the infiltrated content for LSF turns fully into perovskite and no extra peaks are found. After the infiltration of dopants, no peak for the possible MnOx or CoOx is visible after the calcinations at 850 °C, while NiO can be easily identified in the sample with nickel nitrate infiltration. No impurity phases, such as $La_2Zr_2O_7$

and $SrZrO_3$, as observed for Ni- or Co- containing perovskite, is found after the addition of dopants plus calcination at 850 ^oC. The magnified peaks in 2θ range between 56-59^o, Figure 66(d), suggest that the infiltration of Ni-, Mn-, or Co- oxide changes the intensity as well as the position of the second strongest peaks of the perovskites. The infiltrated electrode with dopants can be perceived as a mixture of LSF perovskite with a modified surface layer in contact with the dopants, so the lattice-parameters change owing to the incorporation of Mn, Co, Ni into the lattice of LSF perovskite shifts the peaks towards the high–angle direction. The widths of the diffraction intensity distribution for the samples with dopants are larger than those without. Although a decrease of crystallite size could be an explanation to the distribution of XRD intensity, the wider peaks for the sample with dopants can also be a result of mixed phases in this case.

10.3.2 Microstructure analysis

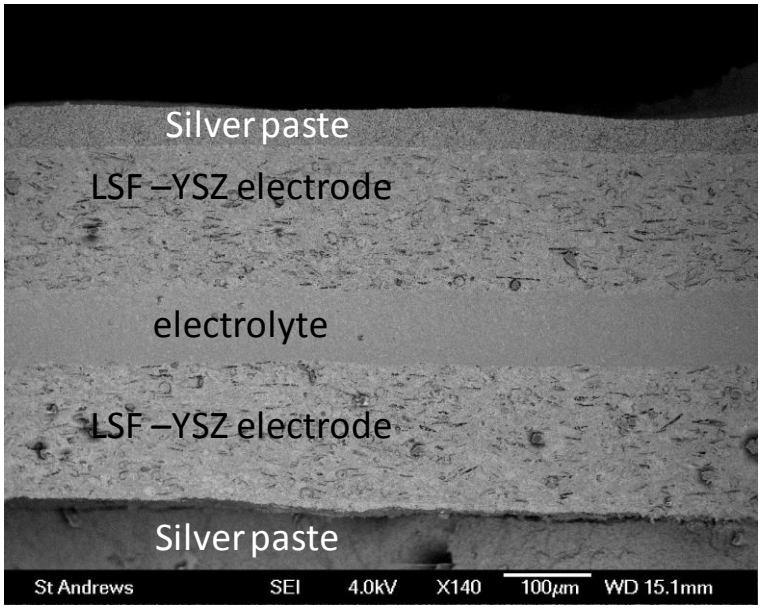

Figure 67 SEM image for fuel cell after testing at 700 ^oC

Figure 67 shows the SEM of symmetrical cell with a 35 wt.% loading of LSF after being calcined at 850 for 4 hours. A dense electrolyte of about 90 μm is sandwiched between two 165-μm electrodes after the sintering at 1375 ^oC for 4 hours. If the conductivity of YSZ[140] of 0.0205 S cm^{-1} is considered, the contribution from this electrolyte is 0.44 Ω cm^2. After the calcinations at 700 ^oC, the porous silver paste is about 40μm and adheres well to the surface of the electrodes.

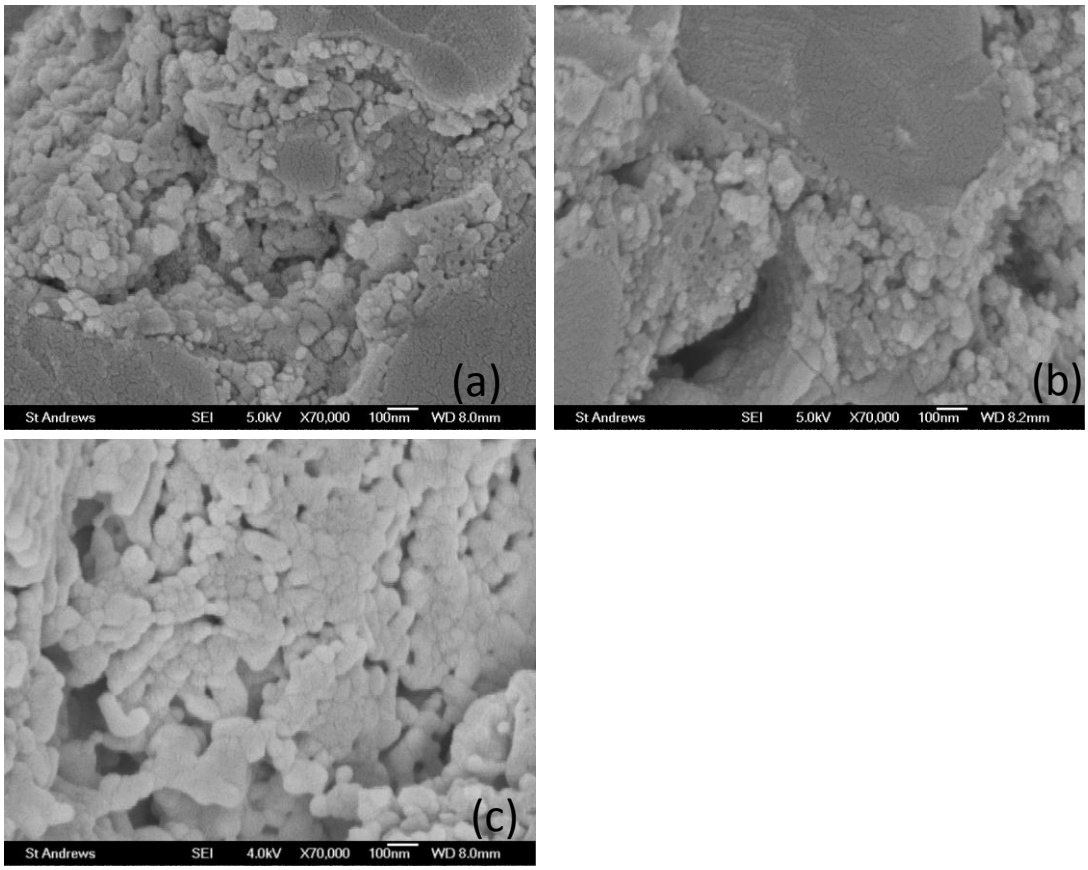

Figure 68 SEM images of the sample (a) LSF_700_only, (b) Co-700_only and (c) LSF_850.

Figure 68 (a) and (b) shows the images of the sample calcined at 700 ^{o}C with and without Co-doping, and no cobalt oxide can be distinguished from these images thanks to the heterogeneity of the LSF_700_only sample. The crystallite size for the LSF_850 (Figure 68 (c)) is in a narrow range between 30-100 nm, in contrast to the small grains (10 nm) for the sample calcined only at 700 ^{o}C. It can also be seen that the larger LSF grains are separated by larger pores after the calcinations at 850 ^{o}C in comparison with those calcined at 700 ^{o}C.

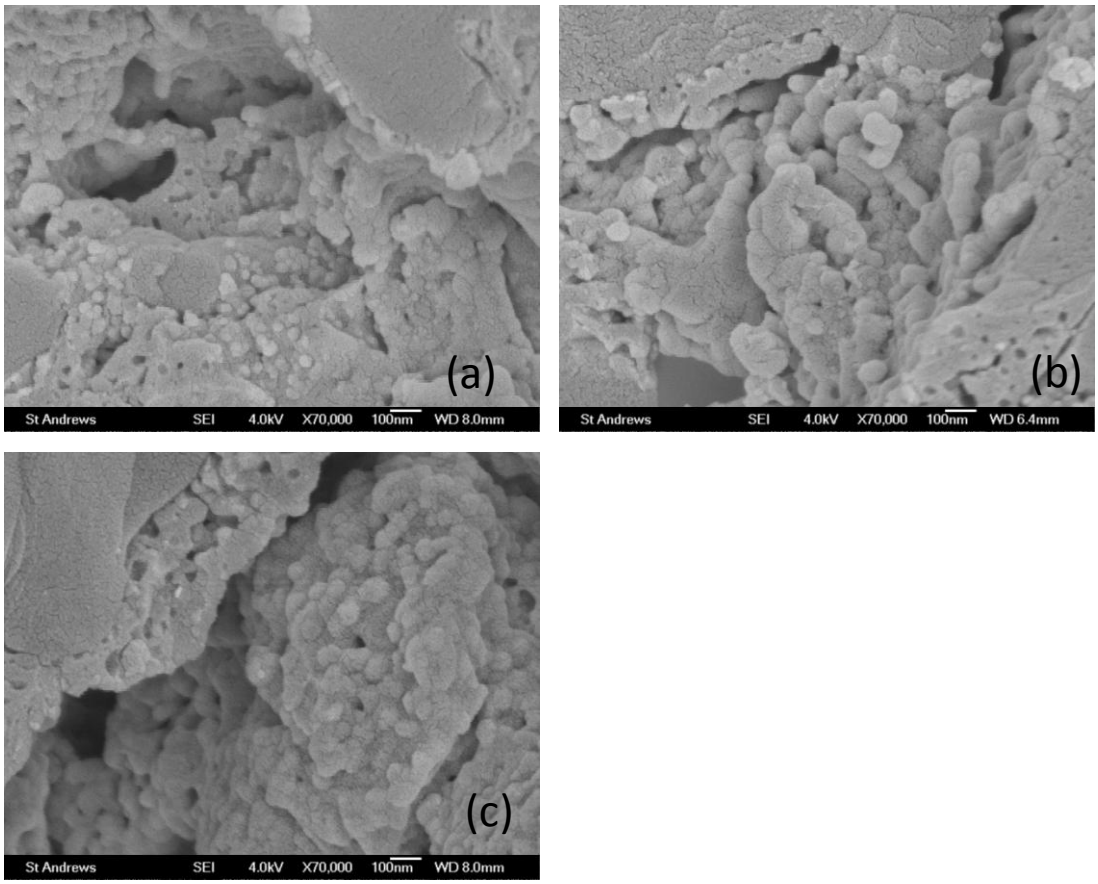

Figure 69 SEM images for the sample (a) Co_700, (b) Co_850_8hrs and (c) Co_850.

The sample with Co doping into the LSF_850 with a calcination at 700 ^{o}C is shown in Figure 69(a), and the cobalt oxide or its possible product with LSF can be easily singled out because of their extremely small grain size (20 nm). However, the small particles in (a) will grow after firing at 850 ^{o}C for four hours, as shown in Figure 69(b), where the grains on the surface are larger than 200 nm. The fast growth of grain could be rationalized by the low melting point of Co_3O_4, 895 ^{o}C, and the instability of the possible Co-doped LSCF perovskite. If the cobalt nitrate is impregnated into a LSF pre-calcined at 700 ^{o}C, the grains of the final product will agglomerate to produce a relatively dense surface with extraneous dopants, as shown in Figure 69 (c).

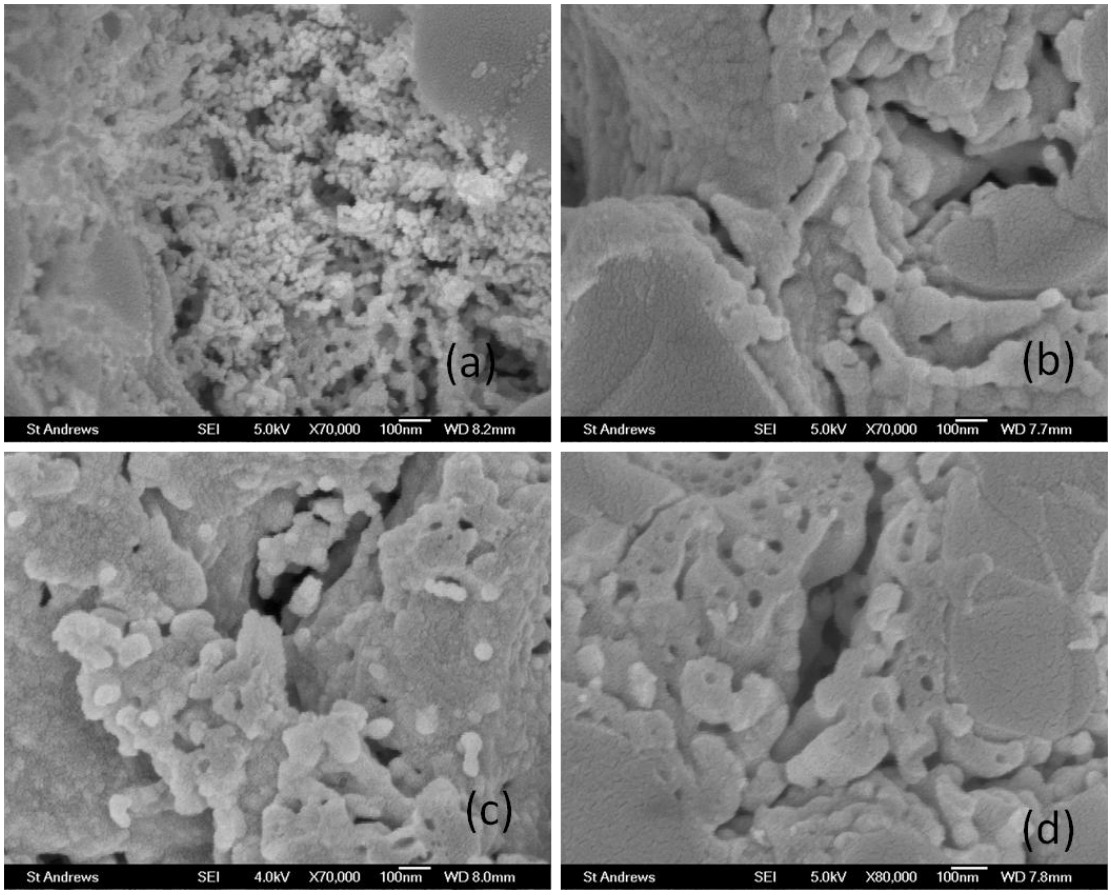

Figure 70 SEM images for the sample (a) Ni_700, (b,d) Ni_850_8hrs and (c) Ni_850.

The particles of NiO (Figure 70 (a)) on the surface of LSF with a pre-calcination at 850 ^{o}C are about 5 nm, much smaller than those of Co. Unfortunately, a further calcination of these particles at 850 ^{o}C causes severe growth on the surface of the LSF (Figure 70 (b, d)). Moreover, the doping of nickel in to the LSF perovskite is reported to enhance the sinterability [153,154]and thus the aggregation particles exceeding 100 nm can be easily observed on the surface, as shown in Figure 70 (d). With the sintering scheme Ni_850, the extrinsic Ni-containing species resides in the matrix of LSF to form a heterogeneous coating on YSZ scaffold, similar to the Co_850 sample.

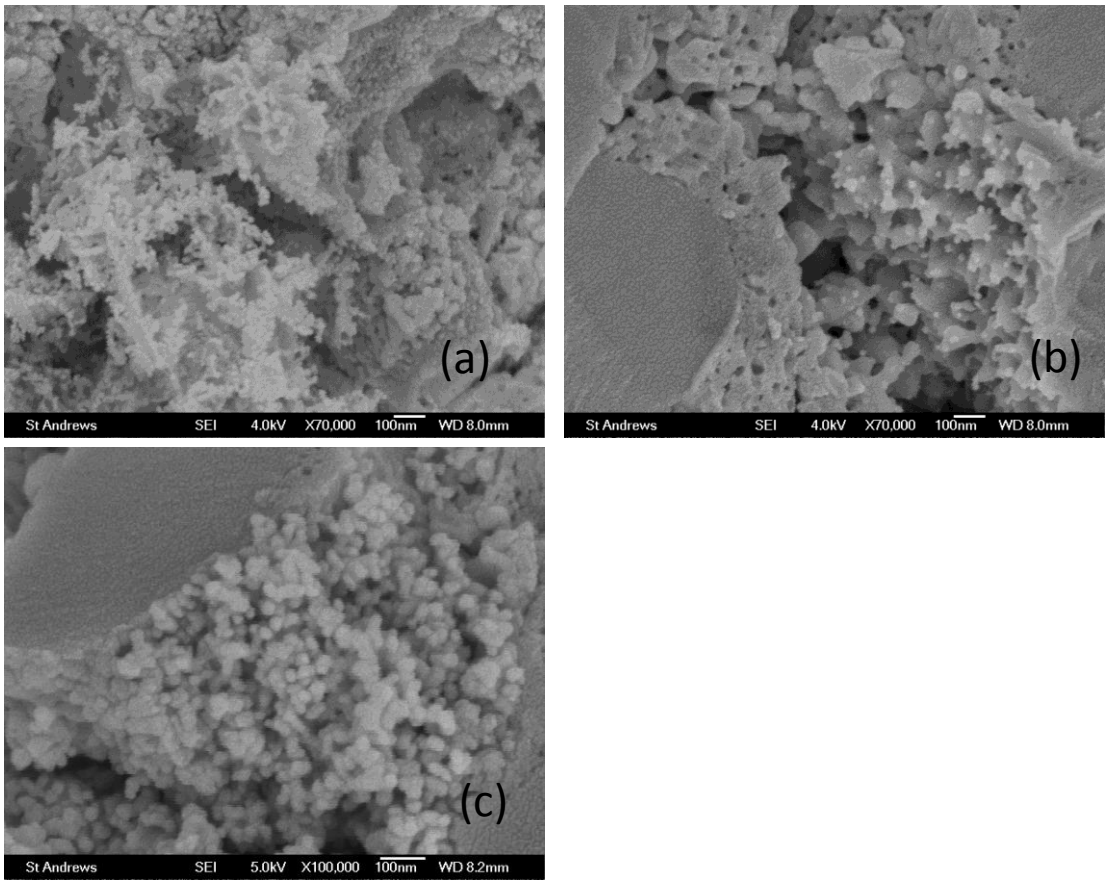

Figure 71 SEM images for the sample (a) Mn_700, (b) Mn_850_8hrs and (c) Mn_850.

The additional Mn impregnated into the LSF –YSZ scaffold will produce a coating containing the characteristic plate-like particles on the surface of LSF after being calcined at 850 ^{o}C (Figure 71(b)). The Mn-containing species hold their nanometric shape either when calcined at 700 ^{o}C (Figure 71(a)) or calcined at 850 ^{o}C (Figure 71(c)). The decomposition of manganese nitrate results in the formation of MnO_2 between 200-300 ^{o}C, then α-Mn_2O_3 between 500-550 ^{o}C and Mn_3O_4 at temperature above 800 ^{o}C[155]. The MnO_x (10 nm in diameter) particles at 700 ^{o}C either assembled to form whiskers in the pores or distributed on the surface of LSF particles. The calcination of MnO_x (α-Mn_2O_3 or Mn_3O_4 at 850 ^{o}C) of Mn_850_8hrs will produce a fairly dense film on the surface of LSF perovskite. For the Mn_850 sample, the particles show better thermal stability than LSF at 850 ^{o}C, and this could be a result of the incorporation of Mn into the LSF lattice.

10.3.3 Impedance measurement at 700 °C

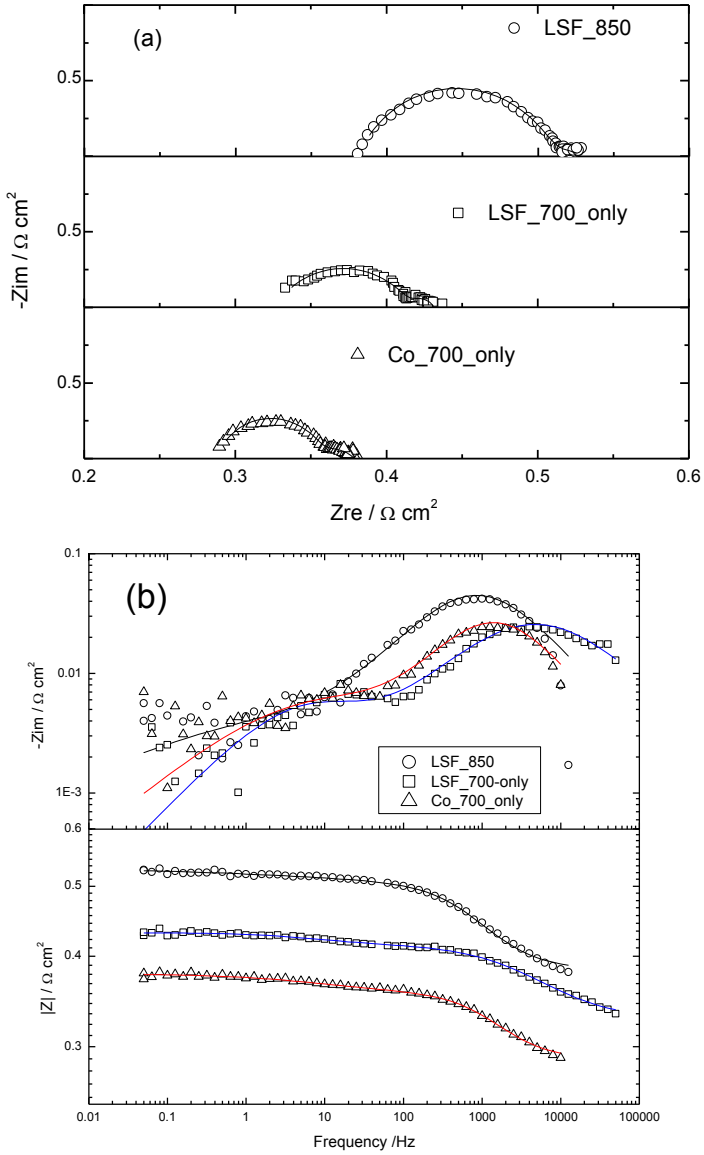

Figure 72 Nyquist (a) and Bode plots (b) of the symmetrical cell calcined at 700 °C only with or without Co doping; the electrode with LSF calcined at 850 °C is provided for comparison. The simulated data are plotted in lines.

Figure 72 shows the Nyquist plots of the symmetrical cell calcined at 700 °C with or without Co doping. The original data are normalized to the area and divided by a factor of 2 because there are two identical electrodes in series with each other. As a result, the R_s in the Nyquist will represent half of the ohmic resistance. Two arcs can be identified in the Nyquist plots; one at a characteristic frequency higher than 1000 Hz and the other at ca. 10 Hz as shown in the Frequency-Z_{im} plots.

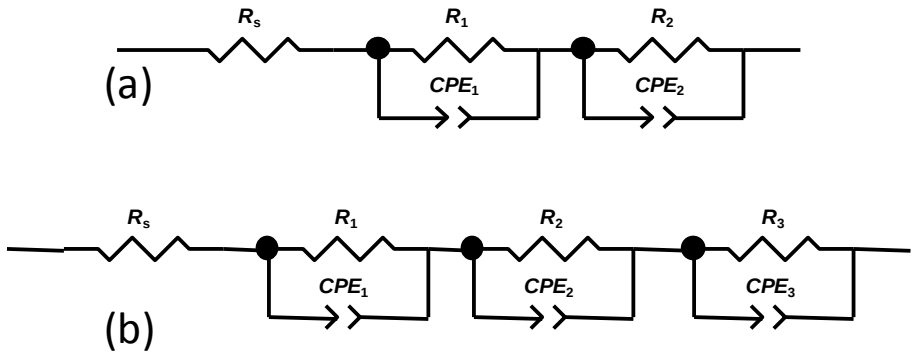

Figure 73 Graphic illustration of the equivalent circuits for R_s with two (a) or three (b) Voigt elements

In order to quantify the contribution of the impedance at different frequencies, a series resistance, R_s, in series with two Voigt elements (Figure 73 (a)) are used to simulate the impedance data and the parameters are shown in Table 8. Considering the obvious depression of the arcs in the impedance plots, constant phase elements (CPEs) are used to replace the capacitance for better simulation. The arc with a characteristic frequency of higher than 1000 Hz is represented by R_1 and CPE_1 and the arc at 10 Hz is represented by R_2 and CPE_2.

Table 8 Parameters from the simulation of the impedance data tested at 704 °C using the equivalent circuits containing two Voigt elements.

	Unit	LSF_700_only	Co_700_only	LSF_850
R_s	Ω cm^2	0.33	0.29	0.38
Y_1	Ω^{-1} s^{n}cm^2	1.28x10^{-2}	8.42x10^{-3}	1.14x10^{-2}
n_1		0.66	0.82	0.76
R_1	Ω cm^2	9.02x10^{-2}	6.82x10^{-2}	0.12
C_1	F cm^{-2}	3.94x10^{-4}	1.64x10^{-3}	1.42x10^{-3}
Y_2	Ω^{-1} s^{n}cm^2	4.99	5.18	16.31
n_2		0.69	0.54	0.28
R_2	Ω cm^2	1.52x10^{-2}	2.27x10^{-2}	2.97x10^{-3}
C_2	F cm^{-2}	1.57	0.84	6.79x10^{-3}

In Table 7, Y and n are parameters associated with a constant-phase element (CPE). The impedance of an CPE can be written as $Z_{CPE} = Y(j\omega)^{-n}$. The unit of Y can be either Ω^{-1} s^{n}cm^{2}or Fs$^{(n-1)}$cm^{-2} and the dimensionless n ranges from 0 to 1. When n=1, Y has units of a capacitance, i.e., F cm^{-2}, and represents the capacitance of the interface. The

distribution of physical properties in terms of structure, reactivity, dielectric constant and resistivity causes the deviation of n-value from 1. The exceptionally low n_1 value for the LSF_700_only sample could be explained by the rough particles/YSZ interface or possible impure phases thanks to low firing temperature. Because the arc at 1 kHz is generally associated with the charge transfer process in which the oxygen ions dissolve in the electrolyte possibly at the three phase boundary[126,144], R_1 is regarded as the charge transfer resistance and the double layer capacitance is represented by Y_1 and the n-value. The arc at 10 Hz is generally associated with the adsorption and surface diffusion process that may proceed through oxygen-vacancy transportation [156], and is quantified with the parameter R_2, Y_2 and n_2. The pseusocapacitance for each CPE is calculated from the expression as $C = (R^{1-n}Y_o)^{1/n}$. The R_s increases from 0.33 to 0.38 Ω cm^2 if the LSF-YSZ electrode is calcined from 700 ^{o}C to 850 ^{o}C, while the LSF_700_only sample decreases the R_s by 0.04 Ω cm^2, comparing to the LSF_700_only sample. These values are still higher than half of the calculated resistance of dense electrolyte, 0.22 Ω cm^2. The charge transfer resistance, R_1, shows the same trend among the three electrodes: LSF_850 > LSF_700_only > Co_700_only. The second arc for the LSF_850 sample is negligible because of the small value of R_2 and low n-value. R_2 for the Co_700_only sample is larger than that for the LSF_700_only sample, indicating the adsorption or surface diffusion of oxygen species plays a more important role in the Co-doping sample. The simulated pseudocapacitance value of the low frequency Voigt element for LSF_850 sample, C_2, is 6.79 x10^{-3} F cm^{-2}, one order of magnitude larger than the measure value of LSF dense layer on YSZ electrolyte [157]. However, the low n-value for the chemical capacitance, 0.28, indicates the leakage of current through the oxide/gas interface, so the assumption underlying the chemical capacitance, i.e. the oxygen ions transport through the LSF film, does not hold thanks to the universal existence of TPB. The C_2 values for the sample LSF_700_only and Co_700_only (about 1F cm^{-2}) are much higher than that of LSF_850. The high pseudocapacitance can be a result of the ionic diffusion in the perovskite, given the small grain size of the LSF particles on the surface of YSZ scaffold[2].

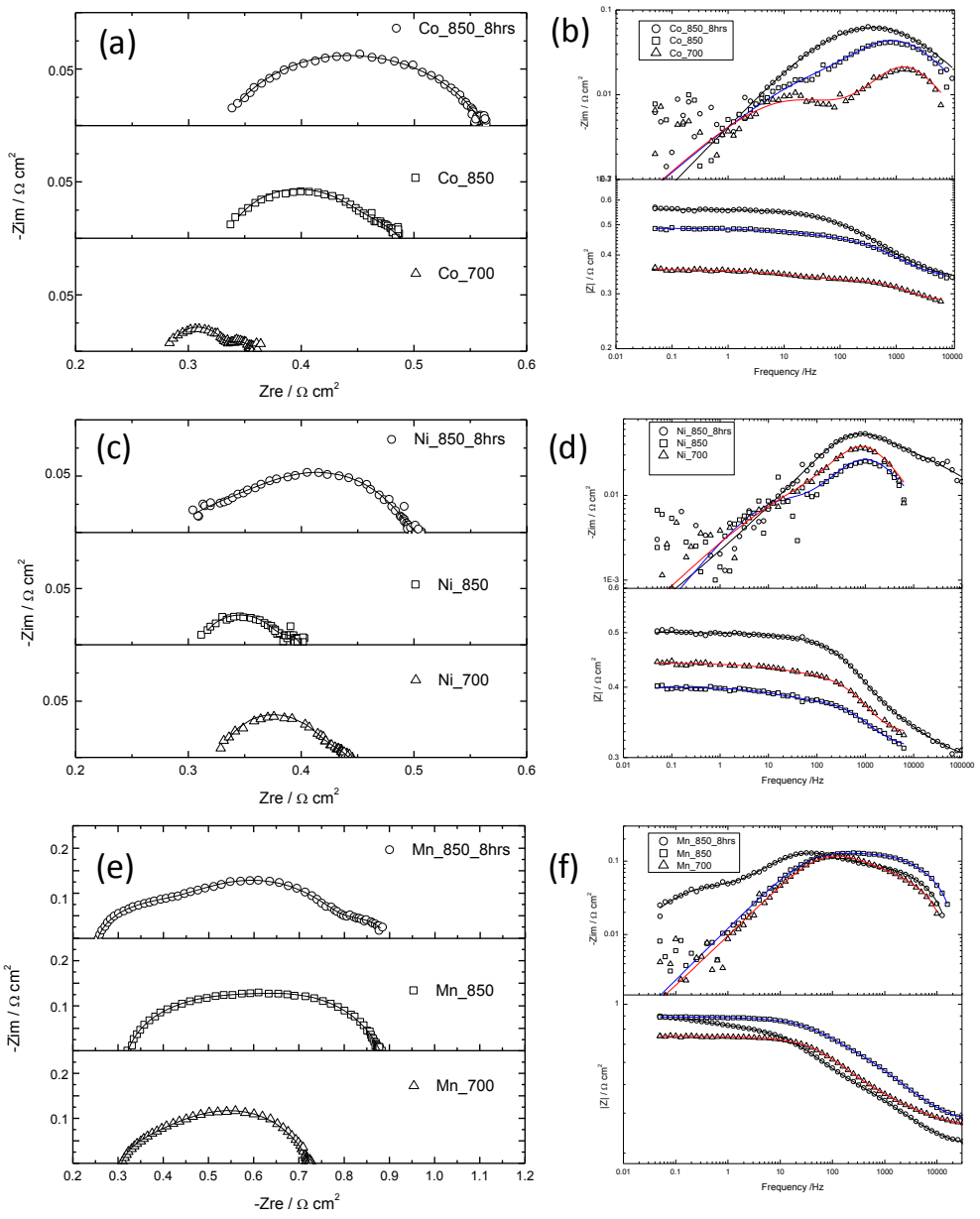

Figure 74 Nyquist and Bode plots of the symmetrical cell with Co, Ni Mn dopant from different calcinations schemes; testing temperature for Mn doped samples is 704 °C, and that for the rest is 700 °C. The simulated data are plotted in lines.

Table 9 Parameters from the simulation of the impedance data using the equivalent circuits shown in Figure 73

	R_s	Y_1	n_1	R_1	C_1	Y_2	n_2	R_2	C_2	Y_3	n_3	R_3	C_3
Unit	Ω cm^2	Ω^{-1} s^{n}cm^2		Ω cm^2	F cm^{-2}	Ω^{-1} s^{n}cm^2		Ω cm^2	F cm^{-2}	Ω^{-1} s^{n}cm^2		Ω cm^2	F cm^{-2}
LSF_850	0.38	1.14×10^{-2}	0.76	0.12	1.41×10^{-3}	16.31	0.28	2.97×10^{-3}	6.79×10^{-3}				
Co_700	0.28	4.85×10^{-3}	0.93	4.62×10^{-2}	2.51×10^{-3}	2.2	0.6	3.13×10^{-2}	0.37				
Co_850	0.33	9.86×10^{-3}	0.79	0.11	1.52×10^{-3}	0.98	0.56	4.51×10^{-2}	8.32×10^{-2}				
Co_850_8hrs	0.33	2.56×10^{-2}	0.66	0.19	1.63×10^{-3}	0.28	0.73	3.96×10^{-2}	5.45×10^{-2}				
Ni_700	0.33	5.63×10^{-3}	0.89	8.10×10^{-2}	2.21×10^{-3}	1.42	0.54	3.24×10^{-2}	0.11				
Ni_850	0.31	1.06×10^{-2}	0.82	6.76×10^{-2}	2.24×10^{-3}	1.95	0.69	2.17×10^{-2}	0.48				
Ni_850_8hrs	0.28	1.13×10^{-2}	0.84	8.35×10^{-2}	3.00×10^{-3}	6.94×10^{-2}	0.45	0.14	2.54×10^{-4}				
Mn_700[a]	0.31	7.15×10^{-3}	0.8	0.1	1.18×10^{-3}	2.44×10^{-2}	0.77	0.3	5.52×10^{-3}				
Mn_850[a]	0.33	1.59×10^{-3}	0.87	0.17	4.74×10^{-4}	2.84×10^{-2}	0.69	0.38	3.71×10^{-3}				
Mn_850_8hrs[a,b]	0.26	2.74×10^{-3}	0.87	0.11	7.99×10^{-4}	6.65×10^{-2}	0.64	0.45	9.22×10^{-3}	10.51	0.81	7.34×10^{-2}	9.87

[a]: testing temperature for Mn doped samples is 704 °C, and that for the rest is 700 °C.

[b]: an R_s with three serial Voigt elements (Figure 73(b)) are used for the simulation.

The Nyquist plots and Bode plots for the symmetrical cells tested at 700 ^{o}C or 704 ^{o}C in ambient air with Co, Ni or Mn doping from different calcinations schemes are presented in Figure 74. The R_p values for Dopant_850_8hrs are higher than the other two calcinations schemes. Moreover, for the Dopant_850 or Dopant_700 samples, two arcs can be identified very easily, but the visible arcs for Dopant_850-8-hrs samples depends on the impregnated materials: three arcs for the Mn-doping sample and one arc for the Co-doping sample.

Table 9 shows parameters of the data simulated with equivalent circuits containing an R_s with two or three serial Voigt elements as shown in Figure 73. Generally, the samples with dopants show lower R_s than the one without. Of the samples with the same dopant, the smallest R_s is from the Co_700, Mn_850_8hrs and Ni_850_8hrs sample. The capacitance for the arc at high frequency, above 1000 Hz, is around 1 mF cm^{-2} and n-value is higher than 0.66, depending on the infiltrated materials and calcinations schemes. The charge transfer resistance reaches the minimum of 46.2 mΩ cm^2 for the Co_700 sample but peaked at 0.19 Ω cm^2 if this sample was heated up to 850 ^{o}C for 4 hours (Co_850_8hrs).

The R_2 values for the Co-doping sample with calcinations at 850 ^{o}C vary in the range of 3.31-4.51x10^{-2} Ω cm^2, higher than the one with a maximum firing temperature at 700 ^{o}C (2.27x10^{-2} Ω cm^2). The Ni_700, Ni_850 and Co_700 sample shows small R_2 and high C_2 (ca. 1 F cm^{-2}), indicating the ionic diffusion through the surface or bulk plays an important role in the oxygen reduction reaction. The calcination at 850 ^{o}C of nickel oxide on the surface of LSF pre-calcined at 850 ^{o}C (Ni_LSF_8hrs sample) shows a similar R_2 and C_2 value to Mn-doping samples, suggesting the surface exchange could be the rate determining step for the Ni_850_8hrs and Mn-doped samples. The Nyquist plot for the Mn_850_8hrs sample is the only one with an arc showing a characteristic frequency of 1 Hz, indicating the diffusion of oxygen could be blocked by the fairly dense Mn oxide on the surface. The large pseudocapacitance of C_3 could indicate a process involved with the gas diffusion process in the porous structure. The value of R_2 for the Mn doped sample is 0.3 Ω cm^2 even calcined at a temperature as low as 700 ^{o}C, indicating a dramatic change of the surface of the electrode. The R_p value of Mn_700 sample is close to the LSM impregnated sample as reported[97,128,158].

10.3.4 Temperature dependence of the impedance

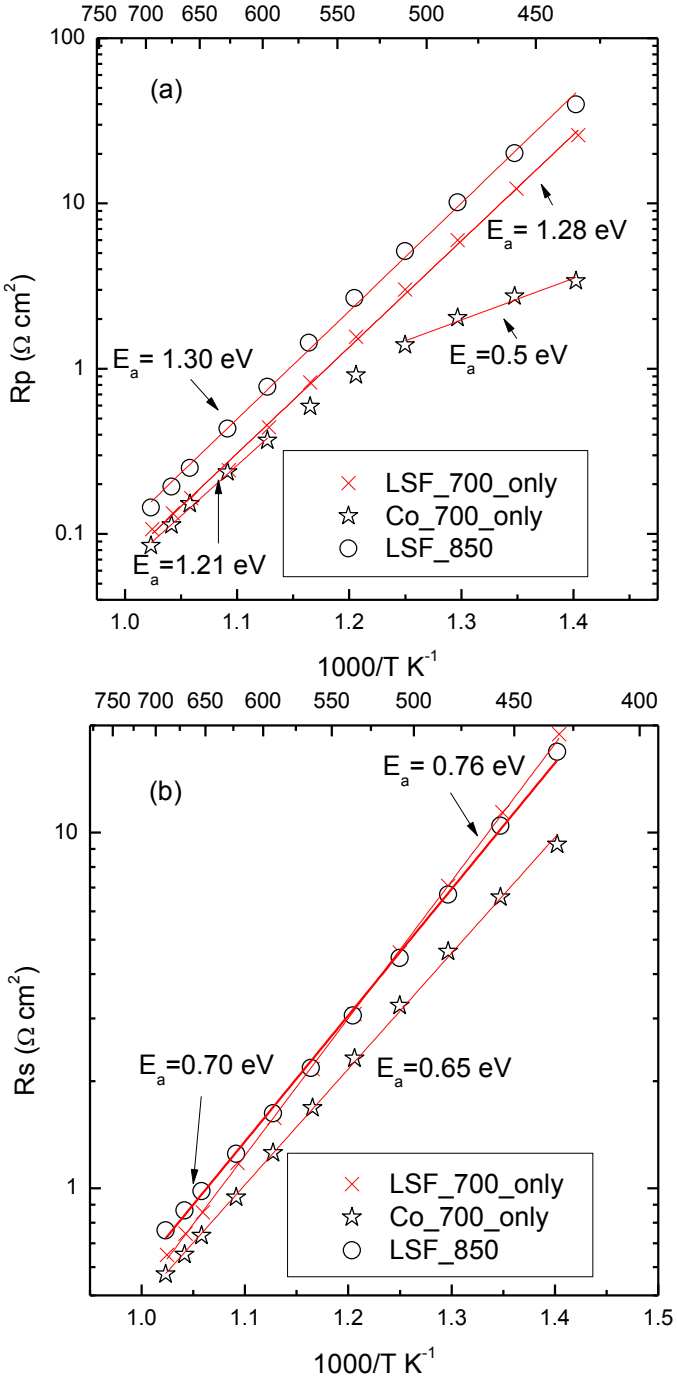

Figure 75 Arrhenius plots of the R_p (a) and R_s (b) of the LSF-YSZ electrode calcined at 700 °C only with and without Co doping in the temperature range between 439 and 700 °C. Data for the sample calcined at 850 °C without doping is provided for comparison.

In order to study the temperature dependence of R_p and R_s, the Arrhenius plots of the samples with and without Co doping are shown in Figure 75. The sample calcined at

700 ^{o}C shows similar R_s at 700 ^{o}C to the one calcined at 850 ^{o}C, but with higher activation energy (0.76 eV vs. 0.69 eV). The deviation of the activation energy of electrolyte from that of pure 8YSZ indicates that the thick electrode contributes to the series resistance. The activation energy for the resistivity of 8-YSZ is above 1 eV below 700 ^{o}C[159], but this value for $La_{0.8}Sr_{0.2}FeO_3$ is 0.09 eV in the temperature range between 400-800 ^{o}C[160]. The existence of strontium carbonate in the LSF_700_only sample is supposed to lower the conductivity of LSF and increase the activation energy, similar to the effect of the less conductive crystals in $La_{1-x}Sr_xFe_{0.6}Ni_{0.4}O_3$-δ (x=0.2 or 0.3)[161]. The higher conductivity for LSF_700_only could be a better interconnectivity of the LSF particles than the LSF_850 sample, since the A-site deficiency caused by the lacking of Sr in the perovskite is reported to decrease the conductivity at 700 ^{o}C[153]. With the doping of cobalt, the R_s decreases in the whole temperature range and shows lowest temperature dependence. The dramatic change of conductivity of electrode could be a result of the formation of Co-balt rich (La.Sr)(Co,Fe)$O_{3-\delta}$ perovskite, owing to the low-temperature firing [160].

The difference in heat treatment and doping changes not only the series resistance, but also the polarization resistance as shown in Figure 75 (b). The plots of R_p for the sample calcined at 700 ^{o}C and 850 ^{o}C are in good linearity with activation energies above 1.2 eV. In contrast, the plot of R_p for the sample with Co-doping shows obvious curvature in the low temperature range: the activation energy in the temperature range between 600 ^{o}C to 700 ^{o}C is 1.21 eV and that between 575 ^{o}C and 437 ^{o}C is 0.5 eV. The low calcination temperature will produce sufficient TPBs that the production of MIEC (LSC or LSCF) on the surface of LSF will cross-link the TPBs as alternative ionic and surface transport to the electrolyte, extension the reaction region. The dramatic change of activation of activation energy could result from the change of the rate determining step. The activation energies for the chemical diffusion coefficient and the surface exchange coefficient of $La_{0.5}Sr_{0.5}CoO_{3-\delta}$ as an example are 1.37 eV (133 kJ mol^{-1}) and 0.69 eV (67 kJ mol^{-1})[162], respectively. The comparable activation energy between the polarization resistance and that of the surface exchange coefficient could indicate that the oxygen ion could transfer through the surface of LSC as an alternative route other than YSZ or LSF at low temperature. The scattering particles of highly ionic conductive cobalt-containing perovskite at the short-distance extension from the electrolyte/electrode interface ser function as the fast O^{2-} transport

route[74]. At high temperature range (700 -600 ^{o}C), this improvement diminishes because the fast ionic conductance of YSZ.

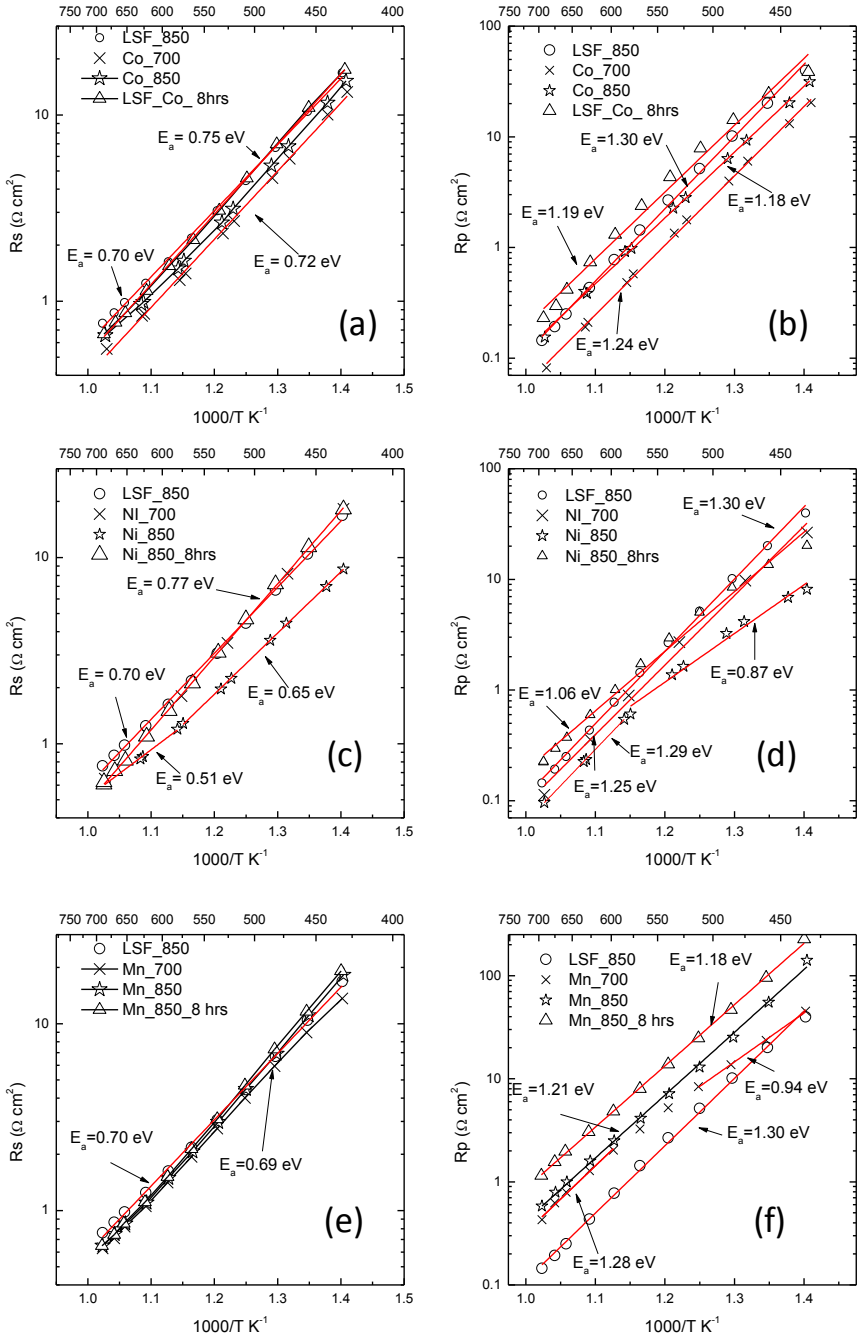

Figure 76 Arrhenius plots for the electrode with doping of Co, Ni and Mn using different calcinations process: (a, c, e) and (b, d, f) are the plots of R_s and R_p, respectively.

The temperature dependence of R_s and R_p for the electrodes with Mn, Co and Ni doping with calcinations at 850 ^oC is shown in Figure 76. The activation energies of R_s for the sample calcined at 850 ^oC are in a small range close to 0.70 eV, except for the sample of Ni_850. The R_s value is the combined resistance of electrolyte, the electrode and interface resistance. The resistance from electrolyte and interface are assumed to be invariant amongst all the samples and the former one shows activation energy of 1.0 eV. To be specific, the activation energies for the Co-doping samples are slightly higher than the one without doping. The Co_700 sample shows a set of obviously smaller R_s values than that of LSF_850, indicating the formation of conducting Co-containing perovskite because the conductivity of Co_3O_4 is negligible in relation to LSF. The conductivity of LSF and related materials at 700 ^oC is shown in Table 10. The improvement in R_s diminishes if the sample is calcined at 850 ^oC, a result of the further dissolution of Co into LSF that decreases the conductivity of thus formed perovskite[160]. The Ni_850 sample is the only firing scheme that changes the series resistance of LSF-YSZ electrode. The obvious drop of R_s is in temperature range between 439 -550 ^oC, but this improvement starting to decrease at higher temperature. The highly conductive Ni-rich $La(Ni,Fe)O_3$ perovskite shows typical high metallic conductivity [163] up to 500 S $cm^{-1}$and this can be used to explain the low activation energy of R_s. The doping of Mn slightly changes the R_s value and the activation energy because the doping of Mn into does show obvious conductivity improvement except for the high conductivity of LSM[164,165].

Table 10 Electronic conductivity, σ_e, and ionic conductivity, σ_i, at 700 °C. The activation energy of the electronic conductivity is also included.

	σ_e	E_a of σ_e	σ_i
Units	S cm^{-1}	eV	S cm^{-1}
YSZ[140]	-	-	0.0205
$La_{0.8}Sr_{0.2}FeO_3$[160,166]	80	0.09	8.30x 10^{-4}
$La_{0.8}Sr_{0.2}Fe_{0.8}Co_{0.2}O_3$[160]	100	0.14	-
$La_{0.8}Sr_{0.2}CoO_3$[160]	1.30x10^3	0.04	-
$La_{0.91}Sr_{0.09}Ni_{0.6}Fe_{0.4}O_3$[166,161]	385	0.045	4.90 x10^{-5}
$La_{0.8}Sr_{0.2}Fe_{0.9}Ni_{0.1}O_3$[167]	225	-	-
$LaNi_{0.6}Fe_{0.4}O_3$[161]	235	0.050	1.60 x10^{-6}
$La_{0.5}Sr_{0.5}Fe_{0.2}Ni_{0.8}O_3$[168]	400	Metallic above 600 °C	-
La_2NiO_4[169,170]	45	Metallic above 500 °C	>8YSZ
$La_{0.8}Sr_{0.2}MnO_3$[171]	160	0.09	<10^{-10}
$La_{0.8}Sr_{0.2}Fe_{0.5}Mn_{0.5}O_3$[165]	10	0.26	<10^{-10}

The addition of Co into the LSF-YSZ electrode with a further calcination at 850 °C (Co_850 or Co_850_8hrs sample) increases the R_p values in the whole temperature range, but the doped Co with calcination at 700 °C is beneficial to the decrease of R_p value. The activation energy of R_p for the Co doped sample is quite similar to that for the undoped sample in whole temperature range, but the addition of nickel changes the activation energy only at low temperature range, a similar observation in the Co_700_only sample. The Ni_850 sample shows low activation energy (0.87 eV) at the temperatures below 600 °C, but the activation energy increase to 1.25 eV in the temperature range of 600-700 °C, very close to that of LSF_850 sample. The ionic conductivity of perovskite $LaNi_{0.6}Fe_{0.4}O_3$ is two orders of magnitude lower than that of LSF, as indicated in Table 10[172], but will be increased one order of magnitude by the addition of Sr to the A-site. The formation of a highly ionic conductive Ruddlesden-Popper phases, e.g. La_2NiO_4[173,174,170], could be an explanation for the low activation energy and the improved performance at low temperature. The ionic conductivity of La_2NiO_4 is higher than that of 8YSZ[144], while the oxygen surface exchange coefficient is two-order of magnitude higher than that of $La_{0.6}Sr_{0.4}Co_{0.2}Fe_{0.8}O_3$[175]. The formation of $(La,Sr)_2(Ni,Fe)O_4$ is observed in perovskite

$La_{1-x}Sr_xNi_{0.6}Fe_{0.4}O_3$ (x>0.2) [161]. The respective activation energy of the bulk and surface oxygen ion diffusion is 0.85 eV and 1.61 eV for La_2NiO_4 and the slight doping (<10 at. %) of Fe in the place of Ni barely changes the oxygen exchange properties[174]. The high activation energies in this temperature range are also observed for the Mn-doped samples, but the R_p values for the Mn-doping samples are higher than the undoped sample in the whole temperature range, since the doping of Mn into LSF is detrimental to both the bulk and surface transport properties of oxygen ions[164].

10.4 Discussion

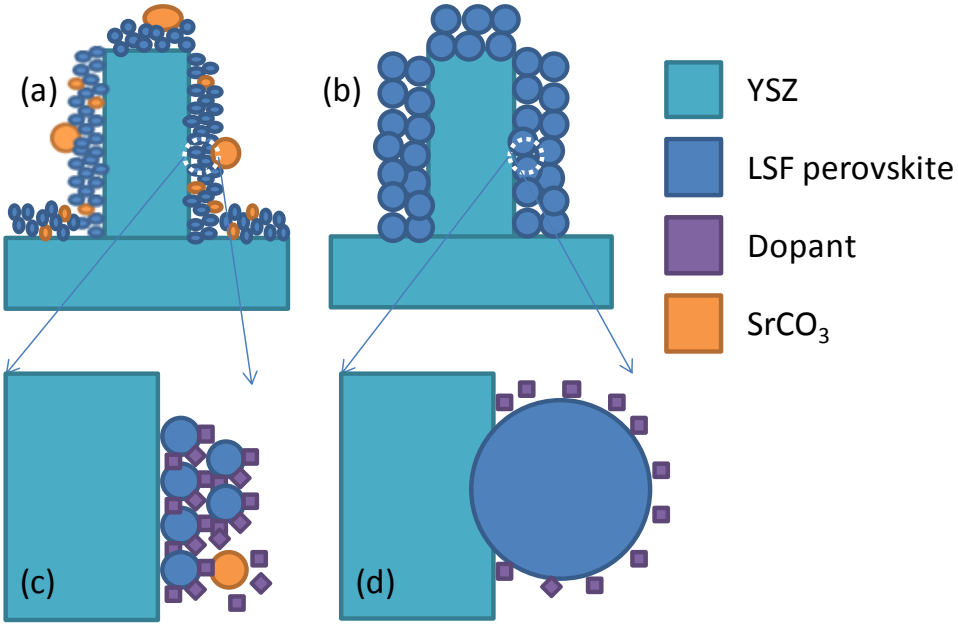

Figure 77 Schematic demonstration of the morphology of the LSF-YSZ electrode calcined at 700 °C (a, LSF_700_only) and 850 °C (b, LSF_850). (c) and (d) shows the morphology after the infiltration of nitrate precursors for MOx (M=Ni, Mn and Co) into the scaffold with a pre-calcination at 700 °C and 800 °C, respectively.

The calcination schemes are effective in changing the microstructure of LSF and the reactivity between the infiltrated content for LSF and oxide dopants. Figure 77 (a, b) shows the effect of calcination temperature on the microstructure and phase purity of un-doped LSF-YSZ electrode. The low calcination at 700 °C produces a fluffy LSF with fine grains scattered with unconsumed reactants, such as $SrCO_3$ or possible La_2O_3, while the LSF calcined at 850 °C shows much larger grains and intergranular pores. The addition of the oxide dopant in the secondary infiltration to a LSF nanostructure with a pre-calcination at 700 °C will induce better interaction with the

previously infiltrated LSF in terms of physical mixing and chemical reaction as shown in Figure 77 (c).

The second infiltration of oxide dopant shows significant effect on the microstructure of the final composite electrode. The addition of doping oxides to LSF_850 sample will produce a fine-structured surface with calcination at 700 ^{o}C, but induce severe grain growth after heat treatment at 850 ^{o}C. However, the microstructure of the dopants in LSF_700_only sample differs after the calcination at 850 ^{o}C with each other: the addition of cobalt and nickel tends to induce the formation of dense film after calcination at 850 ^{o}C, but the Mn_850 sample shows an improvement in the thermal stability due to the doping of Mn into the lattice of LSF.

The performance of electrode depends on both the microstructure and the property of dopant. Fine CoO_x particles on surface of LSF tend to enhance the performance, but annealing will diminish this advantage, due to the change of microstructure and composition of the possible composition change. In contrast, the fairly dense coating in Ni_850 sample gives better performance than LSF_850. With very fine grains on the surface of YSZ, the sample Mn_700 and Mn_850 unexpectedly shows worse performance than LSF_850 sample

The initial calcination of LSF before the addition of dopants is very important in determining their interaction. On the one hand, the annealing of LSF at 850 ^{o}C decreases the surface area that the dopants will sit on and possibly the leftover reactant (La/Sr) for new perovskite. On the other hand, the surface of $La_{0.8}Sr_{0.2}FeO_3$ annealed at 800 ^{o}C always deviates from the stoichiometric composition and turns to be B-site deficient[157,176], with a ratio of La/Sr close to the bulk perovskite. The surface reaction between the enriched La/Sr on the surface for the LSF annealed at 850 ^{o}C and the doping oxide can alter the surface diffusion of the oxygen species by forming new perovskite[177]. This explains why Mn_700 sample is able to change the surface reaction without changing the charge transfer resistance, indicating the possible deposit of Mn on TPB is not very high.

The product of the surface reaction between the dopant and LSF shows obvious link to the performance of the electrode, in terms of ionic conductivity and surface stability. The interactions between the doping oxide and the LSF pre-calcined at 850 ^{o}C involve the incorporation of B site into the lattice of stoichiometric perovskite, a process of producing A-site deficiency. The A-site deficiency in $(La_{1-x}Sr_x)_yFeO_3$ has

been shown to be meta-stable when x is less than 0.4[178]. To make things complex, the degree of A-site deficiency is dependent on the B-site; a high content of Ni is involved in the B-site, the tolerance of A-site deficiency is very low[176]. If multiple phases are assumed, the substitution of the B-site dopant for Fe in LSF could result in iron-rich oxide. According to the enthalpy of formation of $LaMO_3$ (M=Mn, Fe, Co, Ni)[177,179] from elements, the stability is in the sequence of $LaMnO_3$ > $LaFeO_3$ > $LaCoO_3$ > $LaNiO_3$ at 25 ^oC. However, the interaction between the dopant oxide and the LSF calcined at 850 ^oC is controlled by the diffusion kinetics. Cobalt is the only element that homogenizes over a 48-nm diffusion couple of $La_{0.85}Sr_{0.15}MnO_3$-$La_{0.6}Sr_{0.4}Co0_{.2}Fe_{0.8}O_3$ after 900 h at 850 ^oC, and the interdiffusion zone for Mn, Fe, La and Sr is confined within 10 nm[146]. The fast mobility of Co for Co_850_8hrs sample could result in cobalt-containing perovskite and oxides (Fe_2O_3 and Co_3O_4 or even Co-Fe spinels) that tend to grow in grain size. The growth of grains is surely to decrease the TPB where the charge transfer takes places, and thus increases the charge transfer resistance. The Ni_850_8hrs and Mn_850_8hrs sample shows large R_2 and small C_2, a paradigm that surface diffusion of oxygen species is blocked by the Ni- or Mn- doped LSF with low surface exchange coefficient or excessive densified NiO and MnOx. These blocking effects can even induce gas diffusion impedance as Mn_850_8hrs, but the charge transfter resistance at around 700 ^oC is not affected, compared with Mn_700 sample.

10.5 Conclusions

Dopants including Co, Ni and Mn have been used a dopants to modify the performance of the infiltrated LSF-YSZ nanostructure cathode for solid oxide fuel cell. The pre-calcination of LSF_YSZ before the impregnation of the dopants controls the phase purity of LSF and structure of the final structure by altering the distribution of nitrate solution. The infiltration of Co or Ni nitrate into LSF precalcined at 700 ^oC, followed by respective secondary calcinations at 700 ^oC or 850 ^oC, improves the low-temperature (below 500 ^oC) performance of LSF_YSZ electrode dramatically. This improvement can be a result of the high ionic conductivity of $(LaSr)CoO_3$- or La_2NiO_4-related materials.

The additions of dopants alter the morphology of the perovskite lying on the YSZ scaffold. The sintering of Co- or Ni- doped samples at 850 ^oC tends to produce a layer of oxide with large grains, while the doping of Mn into LSF precalcined at 700 ^oC is

able to stabilize the nanostructure even if being finally fired at 850 ^{o}C. The increase of charge transfer resistance is associated with (1) grain growth as in Co_850_8hrs sample and (2) surface modification as in Mn_850 ^{o}C sample. For an electrode of 165-μm thickness electrode, the lateral resistance can be an issue and the formation of Ni- or Co-containing perovskite is able to decrease the series resistance effectively.

Conclusion

The design of SOFC requires consideration of many factors. The work presented in this dissertation demonstrates and raises a number of important issues for the future development of infiltration as a method to fabricate high performance solid oxide fuel cells. The fabrication and testing of large-scale fuel cells via infiltration makes the fabrication of scaffold the first priority, which is neglected very often in testing of button cells. Both the macrostructure and microstructure of the scaffold are important in determining the quality of the thus produced fuel cell. The preparation of porous/dense/porous sandwich from the same materials alleviates the demand on sinterability and thermal expansion coefficient, but it raises requirement on the porosity and orientation of the pores. To further the study on the performance of the electrode prepared via infiltration, the microstructures of cathodes prepared with infiltration are studied with image analysis and doping of transition metal oxides.

Five chapters are concerned with the scalability of the making of fuel cells out of infiltration method. The scalability of infiltration is demonstrated with four configurations of varied thickness in electrolyte and electrodes. Electrolyte-supporting thin porous films are infiltrated to make a fuel cell with nanostructure electrodes. Techniques are developed to fabricate thin supported electrolyte on porous structure by considering the mechanical stability and flatness of the scaffold. Results show that identical porous structures sandwiching the electrolyte are efficient in decreasing the diffusional losses from the thick cathode or the ohmic losses from a thick anode. Methane is also used as fuel apart from hydrogen, the deposition of carbon can be inferred from the change of ohmic resistance of the thick LSV_{red}-ceria-Ni/Pd electrode. (Chapter 3-7)

Microstructures of the porous structure are intensively studied to understand the change of pores during the sintering process in respect of scales and stages. Modelling shows that the texturing of the porous structure containing plate-like pores /PFAs tends to intensify immediately after the deposition of viscous ink on the substrate, if transport of the material in the sintering process is insignificant in changing the shape. The inks made from pure YSZ as ceramic, with graphite or glassy carbon are used to detect the change of microstructure at different stages and scales. (Chapter 8)

The processing of infiltrated porous scaffolds is quantified to establish a correlation between the particle size distribution of the raw powder and the performance of the

infiltrated electrodes. The quantification of the edge length of a 2-D SEM image is advisable in determining the TPB for reaction. The YSZ powder with bi-modal particle size distribution is worse in creating long surface edges and finally results in an inferior electrochemical performance of the infiltrated electrode. (Chapter 9)

Chapter 10 is devoted to study the effect of doping transition metal oxide on the performance of LSF/YSZ electrode. The microstructure and phase purity of the electrodes calcined at 700 ^{o}C and 850 ^{o}C are correlated to the performance of LSF/YSZ electrode. The addition of nickel increases the conductivity of the electrode and polarisation resistance only after well-mixing with LSF with firing at 850 ^{o}C, but the nanostructure of cobalt oxide fired at 700 ^{o}C provide highest conductivity and electrode performance.(Chapter 10)

References

[1] Fuel cell handbook 7th edition. . U.S. Department of Energy; 2004.

http://www.netl.doe.gov/technologies/coalpower/fuelcells/seca/pubs/FCHandbook7.pdf.

[2] S. B. Adler, "Factors Governing Oxygen Reduction in Solid Oxide Fuel Cell Cathodes." *Chem. Rev.*, **104**[10]: 4791-4844 (2004).

[3] F. Bidrawn, S. Lee, J. M. Vohs, and R. J. Gorte, "The Effect of Ca, Sr, and Ba Doping on the Ionic Conductivity and Cathode Performance of $LaFeO_3$," J. Electrochem. Soc.,**155**[7] B660-B65 (2008).

[4] S. M. Haile, "Materials for fuel cells," *Materials Today*,**63** 24-29 (2003).

[5] M. Mogensen, N. M. Sammes, and G. A. Tompsett, "Physical, chemical and electrochemical properties of pure and doped ceria," *Solid State Ionics*,**129**[1-4] 63-94 (2000).

[6] T. Ishihara, T. Shibayama, M. Honda, H. Nishiguchi, and Y. Takita, "Transition metal doped $LaGaO_3$ perovskite fast oxide ion conductor and intermediate temperature solid oxide fuel cell," pp. 283-94. in New Materials for Batteries and Fuel Cells, Vol. 575. *Materials Research Society Symposium Proceedings.* Edited by D. H. Doughty, L. F. Nazar, M. Arakawa, H. P. Brack, and K. Naoi, 2000.

[7] Z. Janusz, Ł. Iwona, B.-P. Ewa, andM. Beata, "Low temperature growth of carbon nanotubes from methane catalytic decomposition over nickel supported on a zeolite," *Nanotechnology*,**21**[14] 145308 (2010).

[8] R. T. K. Baker, "Catalytic growth of carbon filaments," *Carbon*,**273** 315-23 (1989).

[9] W. Wang, C. Su, Y. Wu, R. Ran, and Z. Shao, "Progress in Solid Oxide Fuel Cells with Nickel-Based Anodes Operating on Methane and Related Fuels," *Chem. Rev. (Washington, DC, U. S.)*, (2013). Doi: 10.1021/cr300491e

[10] S. McIntosh, "Development of direct hydrocarbon solid oxide fuel cells," pp.29 in, Ph.D thesis. University of Pennsylvania, 2004.

[11] S. Park, J. M. Vohs, and R. J. Gorte, "Direct oxidation of hydrocarbons in a solid-oxide fuel cell," *Nature*,**404**[6775] 265-67 (2000).

[12] M. C. Tucker, G. Y. Lau, C. P. Jacobson, S. J. Visco, and L. C. De Jonghe, "Cu–YSZ cermet solid oxide fuel cell anode prepared by high-temperature sintering," *J. Power Sources*,**195**[10] 3119-23 (2010).

[13] S. Jung, C. Lu, H. He, K. Ahn, R. J. Gorte, and J. M. Vohs, "Influence of composition and Cu impregnation method on the performance of Cu/CeO_2/YSZ SOFC anodes," *J. Power Sources*,**154**[1] 42-50 (2006).

[14] P. I. Cowin, C. T. G. Petit, R. Lan, J. T. S. Irvine, and S. Tao, "Recent Progress in the Development of Anode Materials for Solid Oxide Fuel Cells,"*Adv. Energy Mater.*,**1**[3] 314-32 (2011).

15 S. Tao and J. T. S. Irvine, "Discovery and characterization of novel oxide anodes for solid oxide fuel cells,"*Chem. Rec.*,**4**[2] 83-95 (2004).

[16] S. W. Tao and J. T. S. Irvine, "Synthesis and characterization of $(La_{0.75}Sr_{0.25})Cr_{0.5}Mn_{0.5}O_{3-\delta}$, a redox-stable, efficient perovskite anode for SOFCs," *J. Electrochem. Soc.*,**151**[2] A252-A59 (2004).

[17] H. He, Y. Huang, J. Regal, M. Boaro, J. M. Vohs, and R. J. Gorte, "Low-Temperature Fabrication of Oxide Composites for Solid-Oxide Fuel Cells," *J. Am. Ceram. Soc.*,**87**[3] 331-36 (2004).

[18] E. D. Wachsman and K. T. Lee, "Lowering the Temperature of Solid Oxide Fuel Cells," *Science*,**334** 935-39 (2011).

[19] http://www.gwent.org/gem_screen_printing.html

[20] R.E. Mistler and E. R. Twiname, Tape casting: Theory and Practice, The American Ceramic Society, Ohio, 2000

[21] O. Yamamoto, Y. Takeda, R. Kanno, and M. Noda, "Perovskite-type oxides as oxygen electrodes for high temperature oxide fuel cells," *Solid State Ionics,***22**[2-3] 241-46 (1987).

[22] J. R. Smith, A. Chen, D. Gostovic, D. Hickey, D. Kundinger, K. L. Duncan, R. T. DeHoff, K. S. Jones, and E. D. Wachsman, "Evaluation of the relationship between cathode microstructure and electrochemical behavior for SOFCs," *Solid State Ionics,***180**[1] 90-98 (2009).

[23] J. M. Vohs and R. J. Gorte, "High-performance SOFC cathodes prepared by infiltration," *Adv. Mater. (Weinheim, Ger.),***21**[9] 943-56 (2009).

[24] R. J. Gorte and J. M. Vohs, "Nanostructured anodes for solid oxide fuel cells," *Curr. Opin. Colloid Interface Sci.,***14**[4] 236-44 (2009).

[25] S. P. Jiang, "Nanoscale and nano-structured electrodes of solid oxide fuel cells by infiltration: Advances and challenges," *Int. J. Hydrogen Energy,***37**[1] 449-70 (2012).

[26] P. I. Cowin, C. T. G. Petit, R. Lan, J. T. S. Irvine, and S. Tao, "Recent Progress in the Development of Anode Materials for Solid Oxide Fuel Cells," *Adv. Energy Mater.,***1**[3] 314-32 (2011).

[27] W W. Wang, M. D. Gross, J. M. Vohs, and R. J. Gorte, "The Stability of LSF-YSZ Electrodes Prepared by Infiltration," *J. Electrochem. Soc.,***154**[5] B439-B45 (2007).

[28] R. Küngas, J.-S. Kim, J. M. Vohs, and R. J. Gorte, "Restructuring Porous YSZ by Treatment in Hydrofluoric Acid for Use in SOFC Cathodes," *J. Am. Ceram. Soc.,***94**[7] 2220-24 (2011).

[29] R. Kungas, J. M. Vohs, and R. J. Gorte, "Effect of the Ionic Conductivity of the Electrolyte in Composite SOFC Cathodes," *J. Electrochem. Soc.,***158**[6] B743-B48 (2011).

[30] S. B. Adler, "Factors Governing Oxygen Reduction in Solid Oxide Fuel Cell Cathodes†," *Chem. Rev. (Washington, DC, U. S.),***104**[10] 4791-844 (2004).

[31] G. Corre, G. Kim, M. Cassidy, J. M. Vohs, R. J. Gorte, and J. T. S. Irvine, "Activation and Ripening of Impregnated Manganese Containing Perovskite SOFC Electrodes under Redox Cycling," *Chem. Mater.,***21**[6] 1077-84 (2009).

[32] J.-S. Kim, V. V. Nair, J. M. Vohs, and R. J. Gorte, "A study of the methane tolerance of LSCM–YSZ composite anodes with Pt, Ni, Pd and ceria catalysts," *Scr. Mater.,***65**[2] 90-95 (2011).

[33] G. Kim, S. Lee, J. Y. Shin, G. Corre, J. T. S. Irvine, J. M. Vohs, and R. J. Gorte, "Investigation of the Structural and Catalytic Requirements for High-Performance SOFC Anodes Formed by Infiltration of LSCM," *Electrochem. Solid-State Lett.*,**12**[3] B48-B52 (2009).

[34] J. Chen, F. Liang, D. Yan, J. Pu, B. Chi, S. P. Jiang, and L. Jian, "Performance of large-scale anode-supported solid oxide fuel cells with impregnated $La_{0.6}Sr_{0.4}Co_{0.2}Fe_{0.8}O_{3-\delta}+Y_2O_3$ stabilized ZrO_2 composite cathodes," *J. Power Sources*,**195**[16] 5201-05 (2010).

[35] S. Tao and J. T. S. Irvine, "A redox-stable efficient anode for solid-oxide fuel cells," *Nat. Mater.*,**2**[5] 320-23 (2003).

[36] X. Yue and J. T. S. Irvine, "Impedance Studies on LSCM/GDC Cathode for High Temperature CO_2 Electrolysis," *Electrochem. Solid-State Lett.*,**15**[3] B31-B34 (2012).

37 Y. Huang, J. M. Vohs, and R. J. Gorte, "Fabrication of Sr-Doped $LaFeO_3$ YSZ Composite Cathodes," *J. Electrochem. Soc.*,**151**[4] A646-A51 (2004).

[38] S. P. Jiang, "Resistance Measurement in Solid Oxide Fuel Cells," *J. Electrochem. Soc.*,**148**[8] A887-A97 (2001).

[39] G. Kim, G. Corre, J. T. S. Irvine, J. M. Vohs, and R. J. Gorte, "Engineering composite oxide SOFC anodes for efficient oxidation of methane," *Electrochem. Solid-State Lett.*,**11**[2] B16-B19 (2008).

[40] M. D. Gross, J. M. Vohs, and R. J. Gorte, "An examination of SOFC anode functional layers based on ceria in YSZ," *J. Electrochem. Soc.*,**154**[7] B694-B99 (2007).

[41] W. G. Bessler, "Gas Concentration Impedance of Solid Oxide Fuel Cell Anodes," *J. Electrochem. Soc.*,**153**[8] A1492-A504 (2006).

[42] D. M. Bastidas, S. Tao, and J. T. S. Irvine, "A symmetrical solid oxide fuel cell demonstrating redox stable perovskite electrodes," *J. Mater. Chem.*,**16**[17] 1603-05 (2006).

[43] J. S. Kim, N. L. Wieder, A. J. Abraham, M. Cargnello, P. Fornasiero, R. J. Gorte, and J. M. Vohs, "Highly Active and Thermally Stable Core-Shell Catalysts for Solid Oxide Fuel Cells," *J. Electrochem. Soc.*,**158**[6] B596-B600 (2011).

[44] A. S. Thorel, "Tape Casting Ceramics for high temperature Fuel Cell applications," pp. 49-67. in Ceramic materials**.** Edited by W. Wunderlich. Sciyo, Croatia, 2010.

[45] Z. Shen, X. Zhu, S. Le, W. Sun, and K. Sun, "Co-sintering anode and Y_2O_3 stabilized ZrO_2 thin electrolyte film for solid oxide fuel cell fabricated by co-tape casting," *Int. J. Hydrogen Energy*,**37**[13] 10337-45 (2012).

[46] R. K. Bordia and A. Jagota, "Crack Growth and Damage in Constrained Sintering Films," *J. Am. Ceram. Soc.*,**76**[10] 2475-85 (1993).

[47] K. Huang and S. C. Singhal, "Cathode-supported tubular solid oxide fuel cell technology: A critical review," *J. Power Sources*,**237**[0] 84-97 (2013).

[48] X.-M. Ge, S.-H. Chan, Q.-L. Liu, and Q. Sun, "Solid Oxide Fuel Cell Anode Materials for Direct Hydrocarbon Utilization," *Adv. Energy Mater.*,**2**[10] 1156-81 (2012)

[49] B. H. Smith and M. D. Gross, "A Highly Conductive Oxide Anode for Solid Oxide Fuel Cells," Electrochem.. *Solid State Let.*,**14**[1] B1-B5 (2011).

[50] Q. Liu, X. Dong, G. Xiao, F. Zhao, and F. Chen, "A novel electrode material for symmetrical SOFCs," *Adv. Mater. (Weinheim, Ger.)*,**22**[48] 5478-82 (2010).

[51] A. Atkinson, S. Barnett, R. J. Gorte, J. T. S. Irvine, A. J. McEvoy, M. Mogensen, S. C. Singhal, and J. Vohs, "Advanced anodes for high-temperature fuel cells," *Nat. Mater.*,**3**[1] 17-27 (2004).

[52] Y.-P. Xiong, H. Kishimoto, K. Yamaji, M. Yoshinaga, T. Horita, M. E. Brito, and H. Yokokawa, "Electronic conductivity of pure ceria," *Solid State Ionics*,**192**[1] 476-79 (2011).

[53] D. Marrocchelli, S. R. Bishop, H. L. Tuller, and B. Yildiz, "Understanding Chemical Expansion in Non-Stoichiometric Oxides: Ceria and Zirconia Case Studies," *Adv. Funct. Mater.*,**22**[9] 1958-65 (2012).

[54]C. Zhang, M. E. Grass, A. H. McDaniel, S. C. DeCaluwe, F. E. Gabaly, Z. Liu, K. F. McCarty, R. L. Farrow, M. A. Linne, Z. Hussain, G. S. Jackson, H. Bluhm, and B. W. Eichhorn, "Measuring fundamental properties in operating solid oxide electrochemical cells by using in situ X-ray photoelectron spectroscopy," *Nat. Mater.*,**9**[11] 944-49 (2010).

[55] C. Zhang, M. E. Grass, Y. I. Yu, K. J. Gaskell, S. C. DeCaluwe, R. Chang, G. S. Jackson, Z. Hussain, H. Bluhm, B. W. Eichhorn, and Z. Liu, "Multi-element Activity Mapping and Potential Mapping in Solid Oxide Electrochemical Cells through the use of operando XPS," *ACS Catalysis,* **2**[11] 2297-304 (2012).

[56] W. C. Chueh, Y. Hao, W. Jung, and S. M. Haile, "High electrochemical activity of the oxide phase in model ceria–Pt and ceria–Ni composite anodes," *Nat. Mater.,***11** 155-61 (2011).

[57] M. Søgaard, P. Vang Hendriksen, and M. Mogensen, "Oxygen nonstoichiometry and transport properties of strontium substituted lanthanum ferrite," *J. Solid State Chem.,* **180**[4] 1489-503 (2007).

[58] M. Martin, "Oxygen Potential Gradient Induced Degradation of Oxides," *J. Korean Ceram. Soc.*,**49**[1] 29-36 (2012).

[59]T. Z. Sholklapper, C. P. Jacobson, S. J. Visco, and L. C. De Jonghe, "Synthesis of Dispersed and Contiguous Nanoparticles in Solid Oxide Fuel Cell Electrodes," *Fuel Cells*,**8**[5] 303-12 (2008).

[60] S. McIntosh and R. J. Gorte, "Direct hydrocarbon solid oxide fuel cells," *Chem. Rev. (Washington, DC, U. S.),***104**[10] 4845-65 (2004).

[61] S. C. Singhal and K. Kendall, "High-temperature Solid Oxide Fuel Cells: Fundamentals, Design and Applications: Fundamentals, Design and Applications," pp. 406. Elsevier, (2003).

[62] S. H. Chan, K. A. Khor, and Z. T. Xia, "A complete polarization model of a solid oxide fuel cell and its sensitivity to the change of cell component thickness," *J. Power Sources*,**93**[1–2] 130-40 (2001).

[63] J.-S. Park, J. Luo, L. Adijanto, J. M. Vohs, and R. J. Gorte, "The stability of lanthanum strontium vanadate for solid oxide fuel cells," *J. Power Sources,***222**[0] 123-28 (2013).

[64] X. M. Ge and S. H. Chan, "Lanthanum Strontium Vanadate as Potential Anodes for Solid Oxide Fuel Cells," *J. Electrochem. Soc.,***156**[3] B386-B91 (2009).

[65] M. Sayer, P. Chen, R. Fletcher, andA. Mansingh, "The metal-insulator transition in lanthanum strontium vanadate," *Journal of Physics C: Solid State Physics,***8**[13] 2059 (1975).

[66] M. Kestigian, J. G. Dickinson, andR. Ward, "Ion-deficient Phases in Titanium and Vanadium Compounds of the Perovskite Type1,2," *J. Am. Chem. Soc.,***79**[21] 5598-601 (1957).

[67] W. Y. Lee, J. Hanna, and A. F. Ghoniem, "On the Predictions of Carbon Deposition on the Nickel Anode of a SOFC and Its Impact on Open-Circuit Conditions," J. Electrochem. Soc.,**160**[2] F94-F105 (2013).

[68] O. A. Marina, N. L. Canfield, and J. W. Stevenson, "Thermal, electrical, and electrocatalytical properties of lanthanum-doped strontium titanate," *Solid State Ionics,***149**[1–2] 21-28 (2002).

[69] J. C. Ruiz-Morales, J. Canales-Vázquez, C. Savaniu, D. Marrero-López, W. Zhou, and J. T. S. Irvine, "Disruption of extended defects in solid oxide fuel cell anodes for methane oxidation," *Nature,***439**[7076] 568-71 (2006).

[70] S. W. Tao, J. T. S. Irvine, and J. A. Kilner, "An Efficient Solid Oxide Fuel Cell Based upon Single-Phase Perovskites," *Adv. Mater. (Weinheim, Ger.),***17**[14] 1734-37 (2005).

[71] Y. H. Huang, R. I. Dass, Z. L. Xing, and J. B. Goodenough, "Double perovskites as anode materials for solid-oxide fuel cells," *Science,***312**[5771] 254-57 (2006).

[72] R. J. Gorte and J. M. Vohs, "Catalysis in Solid Oxide Fuel Cells," *Annu Rev Chem Biomol Eng,***2**[1] 9-30 (2011).

73 R. J. Gorte, S. Park, J. M. Vohs, and C. Wang, "Anodes for direct oxidation of dry hydrocarbons in a solid-oxide fuel cell," *Adv. Mater. (Weinheim, Ger.),***12**[19] 1465-69 (2000).

[74] T. Z. Sholklapper, H. Kurokawa, C. P. Jacobson, S. J. Visco, and L. C. De Jonghe, "Nanostructured solid oxide fuel cell electrodes," *Nano Lett.,***7**[7] 2136-41 (2007).

[75] J.-S. Park, I. D. Hasson, M. D. Gross, C. Chen, J. M. Vohs, and R. J. Gorte, "A high-performance solid oxide fuel cell anode based on lanthanum strontium vanadate," *J. Power Sources,***196**[18] 7488-94 (2011).

[76] Z. Cheng, S. Zha, L. Aguilar, and M. Liu, "Chemical, electrical, and thermal properties of strontium doped lanthanum vanadate," *Solid State Ionics,***176**[23–24] 1921-28 (2005).

[77] L. Adijanto, V. Balaji Padmanabhan, K. J. Holmes, R. J. Gorte, and J. M. Vohs, "Physical and electrochemical properties of alkaline earth doped, rare earth vanadates," *J. Solid State Chem.,***190**[0] 12-17 (2012).

[78] L. K. Taek, H. S. Yoon, J. S. Ahn, and E. D. Wachsman, "Bimodally integrated anode functional layer for lower temperature solid oxide fuel cells," *J. Mater. Chem.*,**22** 17113-20 (2012).

[79] L. C. De Jonghe, C. P. Jacobson, and S. J. Visco, "Supported Electrolyte Thin Film Synthesis of Solid Oxide Fuel Cells," *Annu. Rev. Mater. Res.*,**33**[1] 169-82 (2003).

[80] S. Le, K. N. Sun, N. Zhang, X. Zhu, H. Sun, Y. X. Yuan, and X. Zhou, "Fabrication and evaluation of anode and thin Y_2O_3-stabilized ZrO_2 film by co-tape casting and co-firing technique," *J. Power Sources,***195**[9] 2644-48 (2010).

[81] M. C. Verbraeken, B. Iwanschitz, A. Mai, and J. T. S. Irvine, "Evaluation of Ca Doped $La_{0.2}Sr_{0.7}TiO_3$ as an Alternative Material for Use in SOFC Anodes," *J. Electrochem. Soc.,***159**[11] F757-F62 (2012).

[82] C.-D. Savaniu, D. N. Miller, and J. T. S. Irvine, "Scale Up and Anode Development for La-Doped $SrTiO_3$ Anode-Supported SOFCs," *J. Am. Ceram. Soc.,* **96**[6] 1718–23 (2013).

[83] C. M. An, J.-H. Song, I. Kang, and N. Sammes, "The effect of porosity gradient in a Nickel/Yttria Stabilized Zirconia anode for an anode-supported planar solid oxide fuel cell," *J. Power Sources,***195**[3] 821-24 (2010).

[84] J-S. Kim, V. V. Nair, J. M. Vohs, and R. J. Gorte, "A study of the methane tolerance of LSCM–YSZ composite anodes with Pt, Ni, Pd and ceria catalysts," *Scr. Mater.*,**65**[2] 90-95 (2011).

[85] M. Cassidy, G. Lindsay, and K. Kendall, "The reduction of nickel zirconia cermet anodes and the effects on supported thin electrolytes," *J. Power Sources,***61**[1–2] 189-92 (1996).).

[86] N. L. Wieder, M. Cargnello, K. Bakhmutsky, T. Montini, P. Fornasiero, and R. J. Gorte, "Study of the Water-Gas-Shift Reaction on $Pd@CeO_2/Al_2O_3$ Core-Shell Catalysts," *J. Phys. Chem. C,***115**[4] 915-19 (2011).

[87] R. Küngas, A. S. Yu, J. Levine, J. M. Vohs, and R. J. Gorte, "An Investigation of Oxygen Reduction Kinetics in LSF Electrodes," *J. Electrochem. Soc.*,**160**[2] F205-F11 (2013).

88 S. Somiya, F. Aldinger, N. Claussen, R.M. Spriggs, K. Uchino, K. Koumoto and M. Kaneno, Handbook of Advanced Ceramics. Volume II: Processing and Their Applications. Academic Press, Oxford, 2003.

[89] A. Torabi, A. R. Hanifi, T. H. Etsell, and P. Sarkar, "Effects of Porous Support Microstructure on Performance of Infiltrated Electrodes in Solid Oxide Fuel Cells," *J. Electrochem. Soc.*,**159[**2] B201-B10 (2012).

[90] T. Ohji, "Microstructural Design and Mechanical Properties of Porous Silicon Nitride Ceramics," *Mater. Sci. Eng.: A*,**498[**1–2] 5-11 (2008).

[91] J. R. Wilson, W. Kobsiriphat, R. Mendoza, H.-Y. Chen, J. M. Hiller, D. J. Miller, K. Thornton, P. W. Voorhees, S. B. Adler, and S. A. Barnett, "Three-dimensional Reconstruction of a Solid-oxide-fuel-cell Anode," *Nat. Mater.*,**5[**7] 541-44 (2006).

[92] S. W. Sofie, "Fabrication of Functionally Graded and Aligned Porosity in Thin Ceramic Substrates with the Novel Freeze-tape-casting Process," *J. Am. Ceram. Soc.*,**90[**7] 2024-31 (2007).

[93] J. Mizusaki, K. Waragai, S. Tsuchiya, H. Tagawa, Y. Arai, and Y. Kuwayama, "Simple Mathematical Model for the Electrical Conductivity of Highly Porous Ceramics," *J. Am. Ceram. Soc.*,**79**[1] 109-13 (1996).

[94] J. Kim, J. Peretti, K. Lahlil, J.-P. Boilot, and T. Gacoin, "Optically Anisotropic Thin Films by Shear-oriented Assembly of Colloidal Nanorods," *Adv. Mater. (Weinheim, Ger.)*, Doi: 10.1002/Adma.201300594 (2013).

[95] A. D. Rey and M. M. Denn, "Dynamical Phenomena in Liquid-crystalline Materials," *Annu. Rev. Fluid Mech.*,**34[**1] 233-66 (2002).

[96] T. Isobe, Y. Kameshima, A. Nakajima, and K. Okada, "Preparation and properties of porous alumina ceramics with uni-directionally oriented pores by extrusion method using a plastic substance as a pore former," *J. Eur. Ceram. Soc.*,**27**[1] 61-66 (2007).

[97] M. J. Zhi, N. Mariani, R. Gemmen, K. Gerdes, and N. Q. Wu, "Nanofiber Scaffold for Cathode of Solid Oxide Fuel Cell," *Energy Environ. Sci.*,**4[**2] 417-20 (2011).

[98] C.S. Ni, M. Cassidy and J. T. S. Irvine, “Image Analysis of the Porous Yttria-Stabilized Zirconia (YSZ) Structure for the Impregnated Electrode of Solid Oxide Fuel Cell (SOFC)," to be published.

[99] J. L. Jones, B. J. Iverson, and K. J. Bowman, "Texture and Anisotropy of Polycrystalline Piezoelectrics," *J. Am. Ceram. Soc.*,**90[**8] 2297-314 (2007).

[100] A. Heunisch, A. Dellert, and A. Roosen, "Effect of Powder, Binder and Process Parameters on Anisotropic Shrinkage in Tape Cast Ceramic Products," *J. Eur. Ceram. Soc.*,**30[**16] 3397-406 (2010).

[101] F. V. Dimarcello, P. L. Key, and J. C. Williams, "Preferred Orientation in Al_2O_3 Substrates," *J. Am. Ceram. Soc.*,**55[**10] 509-14 (1972).

[102] S. Tanaka, Y. Kuwano, and K. Uematsu, "Packing Structure of Particles in a Green Compact and Its Influence on Sintering Deformation," *J. Am. Ceram. Soc.*,**90[**11] 3717-19 (2007).

[103] K. Uematsu, S. Ohsaka, N. Shinohara, and M. Okumiya, "Grain-Oriented Microstructure of Alumina Ceramics Made through the Injection Molding Process," *J. Am. Ceram. Soc.*,**80[**5] 1313-15 (1997).

[104] O. Guillon, L. Weiler, and J. Rödel, "Anisotropic Microstructural Development During the Constrained Sintering of Dip-Coated Alumina Thin Films," *J. Am. Ceram. Soc.*,**90[**5] 1394-400 (2007).

[105] X. Wang and A. Atkinson, "Microstructure Evolution in Thin Zirconia Films: Experimental Observation and Modelling," *Acta Mater.*,**59[**6] 2514-25 (2011).

[106] E. A. Olevsky, "Theory of Sintering: From Discrete to Continuum," *Mater. Sci. Eng. R-Rep.*,**23[**2] 41-100 (1998).

[107] J. S. Patwardhan and W. R. Cannon, "Factors Influencing Anisotropic Sintering Shrinkage in Tape-cast Alumina: Effect of Processing Variables," *J. Am. Ceram. Soc.*,**89[**10] 3019-26 (2006).

[108] M. I. Zainuddin, S. Tanaka, R. Furushima, and K. Uematsu, "Influence of Particles Packing in Granules on the Particles Orientation in Compacts," *J. Eur. Ceram. Soc.*,**31[**1-2] 3-11 (2011).

[109] A. Dellert, A. Heunisch, and A. Roosen, "The Origin of Anisotropic Shrinkage in Tape-cast Green Tapes," *Int. J. Appl. Ceram. Technol.*,**8[**6] 1312-19 (2011).

[110] G. Besendörfer and A. Roosen, "Particle Shape and Size Effects on Anisotropic Shrinkage in Tape-cast Ceramic Layers," *J. Am. Ceram. Soc.*,**91[**8] 2514-20 (2008).

[111] J.-B. Ollagnier, O. Guillon, and J. Rödel, "Effect of Anisotropic Microstructure on the Viscous Properties of an LTCC Material," *J. Am. Ceram. Soc.*,**90[**12] 3846-51 (2007).

[112] R. Mücke, N. H. Menzler, H. P. Buchkremer, and D. Stöver, "Cofiring of Thin Zirconia Films During Sofc Manufacturing," *J. Am. Ceram. Soc.*,**92** S95-S102 (2009).

[113] J.-S. Kim, R. A. Rudkin, X. Wang, and A. Atkinson, "Constrained Sintering Kinetics of 3YSZ Films," *J. Eur. Ceram. Soc.*,**31[**13] 2231-39 (2011).

[114] D. W. Ni, E. Olevsky, V. Esposito, T. T. Molla, S. P. V. Foghmoes, R. Bjørk, H. L. Frandsen, E. Aleksandrova, and N. Pryds, "Sintering of Multilayered Porous Structures: Part II–Experiments and Model Applications," *J. Am. Ceram. Soc.*, (2013). Doi: 10.1111/Jace.12374

[115] W. R. Cannon and P. M. Raj, "Evolution of Sintering Anisotropy Using a 2D Finite Difference Method," *J. Am. Ceram. Soc.*,**92[**7] 1391-95 (2009).

[116] P. M. Raj, A. Odulena, and W. R. Cannon, "Anisotropic Shrinkage During Sintering of Particle-oriented Systems—Numerical Simulation and Experimental Studies," *Acta Mater.*,**50[**10] 2559-70 (2002).

[117] L. Amaral, C. Jamin, A. M. R. Senos, P. M. Vilarinho, and O. Guillon, "Constrained sintering of $BaLa_4Ti_4O_{15}$ thick films: Pore and grain anisotropy," *J. Eur. Ceram. Soc.*,**33[**10] 1801-08 (2013).

[118] M. Albano, L. Garrido, K. Plucknett, and L. Genova, "Influence of Starch Content and Sintering Temperature on the Microstructure of Porous Yttria-stabilized Zirconia Tapes," *J. Mater. Sci.*,**44[**10] 2581-89 (2009).

[119] R. Zuo, E. Aulbach, R. K. Bordia, and J. Rödel, "Critical Evaluation of Hot Forging Experiments: Case Study in Alumina," *J. Am. Ceram. Soc.*,**86[**7] 1099-105 (2003).

[120] A. Shui, Z. Kato, S. Tanaka, N. Uchida, and K. Uematsu, "Sintering Deformation Caused by Particle Orientation in Uniaxially and Isostatically Pressed Alumina Compacts," *J. Eur. Ceram. Soc.*,**22[**3] 311-16 (2002).

[121] Y. Zhao and L. R. Dharani, "Theoretical-Model for the Analysis of a Ceramic Thin-Film Sintering on a Non-Sintering Substrate," *Thin Solid Films,* **245[**1-2] 109-14 (1994).

[122] H. L. Zhang, J. F. Li, and B. P. Zhang, "Microstructure and Electrical Properties of Porous Pzt Ceramics Derived From Different Pore-forming Agents," *Acta Mater.,* **55**1 171-81 (2007).

[123] C. L. Martin, H. Camacho-Montes, L. Olmos, D. Bouvard, and R. K. Bordia, "Evolution of Defects During Sintering: Discrete Element Simulations," *J. Am. Ceram. Soc.,* **92**7 1435-41 (2009).

[124] J. M. Ralph, C. Rossignol, and R. Kumar, "Cathode Materials for Reduced-Temperature SOFCs," *J. Electrochem. Soc.*, **150**[11] A1518-A22 (2003).

[125] Adijanto, R. Küngas, F. Bidrawn, R. J. Gorte, and J. M. Vohs, "Stability and Performance of Infiltrated $La_{0.8}Sr_{0.2}Co_xFe_{1-x}O_3$ Electrodes with and without $Sm_{0.2}Ce_{0.8}O_{1.9}$ Interlayers," *J. Power Sources*, **196**[14] 5797-802 (2011).

[126] Y. Y. Huang, K. Ahn, J. M. Vohs, and R. J. Gorte, "Characterization of Sr-doped $LaCoO_3$-YSZ Composites Prepared by Impregnation Methods," *J. Electrochem. Soc.*, **151**[10] A1592-A97 (2004).

[127] F. Bidrawn, G. Kim, N. Aramrueang, J. M. Vohs, and R. J. Gorte, "Dopants to Enhance SOFC Cathodes Based on Sr-doped $LaFeO_3$ and $LaMnO_3$," *J. Power Sources*, **195**[3] 720-28 (2010).

[128] J. Hojberg and M. Sogaard, "Impregnation of LSM Based Cathodes for Solid Oxide Fuel Cells," *Electrochem. Solid-State Lett.*, **14**[7] B77-B79 (2011).

[129] J. C. Ruiz-Morales, D. Marrero-Lopez, M. Galvez-Sanchez, J. Canales-Vazquez, C. Savaniu, and S. N. Savvin, "Engineering of Materials for Solid Oxide Fuel Cells and Other Energy and Environmental Applications," *Energy Environ. Sci.*, **3**[11] 1670-81 (2010).

[130] J. C. Ruiz-Morales, J. Canales-Vazquez, J. Pena-Martinez, D. Marrero-Lopez, J. T. S. Irvine, and P. Nunez, "Microstructural Optimisation of Materials for SOFC Applications Using PMMA Microspheres," *J. Mater. Chem.*, **16**[6] 540-42 (2006).

[131] J. S. Cronin, J. R. Wilson, and S. A. Barnett, "Impact of Pore Microstructure Evolution on Polarization Resistance of Ni-Yttria-stabilized Zirconia Fuel Cell Anodes," *J. Power Sources*, **196**[5] 2640-43 (2011).

[132]J. H. Lee, J. W. Heo, D. S. Lee, J. Kim, G. H. Kim, H. W. Lee, H. S. Song, and J. H. Moon, "the Impact of Anode Microstructure on the Power Generating Characteristics of SOFC," *Solid State Ionics*, **158**[3-4] 225-32 (2003).

[133]A. T. Duong and D. R. Mumm, "Microstructural Optimization by Tailoring Particle Sizes for LSM-YSZ Solid Oxide Fuel Cell Composite Cathodes," *J. Electrochem. Soc.*, **159**[1] B40-B53 (2012).

[134]S. Chung and M. W. King, "Design Concepts and Strategies for Tissue Engineering Scaffolds," *Biotechnol. Appl. Biochem.*, **58**[6]423-38 (2011).

[135] M. Y. M. Chiang, X. Wang, F. A. Landis, J. Dunkers, and C. R. Snyder, "Quantifying the Directional Parameter of Structural Anisotropy in Porous Media," *Tissue Eng.*, **12[**6] 1597-606 (2006).

[136]Volker Baecker, Workshop: image processing and analysis with ImageJ Image Analyzer, 2010, page 69-70 www.mri.cnrs.fr/datas/fichiers/articles/60/183.pdf

[137]A. Wonisch, O. Guillon, T. Kraft, M. Moseler, H. Riedel, and J. Rödel, "Stress-induced Anisotropy of Sintering Alumina: Discrete Element Modelling and Experiments," *Acta Mater.*, **55**[15] 5187-99 (2007).

[138] W. H. Rhodes, "Agglomerate and Particle Size Effects on Sintering Yttria-Stabilized Zirconia," *J. Am. Ceram. Soc.*, **64**[1] 19-22 (1981).

[139] Z. Zhan, D. M. Bierschenk, J. S. Cronin, and S. A. Barnett, "A Reduced Temperature Solid Oxide Fuel Cell with Nanostructured Anodes," *Energy Environ. Sci.*, **4[**10] 3951-54 (2011).

[140]K. Yamahara, C. P. Jacobson, S. J. Visco, and L. C. De Jonghe, "Influence of Powders on Ionic Conductivity of Polycrystalline Zirconias," pp. 187-95. in Solid Oxide Fuel Cells Viii, **Vol. 2003.** Edited by S. C. Singhal and M. Dokiya, 2003.

[141]F. Bidrawn, J. M. Vohs, and R. J. Gorte, "Fabrication of LSM-YSZ Composite Electrodes by Electrodeposition," *J. Electrochem. Soc.*, **157**[11] B1629-B33 (2010).

[142]W. Zhu, D. Ding, and C. Xia, "Enhancement in Three-phase Boundary of SOFC Electrodes by an Ion Impregnation Method: A Modeling Comparison," *Electrochem. Solid-State Lett.*, **11**[6] B83-B86 (2008).

[143] T. J. Armstrong and J. G. Rich, "Anode-Supported Solid Oxide Fuel Cells with $La_{0.6}Sr_{0.4}CoO_{3-}$ $Zr_{0.84}Y0_{.16}O_{2-\delta}$ Composite Cathodes Fabricated by an Infiltration Method," *J. Electrochem. Soc.*,**153[**3] A515-A20 (2006).

[144] N. P. Brandon, S. Skinner, and B. C. H. Steele, "Recent Advances in Materials for Fuel Cells," *Annu. Rev. Mater. Res.*,**33[**1] 183-213 (2003).

[145] Y. Takeda, R. Kanno, M. Noda, Y. Tomida, and O. Yamamoto, "Cathodic Polarization Phenomena of Perovskite Oxide Electrodes with Stabilized Zirconia," *J. Electrochem. Soc.*,**134[**11] 2656-61 (1987).

[146] M. E. Lynch, L. Yang, W. Qin, J.-J. Choi, M. Liu, K. Blinn, and M. Liu, "Enhancement of $La_{0.6}Sr_{0.4}Co_{0.2}Fe_{0.8}O_{3-\delta}$ durability and surface electrocatalytic activity by $La_{0.85}Sr_{0.15}MnO_{3\pm\delta}$ investigated using a new test electrode platform," *Energ. & Environ. Sci.*,**4[**6] 2249-58 (2011).

[147] C. C. Kan and E. D. Wachsman, "Identifying Drivers of Catalytic Activity Through Systematic Surface Modification of Cathode Materials," *J. Electrochem. Soc.*,**156[**6] B695-B702 (2009).

[148] K. Yamahara, C. P. Jacobson, S. J. Visco, X. F. Zhang, and L. C. de Jonghe, "Thin film SOFCs with cobalt-infiltrated cathodes," *Solid State Ionics*,**176[**3-4] 275-79 (2005).

149 K. Yamahara, C. P. Jacobson, S. J. Visco, and L. C. De Jonghe, "Catalyst-infiltrated supporting cathode for thin-film SOFCs," *Solid State Ionics*,**17**[65–6] 451-56 (2005).

[150] Q. S. Zhang and T. Yasuo, "Transition metal oxide infiltration effect on the performance of LSM-YSZ cathode," *Chin. J. Inorg. Chem.*,**23[**7] 1287-90 (2007).

[151] Y. Y. Huang, J. M. Vohs, and R. J. Gorte, "An examination of LSM-LSCo mixtures for use in SOFC cathodes," *J. Electrochem. Soc.*,**153[**6] A951-A55 (2006).

[152] C. Lu, T. Z. Sholklapper, C. P. Jacobson, S. J. Visco, and L. C. D. Jonghe, "LSM-YSZ Cathodes with Reaction-Infiltrated Nanoparticles," *J. Electrochem. Soc.*,**153[**6] A1115-A19 (2006).

[153] U. F. Vogt, P. Holtappels, J. Sfeir, J. Richter, S. Duval, D. Wiedenmann, and A. Züttel, "Influence of A-Site Variation B-Site Substitution on the Physical Properties of (La,Sr)FeO_3 Based Perovskites," *Fuel Cells*,**9[**6] 899-906 (2009).

[154] U. F. Vogt, J. Sfeir, J. Richter, C. Soltmann, and P. Holtappels, "B-site substituted lanthanum strontium ferrites as electrode materials for electrochemical applications," *Pure Appl. Chem.*,**80[**11] 2543-52 (2008).

[155] P. K. Gallagher, F. Schrey, and B. Prescott, "The thermal decomposition of aqueous manganese (II) nitrate solution," *Thermochim. Acta*,**2**[5] 405-12 (1971).

[156] S. P. Jiang, J. G. Love, and Y. Ramprakash, "Electrode behaviour at (La,Sr)MnO_3/Y_2O_3–ZrO_2 interface by electrochemical impedance spectroscopy," *J. Power Sources*,**110[**1] 201-08 (2002).

[157] G. J. la O' and Y. Shao-Horn, "Oxygen Surface Exchange Kinetics on Sr-Substituted Lanthanum Manganite and Ferrite Thin-Film Microelectrodes," *J. Electrochem. Soc.*,**156**7 B816-B24 (2009).

[158] Y. Huang, J. M. Vohs, and R. J. Gorte, "SOFC cathodes prepared by infiltration with various LSM precursors," *Electrochem. Solid-State Lett.*,**9**5 A237-A40 (2006).

[159] J. H. Joo and G. M. Choi, "Electrical conductivity of YSZ film grown by pulsed laser deposition," *Solid State Ionics*,**177[**11–12] 1053-57 (2006).

[160] L. W. Tai, M. M. Nasrallah, H. U. Anderson, D. M. Sparlin, and S. R. Sehlin, "Structure and electrical properties of $La_{1-x}Sr_xCo_{1-y}Fe_yO_3$. Part 1. The system $La_{0.8}Sr_{0.2}Co_{1-y}Fe_yO_3$," *Solid State Ionics*,**76**3[4] 259-71 (1995).

[161] T. Montini, M. Bevilacqua, E. Fonda, M. F. Casula, S. Lee, C. Tavagnacco, R. J. Gorte, and P. Fornasiero, "Relationship between Electrical Behavior and Structural Characteristics in Sr-Doped $LaNi_{0.6}Fe_{0.4}O_{3-\delta}$ Mixed Oxides," *Chem. Mater.*,**21[**8] 1768-74 (2009).

[162] S. Wang, A. Verma, Y. L. Yang, A. J. Jacobson, and B. Abeles, "The effect of the magnitude of the oxygen partial pressure change in electrical conductivity relaxation measurements: oxygen transport kinetics in $La_{0.5}Sr_{0.5}CoO_{3-\delta}$," *Solid State Ionics*,**140-**1-2] 125-33 (2001).

[163] R. Chiba, F. Yoshimura, and Y. Sakurai, "An investigation of $LaNi_{1-x}Fe_xO_3$ as a cathode material for solid oxide fuel cells," *Solid State Ionics*,**124[**3-4] 281-88 (1999).

[164] M. Petitjean, G. Caboche, E. Siebert, L. Dessemond, and L. C. Dufour, "$(La_{0.8}Sr_{0.2})(Mn_{1-y}Fe_y)O_{3\pm\delta}$ oxides for ITSOFC cathode materials?: Electrical and ionic transport properties," *J. Eur. Ceram. Soc.*,**25[**12] 2651-54 (2005).

[165] F. Tietz, I. Arul Raj, M. Zahid, and D. Stöver, "Electrical conductivity and thermal expansion of $La_{0.8}Sr_{0.2}(Mn,Fe,Co)O_{3-\delta}$ perovskites," *Solid State Ionics,***177[**19]–25 1753-56 (2006).

[166] S. Lee, M. Bevilacqua, P. Fornasiero, J. M. Vohs, and R. J. Gorte, "Solid oxide fuel cell cathodes prepared by infiltration of $LaNi_{0.6}Fe_{0.4}O_3$ and $La_{0.91}Sr_{0.09}Ni_{0.6}Fe_{0.4}O_3$ in porous yttria-stabilized zirconia," *J. Power Sources,***193[**2] 747-53 (2009).

[167] E. V. Tsipis, E. A. Kiselev, V. A. Kolotygin, J. C. Waerenborgh, V. A. Cherepanov, and V. V. Kharton, "Mixed conductivity, Mössbauer spectra and thermal expansion of $(La,Sr)(Fe,Ni)O_{3-\delta}$ perovskites," *Solid State Ionics,***179[**38] 2170-80 (2008).

[168] R. Chiba, F. Yoshimura, and Y. Sakurai, "Properties of $La_{1-y}Sr_yNi_{1-x}Fe_xO_3$ as a cathode material for a low-temperature operating SOFC," *Solid State Ionics,***152–153[**0] 575-82 (2002).

[169] G. Amow and S. Skinner, "Recent developments in Ruddlesden–Popper nickelate systems for solid oxide fuel cell cathodes," *J. Solid State Electrochem.,***10[**8] 538-46 (2006).

[170] E. Boehm, J. M. Bassat, M. C. Steil, P. Dordor, F. Mauvy, and J. C. Grenier, "Oxygen transport properties of $La_2Ni_{1-x}Cu_xO_{4+\delta}$ mixed conducting oxides," *Solid State Sci.,***5[**7] 973-81 (2003).

[171] J. H. Kuo, H. U. Anderson, and D. M. Sparlin, "Oxidation-reduction behavior of undoped and Sr-doped $LaMnO_3$: Defect structure, electrical conductivity, and thermoelectric power," *J. Solid State Chem.,***87[**1] 55-63 (1990).

[172] M. Bevilacqua, T. Montini, C. Tavagnacco, E. Fonda, P. Fornasiero, and M. Graziani, "Preparation, Characterization, and Electrochemical Properties of Pure and Composite $LaNi_{0.6}Fe_{0.4}O_3$-Based Cathodes for IT-SOFC," *Chem. Mater.,***19[**24] 5926-36 (2007).

[173] S. J. Skinner and J. A. Kilner, "Oxygen diffusion and surface exchange in $La_{2-x}Sr_xNiO_{4+\delta}$," *Solid State Ionics,***135[**1–4] 709-12 (2000).

[174] S. J. Skinner and J. A. Kilner, "A comparison of the transport properties of $La_{2-x}Sr_xNi_{1-y}Fe_yO_{4+\delta}$ where $0<x<0.2$ and $0<y<0.2$," *Ionics,***5[**3-4] 171-74 (1999).

[175] J. C. Grenier, F. Mauvy, C. Lalanne, J.-M. Bassat, F. Chauveau, J. Mougin, J. Dailly, and M. Marrony, "$A_2MO_{4+\delta}$ Oxides: Flexible Electrode Materials for Solid Oxide Cells," *ECS Trans.*,**25[**2] 2537-46 (2009).

[176] E. Y. Konysheva, X. Xu, and J. T. S. Irvine, "On the Existence of A-Site Deficiency in Perovskites and Its Relation to the Electrochemical Performance," *Adv. Mater. (Weinheim, Ger.)*,**24[**4] 528-32 (2012).

[177] J. Cheng, A. Navrotsky, X.-D. zhou, and H. U. Anderson, "Enthalpies of Formation of $LaMO_3$ Perovskites (M = Cr, Fe, Co, and Ni)," *J. Mater. Res.*,**20[**01] 191-200 (2011).

[178] T. Striker, J. A. Ruud, Y. Gao, W. J. Heward, and C. Steinbruchel, "A-site deficiency, phase purity and crystal structure in lanthanum strontium ferrite powders," *Solid State Ionics*,**178[**21–22] 1326-36 (2007).

[179]K. T. Jacob and M. Attaluri, "Refinement of thermodynamic data for $LaMnO_3$," *J. Mater. Chem.*,**13[**4] 934-42 (2003).